

**IMPROVING OPTICAL TRAP MEASUREMENTS  
WITH ADAPTIVE NONLINEAR CONTROL  
METHODS**

by

**Jason Gregory Pickel**

B.S. Mechanical Engineering, University of Pittsburgh, 2007

M.S. Mechanical Engineering, University of Pittsburgh, 2009

Submitted to the Graduate Faculty of  
the Swanson School of Engineering in partial fulfillment  
of the requirements for the degree of  
Ph.D. in Mechanical Engineering

University of Pittsburgh

2016

UNIVERSITY OF PITTSBURGH  
SWANSON SCHOOL OF ENGINEERING

This dissertation was presented

by

Jason Gregory Pickel

It was defended on

August 29, 2016

and approved by

Daniel G. Cole, Ph.D., P.E., Associate Professor

William W. Clark, Ph.D., Professor

Jeffrey S. Viperman, Ph.D., Professor

Zhi-Hong Mao, Ph.D., Associate Professor

Lance Davidson, Ph.D., Associate Professor

Dissertation Director: Daniel G. Cole, Ph.D., P.E., Associate Professor

Copyright © by Jason Gregory Pickel  
2016

# IMPROVING OPTICAL TRAP MEASUREMENTS WITH ADAPTIVE NONLINEAR CONTROL METHODS

Jason Gregory Pickel, PhD

University of Pittsburgh, 2016

An optical trap uses radiation pressure of light to manipulate microscopic objects. The interaction between the light and the microscopic objects result in the objects experiencing optical forces. These forces are on the same order of magnitude as biological forces (typically 0.1 to 100 pN) and this feature makes optical traps appropriate for single-molecule studies. Currently, there is a growing need to create an automated optical trap that uses the entire operating range of the optical trap to study the biological forces. Spatial nonlinearities in the optical force and parameter uncertainty complicate feedback control for optical traps. A consequence is that users are spending an enormous amount of time calibrating the instrument and designing a controller, and this diverts their time away from studying the biophysics. This research explores the use of nonlinear and adaptive feedback methods to create an automated optical trap.

A model is defined to describe the coupling between the dynamics of the optical trap and molecule, and the nominal force within the molecule is treated as a disturbance. The disturbance information is obtained by creating a disturbance model and combining its dynamics with the system dynamics. The system nonlinearities are addressed by using a nonlinear Kalman filter to estimate the system state, then the system state is used in a input-output feedback linearization and linear quadratic structure to satisfy performance requirements. Statistical analyses are performed to assess the effectiveness the feedback methods have on the open-loop and closed-loop systems. Its performance is compared with that of linear integral control used in practice to quantify the performance improvement when considering

the system nonlinearities in the control design. The system nonlinearities and parameter uncertainty are addressed by using adaptive and nonlinear feedback methods. An adaptive state observer provides a simultaneous estimate of the system state and parameters, then these estimated entities are used in an adaptive input-output feedback linearization and LQ structure. The result is the creation of an automated self-tuning optical trap that minimizes the user interaction with the instrument calibration and control design, uses the entire operating range of the optical trap, and obtains an unbiased estimate of the molecule force. The closed-loop performance of these feedback methods are demonstrated by replicating the force-extension curve of a DNA molecule.

## TABLE OF CONTENTS

<b>1.0</b>	<b>INTRODUCTION</b>	1
1.1	Motivation	1
1.2	Feedback Methods in Practice	5
1.3	Research Problem	9
1.3.1	Research Objectives	11
1.3.2	Simulations	12
1.4	Research Impact and Significance	13
1.5	Dissertation Organization	15
<b>2.0</b>	<b>OPTICAL TRAP THEORY</b>	16
2.1	Optical Forces	16
2.2	Optical Trap Considerations	20
2.3	Optical Trap Setup	22
2.3.1	Choosing the Proper Lenses	24
2.3.2	Actuation Misalignment Issues	29
2.3.3	Sensing Alignment Issues	30
2.3.4	Position Sensing Methods	32
2.3.5	Actuation Methods	33
2.4	Alignment Procedures	36
<b>3.0</b>	<b>SYSTEM CALIBRATION</b>	39
3.1	Fast Steering Mirror Calibration	39
3.2	Quadrant Photodiode Calibration	41
3.2.1	Sensor Modeling	41

3.2.2	Direct Method Calibration . . . . .	45
3.3	Optical Stiffness Calibration . . . . .	45
<b>4.0</b>	<b>OPTICAL TRAP SYSTEM DYNAMICS</b> . . . . .	<b>48</b>
4.1	Bead Deflection Dynamics . . . . .	48
4.2	Molecule and Disturbance Dynamics . . . . .	53
4.2.1	Bead-Molecule System . . . . .	57
4.2.2	Bead-Molecule-Disturbance Dynamics . . . . .	60
4.2.3	Relating The Disturbance to the Molecule Stiffness . . . . .	61
4.3	Sensor Dynamics . . . . .	63
4.4	Actuator Dynamics . . . . .	63
4.5	Optical Trap System . . . . .	65
4.5.1	Output Controllability Condition . . . . .	67
4.5.2	Observability Condition . . . . .	77
4.5.3	Separation Principle . . . . .	78
<b>5.0</b>	<b>LINEAR DESIGN</b> . . . . .	<b>79</b>
5.1	Linearized Optical Trap System . . . . .	80
5.2	State Estimation With a Kalman Filter . . . . .	80
5.3	Statistical Analysis of Kalman Filter . . . . .	83
5.4	Control Structure . . . . .	92
5.5	Statistical Analysis on Closed-Loop Composite System . . . . .	96
5.6	Linear Integral Control . . . . .	103
5.6.1	Comparison of the Linear Controllers . . . . .	113
<b>6.0</b>	<b>NONLINEAR DESIGNS</b> . . . . .	<b>114</b>
6.1	Nonlinear Kalman Filter . . . . .	115
6.2	Statistical Analysis on Nonlinear Kalman Filter . . . . .	120
6.3	Control Structure . . . . .	130
6.4	Statistical Analysis on Nonlinear Control . . . . .	135
6.5	Nonlinear PI controller . . . . .	141
<b>7.0</b>	<b>ADAPTIVE NONLINEAR DESIGN</b> . . . . .	<b>145</b>
7.1	Robustness Characteristics of Nominal Design . . . . .	146

7.2	Adaptive State Observer . . . . .	149
7.3	Adaptive Control Structure . . . . .	163
7.4	Statistical Analysis on the Closed-Loop Composite System . . . . .	175
<b>8.0</b>	<b>SIMULATIONS</b> . . . . .	<b>189</b>
8.1	Simulation Setup . . . . .	189
8.2	LQG Results . . . . .	191
8.3	Nominal Nonlinear Design Results . . . . .	196
8.4	Nonlinear PI Control Results . . . . .	204
8.4.1	Comparison Between the Nonlinear Control Methods . . . . .	204
8.5	Adaptive Nonlinear Design Results . . . . .	212
<b>9.0</b>	<b>CONCLUSION</b> . . . . .	<b>219</b>
9.1	Future Work . . . . .	222
9.1.1	Fixed gain robustness analysis . . . . .	222
9.1.2	MIMO control problem . . . . .	222
9.1.3	Magnetic Traps . . . . .	223
9.1.4	Proof of Concept Demonstration . . . . .	224
9.1.4.1	Experimental Setup . . . . .	225
9.1.4.2	Materials and Methods . . . . .	225
	<b>BIBLIOGRAPHY</b> . . . . .	<b>240</b>

## LIST OF TABLES

1	Trapping efficiency, $Q$ for polystyrene beads of different sizes and with using objectives with different NA. [1, 2]. . . . .	19
2	The focal lengths for the lens chosen in the optical trap setup. . . . .	27
3	The FSM input voltages and the corresponding laser position given in pixels to calibrate the FSM. . . . .	40
4	Relaxation times and bandwidths for representative molecules [3, 4]. . . . .	56
5	A comparison of the statistical characteristics of the estimated force disturbance obtained with the LQG design and the linear integral controller. The operating condition is $k_t = 0.1$ pN/nmnd $\kappa = 0.6384$ The molecule is stretched until its force reaches 6 pN . . . . .	113
6	The values of the dimensionless stiffness $\kappa$ for each instance the molecule force is increased by 2 pN. Each pair of $\kappa$ and $k_t$ describes an operating condition. . . . .	191
7	The values of the expected value of the estimated disturbance, molecule extension, and the molecule stiffness for each increment that are obtained using the LQG design. . . . .	195
8	The values of the expected value of the estimated disturbance, molecule extension, and the molecule stiffness for each increment that are obtained using the nominal nonlinear design. . . . .	202
9	The values of the expected value of the $\hat{z}$ , $f_d$ , and the molecule's for each increment that are obtained using the nonlinear PI design. . . . .	210
10	The lifetime of different bonds as a function of force. Source [5]. . . . .	226
11	Material used for the Apa1 restriction digest. . . . .	230

12	Nanodrop results after the APA1 digests to determine the sample density and the DNA purity. . . . .	233
13	Nanodrop results after the APA1 digests with ethanol precipitation. The Nanodrop determines the sample density and the DNA purity. . . . .	233
14	Nanodrop results after using the second restriction enzyme Sph1 . . . . .	238
15	Nanodrop results after using the second restriction enzyme Sph1 and concentrating the sample. . . . .	238
16	Nanodrop results after double labeling the DNA . . . . .	238

## LIST OF FIGURES

1	<p>Schematic of how individual light rays applies forces on a bead. When the bead is displaced from the focus, optical forces act on the bead to pull it back. A) The bead is displaced downstream from the focus and forces pull the bead upstream. B) The bead is displaced upstream from the focus and the forces pull the bead downstream. C) The bead is displaced off axis of the focus and forces pull the bead back to the axis. . . . .</p>	18
2	<p>A schematic showing the absorption properties for deoxyhemoglobin Hb, oxyhemoglobin HbO<sub>2</sub> and water H<sub>2</sub>O as a function of the wavelength of light. Longer wavelengths in the infrared regime provide better health for biological material because biological material becomes more transparent while the laser energy becomes absorbed by the surrounding water. Source [6]. . . . .</p>	21
3	<p>The schematic of the optical trap setup. The laser beam expands then is collimated with the collimating lens <math>f_1</math>. The collimated light is directed with mirrors to the fast steering mirror (FSM), that is placed at the back Fourier plane of the objective. Then, the light gets expanded by a telescope (<math>f_2</math> and <math>f_3</math>) before entering the microscope's epi-flourence port. Once inside the microscope, the light is redirected with a dichroic mirror to the objective, which focuses the light to the specimen plane. The condenser collects the forward scattered light, which is redirected by a second dichroic mirror to the QPD. . . . .</p>	23
4	<p>The transmission plot for the Zeiss Plan-Apochromat 63x/1.4 NA objective. When the laser has a wavelength of 1064 nm then the resulting laser power at the specimen plan is ~30% of its input power at the objective. . . . .</p>	24

5	A schematic of a cascaded system of three lens that is in between the FSM placed at the object plane and the specimen plane placed at the image plane. The FSM being placed at the BFP of the objective allows for FSM angle inputs be turned into lateral translations of the laser in the specimen plane. . . . .	26
6	A schematic of the sensing system. The sensing system is composed of the condenser, collimating lens, and the QPD. . . . .	28
7	A schematic showing the effects positional misplacements of the optical components on the Fourier transform property of the cascaded three lens system.	29
8	A schematic showing the effects positional misplacements of the optical components on the QPD measurements. . . . .	31
9	Schematic of QPD position detection system. The forward scattered light that is refracted by the dielectric bead is collected by the condenser and transmitted to the QPD. The QPD is located at the BFP of the condenser. . . . .	34
10	Schematic of the intensity profiles at the QPD's surface. When the bead deflection is zero, the resulting intensity profile is symmetric at the QPD. If the bead deflection becomes nonzero, then the resulting intensity profile becomes antisymmetric in the direction of the bead deflection. . . . .	35
11	The coordinate notation used for the QPD modeling. . . . .	42
12	Schematics of the QPD response. Figure (12a) shows the QPD intensity verses bead displacement and figure (12b) shows the QPD sensitivity verses bead displacement. . . . .	44
13	The sensitivity as a function of (13a) the bead radius and (13b) the condenser NA . . . . .	44
14	The QPD response to scanning the laser across a 3 $\mu\text{m}$ diameter polystyrene bead. . . . .	46
15	Schematic of the dimensionless optical force $f_t(z)/(kl_t)$ verses the dimensionless bead's deflection $z/l_t$ and the dimensionless optical stiffness $k_{opt}(z)/k$ verses the dimensionless bead's deflection. . . . .	49

16	A schematic that compares both the dimensionless nonlinear optical force and the dimensionless linear optical force verses the dimensionless bead deflection. This comparison shows that the linearization provides a good approximation when the dimensionless bead deflection is such that $z/l_t \lesssim 0.2$ . The linearization provides a poor approximation when the dimensionless bead deflection is such that $z/l_t > 0.2$ . . . . .	50
17	A schematic that shows the different forces acting on dielectric bead within the optical trap. and the relationship between the different extensions. These forces include an optical force, a viscous drag force, Brownian noise, and the molecule's force. The extensions are the molecule extensions $x_m$ , the bead deflection $z$ , and the laser position $x_t$ . . . . .	51
18	A schematic of the dimensionless molecule force verses the dimensionless molecule extension. . . . .	54
19	A root locus that graphical shows how the poles of the trap-molecule system change when the value of the dimensionless constant $\kappa$ is increased. . . . .	59
20	A root locus showing how increasing the value of $\frac{\bar{d}_m}{l_m}$ affects the value of $\frac{\bar{x}_m}{l_m}$ . . . . .	62
21	Bode plot of actuation dynamics relating the laser position in the specimen plane to the voltage input of the FSM. . . . .	64
22	The block diagram for the optical trap system. The optical trap system is the plant in this research. . . . .	65
23	A schematic of the estimation bandwidth obtained using a Kalman filter. For a given $\kappa$ , as $k_t$ is increased, the estimation bandwidth has an initial high slope, then the slope changes and becomes small in the same direction. For a given $k_t$ , increasing $\kappa$ (the molecule is becoming stiffer) results in the estimation bandwidth increasing. . . . .	85

24	A schematic for the variance of the bead deflection and its estimate obtained using a Kalman filter. For a given $\kappa$ , increasing $k_t$ (also $k_m$ is increased to maintain a constant $\kappa$ ) results in a decrease in the variance for the state and estimated state; a stiffer optical trap and molecule reduces the variance. Then, for a given $k_t$ , an increase in $\kappa$ (a stiffer molecule) results in an decrease in the variance for the state and an increase in variance for the estimated state. . . . .	88
25	A schematic for the variance of the molecule extension and its estimate obtained using a Kalman filter. For a given $\kappa$ , increasing $k_t$ (also $k_m$ is increased to maintain a constant $\kappa$ ) results in a decrease in the variance for the states and their estimates; a stiffer optical trap and molecule reduces the variance. Then, for a given $k_t$ , an increase in $\kappa$ (a stiffer molecule) results in an decrease in the variance for the state and estimated state. . . . .	89
26	A schematic for the variance of the estimated disturbance obtained using a Kalman filter. For a given $\kappa$ , an increase in $k_t$ ( $k_m$ is also increased to maintain $\kappa$ ) initially reduces the variance quickly, then the variance decreases slowly. Then, for a constant $k_t$ , an increase in $\kappa$ (the molecule becoming stiffer) reduces the variance. . . . .	90
27	A schematic for the SNR of the estimated force disturbance obtained using a Kalman filter. For a given $\kappa$ , increasing $k_t$ results in a decrease in the SNR. . . . .	91
28	The schematic of the block diagram for the closed-loop system. The block diagram has two feedback loops. The linearization loop (loop 1) transforms the optical trap system into normal form such that the input-output map is transformed to controllable canonical form by state feedback $u(\hat{x}, v, \ddot{r})$ . The tracking loop (loop 2) uses the controllable canonical state equation in an LQ optimal algorithm to find the state feedback $v = -K_\xi \check{\xi}(\hat{x})$ that drives the tracking error to zero. . . . .	93

29	A schematic for the variance of the bead deflection and its estimate obtained using LQG control. For a given $\kappa$ , increasing $k_t$ (also $k_m$ is increased to maintain a constant $\kappa$ ) results in a decrease in the variance for the states and their estimates; a stiffer optical trap and a stiffer molecule reduces the variance. Then, for a given $k_t$ , an increase in $\kappa$ (a stiffer molecule) results in an decrease in the variance for the states and the variance. . . . .	104
30	A schematic for the variance of the molecule extension and its estimate obtained using LQG control. For a given $\kappa$ , increasing $k_t$ (also $k_m$ is increased to maintain a constant $\kappa$ ) results in a decrease in the variance for the states and their estimates; a stiffer optical trap and a stiffer molecule reduces the variance. Then, for a given $k_t$ , an increase in $\kappa$ (a stiffer molecule) results in an decrease in the variance for the states and the variance. . . . .	105
31	The block diagram schematic of the closed-loop optical trap with integral control. In the diagram, the plant is $G_1$ , the controller is $K$ , the molecule disturbances are filtered by $G_2$ , the Brownian disturbance is filtered by $G_3$ , and the control $u$ is filtered by a phase-lead compensation filter $H$ to form $v$ . The other signals are the reference signal $r$ and the error $e$ . . . . .	107
32	A schematic of the pole-map for the plant $G_1(s)$ . . . . .	109
33	A schematic of the loop gain, sensitivity function, and the complementary sensitivity function obtained using linear integral control. . . . .	110
34	A schematic of the estimation bandwidth obtained using the nonlinear Kalman filter. The bandwidth increases with increasing $\kappa$ and is independent of the value of $k_t$ . . . . .	122
35	A schematic of the sensor gain optical bandwidth difference $\frac{1}{g_s}(\omega_t - \bar{\omega}_t)$ . The optical bandwidth difference is the additional effect the sensor noise has on the estimated bead deflection and the estimated molecule extension as the bead deflection increases. The difference is the result of the nonlinear state observer because nonlinear pseudo measurements are used to yield linear observer error dynamics. . . . .	125

- 36 A schematic for the variance of the bead deflection and its estimate obtained using a nonlinear Kalman filter. For a given  $k_t$ , increasing  $\kappa$  (a stiffer molecule), the variance of the bead deflection decreases, while the variance for the estimated bead deflection increases. The variance decreases for the bead deflection because the molecule becomes stiffer as it is extended and able to suppress the fluctuations. The variance increases for the estimated bead deflection because the estimated bead deflection experiences a greater effect from the sensor noise as  $\kappa$  increases, and this effect is a feature of the state observer. For a given  $\kappa$ , increasing  $k_t$  results in the variance decreases for the bead deflection and the estimated bead deflection. A stiffer optical trap has a larger linear operating range and is able to help suppress the fluctuations. . . . . 127
- 37 A schematic for the variance of the molecule extension and its estimate obtained using a nonlinear Kalman filter. For a given  $k_t$ , increasing  $\kappa$  (a stiffer molecule), the variance of the molecule extension decreases, while the variance for the estimated molecule extension increases. The variance decreases for the molecule extension because the molecule becomes stiffer as it is extended and is able to suppress the fluctuations. The variance increases for the estimated molecule extension because the estimated molecule extension experiences a greater effect from the sensor noise as  $\kappa$  increases, and this effect is a feature of the state observer. For a given  $\kappa$ , increasing  $k_t$  results in the variance decreases for the molecule extension and the estimated molecule extension. A stiffer optical trap has a larger linear operating range and is able to help suppress the fluctuations. . . . . 128
- 38 A schematic for the variance of the estimated disturbance obtained using a nonlinear Kalman filter. For a given  $k_t$ , the variance of the estimated disturbance decreases as  $\kappa$  is increased (the molecule is extended), and the variance is independent of the value of  $k_t$ . . . . . 129
- 39 A schematic for the SNR of the estimated force disturbance obtained using the nonlinear Kalman filter. For a given  $k_t$ , increasing  $\kappa$  results in a decrease in the SNR; for a given  $\kappa$ , increasing  $k_t$  results in the SNR decreasing. . . . . 131

40 The schematic of the block diagram for the closed-loop system. The block diagram has two feedback loops. The linearization loop (loop 1) transforms the optical trap system into normal form such that the input-output map can be linearized using state feedback. The tracking loop (loop 2) uses the linearized input-output map in an LQ optimal algorithm to find the state feedback to drive the tracking error to zero. . . . . 132

41 A schematic for the variance of the bead deflection and its estimate obtained using the closed-loop nominal nonlinear design. For a given  $k_t$ , increasing  $\kappa$  (a stiffer molecule), the variance of the bead deflection decreases, while the variance for the estimated bead deflection increases. The variance decreases for the bead deflection because the molecule becomes stiffer as its extended and able to suppress the fluctuations. The variance increases for the estimated bead deflection because the estimated bead deflection experiences a greater effect from the sensor noise as  $\kappa$  increases, and this effect is a feature of the state observer. For a given  $\kappa$ , increasing  $k_t$  results in the variance decreases for the bead deflection and the estimated bead deflection. A stiffer optical trap has a larger linear operating range and able to help suppress the fluctuations. The control reduces the variance of the estimated state when compared to that of the open-loop case. . . . . 139

42	<p>A schematic for the variance of the molecule extension and its estimate obtained using the closed-loop nominal nonlinear design. For a given <math>k_t</math>, increasing <math>\kappa</math> (a stiffer molecule), the variance of the molecule extension decreases, while the variance for the estimated molecule extension increases. The variance decreases for the molecule extension because the molecule becomes stiffer as its extended and is able to suppress the fluctuations. The variance increases for the estimated molecule extension because the estimated molecule extension experiences a greater effect from the sensor noise as <math>\kappa</math> increases, and this effect is a feature of the state observer. For a given <math>\kappa</math>, increasing <math>k_t</math> results in the variance decreases for the molecule extension and the estimated molecule extension. A stiffer optical trap has a larger linear operating range and able to help suppress the fluctuations. The control reduces the variance of the estimated state when compared to that of the open-loop case. . . . .</p>	140
43	<p>The schematic for the block diagram of the closed-loop block diagram. The block diagram has three feedback loops. The linearization loop (loop 1) transforms the optical trap system into normal form such that the input-output map can be linearized with state feedback. The tracking loop (loop 2) uses the linearized input-output map in an adaptive LQ optimal algorithm to find the state feedback to drive the tracking error to zero. The self-tuning loop (loop 3) performs the identification process and finds the online control solution. . .</p>	165
44	<p>A schematic of the bead deflection and its estimate using the LQG design. Small values are used for the weight on the tracking error in the LQ control algorithm. The result is large transients each instance the molecule is stretched.</p>	193
45	<p>A schematic of the estimated disturbance obtained using the LQG controller. The DNA molecule is extended to have its force increase in increments of 2 pN every 2 s. . . . .</p>	194

46	A schematic showing the estimation force-extension curve and the estimation error of the force-extension curve obtained using the LQG controller. As the molecule is stretched between the dimensionless extensions of 0 and 0.96, the absolute of the maximum estimation error is 0.62 pN. Also, as the molecule is further stretched closer to its contour length (the dimensionless extension $\frac{x_m}{l_m} \rightarrow 1$ ), the estimation error increases to an absolute value of 75 pN. . . . .	197
47	The response of the tracking error using LQG design. At each instance the reference signal is increased, the tracking error has an initial bias that converges to zero at steady-state. . . . .	198
48	The response of the measured bead deflection and the estimation error between the measured bead deflection and the estimated bead deflection using the LQG design. At each instance the measured bead deflection is increased, the estimation error has an initial bias that converges to zero at steady-state. . . . .	199
49	A schematic of the estimated disturbance obtained using the nominal nonlinear controller. The DNA molecule is extended to have its force increase in increments of 2 pN every 2 s. . . . .	201
50	A schematic showing the estimation force-extension curve and the estimation error of the force-extension curve obtained using the nominal nonlinear controller. As the molecule is extended between the dimensionless extensions of 0 and 0.96, the absolute of the maximum estimation error is 0.22 pN. Then, as the molecule is further extended close to its contour length (the dimensionless extension $\frac{x_m}{l_m} \rightarrow 1$ ), the estimation error increases to an estimation error with absolute value of 1.63 pN. . . . .	203
51	The response of the tracking error using the nominal nonlinear design. At each instance the reference signal is increased, the tracking error has an initial bias that converges to zero at steady-state. . . . .	205

52	The response of the measured bead deflection and the estimation error between the measured bead deflection and the estimated bead deflection using the nominal nonlinear design. At each instance the measured bead deflection is increased, the estimation error has an initial bias that converges to zero at steady-state. . . . .	206
53	The response of the reference signal and the tracking error using the nonlinear PI controller. The tracking error has zero bias for each instance the reference signal is increased. Also, the tracking error has a constant variance throughout the optical trap operating range, which is expected because of the controller linearized the input-to-state map. . . . .	207
54	The response of $\hat{z}$ using the nonlinear PI controller. The variable $\hat{z}$ converges to a new steady-state value each instance the reference signal is increased. . .	208
55	The response of the estimated molecule force using the nonlinear PI controller	209
56	A schematic of the estimation force-extension curve and the estimation curve using the nonlinear PI controller. . . . .	211
57	The response of the estimated optical bandwidth $\omega_t$ for different values of $\lambda$ . Increasing the value of $\lambda$ leads to a numerical singularity being approached quicker. The actual value for $\omega_t$ is $6189 \text{ rad s}^{-1}$ . . . . .	216
58	The response of the estimated optical bandwidth $\kappa\omega_t$ for different values of $\lambda$ . Increasing the value of $\lambda$ leads to a numerical singularity being approached quicker. The actual value for $\omega_t$ is $6189 \text{ rad s}^{-1}$ . . . . .	217
59	The response of the estimated optical bandwidth $\omega_p$ for different values of $\lambda$ . Increasing the value of $\lambda$ leads to a numerical singularity being approached quicker. The actual value for $\omega_t$ is $10 \text{ rad s}^{-1}$ . . . . .	218
60	The surface chemistry of attaching DNA to a glass surface. The glass is first cleaned with “piranha solution” to remove any dirt and to increase hydroxylation. The OH groups react with the silane attach the silane-PEG-NHS to the glass surface. The NHS group then reacts with the amino-allyl labeled end of DNA to attach DNA to the surface. Source [5]. . . . .	227

61 A schematic of the DNA preparation process. The DNA (grey) is a plasmid, or circularly configured. The first step used the restriction enzyme Apa1 (blue) to cut the plasmid to yield a linear piece of DNA with 3' overhangs. The 3' overhangs were labeled with biotin (green). A second restriction enzyme Sph1 (blue) cuts the biotin-labeled DNA into two pieces with 3' overhangs. Finally, the 3' overhangs were labeled with aminoallyl (orange). . . . . 230

62 The agarose gel electrophoresis was used to determine the success the Apa1 digest on two different DNAs (P027 and P087). Each DNA has two columns: The negative column contains no Apa1 digest while the positive sign column contains the Apa1 digest. The Apa1 digests for both DNAs show the DNA traveled less than the no Apa1 digests. This indicates the success of the Apa1 digest. . . . . 232

63 Agarose gel analysis to determine the success of the biotin labeling the 3' end of DNA. Each DNA (P027 and P087) had three reactions: Control (no streptavidin added to the biotin labeled DNA, Streptavidin or SA (streptavidin binded to the biotin labeled DNA), and Beads ( streptavidin coated beads binded to the biotin labeled DNA). A successful biotin labeling shows the streptavidin column moves slower in the agarose gel with the addition of streptavidin increases the molecular weight. The streptavidin column contains smears because of Alexa-Floura. The streptavidin column contains more DNA at higher molecular weights than then control columns. This proves the biotin labeling. It is not clear why the beads column appear to be empty. Possible explanations include issues with the binding process, the beads were lost, or the beads did not travel through the agarose gel. . . . . 235

64 Agarose gel electrophoresis on the restriction digest samples: Apa1 digest, and the Apa1 and Sph1 digests. The APa1 digest has one DNA band, which is expected because the Apa1 digest cuts the plasmid at one location. The Apa1 and Sph1 digests shows are two pieces of DNA. One piece traveled slightly farther than the DNA band in the Apa1 column, which indicates the 9.5 kb piece that is expected. The second piece is near the bottom edge of the gel, which indicates the presence of a smaller piece of DNA, the 0.5 kb piece that is expected. . . . . 237

## NOMENCLATURE

- a - Bead radius, Actuator state, Laser derivative state
- b - Arbitrary positive constants, Vector field
- c - Speed of light, Non-negative vector, Characteristics index
- d - Bead diameter, Equivalent deflections/extensions, Taylor-series degree
- e - Error
- f - Force, State dynamic function, Focal lengths
- g - Gain, Arbitrary scalar function
- h - Planck's constant, State output function
- j - Kalman gains, arbitrary function
- k - Wavenumber, Stiffness, Boltzmann's constant, LQ gains
- l - Divergence length, Laser waist, Lipschitz constants, Contour length, Persistence length
- m - Mass, Pseudo measurement function, System state
- n - Index of refraction, Sensor noise
- r - Spherical coordinate direction
- q - Auxiliary state
- s - Laplace domain variable
- t - Time
- u - Control variable
- v - Auxiliary control variable
- w - Process noise, Regression vector
- x - Lateral deflection, Bead deflection, Absolute position, System state
- y - Position
- z - Relative position
- A - Area, State matrix
- B - Input matrix
- C - Output matrix

- D - Feedthrough matrix
- E - Electric field, Expected value
- G - Transfer function
- H - Hamiltonian function, Hamiltonian function, Phase-lead compensation filter
- I - Light intensity, Identity matrix
- J - Kalman gain matrix, Cost function
- K - LQ state feedback matrix, Integral control transfer function
- L - Loop gain
- M - Magnification, State manifold, Regression type matrix, Boundary for parameter estimation
- N - Auxiliary state
- O - Observability matrix
- P - Power, Symmetric positive definite matrix, Estimation error covariance matrix, LQ riccati solution, Time-varying adaptation gain.
- R - Resolution, Regression type matrix.
- Q - Trapping efficiency, Symmetric positive definite matrix, Weight matrix on tracking error
- R - Fresnel coefficient, Weight matrix on control
- S - Sensitivity, Spectral density matrix, Sensitivity function, Symmetric Positive definite matrix
- T - Fresnel coefficient, Temperature, State transformation, Complimentary sensitivity function, Arbitrary constant
- U - Potential field
- W - Lyapunov function
- X - Lyapunov equation solution
- NA - Numerical Aperture
- BFP - Back focal plane
- QPD - Quadrant photodiode
- DIC - Differential interference methods
- AOD - Acousto-optic deflectors

- FSM - Fast steering mirrors
- CCD - CCD camera
- WLC - Worm like chain model
- EI - Flexural rigidity
- $L_f h$  - Lie derivative
- LQG - Linear quadratic gaussian control
- SNR - Signal-to-noise ratio
- LQ - Linear quadratic optical control
- $\alpha$  - Divergence angle, Uniform-field susceptibility, State dynamic function
- $\beta$  - State dynamic function, Arbitrary constant
- $\delta$  - Misalignent, State dynamic function, Arbitrary constants
- $\epsilon$  - Permittivity of solvent, Error
- $\eta$  - Stokes drag, Arbitrary constant
- $\kappa$  - Dimensionless stiffness
- $\lambda$  - Eigenvalues, Costate
- $\theta$  - Angle, parameter
- $\mu$  - Medium viscosity, Arbitrary complex number
- $\lambda$  - Wavelength, Positive constant
- $\Lambda$  - Diagonal matrix
- $\nu$  - Angular frequency
- $\omega$  - Angular frequency
- $\Omega$  - Diagonal matrix
- $\xi$  - State
- $\phi$  - Parameters
- $\Phi$  - Parameter set
- $\tau$  - Time constant, Time
- $\psi$  - Internal state

Subscripts:

- a: Actuator
- c: Closed-loop, Condensor
- d: Disturbance Desired
- e: Effective index
- f: Force
- g: Gradient force
- i: Initial
- k: Control gain
- m : Molecule
- n: Sensor noise
- o: Open-loop
- p: Pole, Plant
- r: Reference signal
- s: Sensor, Solvent, Scattering force
- t: Optical trap, tube lens
- u: Control input
- v: Laser velocity state
- w: Process noise
- x: Original state
- z: Zero
- ss: Steady-state
- obj: Objective
- $\xi$ : tracking error
- $\psi$ : Internal state

Accents:

- $\dot{x}$ : Time derivative
- $\acute{x}$ : Scaled state
- $\tilde{x}$ : Noise
- $\bar{x}$ : Expected value, Nominal value
- $\check{x}$ : Noise
- $\hat{x}$ : Estimate

## 1.0 INTRODUCTION

This research focuses on creating a sensitive and automated optical trap for use in single-molecule studies. An optical trap is an instrument that uses the radiation pressure of light to manipulate microscopic objects. The interaction between the light and the microscopic objects results in the objects experiencing optical forces. These optical forces are on the same order of magnitude as biological forces (typically 0.1 to 100 pN) and this feature makes optical traps appropriate for single-molecule studies.

Currently, there is interest and a need to use the entire operating range of the optical trap to produce the optical forces. Producing these optical forces is challenging due to the inherent system nonlinearities and the parameter uncertainty associated with each experiment. This research addresses these challenges by using adaptive and nonlinear control methods to create an automated self-tuning optical trap that

- uses its entire operating range to produce the optical forces;
- performs parameter identification;
- finds the unique control gains;
- provides an unbiased filtered estimate of the molecular force;
- minimizes the user interaction with the instrument calibration and control design.

## 1.1 MOTIVATION

Biophysicists are studying single-molecules to obtain information about their characteristics. These characteristics include the mechanical flexibility of DNA and the step-size and stall

force of motor proteins and enzymes. The molecular characteristics have an important role in cellular functions; for example, the mechanical flexibility of DNA affects packaging and transcription; the motor proteins kinesin and myosin convert the chemical energy adenosine triphosphate (ATP) into mechanical energy to perform cellular functions including cellular transport and muscle contraction. While many discoveries have been made about the underlying molecule characteristics, there still remains unanswered questions. For example, molecular motors work in groups within the cellular environment and the environmental effects on their behavior remains unknown [7]; during transcription, the RNA polymerase can stall and/or backtrack for unknown reasons [8]; DNA experiences hysteresis behavior when overstretched and the environmental effects on the hysteresis behavior remains unknown [9]. Currently, there is interest to study molecular phenomena to obtain information about their characteristics.

Biophysicists began studying molecular phenomena by performing bulk studies on a molecule population. These studies resulted in average information about the population and no information about a single molecule [10, 11]. Bulk studies present a challenge when studying individual molecules because a molecule population can be heterogeneous and/or stochastic. This challenge has been addressed with the creation of single-molecule instruments, and these instruments have allowed the study of single molecules to gain insight about their mechanical properties and energy landscape [12, 13]. These instruments include atomic force manipulators, magnetic traps, and optical traps [14].

Optical traps are a popular choice because they are noninvasive and versatile. They are created by focusing laser light with a microscope objective to produce an optical force on a dielectric bead. The optical forces are on the same order of magnitude as biological forces, usually from 0.1 pN to 100 pN, and this feature makes optical traps appropriate for single molecule studies. Thus far, optical traps have revealed the stall force of viral packaging motors being 57 pN, the step-size of kinesin being 8 nm, and the effects nucleotides have on RNA polymerase during transcription [15, 16, 17, 18].

There is an interest to stretch molecules to study their characteristics (mechanical properties and energy landscape) as a function of force [19, 20]. Force plays an essential role in the function of motor proteins, nucleic acids, and proteins. For example, the mechani-

cal flexibility of DNA affects its functions, including packaging, transcription, and folding [19]; DNA becomes compacted due to protein wrapping, which creates contractile forces [21]; proteins are essential for cellular functions and can enter different conformation states by folding/unfolding events [22, 23, 24, 20], folding and unfolding events occur at different force scales with the unfolding events occurring at higher forces  $\sim 19$  pN than the folding events  $\sim 5$  pN [25, 26]; DNA viral motors are highly efficient and package their genome into host cells by producing high mechanical forces [16, 27]. These characteristics are studied by detecting local changes in the molecular force about its nominal value.

On average, the molecular force balances the optical force once the bead deflection, the relative displacement between the center of the dielectric bead and the laser, reaches steady state. Small bead deflections allow the linearized optical force to be a good approximation of the optical force and the molecular force be approximated with Hooke's law [28, 29]. If the bead deflection exceeds its linear range, then approximating the molecular force with Hooke's law may yield poor measurements. The molecular force estimate fluctuates at steady state because of thermal fluctuations (Brownian noise). Brownian noise is the result of the free diffusion of water molecules, with each water molecule having  $k_B T$  energy, that continually collides with the dielectric bead and the molecule.

The molecule characteristics are studied by detecting local changes in the molecular force about its nominal value. One approach to detect the force changes is to detect the changes in the bead deflection, then use Hooke's law to relate the change in the bead deflection to a force [30]. However, the presence of Brownian noise makes it difficult to detect small changes in the bead deflection. Brownian noise is Gaussian, white noise that effects the response of the bead deflection over a broad range of frequencies, which results in the bead deflection having a large variance. Consequently, the user is unable to detect small changes in the bead deflection, which presents a challenge when detecting changes in the molecular force or the discrete steps of molecular motors and enzymes [31, 6, 32, 33]. For example, in a typical optical trap experiment, an optical force of 10 pN is applied to a molecular motor, resulting in a bead deflection having a mean value of 70 nm with a standard deviation of 5.3 nm due to Brownian motion [31]. The standard deviation of the bead deflection is on the same order of magnitude as the discrete step-size of molecular motors and the base pair resolution of

nucleic acids: kinesin has a step-size of 8 nm, myosin-2 has a step-size of 5.5 nm, and the DNA base pair resolution is 0.34 nm [31]. The optical trap's performance is hindered by the presence of Brownian noise and hence, currently there is a need to improve the sensitivity of the optical trap.

Brownian noise presents a fundamental limit to detect changes in the bead deflection. The Brownian noise effect on the response of the bead deflection can be reduced with the use of low-pass filtering or feedback control. Low-pass filtering the response of the bead deflection reduces its frequency content (filtered bandwidth) by smoothing out its response and removing the short-period fluctuations. The tradeoff is a reduction in the measurement bandwidth. The disadvantage is low-pass filters only remove frequency content and cannot manipulate other variables (e.g., the bead deflection (molecule extension) or the applied optical trap). Feedback control can also reduce the effects of the Brownian noise, and has an additional advantage of manipulating other variables. Controlling the bead deflection in the presence of Brownian noise is a servocontrol problem. Improving the servocontrol problem (i.e., disturbance rejection) will lead to better information about the molecule's characteristics.

Servocontrol has been used to create two feedback configurations: position clamps and force clamps [28, 34]. Position clamps servocontrol the bead deflection while providing force measurements; force clamps servocontrol the applied optical force while providing deflection measurements. These feedback configurations were originally created with proportional (P) control. Position clamps with P-control servocontrol the bead deflection in one of two ways: either moving the laser beam with respect to the dielectric bead, or dynamically changing the stiffness of the optical trap [28]. This feedback configuration were used to study: the interaction between myosin and actin filaments, which showed that myosin has discrete step-sizes of 11 nm and force transients of 3 to 4 pN [35]; the compliance of DNA by dynamically changing the stiffness of the optical trap [19]. Combining position clamps with a high resolution photodiode detector has yielded displacement and force measurements on the order of nanometers and piconewtons with millisecond resolution [36]. Force clamps were first demonstrated by quantifying the stall force of kinesin through maintaining a constant optical force [28]. These feedback configurations provide a molecular force estimate, and

determining its quality requires studying its signal-to-noise ratio (SNR). Position clamps have a detrimental effect on the unfiltered bandwidth SNR and have no effects on the filtered bandwidth SNR; force clamps have an upper bound on the unfiltered bandwidth SNR and have no effect on the filtered bandwidth SNR [37, 38]. Proportional control having no effect on the filtered bandwidth SNR has allowed some researchers to claim feedback control cannot improve the SNR of the force estimate [38]. This statement overlooks the fact that frequency shaped controllers can shape the system response, increase SNR of a signal, and reject disturbances all while manipulating other variables.

These feedback configurations operate about a setpoint (e.g., the molecule is elongated a desired amount or a desired optical force is applied) and have satisfactory performance when the optical trap does not deviate significantly far from that setpoint [28]. If the trapped bead does deviate significantly from the setpoint, then the instrument may exhibit poor response, which may include poor measurements or the dielectric bead leaving the optical trap altogether. As a result, maintaining the optical trap near the setpoint requires considerable user interaction with the controller to yield satisfactory performance. Consequently, users are diverting their time and resources away from studying the biophysics. Thus, there is interest and a need to design feedback controllers to minimize the user interaction and to push the limit of performance to enable automated single molecule optical trap studies.

## 1.2 FEEDBACK METHODS IN PRACTICE

The current controllers implemented in optical trap studies have yielded satisfactory closed-loop performance under strict conditions. The strict conditions include limited operating range, the molecular dynamics being simplified or neglected during the control design process, and assuming exact model knowledge. These conditions inhibit the creation of an automated optical trap.

Researchers have incorporated linear control structures into the optical trap design to improve its closed-loop performance. These control structures include a proportional plus integral controllers (linear PI control), system inversion approach, and the combination of

state observers with state feedback. The first type of controller is linear PI control and it has the advantages of reducing the effects of Brownian noise, increasing the system type, and providing an unbiased estimate of the molecule force with an increase in its SNR. [37].

The second type of controller is the combination of a system inverse approach with PI control and robust control. This controller manipulates the dielectric bead and provides an estimate of the molecule force by multiplying the system output by the transfer function relating the system output to the molecular force [39]. Note, care is needed because increasing the proportional gain leads to a peak forming in the power spectral density (PSD) of the sensitivity function due to latencies in the actuation dynamics [40]. The presence of the peak causes a problem by reducing the bandwidth of the molecular force estimate. These latencies are addressed with robust control methods by using weighted functions to show the tradeoffs between robustness and performance. The system inversion approach has been used to detect the discrete step-sizes of molecular motors when combined with a mixed  $H_2/H_\infty$  control structure, where the  $H_\infty$  norm is minimized for force regulation by reducing the  $H_2$  norm of the Brownian noise [41].

Finally, the third controller is a combination of a state observer and state feedback. The controller provides the molecule force estimate by augmenting the optical trap state to include a fictitious state describing the molecule force. The augmented optical trap is placed in a state observer architecture to allow a Luenberger state observer to provide a state estimate; the state estimate is then used in state feedback to manipulate the molecule. This controller has been demonstrated with an adaptive Luenberger state observer to simultaneously estimate the system parameters and the molecular force when the molecular force dynamics are approximated as a second-order regression model [42].

Linear controllers yield satisfactory closed-loop performance when the optical forces are small. The limited operating range presents challenges when the optical trap needs to produce higher optical forces. Higher optical forces are necessary when studying, for example, the stall force of viral packaging motors, DNA hysteresis, and RNA polymerase backstepping [9, 43, 8]. There are two approaches to produce the higher optical forces. The first approach expands the linear operating range by increasing the laser power to continue using the linear control methods. The disadvantage to increasing the laser power is the increase in the

undesirable photodamage [44]. The second approach produces the optical forces within the entire operating range by considering the system nonlinearities in the control design. The advantage is the photodamage reduction because low laser power is used; the disadvantage is the bead deflection becomes large, which causes stability issues due to the decreasing optical stiffness and difficulties in estimating the molecular force. These issues are addressed with nonlinear feedback methods, which provides one method to account for the system nonlinearities in the control design.

Nonlinear control has been incorporated into the optical trap design to improve its closed-loop performance. The nonlinear controllers used are global asymptotic stabilizing control and nonlinear PI control [45, 46, 47, 48]. The global asymptotic stabilizing control uses a hyperbolic tangent function to cancel the effects of the spatial nonlinearities and to regulate the bead deflection. Nonlinear PI control reduces the effects of the Brownian noise, provides an unbiased molecular force estimate, and manipulates the bead deflection to track a reference signal [49, 48]. These control structures are designed when the molecular force dynamics are simplified or neglected. Simplifying or neglecting the molecular dynamics leads to inaccurate information about molecule characteristics. One approach to improve the quality of the molecule characteristics is to consider the molecule dynamics during the control design. The molecule dynamics have been considered during the design of the nonlinear PI controller and this placed additional constraints on the control gains [46].

The control structures mentioned are model based designs based on the assumption of exact model knowledge. Exact physical models are rarely available due to modeling errors, parameter uncertainty, and computational cost [50, 51]. In optical traps studies, exact model knowledge is a bad assumption due to parameter uncertainty. Parameter uncertainty is present due to the surrounding medium's properties changing per experiment and the optical trap stiffness being affected by the bead's attachment to the molecule [52, 53, 54, 55, 31, 52]. The interaction between the laser and the surrounding medium causes the medium's temperature to increase. The temperature increase affects the medium's viscosity and the power spectral density of the Brownian noise. For example, in a typical optical trap experiment, a laser beam of wavelength 1064 nm with an approximate power of 100 mW causes a temperature increase of  $\sim 1.2$  K. Further increasing the laser power to 500 mW

causes the temperature to increase by  $\sim 6$  K and the viscosity being underestimated by  $\sim 12\%$ . This viscosity change affects the value of the other parameters because many calibration methods use Stokes' drag as a reference force [28]. Parameter uncertainty causes robustness issues in the closed-loop optical trap performance. A consequence is that users are spending an enormous amount of time calibrating the instrument and designing the controller, and this diverts their time away from studying the biophysics. Currently, there is a need and interest to create an automated optical trap that minimizes the user interaction with the calibration process and the control design. One approach to address this need is to use a low authority controller robust enough for the parameter range. The drawback is there is a tradeoff between performance and robustness. A second approach uses adaptive control methods that can perform parameter identification and find the unique control gains for each experiment.

Adaptive feedback methods has been incorporated into the optical trap design to address the parameter uncertainty and improve its closed-loop performance. These feedback methods include parameter identification, adaptive Q-parameterization, adaptive state observers, and adaptive controller. The first adaptive method used a least mean-squared approach for parameter identification and control [56, 57]. Parameter identification on the optical trap system through was performed using LMS to adjust weights in a tapped delay line using a gradient descent method [56]. The LMS approach was used in an adaptive controller to provide estimates of the actuator dynamics and the Brownian noise, and to minimize the weighted error. This adaptive controller is a feedforward controller, where the estimated disturbance is fedforward in a model-matching scheme and using filtered x-LMS algorithm to minimized the error to create an adaptive Q-parameterization controller.

The second type of adaptive method uses adaptive state observers to simultaneously provide state and parameter estimates. The first state observer was a reduced order adaptive Kalman filter to provide parameter estimates and the molecular force estimate. These estimates were used in a digital controller to satisfy performance requirements [42]. The second state observer was a full order adaptive state observer to provide an estimate of the parameters and states to the combined actuator and optical trap system [58].

The third type of adaptive method manipulates the bead deflection using a Lyapunov design approach [59]. The Lyapunov design approach provides a parameter update equation with zero estimation error if the persistently exciting condition is satisfied. The bead deflection is manipulated by designing a sliding mode controller such that the tracking error is asymptotically stable via LaSalle's Invariance Principle.

These adaptive methods yield satisfactory closed-loop performance, but each method has at least one following limitations. The first limitation is the operating range because the adaptive methods all operate within the linear operating range of the optical trap. The second limitation is the molecular force is not estimated, which creates a challenge when studying biological phenomena. The third limitation is the entire system dynamics is not considered in the control design because the actuator and/or the molecule dynamics are neglected. These limitations need to be addressed to create a fully automated optical trap for single-molecule studies.

### 1.3 RESEARCH PROBLEM

There is an interest and need to create an automated optical trap that uses its entire operating range, addresses the parameter uncertainty, and considers the molecular dynamics. This research has aimed to create an automated optical trap that addressed these challenges. The first challenge requires the molecular dynamics be considered during the control design. The molecular dynamics are modeled and included with the optical trap to form the optical trap system. The optical trap system can then be manipulated in such a way that addresses the problems of operating range and parameter uncertainty. In this research, these problems are addressed with adaptive and nonlinear feedback methods. The proposed control structure uses the combination of an adaptive Luenberger type state observer with a feedback linearization and linear quadratic (LQ) structure. This proposed controller addresses three problems: the operating range problem, the estimation problem, and the control problem. The operating range problem is addressed with nonlinear feedback methods to use the entire operating range of the optical trap. The estimation problem uses a Luenberger type state

observer with the system model to reconstruct the system's state. The control problem uses a feedback linearization and LQ structure to have the system satisfy the performance requirements. The first part of the control problem uses feedback linearization to linearize the input-output map of the system and to decouple the effects of the nominal molecular force on the response of the system output. The second part of the control problem uses an LQ optimal control algorithm to find the state feedback to satisfy the performance requirements. Both the estimation and the control problems contain parameter uncertainty, which is addressed with adaptive self-tuning feedback methods to improve the closed-loop performance. Adaptive self-tuning methods can improve the estimation and the control problems by performing real-time parameter estimation, using the parameter estimate as the true parameter value, and finding the map between the parameter estimate and the control values. This ensures the closed-loop performance satisfies the performance requirements while accounting for the parameter uncertainty in the optical trap.

The proposed controller is analyzed and separated into two parts: a nominal nonlinear design and the adaptive nonlinear design.

1. The nominal nonlinear design assumes exact model knowledge. The purpose of the nominal nonlinear design is to demonstrate the control methodology using fixed-gain feedback methods before adaptive feedback methods are used. The Luenberger state observer uses a state-dependent observer gain to provide the state estimate. The problem of finding the state dependent observer gain is turned into a problem of finding a state transformation such that, in the transformed state, the state estimation error dynamics exhibit linear behavior. The state estimate is then used in the feedback linearization with LQ structure to satisfy performance requirements.
2. The adaptive nonlinear design assumes the plant parameters are unknown constants. The adaptive Luenberger type state observer is used to simultaneously perform state and parameter estimation. These estimated entities are used in an adaptive feedback linearization with LQ structure to satisfy performance requirements.

The proposed control structure creates an automated self-tuning optical trap that:

- uses the entire operating range to produce optical forces;
- performs parameter identification;
- finds the unique control gains;
- provides an unbiased filtered estimate of the molecule force;
- minimizes the user interaction with the instrument calibration and control design.

### 1.3.1 Research Objectives

The following objectives aid in the creation of the automated optical trap.

- **Objective 1: Find the functional structures of the state observers**

The bead deflection measurement contains the information about the molecule characteristics. The challenge in obtaining the molecule characteristics is that optical traps operate in a noisy environment due to Brownian noise, which places a fundamental limit for detecting changes in the bead deflection. Currently, there is a need to improve the measurement sensitivity to enhance further discoveries in single molecule studies. Here, measurement sensitivity is improved by using a state observer to simultaneously provide a state estimate and parameter estimate.

- **Objective 2: Design the control structure to satisfy experimental conditions**

The molecule characteristics are studied by manipulating the bead deflection in a systematic and reliable manner. Feedback control manipulates the bead deflection in a systematic way to allow the molecule to enter different conformations to study its characteristics.

- **Objective 3: Analyze noise effects on the closed-loop nominal system**

Feedback control changes the system dynamics. Care is needed during the control design because poor designs may have detrimental effects on the system performance. In order to assess the effectiveness of the nominal design on the quality of the measurements, statistical analyses are performed to quantify the control effects on the system bandwidth

and the statistical properties of the system state. The statistical analysis shows any tradeoffs in performance to provide insight when choosing control gains for individual experiments.

- **Objective 4: Demonstrate the control structure**

Proof of concept demonstrates the closed-loop performance of the optical trap when using adaptive and nonlinear feedback methods. The demonstration allows for the comparison of the closed-loop performance of the proposed controller to the current controllers in practice. The comparison quantifies the improvement in the closed-loop performance when considering the system nonlinearities and parameter uncertainty in the control design.

### 1.3.2 Simulations

Proof of concept is needed to demonstrate the performance of the proposed controller on a single-molecule study. The study chosen is the stretching of DNA to replicate its force-extension curve. In the study, it is assumed the DNA molecule is attached at one end to a glass surface, while its other end is attached to a polystyrene bead. The molecule's end-to-end distance determines its extension, and its extension is manipulated by controlling the position of the dielectric bead [60]. The information obtained about the molecule's extension is then related to the corresponding molecular force. The simulation allows for the comparison of the closed-loop performance of the proposed controller to that of controllers used in practice. The two metrics to be quantified are:

1. The improvement in the closed-loop performance when using nonlinear control instead of linear control when considering the system nonlinearities in the control design.
2. The closed-loop performance of an automated optical trap using adaptive self-tuning feedback compared to that using fixed-gain feedback methods and assuming exact model knowledge.

Current control methods use linear proportional plus integral control or only integral control because of its ability to increase the system type, reject constant disturbances, reduce the effects of the Brownian noise, and provide a disturbance estimate. The statistical character-

istics of the estimated molecule force can also be obtained with linear quadratic Gaussian (LQG) control. This statistical equivalence is crucial because LQG control has a similar architecture to that of the proposed nonlinear feedback designs to address the estimation and control problems. The similar architecture of the LQG control with the nonlinear feedback designs allow the comparison of the statistical characteristics of the estimated molecule force with a controller used in practice to the statistical characteristics of the estimated molecule force obtained with the proposed nonlinear feedback designs. In addition, the closed-loop performance of the proposed nonlinear feedback designs are compared with the closed-loop performance of a nonlinear PI controller, a controller used in practice. The second metric compares the closed-loop performance using adaptive self-tuning control methods to that of fixed-gain control methods. Fixed gain control methods yield satisfactory performance after the user spends considerable time interacting with the instrument and the control design. Adaptive self-tuning control methods can provide similar performance as fixed-gain controllers by performing real-time parameter estimation, using the parameter estimates as the true parameter in the control design, and finding the map between the parameter estimate and the control parameters.

#### 1.4 RESEARCH IMPACT AND SIGNIFICANCE

This research has aimed to create an automated optical trap by expanding on its areas of sensing and control. Typically, users spend an enormous amount of time interacting with the optical trap during the calibration process and the controller design due to their limited knowledge with feedback control. A consequence is that users are diverting their resources away from studying the biophysics at hand. To date, there is no automated optical trap to probe molecules. One method to address this need is to use adaptive and nonlinear control methods to create an automated self-tuning optical trap. The combination of adaptive and nonlinear control creates a new controller to allow optical traps be used in single-molecule studies that allows the users to redirect their resources back to studying the biophysics at hand.

Improving single-molecule studies has a direct impact in medicine, especially the understanding of disease pathology and the monitoring of disease activity. Single molecule malfunction leads to disease. Aging is a risk factor for degenerative diseases like Huntington's and Alzheimers due to protein misfolding and amyloid aggregation [61, 22]. The motor proteins kinesin, myosin, and dynein transport cargo and it recently has been discovered that these motor proteins have an unexpected role in brain wiring and neural survival. A functional defect in these motor proteins can lead to ALS, Huntington's disease, and Alzheimer disease [62]. DNA is essential for transcription and replication, and defective DNA due to lesions or mismatch can interfere with these processes and cause genome instability, which can lead to neurodegenerative diseases and cancer [63]. Disease monitoring can also be achieved. Red blood cells can aggregate and the corresponding force between membranes can be an additional tool to monitor disease activity, especially in lupus patients. The aggregation force is approximately doubled in lupus patients rather than in healthy patients [64]. The result of creating an automated optical trap can provide one platform to allow medical researchers to study the characteristics of single-molecules to improve their understanding of disease pathology, monitor diseases, and hopefully improve treatments.

Finally, improving the state-of-the-art of optical traps can impact other applications, including the physical sciences and nano-fabrication. In the physical sciences, optical traps can create features smaller than the wavelength of light and also study optically modulated collisions and thermal rackets. In nano-fabrication applications, optical traps have been used to manipulate nanotubes and nano wires [65, 66]. Advancing the state-of-the-art of optical traps will have a broad impact in many applications.

## 1.5 DISSERTATION ORGANIZATION

This dissertation is organized as follows:

Chapters two and three describe the process of constructing and calibrating the optical trap. The construction of an optical trap requires the consideration of many components. The optical trap is constructed to demonstrate and compare the performance of the different control structures on an actual single-molecule experiment.

Chapter four describes the dynamics of the optical trap system. The optical trap system is composed of the actuator, the dielectric bead, sensor, and the molecule. The model of these dynamics will be used to design the control structures.

Chapters five, six, and seven discuss the design and the performance of the different control structures: the LQG design, linear integral control, the nominal nonlinear design, the nonlinear PI control, and the adaptive nonlinear design.

Chapter eight discusses the simulations and proof of concept by demonstrating and comparing the closed-loop performance of the optical trap with the different control structures on an actual single-molecule experiment .

Chapter nine is the conclusion and future work.

## 2.0 OPTICAL TRAP THEORY

Optical traps are instruments capable of manipulate microscopic objects using the momentum of light. The light is focused with a high numerical aperture microscope objective to produce the optical forces. These optical forces are small, typically 0.1 pN to 100 pN, and this feature makes optical traps appropriate for single molecule studies. In single-molecule studies, optical traps have been used in many configurations, including single-beam, dual-beam, and holographic [30, 67]. This research will use the optical trap in a single-beam configuration. The process of constructing an optical trap involves the consideration of many components, including the choice of laser, objective, actuation method, and detection method. This chapter discusses the theory of the optical forces, the design considerations during the construction process, and the optical trap design.

### 2.1 OPTICAL FORCES

Optical traps use the radiation pressure from a tightly focused laser beam to manipulate microscopic objects. The idea first arose in 1969 when Arthur Ashkin became interested in calculating the radiation pressure force on a reflecting mirror [68]. Each photon has a momentum of  $h/vc$  (where  $h$  is Plank's constant,  $c$  is the speed of light, and  $v$  is frequency) and given an incident laser power of  $P$ , then there is  $P/hv$  photons per second striking the mirror. Assuming an incident laser power of 1 W results in a the force of 10 nN applied to the mirror [69, 68]. These results were experimentally verified by Ashkin in 1970 [69] and showed the presence of two forces: a scattering force and an unexpected gradient force. The scattering force pushes the bead downstream and acts in the direction of the light

propagation; the gradient force pulls the bead to the region of highest intensity and acts in the direction of the highest intensity gradient. The presence of the gradient force led to the discovery of the single-beam gradient optical trap [70]. The single-beam gradient optical trap is formed when the gradient force overcomes the scattering force to stabilize the bead deflection.

The scattering and gradient forces have been described in two regimes and these regimes depends on the dimension of the bead, its diameter  $d$ , to that of the light wavelength  $\lambda$ . When the bead's diameter is much greater than that of the light's wavelength,  $d \gg \lambda$ , the optical trap is operating within the Mie scattering regime. Mie scattering allows for geometric optics or ray optics to describe the optical forces. If the bead's diameter is much less than that of the light's wavelength,  $d \ll \lambda$ , then the optical trap is operating within the Rayleigh scattering regime. Rayleigh scattering uses electromagnetic theory to describe the optical forces because the dielectric bead behaves as a point dipole in the electric field.

In the Mie scattering regime, ray optics is used to describe the optical forces, as shown in figure 1. Displacing the bead with respect to the objective's focus results in the gradient force overcoming the scattering force to pull the bead to the location where these forces are balanced. The scattering force  $f_s$  and the gradient force  $f_g$  are described by [71],

$$f_s = \frac{nP}{c} \left( 1 + R \cos 2\theta - \frac{T^2 [\cos (2\theta - 2\phi) + R \cos 2\theta]}{1 + R^2 2R \cos 2\phi} \right), \quad (2.1a)$$

$$f_g = \frac{nP}{c} \left( R \sin 2\theta - \frac{T^2 [\sin (2\theta - 2\phi) + R \sin 2\theta]}{1 + R^2 + 2R \cos 2\phi} \right), \quad (2.1b)$$

where  $R$  and  $T$  is the Fresnel reflection and transmission coefficients of the bead's surface,  $\theta$  and  $\phi$  are the angles of incidence and refraction, and  $nP/c$  is the incident momentum per second in a medium of index of refraction  $n$ . Equation (2.1) describes the forces that are polarization dependent because the Fresnel coefficients  $R$  and  $T$  are different for rays polarized parallel or perpendicular to the plane of incidence [71].

Rayleigh scattering uses electromagnetic theory to describe the optical forces because the dielectric bead behaves as a point dipole in the electric field. The optical forces depend on the laser's intensity  $I$ , the bead's radius  $r$ , the medium's index of refraction  $n$ , and the effective index  $n_e$ , which is defined as the ratio of the refractive index of the bead to the

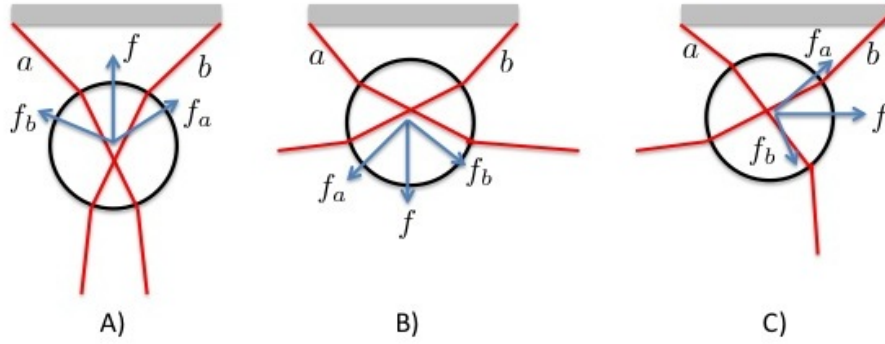


Figure 1: Schematic of how individual light rays apply forces on a bead. When the bead is displaced from the focus, optical forces act on the bead to pull it back. A) The bead is displaced downstream from the focus, optical forces act on the bead to pull it back. B) The bead is displaced upstream from the focus and forces pull the bead downstream. C) The bead is displaced off axis of the focus and forces pull the bead back to the axis.

refractive index of the medium. The scattering force and the gradient force are described by [70].

$$f_s = \frac{I}{c} \frac{128\pi^5 r^6}{3\lambda^4} \left( \frac{n_e^2 - 1}{n_e^2 + 2} \right)^2 n, \quad (2.2a)$$

$$f_g = -\frac{n^3 r^3}{2} \left( \frac{n_e^2 - 1}{n_e^2 - 2} \right) \nabla E^2. \quad (2.2b)$$

In most experiments, the dimension of the bead has the same order of magnitude as the light's wavelength, typically between  $0.5\mu\text{m}$  to  $5\mu\text{m}$ . Even though there have been advancements in describing the optical forces within this size range, [72, 73], they do not provide a further understanding of the optical traps. In general, the optical forces are described by [1]

$$f = Q \frac{nP}{c} \quad (2.3)$$

where  $Q$  is the trapping efficiency. The trapping efficiency is determined experimentally and its value is different for axial and lateral trapping forces, as shown in table 1.

Table 1: Trapping efficiency,  $Q$  for polystyrene beads of different sizes and with using objectives with different NA. [1, 2].

Diameter ( $\mu\text{m}$ )	n	NA	Depth ( $\mu\text{m}$ )	P (mW)	Q
		Lateral			
0.303	1.57	1.3	13	1-90	0.012
1.02	1.57	1.3	13	1-90	0.085
2.97	1.57	1.3	13	1-90	0.21
0.4	1.57	1.25	8.3	60	0.01
1	1.57	1.25	8.3	60	0.08
2.1	1.57	1.25	8.3	60	0.16
6.1	1.57	1.25	8.3	60	0.20
		Axial			
1.2	1.57	1.3	9	1-90	0.0058
0.4	1.57	1.25	8.3	60	0.02
1	1.57	1.25	8.3	60	0.07
2.1	1.57	1.25	8.3	60	0.08
6.1	1.57	1.25	8.3	60	0.29

## 2.2 OPTICAL TRAP CONSIDERATIONS

The construction of an optical trap requires the consideration of the choice of actuation method, detection method, laser, and the microscope objective that focuses the laser and images the specimen plane.

In biological applications, the choice of laser, particularly its wavelength, is crucial to reduce biological photodamage and optocution [74, 75, 44]. Wavelengths within the visible spectrum are absorbed by naturally occurring pigments found in biological material, and this fact may lead to damage and cell death. Longer wavelengths in the infrared spectrum are better for the health of biological material because biological material becomes more transparent and the surrounding medium absorbs the laser energy, as shown in figure 2 [74, 6]. The photodamage is minimized when using wavelengths of 830 nm and 970 nm [44]. The popular choice of wavelength is 1064 nm because its economical and results in small amounts of photodamage. Lasers at this wavelength are available and the common used laser is the diode pumped Nd:YAG laser.

The most important component is the microscope objective that is used for trapping and imaging. The objective choice affects the efficiency of the optical trap system, which depends on the objective's numerical aperture (NA) and transmittance [76]. Numerical aperture quantifies the objective's ability to collect light and is defined by

$$\text{NA} = n \sin \theta$$

where  $n$  is the refractive index of the medium and  $\theta$  is the half-angle of the angular aperture [77]. In trapping applications, the laser beam is focused with a high NA (typically 1.2 NA to 1.4 NA) objective to create the steep gradients and high intensities to have the gradient force overcome the scattering force. When choosing the objective, its immersion medium is crucial because the immersion medium affects the trapping depth. Oil immersion objectives have high NA with the tradeoff of a refractive index mismatch with the surrounding medium [76]. The refractive index mismatch results in spherical aberrations that limit the trapping depth. Water immersion objectives provide a deeper trapping depth because these objectives

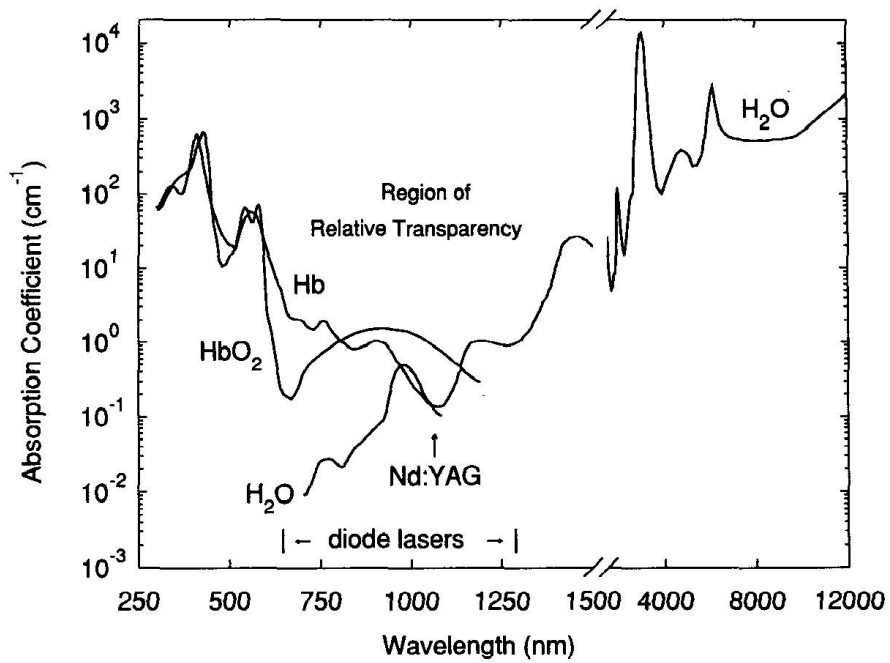


Figure 2: A schematic showing the absorption properties for deoxyhemoglobin Hb, oxyhemoglobin HbO<sub>2</sub> and water H<sub>2</sub>O as a function of the wavelength of light. Longer wavelengths in the infrared regime provide better health for biological material because biological material becomes more transparent while the laser energy becomes absorbed by the surrounding water. Source [6].

do not cause spherical aberrations, however, water immersion objectives have smaller NA than oil immersion objectives.

The objective is placed in an imaging system that can either be a commercial or custom microscope. Custom microscopes allow for design flexibility, which can overcome the increased complexity of building the optical paths for trapping and imaging. The preferred imaging system is a commercially inverted microscope because of their stability, the fixed stage, and the objective moves in the vertical direction [76].

Typically, the microscope and laser are placed on a vibration isolation table to reduce the influence of building equipment on the measurements. Building equipment (e.g., compressors and HVAC systems) and renovations can cause vibrations in the low frequency range to be present in the floor. The vibrations are transmitted to the top surface of the platform containing the optical trap, which cause fluctuations in the optical components and leads to measurement degradation. These issues can be addressed by placing the microscope and optical components on a vibration isolation table with active vibration legs that uses air to change their stiffness to reduce the vibrations.

### 2.3 OPTICAL TRAP SETUP

The optical trap setup is composed of a Zeiss Axiovert 200 inverted microscope and a Nd:YAG laser at 1064nm (Coherent Compass 1064-2500 MN diode-pumped Continuous Wave IR laser) that are placed on a vibration isolation table (Thorlabs). The schematic of the optical trap design is shown in figure 3. The beam path is initially collimated with lens  $f_1$  before being directed onto the fast steering mirror (FSM, Newport FSM-300). The FSM can tilt along two orthogonal axes by changing its voltage input and is located at the back Fourier plane (BFP) of the objective. After the FSM, the beam path is expanded with a telescope (lenses  $f_2$  and  $f_3$ ) to slightly overfill the back aperture of the objective, before entering into the epi-fluorescence port of the microscope. Once inside the microscope, the beam path encounters a custom dichroic mirror (Chroma technology), that is placed in the microscope's filter cube turret. The dichroic mirror redirects the beam path to the objective

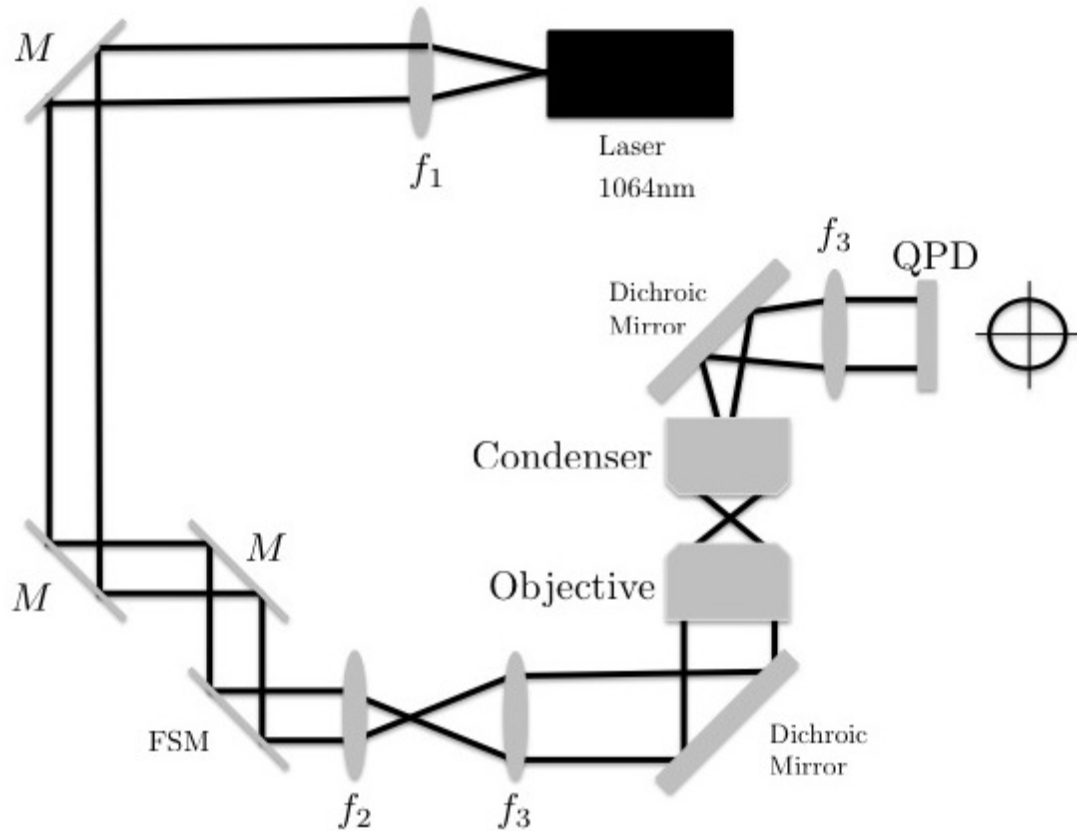


Figure 3: The schematic of the optical trap setup. The laser beam expands then is collimated with the collimating lens  $f_1$ . The collimated light is directed with mirrors to the fast steering mirror (FSM), that is placed at the back Fourier plane of the objective. Then, the light gets expanded by a telescope ( $f_2$  and  $f_3$ ) before entering the microscope's epi-illumination port. Once inside the microscope, the light is redirected with a dichroic mirror to the objective, which focuses the light to the specimen plane. The condenser collects the forward scattered light, which is redirected by a second dichroic mirror to the QPD.

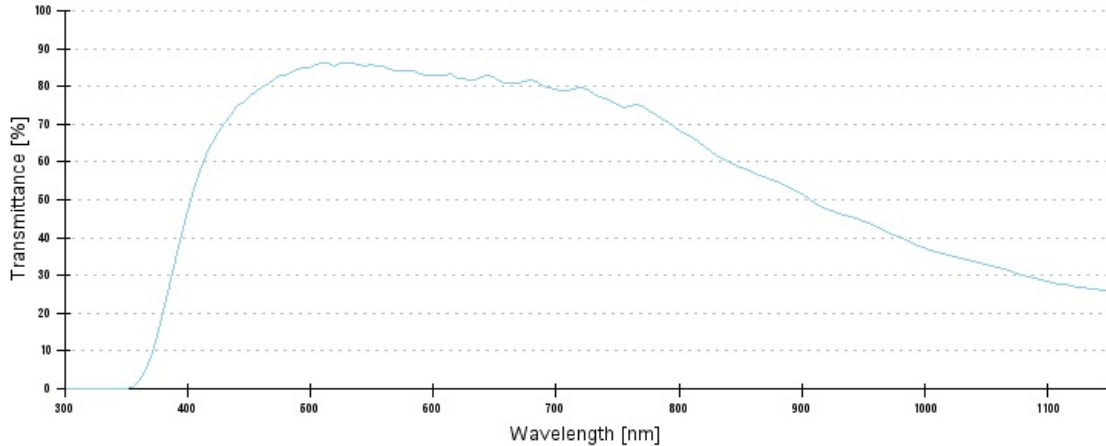


Figure 4: The transmission plot for the Zeiss Plan-Apochromat 63x/1.4 NA objective. When the laser has a wavelength of 1064 nm then the resulting laser power at the specimen plane is  $\sim 30\%$  of its input power at the objective.

while transmitting the illumination light to image the specimen plane with a CCD camera (Hitachi). The high NA objective (Zeiss Plan-Apochromat 63 $\times$ /1.4 NA) creates the steep gradients for trapping and imaging. The objective is highly corrected with many lens, which reduces the laser power at the specimen plane to  $\sim 30\%$  of its input power, as shown in figure 4. The interaction between the light and the bead results in forward scattered light, or the light being scattered in different directions (at different angles). The forward scattered light is collected with a high NA condenser (Zeiss Achromatic-aplanatic condenser with 1.4 NA). The collected light is redirected with a second custom dichroic mirror (Chroma Technology) to a collimated lens  $f_3$  and the quadrant photodiode (QPD, First Sensor). The QPD measures the intensity profile of the forward scattered light at the BFP of the condenser to measure the bead deflection.

### 2.3.1 Choosing the Proper Lenses

The optical trap setup is designed in three parts. The first part places the FSM at the BFP of the objective using a three lens system; the second part directs the beam path from the

laser to the FSM; the third part collects the forward scattered light and directs the light to the QPD. Each part requires the use of lenses. The proper focal lengths are chosen using a ray-transfer matrix approach to relate the light's position and angle at the object plane to that at the image plane [78]. The two ray-transfer matrices used in the analysis describe the propagation through free space

$$\begin{bmatrix} y_i \\ \theta_i \end{bmatrix} = \begin{bmatrix} 1 & d \\ 0 & 1 \end{bmatrix} \begin{bmatrix} y_o \\ \theta_o \end{bmatrix}, \quad (2.4)$$

and the passage through a thin lens

$$\begin{bmatrix} y_i \\ \theta_i \end{bmatrix} = \begin{bmatrix} 1 & 0 \\ -\frac{1}{f} & 1 \end{bmatrix} \begin{bmatrix} y_o \\ \theta_o \end{bmatrix}, \quad (2.5)$$

where  $d$  is the distance propagated,  $f$  is the focal length,  $y_o$  and  $y_i$  are the positions at the object and image planes respectively, and  $\theta_o$  and  $\theta_i$  are the angles at the object and image planes respectively. Equations (2.4) and (2.5) are combined to describe the light propagation through a single thin lens when the object and image planes are located a focal length away by

$$\begin{bmatrix} y_i \\ \theta_i \end{bmatrix} = \begin{bmatrix} 1 & f \\ 0 & 1 \end{bmatrix} \begin{bmatrix} 1 & 0 \\ -\frac{1}{f} & 1 \end{bmatrix} \begin{bmatrix} 1 & f \\ 0 & 1 \end{bmatrix} \begin{bmatrix} y_o \\ \theta_o \end{bmatrix} = \begin{bmatrix} 0 & f \\ -\frac{1}{f} & 0 \end{bmatrix} \begin{bmatrix} y_o \\ \theta_o \end{bmatrix}. \quad (2.6)$$

Equation (2.6) describes the Fourier transform property of a thin lens because angular displacements at the object plane results in position changes at the image plane and also position changes at the object plane results in angular changes at the image plane. The ray-transfer matrix approach can be extended to study light propagation through several cascaded thin lens.

The first part of the optical trap setup places the FSM at the BFP of the objective to use 70% its full dynamic range. The FSM placement requires a lens system be created between the FSM and the specimen plane. A cascaded three thin lens system can describe the light's angle at the FSM to the lateral translations of the light at the specimen plane, as shown in figure 5. The FSM is located at the object plane and the specimen plane is located at the

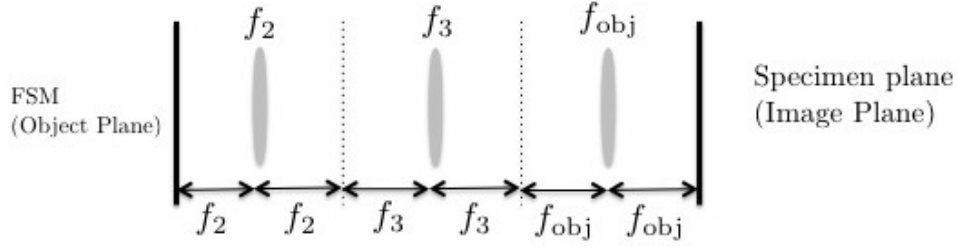


Figure 5: A schematic of a cascaded system of three lens that is in between the FSM placed at the object plane and the specimen plane placed at the image plane. The FSM being placed at the BFP of the objective allows for FSM angle inputs be turned into lateral translations of the laser in the specimen plane.

image plane. The resulting ray-transfer matrix is

$$\begin{bmatrix} y_i \\ \theta_i \end{bmatrix} = \begin{bmatrix} 0 & f_{\text{obj}} \\ -\frac{1}{f_{\text{obj}}} & 0 \end{bmatrix} \begin{bmatrix} 0 & f_3 \\ -\frac{1}{f_3} & 0 \end{bmatrix} \begin{bmatrix} 0 & f_2 \\ -\frac{1}{f_2} & 0 \end{bmatrix} \begin{bmatrix} y_o \\ \theta_o \end{bmatrix} = \begin{bmatrix} 0 & -\frac{f_2 f_{\text{obj}}}{f_3} \\ \frac{f_3}{f_2 f_{\text{obj}}} & 0 \end{bmatrix} \begin{bmatrix} y_o \\ \theta_o \end{bmatrix}, \quad (2.7)$$

which is equivalent to the Fourier transform property for a cascaded three lense system. Assuming only angular displacements at the FSM reduces equation (2.7) to

$$y_i = -\frac{f_2 f_{\text{obj}}}{f_3} \theta_o. \quad (2.8)$$

The focal length of the objective is found through

$$f_{\text{obj}} = \frac{f_t}{M}, \quad (2.9)$$

where  $M$  is the objective's magnification and  $f_t$  is the focal length of the tube lens. The objective is a Zeiss Plan-Apochromat objective with a magnification of  $63\times$  and its tube lens has a focal length of 164.5 mm, resulting in the objective focal length given in table 2. The focal lengths of  $f_2$  and  $f_3$  are design parameters to use the FSM dynamic range and move the laser  $\pm 20\mu\text{m}$  in the specimen plane. The lens  $f_3$  is to be placed outside the microscope, which results in the following condition:  $f_3 \geq 400\text{ mm}$ . These design conditions are considered when choosing standard lens sizes and the focal lengths chosen are given

Table 2: The focal lengths for the lens chosen in the optical trap setup.

Focal length	Numerical length (mm)
$f_{\text{obj}}$	2.61
$f_1$	750
$f_2$	100
$f_3$	400
$f_4$	250

in table 2. The FSM's input range of  $\pm 10$  V allows for angular deflections of  $\pm 52.4$  mrad. Applying 1 V to the FSM results in a  $3.4 \mu\text{m}$  laser beam deflection. The applied voltage comes from a 16 bit D/A board with a range of  $\pm 10$  V and results in the smallest possible laser beam deflection being  $\sim 1$  nm.

The optical trap setup needs to expand the beam diameter to slightly overfill the back aperture of the objective. The back aperture of the objective has a diameter of 10 mm. The beam diameter is expanded with two parts of the optical trap setup: the first part is the lens system between the FSM and specimen plane and the second part is the lens system between the laser and FSM. The total optical magnification is the product of the magnification of each individual part. The first part has a magnification of  $M = f_3/f_2 = 4$ , which implies the beam diameter needs to be 2.5 mm at the FSM. The second part of the optical trap setup is designed to expand the beam diameter to 2.5 mm and to direct the beam path from the laser to the FSM. The beam diameter is expanded using the beam's natural divergence until the desired diameter of 2.5 mm is reached. The laser (Coherent Compass IR laser) operates in the  $\text{TEM}_{00}$  mode with an initial beam diameter at  $1/e^2$  of 0.4 mm and a beam divergence of  $< 3.5$  mrad. The divergence is determined by

$$\tan\left(\frac{\alpha}{2}\right) = \frac{d_d - d_i}{2l}, \quad (2.10)$$

where  $\alpha$  is the divergence angle,  $d_d$  is the desired beam diameter,  $d_i$  is the initial beam diameter, and  $l$  is the divergence length. Equation (2.10) is used to find the divergence

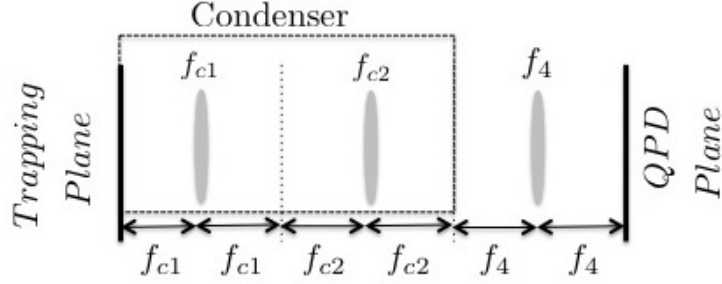


Figure 6: A schematic of the sensing system. The sensing system is composed of the condenser, collimating lens, and the QPD.

length that yields the desired beam diameter. At the divergence distance, the laser beam is collimated by a thin lens with focal length  $f_1 = l$ . The closest standard lens is chosen, given in table 2, and results in the beam diameter being 3.01 mm. The collimated beam is directed to the FSM with stationary mirrors.

The third part is designed to collect the forward scattered light then direct the light to the QPD. The sensing system includes the condenser, a dichroic mirror, a collimating lens, and the QPD, as shown in figure 6. The condenser is a black box with unknown components. It is assumed the condenser is a two lens system with focal lens  $f_{c1}$  and  $f_{c2}$  because the exiting light is converging, and the condenser focal lengths are aligned with each other and with the specimen plane. The condenser having two lenses is assumed because the manufacturer is Zeiss. The light exiting the condenser encounters a second dichroic mirror that redirects the beam path to the QPD and transmits the illumination light.. The redirected light is collimated with lens  $f_4$  so the light slightly overfills the QPD sensing area. The sensing system is described by a three cascaded thin lens system to relate the forward scattered light at the specimen stage to lateral displacements at the QPD. The resulting ray-transfer matrix is

$$\begin{bmatrix} y_i \\ \theta_i \end{bmatrix} = \begin{bmatrix} 0 & f_4 \\ -\frac{1}{f_4} & 0 \end{bmatrix} \begin{bmatrix} 0 & f_{c2} \\ -\frac{1}{f_{c2}} & 0 \end{bmatrix} \begin{bmatrix} 0 & f_{c1} \\ -\frac{1}{f_{c1}} & 0 \end{bmatrix} \begin{bmatrix} y_o \\ \theta_o \end{bmatrix} = \begin{bmatrix} 0 & -\frac{f_{c1}f_4}{f_{c2}} \\ \frac{f_{c2}}{f_{c1}f_4} & 0 \end{bmatrix} \begin{bmatrix} y_o \\ \theta_o \end{bmatrix}, \quad (2.11)$$

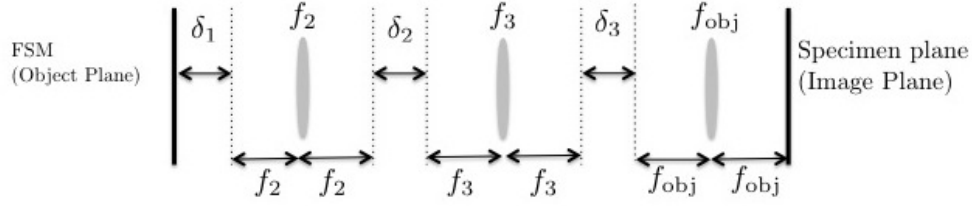


Figure 7: A schematic showing the effects positional misplacements of the optical components on the Fourier transform property of the cascaded three lens system.

which describes the angular spectrum (equivalent to a Fourier transform) of the sensing system [78]. The QPD measures position and this fact simplifies equation (2.11) to

$$y_i = -\frac{f_4 f_{c1}}{f_{c2}} \theta_o. \quad (2.12)$$

The optical trap setup is designed with the assumption that the optical components are placed correctly; however, it is impossible to place these optical components in their exact locations. Positional misalignments can affect the quality of the Fourier transform property of the three cascaded lens system used with the FSM and QPD. It is insightful to quantify the effects the positional misalignments has on the three lens systems.

### 2.3.2 Actuation Misalignment Issues

A three lens system describes the Fourier transform property between the FSM and the specimen plane. The presence of positional misalignments can affect the Fourier transform property of the three lens system. Potential misalignments result in free space between the focal planes, as shown in figure 7. Free space is possible at three locations:  $\delta_1$  is the misalignment of focal length  $f_2$  with the FSM,  $\delta_2$  is the the misalignment of the focal lengths  $f_2$  and  $f_3$ , and  $\delta_3$  is the misalignment of the focal length  $f_3$  with the objective and movements of the objective to focus the specimen plane. The free spaces result in light propagation

according to equation (2.4). The free space effects are quantified with a ray-transfer matrix analysis. The three lens system with the positional misalignments is described by

$$\begin{bmatrix} y_i \\ \theta_i \end{bmatrix} = \begin{bmatrix} \frac{f_{\text{obj}}\delta_2}{f_1f_2} & \frac{f_{\text{obj}}\delta_1\delta_2}{f_1f_2} - \frac{f_1f_{\text{obj}}}{f_2} \\ \frac{f_2}{f_1f_{\text{obj}}} - \frac{\delta_2\delta_3}{f_1f_2f_{\text{obj}}} & \frac{f_2\delta_1}{f_1f_{\text{obj}}} - \frac{\delta_1\delta_2\delta_3}{f_1f_2f_{\text{obj}}} + \frac{f_1\delta_3}{f_2f_{\text{obj}}} \end{bmatrix} \begin{bmatrix} y_o \\ \theta_o \end{bmatrix} \quad (2.13)$$

Assuming only angular deflections at the FSM reduces equation (2.13) to

$$\begin{bmatrix} y_i \\ \theta_i \end{bmatrix} = \begin{bmatrix} \frac{f_{\text{obj}}\delta_1\delta_2}{f_1f_2} - \frac{f_1f_{\text{obj}}}{f_2} \\ \frac{f_2\delta_1}{f_1f_{\text{obj}}} - \frac{\delta_1\delta_2\delta_3}{f_1f_2f_{\text{obj}}} + \frac{f_1\delta_3}{f_2f_{\text{obj}}} \end{bmatrix} \theta_o = \begin{bmatrix} 6.2(10^{-5})\delta_1\delta_2 - 0.65 \\ 1.53\delta_1 - 9.58(10^{-6})\delta_1\delta_2\delta_3 + 0.096\delta_3 \end{bmatrix} \theta_o, \quad (2.14)$$

The resulting laser position is the sum of its value with no misalignment 0.65 and a position error  $6.2(10^{-5})\delta_1\delta_2$  due to the misalignments. The position error is four orders of magnitude smaller than the laser position with no misalignment. The misalignments are no larger than an order of magnitude and even at this extreme, the resulting position error is still two orders of magnitude smaller than the laser position with no misalignment. The position error is independent of the misalignment  $\gamma_3$  and implies the movement of the objective does not contribute to the error. The resulting angular deflections are angular errors due to misalignments. The dominant angular error term is due to the misalignment of the FSM with respect to the lens  $f_1$  and is at least two orders of magnitude larger than the other error terms. This error term can be minimized by placed the FSM as close to a distance  $f_1$  from the lens.

### 2.3.3 Sensing Alignment Issues

A three lens system describes the angular spectrum (Fourier transform) of the forward scattered light at the QPD surface. The presence of positional misalignments can affect the Fourier transform property of the three lens system. Potential misalignments result in free space between the focal planes, as shown in figure 8. Free space is possible at two locations:  $\delta_4$  is the misalignment of the focal length  $f_4$  with the condenser and  $\delta_5$  is the misalignment

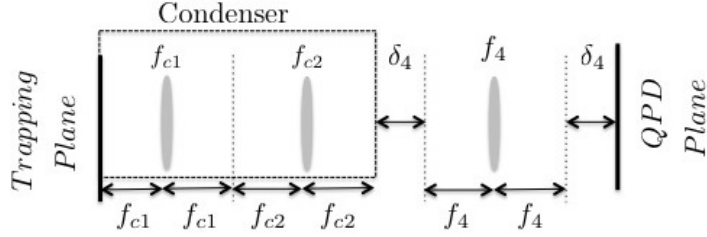


Figure 8: A schematic showing the effects positional misplacements of the optical components on the QPD measurements.

of the focal length  $f_4$  with the QPD. The free space effects are quantified with a ray-transfer matrix analysis. The three lens system with the positional misalignments is described by

$$\begin{bmatrix} y_i \\ \theta_i \end{bmatrix} = \begin{bmatrix} \frac{\delta_5}{f_4} \left( \frac{f_{c2}}{f_{c1}} \right) & \frac{\delta_4 \delta_5 - f_4^2}{f_4} \left( \frac{f_{c1}}{f_{c2}} \right) \\ \frac{1}{f_4} \left( \frac{f_{c2}}{f_{c1}} \right) & \frac{\delta_4}{f_4} \left( \frac{f_{c1}}{f_{c4}} \right) \end{bmatrix} \begin{bmatrix} y_o \\ \theta_o \end{bmatrix}. \quad (2.15)$$

The QPD measures position and this fact implies we are only interested in the position error not the angular error. The resulting position error is

$$y_i = \frac{\delta_5}{f_4} \left( \frac{f_{c2}}{f_{c1}} \right) y_o + \frac{\delta_4 \delta_5 - f_4^2}{f_4} \left( \frac{f_{c1}}{f_{c2}} \right) \theta_o. \quad (2.16)$$

Equation (2.16) shows that placing the QPD correctly,  $\delta_5 = 0$ , allows for small misalignments in the collimating lens (focal length  $f_4$ ) without having detrimental effects on the position measurements.

The optical trap setup can stretch the molecule and study the molecular characteristics through the attachment between the bead and molecule. The molecule can be stretched to desired extensions by changing its end-to-end distance through manipulating the bead deflection. The molecule characteristics can be obtained by detecting force changes through detecting changes in the bead deflection. In this research, the bead deflection is manipulated with the FSM and is measured with the QPD. There are several actuation and sensing methods used with optical traps. The following discusses the different methods for actuation and sensing for completeness.

### 2.3.4 Position Sensing Methods

Many methods exist to measure the bead deflection and these methods range from video to interferometric methods. Video methods provide the absolute position of the bead. These methods use centroid tracking algorithms to track the bead's position [76, 28]. However, the disadvantages are the limited bandwidth of the camera, typically  $\sim 30$  Hz, and no information is obtained about the bead deflection. Therefore, it is desirable to use a detection method that has a faster bandwidth and measures the bead deflection.

Interferometric detection methods measure the bead's deflection using the forward scattered light of the bead. Two interferometric methods are differential interference contrast (DIC) and quadrant photodiodes (QPDs) [79]. DIC methods measure the change in the transmitted polarization to that of the incident polarization; QPDs measure the change in the angular spectrum of the scattered wave about the beam path [80, 79]. Both methods collect the forward scattered light with a condenser that has a similar NA as the objective to obtain similar sensitivities.

DIC interferometry measures the bead deflection from the change in the transmitted polarization to that of the incident polarization. The incident beam with circular polarization encounters a Wollaston prism, placed in front of the objective, to split the laser beam into its orthogonal polarization components [79]. These orthogonal beams overlap each other to form a single optical trap, and are recombined into a single beam by a second Wollaston beam that is placed after the condenser. The polarization of the recombined beam with respect to that of the incident beam obtains the information about the bead's deflection. No change in polarization implies the bead deflection is zero. If the bead deflection is not zero, then there is a phase delay between the two orthogonal beams that results in the recombined beam having an elliptical polarization [79]. The resulting elliptical polarization contains information about the bead deflection in the lateral direction. This detection method is the most sensitive with a power spectral density of  $1 \text{ pm}/\sqrt{\text{Hz}}$  within the frequency range of 0.1 Hz to 100 Hz to yield total noise of  $99.9 \text{ pm}^2$  [81]. The advantages are the detection method is always aligned because the same laser is used for trapping and detection, and movements of the beam path in the specimen plane does not require the detection system

be aligned [82]. However, the disadvantage is the bead deflection is only detected along the Wollaston shear axis, which means you can only measure deflection in one axis.

The second interferometric sensing method uses a QPD to measure the bead deflection. The sensing configuration images the forward scattering light collected by the condenser on the QPD, as shown in figure 9 [28, 83]. The interaction between the laser beam and the dielectric bead causes the light to refract in the direction of the bead deflection. The resulting light intensity pattern at the QPD describes the angular-intensity pattern (the angular spectrum) of the forward scattered light and contains the information of the bead deflection [83]. A symmetric intensity pattern implies the bead deflection is zero; an antisymmetric intensity pattern implies the bead deflection is nonzero and in the direction of the highest light intensity, as shown in figure 10. The sensing system is insensitive to laser movements and only measures the bead deflection [83]. Proper alignment of the QPD at the BFP is necessary because the QPD is fixed in space [82]. Even though QPDS are not as sensitive as the DIC method, QPDS still provide measurements on the order of nanometers and this feature makes the QPD appropriate for single-molecule studies.

### 2.3.5 Actuation Methods

Manipulating the molecule requires the ability to manipulate the bead deflection in a reliable manner. Many methods exist to manipulate the bead deflection, and these methods range from moving the specimen stage with respect to the beam path or moving the beam path with respect to the specimen stage. Piezoelectric stages can move the specimen stage with respect to the beam path in three directions. The stages have nanometer resolution over a limited working area. However, the disadvantages are the cost and the limited bandwidth due to the movement of the mass of the stage [76]. The second method moves the beam path with respect to the specimen stage [76, 6]. One such setup involves moving the rear lens of a telescope with a 3-D position stage that is placed externally in front of the microscope. Lateral translations of the rear lens result in lateral translations of the laser beam in the specimen stage. Axial deflections of the rear lens changes the trapping depth. Similarly with piezoelectric stages, the disadvantage is the limited bandwidth, typically  $\sim 100$  Hz, due to

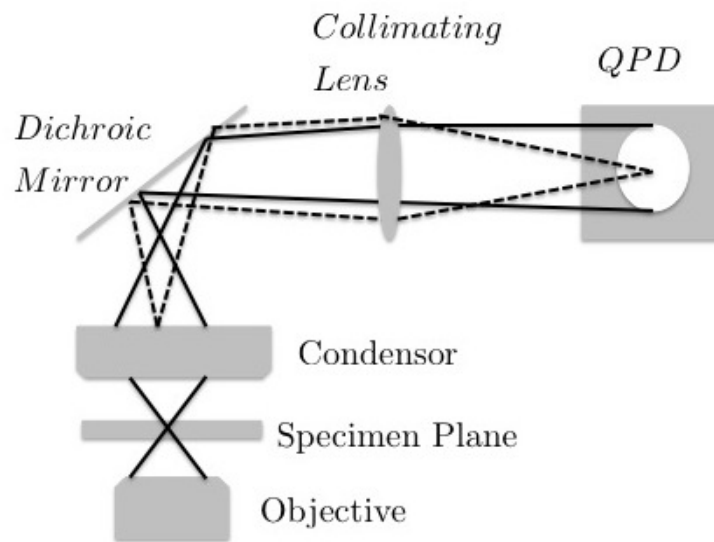


Figure 9: Schematic of QPD position detection system. The forward scattered light that is refracted by the dielectric bead is collected by the condenser and transmitted to the QPD. The QPD is located at the BFP of the condenser.

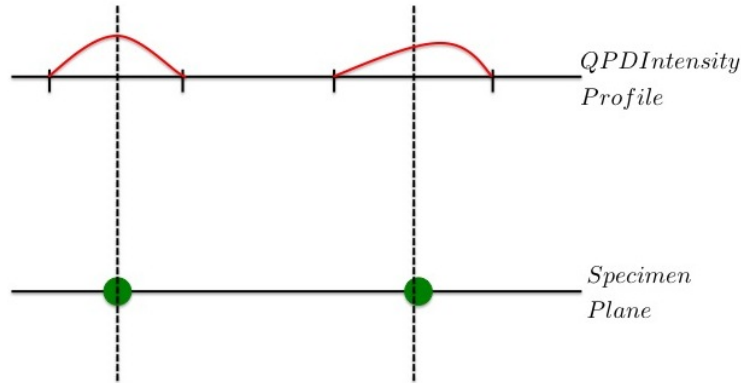


Figure 10: Schematic of the intensity profiles at the QPD’s surface. When the bead deflection is zero, the resulting intensity profile is symmetric at the QPD. If the bead deflection becomes nonzero, then the resulting intensity profile becomes antisymmetric in the direction of the bead deflection.

moving the mass of the lens. The idea of moving the beam path with respect to the specimen stage lead to actuation methods with faster bandwidths.

Actuation methods with faster bandwidths specify the angular spectrum of the light at the back focal-plane (BFP) of the objective. The BFP is a Fourier plane to the specimen plane, and a change in the angle of incidence of the beam path results in a lateral translation of the beam path in the specimen plane. The angular spectrum is specified using either acousto-optic deflectors (AOD) or fast steering mirrors (FSM). AODs are composed of a transparent crystal that has its density grating change by a acoustic wave traveling at ultrasound frequencies [76, 82]. This density grating change results in a change in the light’s angle (translations of the laser position in the specimen plane). AODs provide a fast response with a bandwidth  $\sim 10$  to  $100$  kHz (“note this is the speed with which deflections respond and not the bandwidth of the acousto-carrier frequency”) [80]. However, the disadvantages are the cost and AODs only manipulates the beam path in only one direction. [82]. FSM is a beam steering mirror that can tilt along two orthogonal axes by changing its voltage input. When placed at the BFP, a change in the FSM angle results in a change in the lateral translations

of the laser beam. FSMs provide a fast response, typically on the order of kilohertz, and provides more than adequate bandwidth for feedback control of optical trap studies in water.

## 2.4 ALIGNMENT PROCEDURES

This section discusses the procedures used to align the optical components. Alignment was done in accordance with the University’s safety measures and followed the lab’s SOP. Eye protection was worn, low laser power was used, an IR viewing card was used to determine the location and size of the laser beam, irises were used to ensure the beam path is straight and to act as beam stops, and the laser is turned off each time a component is added, removed, or changed. The alignment process involves coarsely aligning the beam path first, then finely aligning and tuning the beam path.

The schematic of the optical trap layout is shown in figure 3. First, the microscope and laser are placed and secured to the optical trap. Their placement is crucial because any movement in either component will interfere with the alignment process. After securing these components, the optical trap is constructed in two parts: the first part directs the beam path from the laser to the specimen plane, the second part directs the forward scatter light to the QPD. The alignment procedures for directing the beam path to the specimen plane from the laser is

1. The laser beam is expanded with its natural divergence to the desired beam diameter then collimated with a collimating lens  $f_1$ . This collimating lens is placed one focal length from the laser.
2. The FSM is placed at its desired distance from the objective to allow the beam path to enter the back optical port of the microscope. Placing the FSM at its desired distance allows the lenses  $f_2$  and  $f_3$  to be installed later in this alignment procedure.
3. From the collimating lens  $f_1$ , direct the beam path to the FSM with stationary mirrors. A secondary advantage to using stationary mirrors is the ability to “walk” the beam path into position and correct angular misalignments at the specimen plane.

4. At this point, the beam path enters the back optical port of the microscope then redirected with a dichroic mirror to the objective. Next, a sanity check is performed to determine if the beam path is present at the specimen plane by turning the objective turret to an open position (no objective) and placing the IR card at the specimen plane. The beam path should be visible on the IR card. If not, then adjust the tilt of the stationary mirrors until the beam path is visible at the specimen plane.
5. A second sanity check is performed to determine if the beam path is going straight through (orthogonal) to the specimen plane. This sanity check requires turning the objective turret to use the 10x objective to focus on a dirty slide (place fingerprints on slide or use a black marker) and viewing the specimen plane on a CCD camera. After the dirty slide is viewed on the CCD camera, turn off the microscope illumination, when if the beam path is present the monitor should glow. When the beam path is orthogonal to the specimen plane, then the corresponding effects on the monitor should be concentric circles expanding and collapsing when the objective is moved into and out of focus. The stationary mirrors tilt may have to be finely adjusted to have the beam path be orthogonal to the specimen plane.
6. Next, the lenses  $f_2$  and  $f_3$  are placed at their desired locations. The resulting beam path should slightly overfill the back aperture of the objective and be orthogonal to the specimen plane. Two sanity checks are performed to verify these claims. The first sanity check measures the beam path diameter by turning the objective turret to an open position and measuring the diameter. If the measured beam diameter is under/over sized, then the lenses  $f_2$  and  $f_3$  need to be reconsidered using the procedure outlined in section 2.3.1. The second sanity check verifying the beam path is orthogonal to the specimen plane according to the procedure just given for the case when the lenses  $f_2$  and  $f_3$  are not in the optical system.

The alignment procedure for directing the forward scattered light to the QPD is:

1. The forward scattered light is collected with the condenser. This collected light is redirected from the microscope optical path with a dichroic mirror.
2. The QPD is placed in a custom 3-D micro-manipulator apparatus at its desired distance from the condenser. Next, a sanity check is performed to determine if the collected light is hitting the QPD surface. This sanity check requires turning the objective turret to an open position and removing the condenser. The beam path is collimated when striking the QPD surface and this is verified using visible inspection and the QPD voltage signals. Adjust the 3-D manipulator if the beam path is not striking the QPD surface
3. The lens  $f_4$  is placed at its desired location. A sanity check is performed to verify the beam path is striking the center of the QPD surface. This sanity check requires turning the objective turret to an open position and removing the condenser. The lens  $f_4$  converges the beam path to a focal point at the QPD surface. On the QPD surface, the focal point is determined by analyzing the QPD voltage difference channels. The QPD voltage difference channels should be zero for the focal point to be at the center of the QPD. If the QPD voltage difference channels are non-zero, then adjust the 3-D micro-manipulator until the QPD output voltages are zero.
4. Reinstall the condenser.

### 3.0 SYSTEM CALIBRATION

The optical trap setup consists of the FSM (actuator) and the QPD (sensor) that are driven and displayed in voltages. The voltage signals must be calibrated to obtain quantitative results on the optical stiffness, the bead deflection, and the optical forces. A calibrated actuator allows for open-loop manipulation of the bead deflection. The calibrated sensor measures the bead deflections to quantify the optical stiffness and optical forces. This chapter discusses the calibration of the optical trap components and parameters.

#### 3.1 FAST STEERING MIRROR CALIBRATION

A calibrated FSM allows for open-loop manipulation of bead deflection. Calibrating the FSM relates voltage input to beam position. Note that calibration is not required for force control because force is applied via Hooke's law. Force control only requires the bead deflection and optical stiffness be known.

The conversion between the input voltage and the beam position was determined in section 2.3.1. Applying 1 V to the FSM results in a 3.4  $\mu\text{m}$  beam deflection at the specimen plane. The FSM input voltage is the output voltage from a 16 bit D/A board with a range of  $\pm 10$  V; the resulting beam position has a sensitivity of  $\sim 1$  nm. Next, the conversion between FSM input voltage to beam deflection is experimentally verified by using a CCD camera to image the beam position at the specimen plane. The CCD resolution limits are first determined. The resolution  $R$  is described by

$$R = \frac{0.61\lambda}{\text{NA}} \quad (3.1)$$

Table 3: The FSM input voltages and the corresponding laser position given in pixels to calibrate the FSM.

Input Voltage (V)	Pixel Location	Input Voltage (V)	Pixel Location
-7	(262, 118)	1	(262, 309)
-6	(262, 140)	2	(262, 336)
-5	(262, 164)	3	(262, 360)
-4	(262, 186)	4	(262, 383)
-3	(262, 208)	5	(262, 406)
-2	(262, 232)	6	(262, 428)
-1	(262, 257)	7	(262, 452)
0	(262, 283)		

where  $\lambda$  is the laser wavelength [84]. The optical trap design given in section 2.3 has a resolution of  $0.46 \mu\text{m}$ . The CCD camera has a pixel size of  $8.4 \times 9.8 \mu\text{m}$  and is mounted on a  $1x$  c-mount. The resulting image magnification and resolution at the CCD plane are  $63x$  and  $28.9 \mu\text{m}$  respectively. The pixel size is smaller than the resolution and this fact allows the CCD camera to successfully image the displacements. Theoretically, a  $1 \mu\text{m}$  displacement at the specimen plane results in a  $63 \text{ nm}$  displacement at the CCD plane, resulting in a conversion of 7.5 pixels per micrometer. A KR-851 slide (Microscope World) was used to calibrate the conversion rate, which yielded an experimental value of 6.8 pixels per micrometer. Next, the conversion between the FSM input voltage and the laser position is experimentally verified. A blank sample slide was placed in the microscope and the beam position was stepped through integer voltage values from  $\pm 7 \text{ V}$ . At each input voltage, the image was recorded and processed in Matlab to find the centroid. The recorded beam positions are given in table 3. The experimental results show that  $1 \text{ V}$  equals  $3.5 \mu\text{m}$ . The discrepancy is due to small alignment errors that are unavoidable.

## 3.2 QUADRANT PHOTODIODE CALIBRATION

There are two methods for sensor calibration that have been used in this work. The first method directly measures the bead's deflection by scanning the laser with respect to a stationary bead; the second method uses the equipartition theorem. The direct measurement method requires the measured sensor data be curve fitted with the system model. First, a mathematical model of the sensor system is needed.

### 3.2.1 Sensor Modeling

The QPD measures the bead deflection based on scattering theory [77]. The interaction between the laser and dielectric bead results the forward scattered light being refracted in the direction of the bead deflection. The resulting intensity at the QPD describes the angular spectrum of the forward scattered light and information on the bead deflection. This scattered theory approach yields satisfactory results when operating within the Rayleigh scattering regime. The QPD analysis has been provided in the literature for measurements in the lateral directions [83], and then later expanded to include three-dimensional measurements [85]. The analysis is shown for completeness.

The unscattered electric field is described in a spherical coordinate system centered about the origin, as shown in figure 11 [83],

$$E(r) \approx \frac{jk l_t P^{1/2}}{r(\pi \epsilon c)^{1/2}} \exp\left(jkr - \frac{1}{4}k^2 l_t^2 \theta^2\right) \quad (3.2)$$

where  $k$  is the wavenumber,  $\epsilon$  and  $c$  are the permittivity and speed of light in the solvent, and  $l_t$  is the laser's waist.

A dielectric bead with diameter  $d$  is placed at a location  $x$  from the laser focus. Assume  $x$  is a lateral deflection, then the unscattered electric field is described by

$$E(x) = \frac{2P^{1/2}}{l_t(\pi \epsilon c)^{1/2}} \exp\left(-\frac{x^2}{l_t^2}\right). \quad (3.3)$$

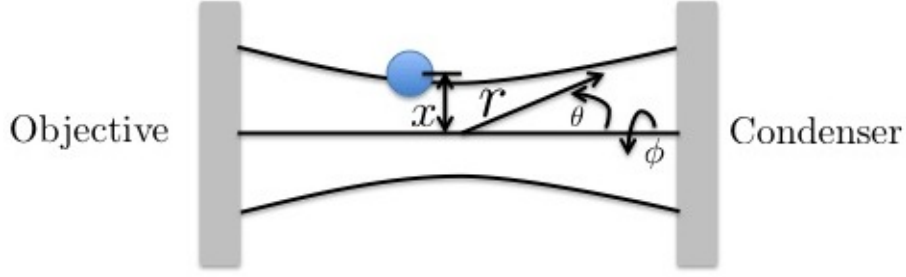


Figure 11: The coordinate notation used for the QPD modeling.

In the electric field, the dielectric bead acts as a point dipole with an induced dipole moment of  $4\pi\epsilon\alpha E$ , where  $\alpha$  is the uniform-field susceptibility. The uniform-field susceptibility is

$$\alpha = \left(\frac{d}{2}\right)^3 \frac{n_e^2 - 1}{n_e^2 + 2}, \quad (3.4)$$

where  $n_e$  is the effective index, which is the ratio of the refractive index of the bead to the refractive index of the medium. Assuming a Rayleigh approximation, the scattered electric field at large  $r$  (far-field) is described by

$$E'(r) \approx \frac{\alpha k^2}{r} E(x) \exp(jk(r - x \sin \theta \cos \phi)) \quad (3.5)$$

Substituting the unscattered electric field in equation (3.3) into equation (3.5) allows the scattered electric field be described by

$$E'(r) = \frac{2\alpha k^2 P^{1/2}}{r l_t (\pi \epsilon c)^{1/2}} \exp\left(-\frac{x^2}{l_t^2}\right) \exp(jk(r - x \sin \theta \cos \phi)). \quad (3.6)$$

The total intensity is the sum of the unscattered and scattered fields. This detection method detects the change in the intensity due to the scattering field. The intensity change is determined using first-order interference because the intensity is small due to the scattering field at the QPD [83]. The change in intensity is approximated by

$$\delta I \approx \frac{\epsilon c}{2} (|E + E'|^2 - |E|^2) \approx \epsilon c \text{Re}(|EE'^*|). \quad (3.7)$$

Substituting equation (3.2) and equation (3.5) into equation (3.7) results in the normalized change in intensity,

$$\frac{\delta I}{P}(x; r, \theta, \phi) = \frac{2\alpha k^3}{\pi r^2} \exp\left(-\frac{x^2}{l_t^2}\right) \exp\left(-\frac{k^2 l_t^2 \theta^2}{4}\right) \sin(kx \sin \theta \cos \phi). \quad (3.8)$$

Equation (3.8) describes the angular-interference pattern caused by a particle displaced by a lateral position  $x$  in the focal plane, observed at angles  $\theta$  and  $\phi$ . Integrating equation (3.8) over one half of the QPD, for angles  $\theta \in [0, \theta_o]$  and  $\phi \in [-\frac{\pi}{2}, \frac{\pi}{2}]$ , results in the change in normalized power due to the interference between the unscattered and scattered waves. The angle  $\theta_o$  is related to the NA of the condenser. The change in the normalized power is

$$\frac{I_+ - I_-}{I_+ + I_-} = \int \int \frac{\delta I}{P}(x; r, \theta, \phi) dA \quad (3.9)$$

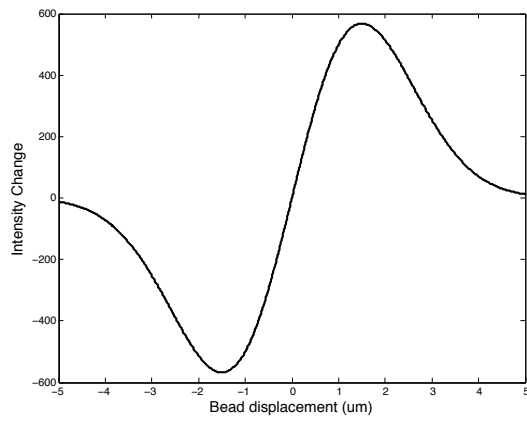
where  $dA = r^2 \sin \theta \cos \theta d\theta d\phi$ . Assuming a paraxial approximation in the  $\theta$  direction, equivalent to a small angle assumption, the integrand in equation (3.9) can be simplified by a series expansion to yield

$$\begin{aligned} \frac{I_+ - I_-}{I_+ + I_-} &\approx \frac{2\alpha k^4}{\pi} x \exp\left(-\frac{x^2}{l_t^2}\right) \int_{-\frac{\pi}{2}}^{\frac{\pi}{2}} \int_0^{\theta_o} \theta^2 \cos \phi d\theta d\phi \\ &\approx \frac{4\alpha k^4 \theta_o^3}{3\pi} x \exp\left(-\frac{x^2}{l_t^2}\right), \end{aligned} \quad (3.10)$$

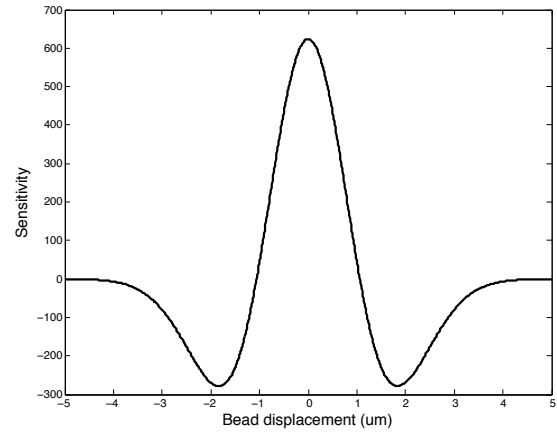
as shown in figure 12a. The expression in equation (3.10) is similar to the expression given in Pralle [85]; however, the difference is the explicit dependence on the NA of the condenser. The sensitivity can be determined by taking the derivative of equation (3.10) to yield

$$S = \frac{4\alpha k^4 \theta_o^3}{3\pi} \exp\left(-\frac{x^2}{l_t^2}\right) \left(1 - \frac{2x^2}{l_t^2}\right). \quad (3.11)$$

A schematic of the sensitivity verses the bead displacement is shown in figure 12b. The sensitivity can be increased by using a condenser with a large NA value to collect the forward scattered light. The QPD sensitivity verses the NA of the condenser and the bead radius is shown in figure 13a and figure 13b.

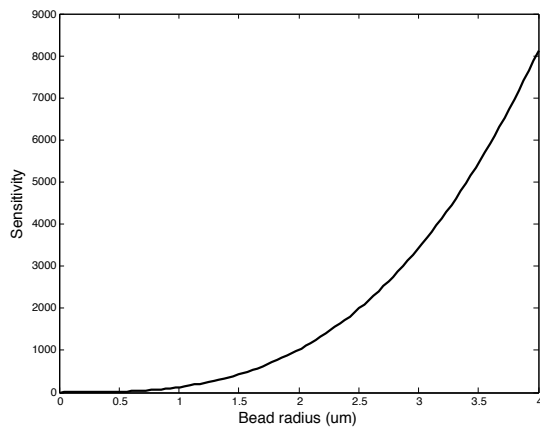


(a) QPD intensity

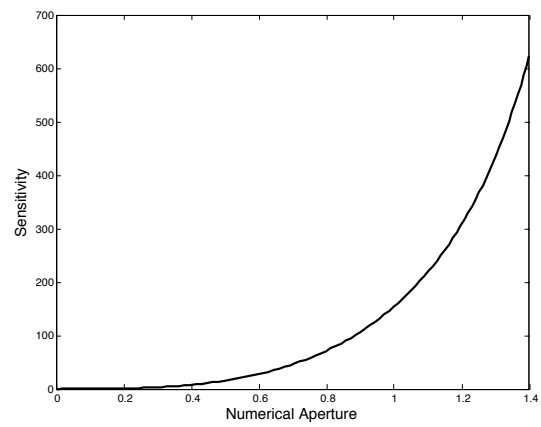


(b) QPD sensitivity

Figure 12: Schematics of the QPD response. Figure (12a) shows the QPD intensity verses bead displacement and figure (12b) shows the QPD sensitivity verses bead displacement.



(a) QPD sensitivity verses NA condenser.



(b) QPD sensitivity verses bead radius.

Figure 13: The sensitivity as a function of (13a) the bead radius and (13b) the condenser NA

### 3.2.2 Direct Method Calibration

The direct method calibrates the QPD by requiring the dielectric bead be immobilized-adhered to the glass surface and the FSM be calibrated. The calibrated FSM moves the laser with respect to the immobilized bead to create known bead deflections. The known bead deflections are measured with the QPD. This direct method experimentally determines the conversion between the bead deflection in nanometers to the QPD voltage. The calibration is performed on the following sample: the sample is prepared by placing 10  $\mu\text{l}$  of bead solution on a coverslip. The beads are adhered to the coverslip by evaporating the excess water off. Next, the coverslip is attached to a microscope slide by double sided tape (3M). Water fills the rest of the sample to mimic the environment of a sample of free beads. The sample is placed on the microscope, the coverslip is brought into focus to reveal the beads, and a single bead is moved to the laser location using the CCD camera for confirmation.

The laser beam is scanned across the bead in increments of 25 nm using custom code that was created in Simulink. At each increment, the beam is held for 2 s and the corresponding QPD signal is sampled at 1 kHz. The QPD voltage is averaged at each bead deflection and is shown in figure 14.

## 3.3 OPTICAL STIFFNESS CALIBRATION

A calibrated position sensor provides the ability to calibrate the optical stiffness. The optical stiffness can be calibrated using one of the following methods: the drag, the equipartition theorem, or the power spectrum methods. Each method will be discussed.

1. Drag Method. This method applies viscous drag forces to the bead by moving the surrounding medium with respect to the bead. The viscous forces are produced by moving the laser beam with respect to the stage or the stage with respect to the laser at a known constant velocity in either a triangular or sinusoidal patterns. The triangular wave input results in the bead having a square-wave velocity (viscous force is also a square wave); a sinusoidal wave input results in the bead having a cosine velocity profile

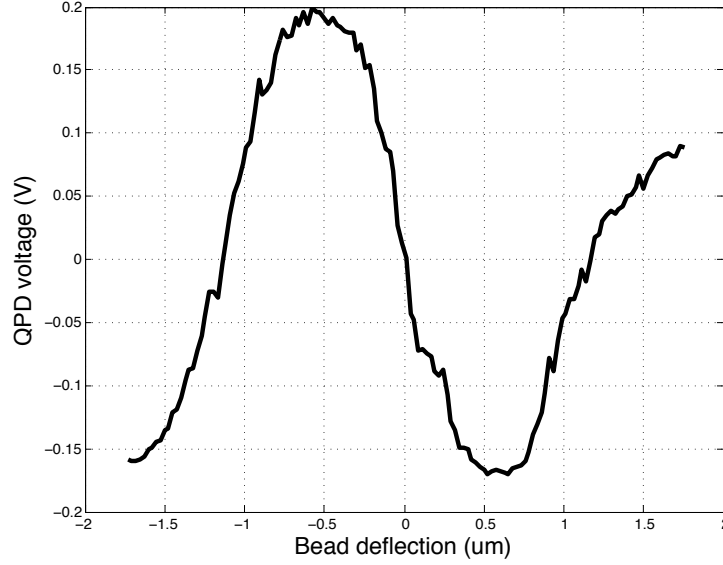


Figure 14: The QPD response to scanning the laser across a 3  $\mu\text{m}$  diameter polystyrene bead.

(viscous force also has a cosine velocity profile) [28]. The viscous drag force is balanced with the optical force,

$$kx = \eta\dot{x}_t, \quad (3.12)$$

where  $k$  is the optical stiffness,  $\eta = 6\pi\mu a$  is the Stokes drag coefficient ( $\mu$  is the medium's velocity and  $a$  is the bead radius),  $x$  is the bead deflection, and  $\dot{x}_t$  is the laser velocity. The bead deflection is measured with the calibrated sensor. The optical stiffness is calibrated by satisfying the force balance in equation (3.12).

2. Power Spectrum Method. This method uses the power spectrum of the trapped bead to calibrate the optical stiffness. The response of the trapped bead behaves as a first-order system that is characterized by the frequency  $\omega = k/\eta$ . The optical stiffness is found by curve fitting the auto-spectrum of the response of the trapped bead with known size. The sensor chosen should have sufficient bandwidth. Note that, caution should be taken to avoid biased estimates due to low-pass filtering. Low-pass filtering the response of the bead deflection reduces the cut-off frequency, leading to an underestimation of the

optical stiffness. Methods exist to address the underestimation have been developing by Berg-sorenson and Flyvbjerg [86, 87, 88].

3. Equipartition Theorem. The equipartition theorem uses the fact that trapped beads are constantly colliding with the surrounding water molecules due to Brownian noise. Trapped beads are in a harmonic potential well that is characterized by a optical spring. Each degree of freedom in a system has  $\frac{1}{2}k_B T$  of energy, where  $k_B$  is the Boltzmann's constant and  $T$  is absolute temperature. For optical traps, the equipartition theorem is expressed as

$$\frac{1}{2}k\langle x^2 \rangle = \frac{1}{2}k_B T, \quad (3.13)$$

where  $\langle x^2 \rangle$  is the mean-squared displacement of the bead deflection and  $k$  is the optical stiffness [76]. This method requires the sensor be calibrated and have sufficient bandwidth to measure the mean-squared bead deflection. Caution should be taken because the mean-squared displacement is a biased estimate due to low-pass filtering or the presence of additional noise sources [28]. Low-pass filtering the response of the bead deflection leads to an underestimation of the mean-squared bead deflection, which results in an overestimation of the optical stiffness. Additional noise sources will inflate the value of the mean-squared bead deflection, which leads to an underestimation of the optical stiffness. Finally, the method cannot be used to calibrate both the sensor and optical stiffness.

## 4.0 OPTICAL TRAP SYSTEM DYNAMICS

The performance and limitation of a closed-loop system depends on the structure of the open-loop system. The ability to design a controller first requires an understanding of the dynamics of the open-loop system. The open-loop system is the optical trap and its dynamics are composed of the following components: the bead deflection, the molecule, the FSM (actuator), and the QPD (sensor). This chapter describes the dynamics for each component and the properties of the optical trap.

### 4.1 BEAD DEFLECTION DYNAMICS

The dielectric bead experiences an optical force in the lateral direction due to its interaction with the laser. This interaction is described by a harmonic Gaussian potential  $U$  [89, 90, 91, 92],

$$U(z) = -U_0 \exp\left(-\frac{z^2}{2l_t^2}\right), \quad (4.1)$$

where  $z$  is the bead deflection,  $l_t$  is the characteristic length of the laser beam, and  $U_0$  depends on the bead volume, the index of refraction of the bead and that of the surrounding medium, the speed of light, and the magnitude of the electric field generated by the laser. The optical force (trapping force) is described by

$$f_t(z) = -\frac{d}{dz}U(z) = -kz \exp\left(-\frac{z^2}{2l_t^2}\right), \quad (4.2)$$

where  $k = U_0/l_t^2$  is the optical stiffness. The schematic of the dimensionless optical force versus the dimensionless bead deflection is shown in figure 15. The dimensionless optical

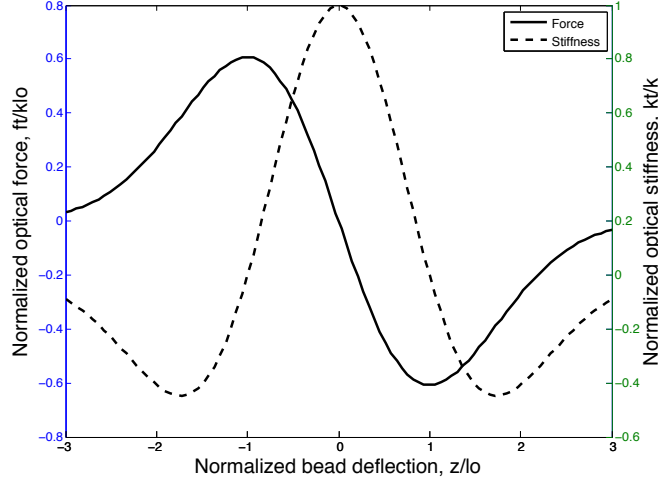


Figure 15: Schematic of the dimensionless optical force  $f_t(z)/(kl_t)$  versus the dimensionless bead's deflection  $z/l_t$  and the dimensionless optical stiffness  $k_{opt}(z)/k$  versus the dimensionless bead's deflection.

force decreases to its minimum value as the dimensionless bead deflection increases to one; as the dimensionless bead deflection increases beyond one, the magnitude of the dimensionless optical force decreases, which implies the bead can leave the optical trap. The physical interpretation is that as the bead moves away from the beam's center, the bead experiences an optical force that acts in the opposite direction to pull the bead towards the trap's center. Typically, the optical trap operates within its linear range and this allows the optical force to be approximated by its linearization  $f_{t_{lin}}(z) = -kz$ . It is insightful to determine the operating range where this linearization is valid by comparing the dimensionless optical force versus the dimensionless bead deflection for both the linear and nonlinear cases, as shown in figure 16. The comparison shows the linearization provides a good approximation when the dimensionless bead deflection is such that  $z/l_t \lesssim 0.2$ .

The optical stiffness is described by

$$k_t(z) = -\frac{d}{dz}f_t(z) = k \left(1 - \frac{z^2}{l_t^2}\right) \exp\left(-\frac{z^2}{2l_t^2}\right). \quad (4.3)$$

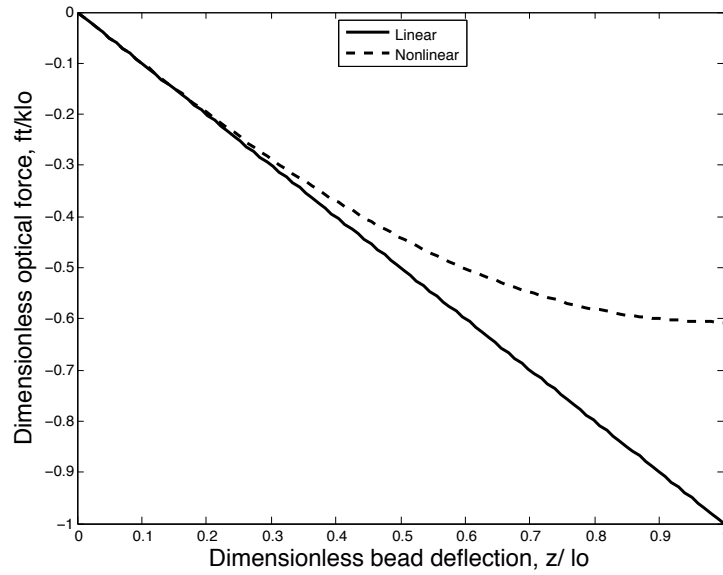


Figure 16: A schematic that compares both the dimensionless nonlinear optical force and the dimensionless linear optical force verses the dimensionless bead deflection. This comparison shows that the linearization provides a good approximation when the dimensionless bead deflection is such that  $z/l_t \lesssim 0.2$ . The linearization provides a poor approximation when the dimensionless bead deflection is such that  $z/l_t > 0.2$ .

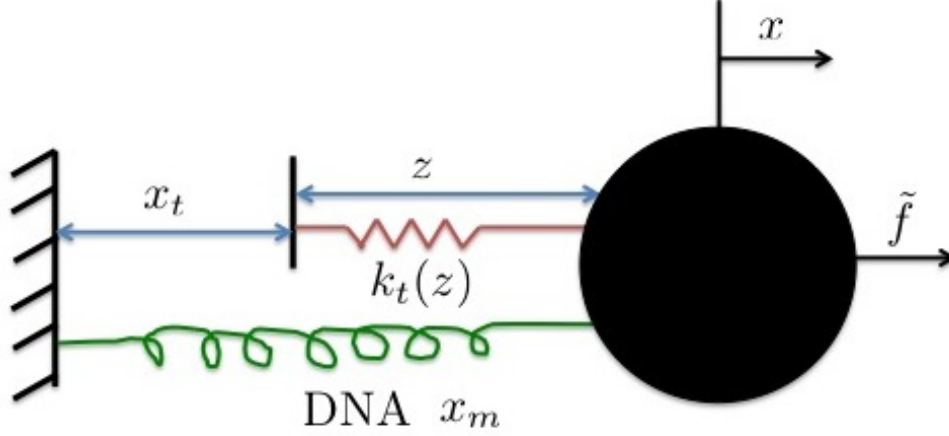


Figure 17: A schematic that shows the different forces acting on dielectric bead within the optical trap. and the relationship between the different extensions. These forces include an optical force, a viscous drag force, Brownian noise, and the molecule's force. The extensions are the molecule extensions  $x_m$ , the bead deflection  $z$ , and the laser position  $x_t$ .

The schematic of the dimensionless optical stiffness versus the dimensionless bead deflection is shown in figure 15. Initially, the dimensionless optical stiffness is at its maximum value, then decreases to zero and even becomes negative, as the dimensionless bead deflection increases. The decreasing dimensionless optical stiffness cause stability issues because the bead exits the optical trap when the dimensionless optical stiffness becomes negative.

The dielectric bead experiences additional forces including a viscous drag force, Brownian noise, and a molecule force, as shown in figure 17. The viscous drag is proportional to the Stokes drag coefficient  $\eta = 6\pi\mu a$  (where  $\mu$  is the medium's viscosity and  $a$  is the bead's radius) when the dielectric bead is near the medium's bulk. When the bead moves away from the medium's bulk towards an object (either another bead, molecule, or surface), then the bead experiences greater viscous forces and the Stokes drag coefficient increases according to Faxon's law [6].

The resulting dynamics describing the bead deflection is

$$m\ddot{z} + \eta\dot{z} - f_t(z) = -m\ddot{x}_t - \eta\dot{x}_t - f_m + \tilde{f}, \quad (4.4)$$

where  $m$  is the bead's mass,  $x_t$  is the laser position,  $\tilde{f}$  is the Brownian noise, and  $f_m$  is the molecular force. Brownian noise is due to the bead colliding with the surrounding water molecules and is characterized by a zero-mean Gaussian white noise with a constant power spectral density (PSD)  $S_f = 2\eta k_B T$  ( $k_B$  is Boltzmann's constant, and  $T$  is the absolute temperature) [6, 93]. The quantitative behavior of the bead deflection can be described by its eigenvalues,

$$\lambda_1 = -\frac{k}{\eta}, \quad \text{and} \quad \lambda_2 = -\frac{\eta}{m}. \quad (4.5)$$

At the molecular scale, the response of the bead deflection is dominated by viscous effects and this fact allows the inertial effects to be ignored [6]. Thus, the eigenvalues  $\lambda_1$  and  $\lambda_2$  are such that  $\lambda_1 \ll \lambda_2$ , and the resulting bead deflection dynamics can be described by a first-order system that is characterized by the frequency  $\omega_t = \lambda_1$ , the optical trap bandwidth. This bandwidth provides an upper bound on the response of the optical trap to external stimuli. The dynamics describing the bead deflection is simplified to

$$\eta \dot{z} = f_t(z) - f_m - \eta \dot{x}_t + \tilde{f}, \quad (4.6)$$

that has the laser's velocity as the controllable input. It is convenient to have the controllable input being the laser position  $x_t$  because the FSM changes the laser position not laser velocity. In theory, we obtain the laser velocity by multiplying the laser position by  $s$  (multiplication by  $s$  in the Laplace domain is equivalent to differentiation in the time domain). In linear system theory, a pure differentiation is equivalent to placing a zero at the origin, which adds  $90^\circ$  of phase to all frequencies. However, a zero placed at the origin causes closed-loop stability issues with the control design architecture. The control design architecture requires the closed-loop system be internally stable (the internal dynamics or zero dynamics be asymptotically or exponentially stable), and the internal dynamics depend on the zero locations. A zero placed at the origin does not guarantee internal stability. The control issues are eliminated by approximating the derivative  $s$  in the desired frequency range by using phase lead compensation type approach (see reference [94] about phase-lead compensation). The derivative is approximated by the transfer function

$$G_v(s) = \frac{\dot{x}_t(s)}{x_t(s)} = g_v \frac{s + \omega_{z_v}}{s + \omega_{p_v}}, \quad \text{with} \quad g_v = \frac{\omega_{p_v}}{\omega_{z_v}} \quad \text{and} \quad \omega_{z_v} < \omega_{p_v}. \quad (4.7)$$

It is convenient to realize the transfer function  $G_v(s)$  into an equivalent state-space representation to yield

$$\dot{a}_1 = -\omega_{p_v} a_1 + x_t \quad (4.8a)$$

$$\dot{x}_t = g_v(\omega_{z_v} - \omega_{p_v})a_1 + g_v x_t. \quad (4.8b)$$

## 4.2 MOLECULE AND DISTURBANCE DYNAMICS

A long-chain molecule acts as an entropic spring, with the molecular force being related to the molecular extension (end-to-end distance) by the worm-like chain (WLC) model [95, 96, 97]. The WLC model describes the molecule as a flexible chain that bends smoothly due to Brownian noise. The dimensionless molecular force is related to the dimensionless molecular extension through the WLC model by

$$\frac{l_p f_m(x_m)}{k_B T} = \frac{x_m}{l_m} + \frac{1}{4} \left(1 - \frac{x_m}{l_m}\right)^{-2} - \frac{1}{4}, \quad (4.9)$$

where  $l_m$  is the molecular contour length, and  $l_p$  is its persistence length, which describes the molecule's resistance to thermal forces [97]. A schematic of the dimensionless molecule force versus the dimensionless molecule extension is shown in figure 18. DNA elasticity behaves as a hardening spring as  $\frac{x_m}{l_m} \rightarrow 1$ , which implies a greater amount of force is needed to farther stretch the molecule. The persistence length describes the molecule's resistance to thermal bending, and can be related to the molecule's flexural rigidity and temperature by applying the Principle of Equipartition of Energy to yield [3]

$$l_p = \frac{EI}{k_B T}. \quad (4.10)$$

In this research, the primary interest is detecting changes in the molecular force about some nominal force and extension,  $\bar{f}_m$  and  $\bar{x}_m$ , which satisfy the WLC model. Moreover, we are also interested in changes in the molecular force due to changes in the molecular extension,  $\tilde{x}_m = x_m - \bar{x}_m$ , and changes in the contour length  $\tilde{l}_m = l_m - \bar{l}_m$ . The molecular force is

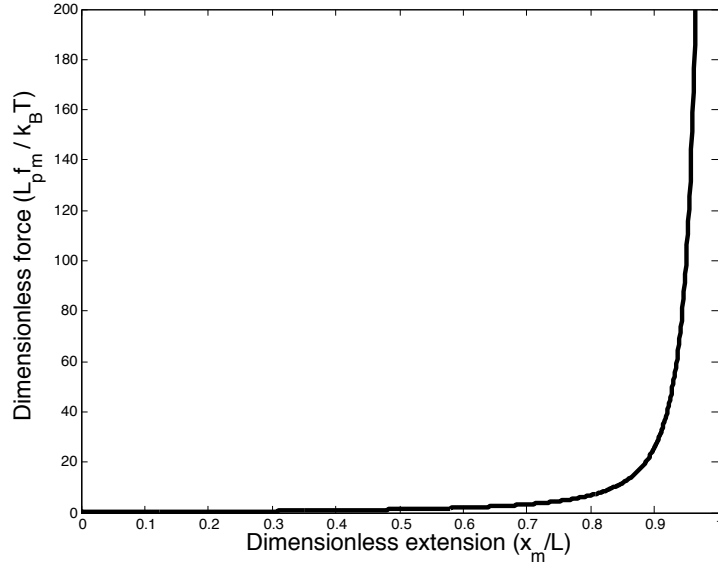


Figure 18: A schematic of the dimensionless molecule force versus the dimensionless molecule extension.

described about its nominal value by performing a first-order Taylor series approximation to yield

$$f_m = \bar{f}_m + k_m \tilde{x}_m - k_m^* \tilde{l}_m, \quad (4.11)$$

where the molecular stiffnesses are

$$k_m = \frac{k_B T}{l_m l_p} \left[ \frac{1}{2} \left( 1 - \frac{\bar{x}_m}{l_m} \right)^{-3} + 1 \right] \simeq \frac{3k_B T}{2l_m l_p}, \quad (4.12)$$

$$k_m^* = \frac{k_B T}{l_m l_p} \left( \frac{\bar{x}_m}{l_m} \right) \left[ \frac{1}{2} \left( 1 - \frac{\bar{x}_m}{l_m} \right)^{-3} + 1 \right] = k_m \frac{\bar{x}_m}{l_m} \simeq \frac{3k_B T}{2l_m l_p} \left( \frac{\bar{x}_m}{l_m} \right). \quad (4.13)$$

The stiffness approximations are valid for small molecular extensions such that  $\bar{x}_m/l_m \ll 1$ . Note, the minus sign in equation 4.11 is due to the fact that increases in the contour length results in a decrease in the molecular force.

When the molecule is held at a nominal extension, a change in the contour length results in the molecule experiencing a change its force to maintain its extension. A decrease in the contour length results in the molecule experiencing an increase in its force (e.g., the

molecule is stretched); an increase in the contour length results in the molecule experiencing a decrease in its force (e.g., the molecule is relaxed). The molecule experiences a new force equal to  $\bar{f}_m - k_m^* \tilde{l}_m$ , and is due to the change in the dimensionless molecule extension  $\frac{x_m}{l_m}$ . The phenomena occurs in DNA transcription when the molecule extension is maintained constant. During transcription, the enzyme RNA polymerase makes a copy of the DNA sequence at a rate of one nucleobase at a time, and the rate is equal to the rate that the contour length is reduced. The DNA molecule maintains its extension by being stretched harder. The increase in force is related to the change in  $\frac{x_m}{l_m}$ , a measurable quantity as shown later in this section. The relationship allows equation 4.11 to be simplified by combining  $\bar{f}_m$  and  $-k_m^* \tilde{l}_m$  into one variable called the disturbance force  $f_d$ . The disturbance force is described by

$$f_d = \bar{f}_m - k_m^* \tilde{l}_m, \quad (4.14)$$

and substituting equation 4.14 in equation 4.11 yields

$$f_m = f_d + k_m \tilde{x}_m. \quad (4.15)$$

**Molecular Constraint:** The molecule extension depends on the laser position and the bead deflection, as shown in figure 17. These variables are constrained by  $x_m = x_t + z$ , where  $x_t = \int_0^t \dot{x}_t(\tau) d\tau$ . Taking a time derivative of the constraint gives the differential constraint,

$$\dot{x}_m = \dot{x}_t + \dot{z}. \quad (4.16)$$

**Molecular dynamics and Relaxation time:** The molecular force changes dynamically due to the relaxation of the molecule and Brownian noise. Polymer relaxation time describes the dynamic behavior of a polymer transitioning from a stretched state to an equilibrium state [98, 99]. Relaxation has been studied with optical traps by attaching the polymer at one end to a polystyrene bead and at its other end to a glass surface. The relaxation phenomena is governed by two forces: the friction force acting on the polystyrene bead and the force the polymer applied to the bead. The friction force on the polymer can be neglected for local stretches about the equilibrium state. There are many factors affecting the relaxation time: the contour length, the solvent temperature, and the initial stretching

Table 4: Relaxation times and bandwidths for representative molecules [3, 4].

Molecule	$\tau$
Microtubule, 50 $\mu\text{m}$ long	1.1 s
Microtubule, 5 $\mu\text{m}$ long	500 $\mu\text{s}$
Actin, 50 $\mu\text{m}$ long	500 s
DNA, 10 $\mu\text{m}$ long	1 s

state [4]. The relaxation can vary order several orders of magnitude, as shown in table 4. In this research, we are interested in the local behavior of the DNA about its equilibrium state (nominal extension) and assume the time constant for relaxation is  $\tau_m = 0.2\text{ s}$ . It will be convenient to use the molecular bandwidth  $\omega_m = 1/\tau_m$ .

The second phenomena affecting the molecular dynamics is Brownian noise. Water molecules continually collide with the molecule as it is held at its nominal extension [98]. These collisions cause the molecule extension to want to shorten, however, the molecule is constrained to its nominal extension. Maintaining the molecule at its nominal extension results in an increase in the force within the molecule, then the force delays back to its nominal value. The effects of the water colliding with the molecule on the molecule force can be modeled as zero mean Gaussian white noise with spectral density of  $S_m$ .

The dynamics for the molecular force is described by

$$\tau_m \dot{f}_m = -f_m + f_d + \tau_m k_m \dot{x}_m + \tilde{f}_m, \quad (4.17)$$

where  $\tilde{f}_m$  are the thermal fluctuations, which are characterized by a zero mean Gaussian white noise process with PSD  $S_m$ . The dynamics for the molecule force depends on the bead deflection through the molecule constraint in equation 4.16,

$$\tau_m \dot{f}_m = -f_m + f_d + \tau_m k_m (\dot{x}_t + \dot{z}) + \tilde{f}_m. \quad (4.18)$$

The force  $f_d$  is treated as an unknown disturbance. The disturbance is of interest because its value changes with changes in the contour length or if the molecule is stretched to relaxed to a new extension.

**Disturbance dynamics** At steady-state, the molecule is held at a constant extension (equivalent to a constant force) and this fact allows its dynamics to be described by  $\dot{f}_d = 0$ . In the analysis to follow, these dynamics must have a nonzero state matrix. Here, we approximate the dynamics  $\dot{f}_d = 0$  by including a pole that is characterized by the frequency  $\omega_d$  such that  $\omega_d \ll 1$ . The dynamics describing the nominal molecular extension is

$$\dot{f}_d = -\omega_d f_d + \omega_e \tilde{f}_d, \quad 0 < \omega_d \ll \omega_e = 1, \quad (4.19)$$

where  $\tilde{f}_d$  is the zero mean white noise with PSD  $S_d$  that drives the disturbance model.

The dynamics describing the bead deflection, equation 4.6, and the molecular force, equation 4.18, are coupled. It is insightful to describe the quantitative behavior of the coupled bead-molecule system to understand how changes in the bead deflection affect the molecule force, and also how changes in the molecule force affect the bead deflection. The two system metrics to be quantified are the system bandwidth and the steady-state response.

### 4.2.1 Bead-Molecule System

The dynamics describing the bead deflection and the molecular force, equation 4.6 and equation 4.18 respectively, are coupled and can be combined to form the bead-molecule system. The bead-molecule system can be written in matrix form to yield

$$\begin{bmatrix} \eta & 0 \\ -\tau_m k_m & \tau_m \end{bmatrix} \begin{bmatrix} \dot{z} \\ \dot{f}_m \end{bmatrix} = \begin{bmatrix} f_t(z) - f_m \\ -f_m \end{bmatrix} + \begin{bmatrix} -\eta \\ \tau_m k_m \end{bmatrix} \dot{x}_t + \begin{bmatrix} 0 \\ 1 \end{bmatrix} f_d + \begin{bmatrix} \tilde{f} \\ \tilde{f}_m \end{bmatrix}. \quad (4.20)$$

Equation 4.20 can be simplified by the following:

1. The use of the optical bandwidth  $\omega_t = k_t/\eta$  and the molecular bandwidth  $\omega_m = 1/\tau_m$ ,
2. Defining new dimensionless constants for the stiffnesses  $\kappa = k_m/k_t$  and the molecular extension  $\epsilon = \bar{x}_m/l_m$ ,

3. Normalizing the forces by the stiffnesses, making equivalent deflections/extensions, according to

$$\tilde{d} = \tilde{f}/k_t, \quad d_m = f_m/k_m, \quad \bar{d}_m = \bar{f}_m/k_m, \quad d_d = f_d/k_m, \quad \text{and} \quad \tilde{d}_m = \tilde{f}_m/k_m. \quad (4.21)$$

Substitute the normalizing factors in equation 4.21 into equation 4.20 results in the bead-molecule system being described by the bead deflection and the molecule extension  $d_m$ . The bead-molecule system is described by

$$\begin{bmatrix} \dot{z} \\ \dot{d}_m \end{bmatrix} = \begin{bmatrix} -\omega_t z \exp\left(-\frac{z^2}{2l_t^2}\right) - \kappa\omega_t d_m \\ -\omega_t z \exp\left(-\frac{z^2}{2l_t^2}\right) - (\kappa\omega_t + \omega_m)d_m \end{bmatrix} + \begin{bmatrix} -1 \\ 0 \end{bmatrix} \dot{x}_t + \begin{bmatrix} 0 \\ \omega_m \end{bmatrix} d_d + \begin{bmatrix} \omega_t & 0 \\ \omega_t & \omega_m \end{bmatrix} \begin{bmatrix} \tilde{d} \\ \tilde{d}_m \end{bmatrix}. \quad (4.22)$$

**System Bandwidth** Its quantitative behavior can be studied by linearizing equation 4.22 about  $z = 0$  to yield

$$\begin{bmatrix} \dot{z} \\ \dot{d}_m \end{bmatrix} = \begin{bmatrix} -\omega_t & -\kappa\omega_t \\ -\omega_t & -(\kappa\omega_t + \omega_m) \end{bmatrix} \begin{bmatrix} z \\ d_m \end{bmatrix} + \begin{bmatrix} -1 \\ 0 \end{bmatrix} \dot{x}_t + \begin{bmatrix} 0 \\ \omega_m \end{bmatrix} d_d + \begin{bmatrix} \omega_t & 0 \\ \omega_t & \omega_m \end{bmatrix} \begin{bmatrix} \tilde{d} \\ \tilde{d}_m \end{bmatrix}. \quad (4.23)$$

In open-loop, the bead-molecule system is a second order overdamped system (two distinct real poles), and its poles are the roots of the characteristic equation,

$$s^2 + [(1 + \kappa)\omega_t + \omega_m]s + \omega_t\omega_m = 0, \quad (4.24)$$

where  $s$  is the Laplace domain variable. The poles depend on the dimensionless constant  $\kappa$ ; the pole locations are found for three cases:  $\kappa \ll 1$ ,  $\kappa \gg 1$ , and intermediate values for  $\kappa$ .

1. ( $\kappa \ll 1$ ) *A soft molecule and a stiff optical trap*: This situation occurs when the bead deflection is small (the value of  $k_t$  is large) and the molecular extension is small (the value of  $k_m$  is small). As a result, the molecular dynamics are decoupled from the dynamics of the bead deflection in equation 4.23. The corresponding pole locations are

$$s_1 \approx -\omega_t \quad \text{and} \quad s_2 \approx -\omega_m. \quad (4.25)$$

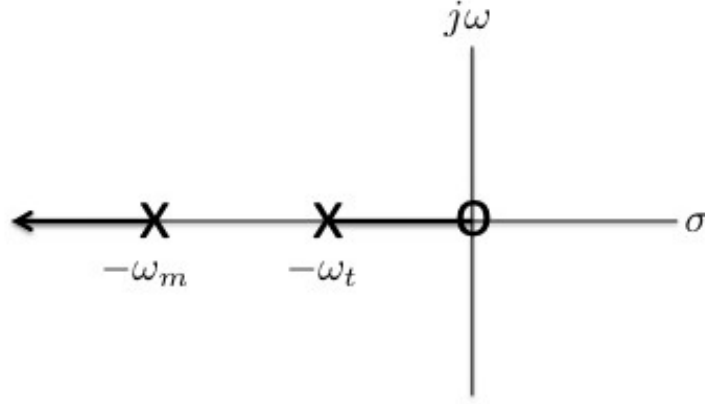


Figure 19: A root locus that graphically shows how the poles of the trap-molecule system change when the value of the dimensionless constant  $\kappa$  is increased.

2. ( $\kappa \gg 1$ ) *A stiff molecule and a soft optical trap*: This situation occurs when the bead deflection is such that  $z/l_t \rightarrow 1$  (the value of  $k_t$  is small) and the molecular extension is such that  $x_m/l_m \rightarrow 1$ , a nearly rigid molecule (the value of  $k_m$  is high). In this case, the nearly rigid molecule is attached at one end to a dielectric bead, resulting in the bead deflection being stationary and nonzero, and the bead deflection not relaxing. The corresponding pole locations are

$$s_1 \approx 0 \quad \text{and} \quad s_2 \approx -\kappa\omega_t - \omega_m. \quad (4.26)$$

3. *Intermediate values for  $\kappa$* . The constant  $\kappa$  is considered a gain. It is convenient to express the characteristic equation in Evan's root locus form to graphically view how the poles change as the constant  $\kappa$  is increased. The characteristic equation in equation 4.24 is expressed in Evan's root locus form,

$$1 + \kappa \frac{\omega_t s}{(s + \omega_t)(s + \omega_m)} = 0 \quad (4.27)$$

and the corresponding root locus is shown in figure 19. Increasing the constant  $\kappa$  is equivalent to the molecule being extended (the value of  $k_m$  increasing), and the bead deflection becomes larger (the value of  $k_t$  decreasing). The molecule being extended

implies the molecule relaxation bandwidth is increased while the optical bandwidth is decreased.

**Steady-state response** The mean steady-state response of the bead-molecule system is described by taking the expected value of equation 4.23 to yield

$$\frac{d}{dt} \begin{bmatrix} E[z] \\ E[d_m] \end{bmatrix} = \begin{bmatrix} -\omega_t & -\kappa\omega_t \\ -\omega_t & -\omega_m - \kappa\omega_t \end{bmatrix} \begin{bmatrix} E[z] \\ E[d_m] \end{bmatrix} + \begin{bmatrix} -1 \\ 0 \end{bmatrix} \dot{x}_t + \begin{bmatrix} 0 \\ \omega_m \end{bmatrix} d_d. \quad (4.28)$$

Recall that the process noise is zero mean,  $E[\tilde{d}] = E[\tilde{d}_m] = 0$ . At steady state,  $\frac{d}{dt}E[z] = \frac{d}{dt}E[d_m] = 0$ , and the corresponding laser position is constant, which implies laser velocity  $\dot{x}_t = 0$ . The resulting mean response of the bead deflection and molecule extension are

$$\langle z \rangle = -\kappa d_d = -\kappa \left( \bar{d}_m - \frac{\bar{x}_m}{l_m} \tilde{l}_m \right), \quad (4.29)$$

$$\langle d_m \rangle = d_d = \bar{d}_m - \frac{\bar{x}_m}{l_m} \tilde{l}_m, \quad (4.30)$$

where  $d_d = \bar{d}_m - \frac{\bar{x}_m}{l_m} \tilde{l}_m$  from equation 4.14 and equation 4.21 to turn force inputs into equivalent displacement inputs. Equation 4.30 shows the mean molecular extension  $E[d_m]$  is the sum of the nominal extension  $\bar{d}_m$ , and the changes about that value due to changes in the molecular contour length  $\tilde{l}_m$ . Equation 4.29 shows the mean bead deflection  $E[z]$  is proportional to  $E[d_m]$  by the dimensionless stiffness  $\kappa$ . These equations imply a positive molecular elongation results in the bead being pulled in the negative direction.

## 4.2.2 Bead-Molecule-Disturbance Dynamics

The dynamics describing the bead-molecule-disturbance dynamics including the bead-molecule system in equation 4.22, the derivative approximate of the laser position in

equation 4.8, the disturbance in equation 4.19, and the normalizing factors in equation 4.21. The bead-molecule-disturbance system can be written in matrix form to yield

$$\frac{d}{dt} \begin{bmatrix} z \\ d_m \\ a_1 \\ d_d \end{bmatrix} = \begin{bmatrix} -\omega_t z \exp\left(-\frac{z^2}{2l_t^2}\right) - \kappa\omega_t d_m - g_v(\omega_{z_v} - \omega_{p_v})a_1 \\ -\omega_t z \exp\left(-\frac{z^2}{2l_t^2}\right) - (\kappa\omega_t + \omega_m)d_m + \omega_m d_d \\ -\omega_{p_v} a_1 \\ -\omega_d d_d \end{bmatrix} \quad (4.31)$$

$$+ \begin{bmatrix} -g_v \\ 0 \\ 1 \\ 0 \end{bmatrix} x_t + \begin{bmatrix} \omega_t & 0 & 0 \\ \omega_t & \omega_m & 0 \\ 0 & 0 & 0 \\ 0 & 0 & \omega_e \end{bmatrix} \begin{bmatrix} \tilde{d} \\ \tilde{d}_m \\ \tilde{d}_d \end{bmatrix}.$$

Implementing equation 4.31 provides the molecule information in terms of extensions not forces. Forces are the desirable parameters, and the extensions are related to forces through the molecule stiffness by the normalizing factors in equation 4.21. However, the molecule stiffness depends on the molecule extension, and the stiffness is not known a priori. The molecule stiffness can be found using the information about the disturbance. The following subsection discussing the relation between the disturbance and the molecule stiffness.

The bead-molecule-disturbance system has the laser position as the controllable input, while the bead deflection has the measurable state. The laser position is controlled using the FSM. The bead deflection is measured using the QPD. The following two sections describe the dynamics for the QPD and the FSM.

### 4.2.3 Relating The Disturbance to the Molecule Stiffness

The challenge with relating the extensions to forces is that the molecular stiffness is unknown apriori. The molecule stiffness can be calculated in real-time using information about the disturbance using the fact there are two one-to-one maps: the first map relates the molecule stiffness and the dimensionless extension  $\frac{\bar{x}_m}{l_m}$  via equation 4.12, and the second map relates the dimensionless extension  $\frac{\bar{x}_m}{l_m}$  and the dimensionless disturbance  $\frac{\bar{d}_m}{l_m}$ . The mapping between the molecule stiffness and the disturbance is determined by first finding the second one-to-one map, then apply  $\frac{\bar{x}_m}{l_m}$  to equation 4.12. The mapping between  $\frac{\bar{d}_m}{l_m}$  and  $\frac{\bar{x}_m}{l_m}$  can be calculated

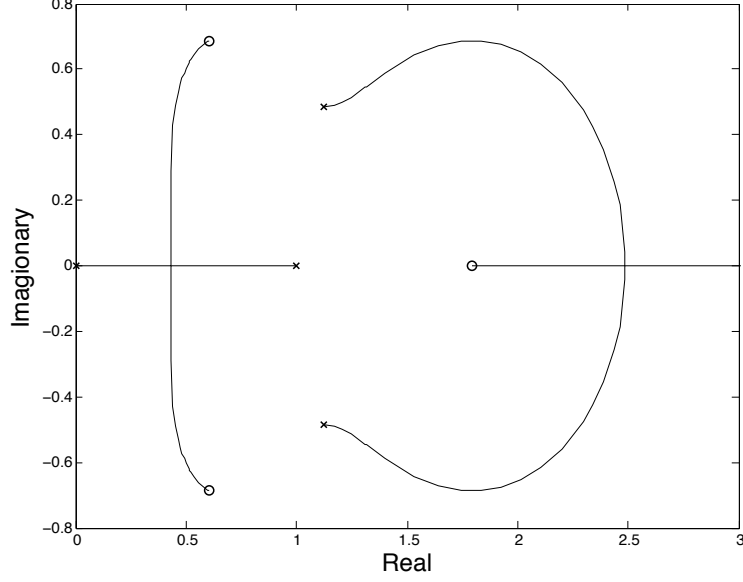


Figure 20: A root locus showing how increasing the value of  $\frac{\bar{d}_m}{l_m}$  affects the value of  $\frac{\bar{x}_m}{l_m}$ .

using the nominal force. The nominal force  $\bar{f}_m$  can be calculated uses the WLC model and the molecule stiffness via  $f_m\left(\frac{\bar{x}_m}{l_m}\right) = l_m k_m \left(\frac{\bar{x}_m}{l_m}\right) \frac{\bar{d}_m}{l_m}$  to result in a quartic polynomial relating the dimensionless extension  $\frac{\bar{d}_m}{l_m}$  to the dimensionless extension  $\frac{\bar{x}_m}{l_m}$ . The quartic polynomial is

$$\left(\frac{\bar{x}_m}{l_m}\right)^4 - \left(\frac{13}{4} + \frac{\bar{d}_m}{l_m}\right) \left(\frac{\bar{x}_m}{l_m}\right)^3 + \left(\frac{15}{4} + \frac{3\bar{d}_m}{l_m}\right) \left(\frac{\bar{x}_m}{l_m}\right)^2 - \left(\frac{3}{2} + \frac{3\bar{d}_m}{l_m}\right) \left(\frac{\bar{x}_m}{l_m}\right) + \frac{3\bar{d}_m}{2l_m} = 0. \quad (4.32)$$

where  $\frac{\bar{x}_m}{l_m} \in [0, 1)$ . It is convenient to graphical view how the solution  $\frac{\bar{x}_m}{l_m}$  changes as the value  $\frac{\bar{d}_m}{l_m}$  is increased. The graphical approach is a Evan's root locus with  $\frac{\bar{x}_m}{l_m} = s$  and  $\frac{\bar{d}_m}{l_m}$  is the gain. Equation 4.32 is expressed in Evan's root locus form,

$$1 + \left(\frac{\bar{d}_m}{l_m}\right) \frac{-s^3 + 3s^2 - 3s + \frac{3}{2}}{s^4 - \frac{13}{4}s^3 + \frac{15}{4}s^2 - \frac{3}{2}s} = 0, \quad (4.33)$$

and the corresponding root locus is shown in figure 20. The value of  $\frac{\bar{x}_m}{l_m}$  can then be used in equation 4.12 to find the molecule stiffness.

### 4.3 SENSOR DYNAMICS

The QPD relates the bead deflection to voltage. These dynamics are characterized with a first-order model

$$G_s(s) = g_s \frac{\omega_s}{s + \omega_s}, \quad (4.34)$$

where  $\omega_s$  is the sensor bandwidth and its value is provided by the manufacturer, and  $g_s$  is a gain that is equal to the slope of the QPD intensity curve in figure 14. The sensor bandwidth is at least two orders of magnitude faster than the bandwidths previously discussed. As a result, within the operating frequency range, the sensor dynamics can be simplified to a constant gain of  $g_s$ .

### 4.4 ACTUATOR DYNAMICS

The FSM relates voltage input to laser position. Even though the FSM had been calibrated in section 3.1, a model of the actuator dynamics is necessary because there are no position sensors on the FSM. The actuator dynamics will implicitly contain the conversion ratio of 1 V equals 3.5  $\mu\text{m}$ . The model is determined by centering the laser beam on a dielectric bead that is adhered to a coverslip. This approach removed the bead deflection dynamics, leaving only the actuator dynamics, and required the QPD to measure the actuator response. A broadband white noise was then used to excite the system and produce the actuator's transfer function relating the laser position to the input voltage. This model was curve fit with a second-order model,

$$G_a(s) = \frac{x_t(s)}{u(s)} = g_a \frac{s + \omega_z}{(s + \omega_{p1})(s + \omega_{p2})}, \quad \text{with} \quad g_a = \frac{g\omega_{p1}\omega_{p2}}{g_s\omega_z}, \quad (4.35)$$

where  $g$  is a gain and  $u$  is the FSM input voltage. The magnitude plot and the phase plot of model dynamics closely resembles that of the actual dynamics, as shown in figure 21 . Note, the transfer function  $G_a(s)$  is a model and can be subjected to possible errors including poor system identification, nonlinearities, and high frequencies dynamics.

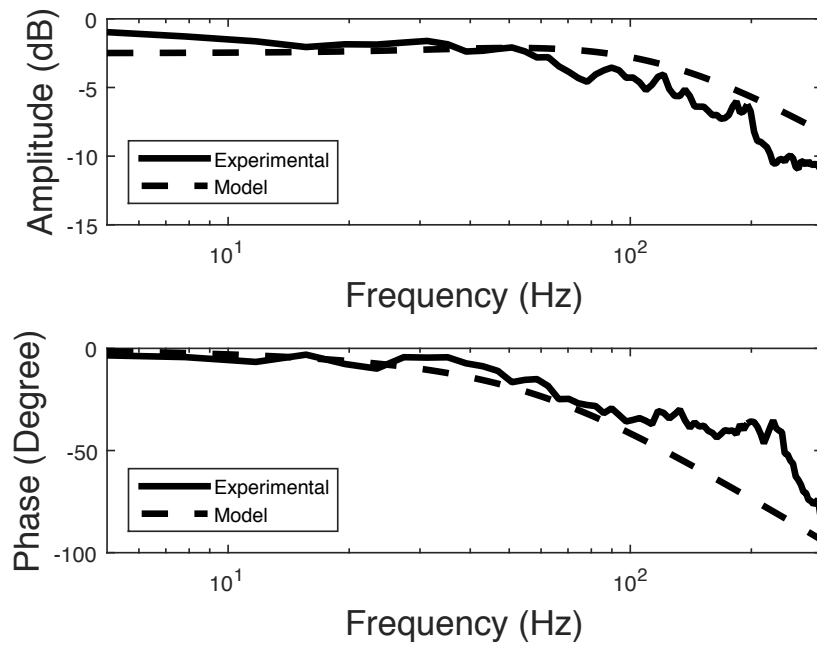


Figure 21: Bode plot of actuation dynamics relating the laser position in the specimen plane to the voltage input of the FSM.

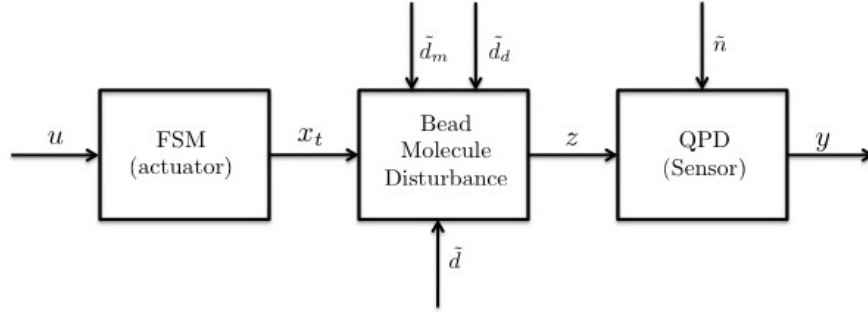


Figure 22: The block diagram for the optical trap system. The optical trap system is the plant in this research.

It is convenient to realize the transfer function  $G_a(s)$  into an equivalent state-space representation to yield

$$\frac{d}{dt} \begin{bmatrix} a_2 \\ a_3 \end{bmatrix} = \begin{bmatrix} 0 & 1 \\ -\omega_{p1}\omega_{p2} & -\omega_{p1} - \omega_{p2} \end{bmatrix} \begin{bmatrix} a_2 \\ a_3 \end{bmatrix} + \begin{bmatrix} 0 \\ 1 \end{bmatrix} u \quad (4.36a)$$

$$x_t = \begin{bmatrix} g_a\omega_z & g_a \end{bmatrix} \begin{bmatrix} a_2 \\ a_3 \end{bmatrix}. \quad (4.36b)$$

## 4.5 OPTICAL TRAP SYSTEM

The optical trap system is composed of following dynamics: the bead-molecule-disturbance system (equation 4.31), the FSM (equation 4.36) and the QPD. A schematic of the optical trap system is shown in the block diagram in figure 22. The optical trap system is expressed in state-space representation with the state  $x = [z, d_m, a_1, a_2, a_3, d_d]^T$ , process noise  $\tilde{w} = [\tilde{d}, \tilde{d}_m, \tilde{d}_d]^T$ , and measurement noise  $\tilde{n}$  to yield

$$\dot{x} = f(x) + B_u u + B_w \tilde{w} \quad (4.37a)$$

$$y = h(x) + \tilde{n} \quad (4.37b)$$

where the state  $x \in \mathbb{R}^6 \subset M$  ( $M$  is the set of admissible states), the control input  $u \in \mathbb{R} \subset U$  ( $U$  is the set of admissible control inputs), the process noise input  $w \in \mathbb{R}^4$ , the measurement  $y \in \mathbb{R}$ , and the measurement noise  $\tilde{n} \in \mathbb{R}$ . The vector field  $f : \mathbb{R}^6 \rightarrow \mathbb{R}^6$  and the scalar field  $h : \mathbb{R}^6 \rightarrow \mathbb{R}$  are smooth and Lipschitz. The input matrices are  $B_u : \mathbb{R} \rightarrow \mathbb{R}^6$  and  $B_w : \mathbb{R}^3 \rightarrow \mathbb{R}^6$ . Equation 4.37 describes a stochastic system with additive white process noise and white measurement noise. The additive noise terms are small, and this fact allows us to consider the noise inputs as a small perturbation about the nominal trajectory [100]. The optical trap system in equation 4.37 is described explicitly as

$$\dot{x} = \begin{bmatrix} -\omega_t z \exp\left(-\frac{z^2}{2l_t^2}\right) - \kappa\omega_t d_m - g_v(\omega_{z_v} - \omega_{p_v})a_1 - g_v g_a \omega_z a_2 - g_v g_a a_3 \\ -\omega_t z \exp\left(-\frac{z^2}{2l_t^2}\right) - (\kappa\omega_t + \omega_m)d_m + \omega_m d_d \\ -\omega_{p_v} a_1 + g_a \omega_z a_2 + g_a a_3 \\ a_3 \\ -\omega_{p_1} \omega_{p_2} a_2 - (\omega_{p_1} + \omega_{p_2})a_3 \\ -\omega_d d_d \end{bmatrix} \quad (4.38a)$$

$$+ \begin{bmatrix} 0 \\ 0 \\ 0 \\ 0 \\ 1 \\ 0 \end{bmatrix} u + \begin{bmatrix} \omega_t & 0 & 0 \\ \omega_t & \omega_m & 0 \\ 0 & 0 & 0 \\ 0 & 0 & 0 \\ 0 & 0 & 0 \\ 0 & 0 & \omega_e \end{bmatrix} \tilde{w}$$

$$y = g_s z + \tilde{n}. \quad (4.38b)$$

The molecule can be stretched to desired extensions by controlling the bead deflection to track a reference signal. It is convenient to turn the tracking control problem into a regulation control problem with the new control objective being to design the control to

drive the tracking error to zero. One question to be asked, is it possible to design a control to drive the tracking error to zero? The answer to this questions leads into the concept of output controllability. The output controllability analysis requires a few definitions first and these define the system relative degree, normal form, and zero dynamics.

#### 4.5.1 Output Controllability Condition

A system is output controllable if for any output  $y(t_0)$ , there exists a control input  $v$  that drives the output to  $y(t_1)$  in finite time  $t_1 > t_0$  [101]. In this research, output controllability is discussed by transforming the optical trap system to a new space such that the map between the control input and system output can be linearized via state feedback. A more formal definition of these concepts are provided in references [102, 103]. The literature provides these definitions for the nominal system or the expected value of the system. The definitions are first given when the system output is  $y = h(x)$ , then these definitions are slightly changed when the system output is the tracking error [102, 103]. These definitions are defined in the same manner as the literature for the expected value of the optical trap system in equation 4.37. The expected value of equation 4.37 is described by the expected value of the state  $\bar{x} = E[x]$  and the measurement  $\bar{y} = E[y]$  to yield

$$\dot{\bar{x}} = f(\bar{x}) + B_u u, \quad (4.39a)$$

$$\bar{y} = h(\bar{x}). \quad (4.39b)$$

Equation 4.39 shows that the control input  $u$  affects the system output  $\bar{y}$  through a nonlinear mapping because of the state equation. The nonlinear mapping presents a challenge when designing a controller to affect the system output. One approach to address the challenge is to transform the system to a new space such that the input-output map can be linearized via state feedback into controllable canonical form. However, the tradeoff is the linearized input-output map may not contain all the system dynamics, and any remaining states are called the internal states [102]. Some questions to ask are: What states are in the input-output map? Are there internal states? If so, then are the internal states stable? The stability of the internal states is crucial because we want these states to be well-behaved (remain bounded). The following discussion uses the concept of Lie derivatives.

**Definition 1** (Lie derivative). *Given a vector  $x \in \mathbb{R}^n$ , smooth vector fields  $f : \mathbb{R}^n \rightarrow \mathbb{R}^n$  and  $g : \mathbb{R}^n \rightarrow \mathbb{R}^n$ , and a smooth scalar field  $h : \mathbb{R}^n \rightarrow \mathbb{R}$ , then the Lie derivative is defined as  $L_f h(x)$ , which is the gradient of  $h$  along the directions of  $f$ . The following notation is used for Lie derivatives [102]:*

$$L_f^0 h(x) = h(x) \quad (4.40a)$$

$$L_f h(x) = \frac{\partial h(x)}{\partial x} f(x) \quad (4.40b)$$

$$L_f^2 h(x) = L_f(L_f h(x)) = \frac{\partial L_f h(x)}{\partial x} f(x) \quad (4.40c)$$

$$L_f^k h(x) = L_f(L_f^{k-1} h(x)) = \frac{\partial L_f^{k-1} h(x)}{\partial x} f(x) \quad \forall k \geq 0 \quad (4.40d)$$

$$L_g L_f h(x) = \frac{\partial L_f h(x)}{\partial x} g(x) \quad (4.40e)$$

The optical trap system is transformed to the new space by taking the time derivative of its output until the control input explicitly appears. The first time derivative of the system output,

$$\dot{y} = L_f h(\bar{x}) + L_{B_u} h(\bar{x})u, \quad \text{with } L_{B_u} h(\bar{x}) = 0 \quad \forall \bar{x} \in M, \quad (4.41)$$

shows that  $\dot{y}$  is independent of the control input  $u$  because the term  $L_{B_u} h(\bar{x}) = 0$ . The time derivative of  $\dot{y}$ ,

$$\ddot{y} = L_f^2 h(\bar{x}) + L_{B_u} L_f h(\bar{x})u, \quad \text{with } L_{B_u} L_f h(\bar{x}) \neq 0 \quad \forall \bar{x} \in M, \quad (4.42)$$

shows that  $\ddot{y}$  depends on the control input because the term  $L_{B_u} L_f h(\bar{x}) \neq 0$ . The total number of derivatives needed for the control input  $u$  to explicitly appear is called the system relative degree.

**Definition 2** (Relative degree). *Given a single-input single-output system,*

$$\dot{x} = f(x) + g(x)u \quad (4.43)$$

$$y = h(x) \quad (4.44)$$

where  $x \in \mathbb{R}^n$  is the state,  $u \in \mathbb{R}$  is the control input, and  $y \in \mathbb{R}$  is the output. The vector fields  $f : \mathbb{R}^n \rightarrow \mathbb{R}^n$  and  $g : \mathbb{R}^n \rightarrow \mathbb{R}^n$  are smooth and Lipschitz in  $x$ , and the scalar field

$h : \mathbb{R}^n \rightarrow \mathbb{R}$  is smooth and Lipschitz in  $x$ . This system has a relative degree  $p$ , with  $p \leq n$ , when

$$L_g L_f^{i-1} h(x) = 0, \quad i = 1, \dots, p-1; \quad L_g L_f^{p-1} h(x) \neq 0 \quad \forall x \in M. \quad (4.45)$$

The optical trap system has a relative degree of 2 because

$$L_{B_u} h(\bar{x}) = 0 \quad \text{and} \quad L_{B_u} L_f h(\bar{x}) \neq 0 \quad \forall \bar{x} \in M. \quad (4.46)$$

Equation 4.42 describes the input-output map of the optical trap system. Choosing the state feedback to be

$$u = \frac{1}{L_{B_u} L_f h(\bar{x})} (-L_f^2 h(\bar{x}) + v), \quad (4.47)$$

linearizes the input-output map,

$$\ddot{y} = v, \quad (4.48)$$

where  $v$  is the auxiliary control. Equation 4.48 describes a linear system with two integrators (two poles located at the origin) that can be described in controllable canonical form with the state  $\bar{\xi} = \xi(\bar{x})$ ,

$$\bar{\xi} = \xi(\bar{x}) = \begin{bmatrix} \xi_1(\bar{x}) \\ \xi_2(\bar{x}) \end{bmatrix} = \begin{bmatrix} h(\bar{x}) \\ L_f h(\bar{x}) \end{bmatrix}, \quad (4.49)$$

to yield

$$\dot{\bar{\xi}} = A_\xi \bar{\xi} + B_\xi v, \quad (4.50a)$$

$$y = \bar{\xi}_1, \quad (4.50b)$$

with

$$A_\xi = \begin{bmatrix} 0 & 1 \\ 0 & 0 \end{bmatrix} \quad \text{and} \quad B_\xi = \begin{bmatrix} 0 \\ 1 \end{bmatrix}. \quad (4.51)$$

The state  $\xi$  can be manipulated by designing the auxiliary control with linear system theory or LQ optimal control theory.

The transformed space is described by two states in the input-output map as given in equation 4.41 and equation 4.42, and four internal (hidden) states. A question to ask:

Are the internal states stable? The answer leads to the concepts of normal form and zero dynamics. The optical trap system is placed in normal form,

$$\dot{\bar{\xi}} = A_{\xi}\bar{\xi} + B_{\xi} (L_f^2 h(\bar{x}) + L_{B_u} L_f h(\bar{x})u) = A_{\xi}\bar{\xi} + B_{\xi} (\alpha(\bar{\xi}, \bar{\psi}) + \beta(\bar{\xi}, \bar{\psi})u) \quad (4.52a)$$

$$\dot{\bar{\psi}} = \delta(\bar{\xi}, \bar{\psi}) \quad (4.52b)$$

where  $\bar{\psi} \in \mathbb{R}^4$  is the internal state and the vector field  $\delta : \mathbb{R}^{2 \times 4} \rightarrow \mathbb{R}^4$  is smooth and Lipschitz in  $\bar{\xi}$  and  $\bar{\psi}$ . The states  $\bar{\xi}$  and  $\bar{\psi}$  experience feedback and coupling. The feedback and coupling can be described as: the state  $\xi$  is linearized and manipulated by designing the state feedback in equation 4.47 that depends on transformed states  $\bar{\xi}$  and  $\bar{\psi}$ ; the state  $\bar{\xi}$  acts as a virtual input that drives the state  $\bar{\psi}$ . During the application of equation 4.47, the system needs to be well-behaved or internally stable, and this fact places an additional constraint on the state transformation that the internal state remains bounded. The internal state remains bounded if its undriven dynamics are asymptotically or exponentially stable.

The optical trap system is expressed in normal form via the state transformation

$$[\xi(\bar{x}), \psi(\bar{x})]^T = T(\bar{x}).$$

The state transformation can be thought of as two parts: the external part described by the input-output map and the internal part. The external part must have its gradients  $\nabla_{\xi_1}$  and  $\nabla_{\xi_2}$  be linearly independent. The internal part must satisfy three conditions:

1. The internal state is independent of the control input. This constraint is equivalent to the  $\bar{\psi}_i$  functions satisfying

$$\frac{\partial \bar{\psi}_i}{\partial a_3} B_u = 0 \quad \text{for } i = 1, 2, 3, 4, \quad \text{and } \forall \bar{x} \in M. \quad (4.53)$$

Please note, equation 4.53 has no unique solution because there is no initial condition, so a constant can always be added to  $\bar{\psi}_i$ .

2. The state transformation  $[\xi(\bar{x}), \psi(\bar{x})]^T = T(\bar{x})$  results in a one-to-one map between the original state  $\bar{x}$  and the transformed state  $\bar{\xi}$  and  $\bar{\psi}$ . The mapping requires the gradients  $\nabla\bar{\psi}_j$  ( $j = 1, 2, 3, 4$ ) be linearly independent with each other and also linearly independent with the gradients  $\nabla\bar{\xi}_i$  ( $i = 1, 2$ ). The linear independence condition is equivalent to

$$\text{rank} \left[ \nabla\bar{\xi}_1 \quad \nabla\bar{\xi}_2 \quad \nabla\bar{\psi}_1 \quad \nabla\bar{\psi}_2 \quad \nabla\bar{\psi}_3 \quad \nabla\bar{\psi}_4 \right]^T = 6 \quad (4.54)$$

3. The internal states are well-behaved (remain bounded) during the application of the control in equation 4.47 and this requires the zero dynamics be asymptotically or exponentially stable.

There exists a set of  $\bar{\psi}_i$  for  $i = 1, \dots, 4$  functions satisfying the first two conditions due to the Frobenius Theorem [103, 102].

The internal states are chosen in terms of the original state to satisfy the first two conditions to yield

$$\bar{\psi}_1 = -\omega_{p_1}\omega_{p_2}\bar{a}_1 - (\omega_{p_1} + \omega_{p_2})\bar{a}_2 \quad (4.55a)$$

$$\bar{\psi}_2 = \bar{d}_d \quad (4.55b)$$

$$\bar{\psi}_3 = \bar{d}_m + \bar{d}_d \quad (4.55c)$$

$$\bar{\psi}_4 = \bar{a}_2 \quad (4.55d)$$

Next, the stability of the internal state is studied. The stability analysis has three steps:

1. The transformed state dynamics are expressed in terms of the transformed state by expressing the original state in terms of the transformed state.
2. The undriven internal state dynamics are derived, and this leads to the concept of zero dynamics.
3. A Lyapunov stability analysis is performed to study the stability of the internal states.

The original state is expressed in terms of the transformed state by

$$\bar{z} = \frac{1}{g_s} \bar{\xi}_1 \quad (4.56a)$$

$$\bar{d}_m = \bar{\psi}_3 - \bar{\psi}_2 \quad (4.56b)$$

$$\bar{a}_1 = -\frac{1}{\omega_{p_1}\omega_{p_2}} \bar{\psi}_1 - \frac{\omega_{p_1} + \omega_{p_2}}{\omega_{p_1}\omega_{p_2}} \bar{\psi}_4 \quad (4.56c)$$

$$\bar{a}_2 = \bar{\psi}_4 \quad (4.56d)$$

$$\bar{a}_3 = -\frac{\omega_{z_v} - \omega_{p_v}}{g_a\omega_{p_1}\omega_{p_2}} \bar{\psi}_1 + \frac{\kappa\omega_t}{g_ag_v} \bar{\psi}_2 - \frac{\kappa\omega_t}{g_ag_v} \bar{\psi}_3 \quad (4.56e)$$

$$\begin{aligned} & - \frac{\omega_{p_2}(\omega_{z_v} - \omega_{p_v}) - \omega_{p_1}(\omega_{p_v} + g_a\omega_{p_2}\omega_z - \omega_{z_v})}{g_a\omega_{p_1}\omega_{p_2}} \bar{\psi}_4 \\ & - \frac{\omega_t}{g_ag_vg_s} \bar{\xi}_1 \exp\left(-\frac{\bar{\xi}_1^2}{2g_s^2l_t^2}\right) - \frac{1}{g_ag_vg_s} \bar{\xi}_2 \\ \bar{d}_d &= \bar{\psi}_2 \end{aligned} \quad (4.56f)$$

The transformed state dynamics is found by taking the time derivative of equation 4.55, substituting in the original state dynamics with equation 4.37, then using equation 4.56 to express the original states in terms of the transformed states. The transformed state dynamics (equivalent the normal form equations) are described by:

$$\dot{\bar{\xi}} = A_\xi \bar{\xi} + B_\xi [\alpha(\bar{\xi}, \bar{\psi}) + \beta(\bar{\xi}, \bar{\psi})u] \quad (4.57a)$$

$$\dot{\bar{\psi}} = \delta(\bar{\xi}, \bar{\psi}) = A_\psi \bar{\psi} + \rho(\bar{\xi}) \quad (4.57b)$$

with the origin  $(\bar{\xi}, \bar{\psi}) = (0, 0)$  being a global equilibrium point.

The internal state is described by a linear system being driven by the nonlinear function of the state  $\bar{\xi}$ ,

$$\dot{\bar{\psi}}_1 = \frac{\omega_{p_2}(\omega_{p_v} - \omega_{z_v}) + \omega_{p_1}(\omega_{p_v} - (1 + g_a\omega_{p_2})\omega_z)}{g_a\omega_{p_1}\omega_{p_2}}\bar{\psi}_1 - \frac{\kappa\omega_t(\omega_{p_1} + \omega_{p_2} + g_a\omega_{p_1}\omega_{p_2})}{g_ag_v}\bar{\psi}_2 \quad (4.57c)$$

$$+ \frac{\kappa\omega_t(\omega_{p_1} + \omega_{p_2} + g_a\omega_{p_1}\omega_{p_2})}{g_ag_v}\bar{\psi}_3$$

$$+ \frac{(\omega_{p_1} + \omega_{p_2})(\omega_{p_2}(\omega_{p_v} - \omega_{z_v}) + \omega_{p_1}(\omega_{p_v} + g_a\omega_{p_2}(\omega_z - \omega_{z_v}) - \omega_{z_v}))}{g_a\omega_{p_1}\omega_{p_2}}\bar{\psi}_4$$

$$+ \frac{\omega_{p_1} + \omega_{p_2} + g_a\omega_{p_1}\omega_{p_2}}{g_ag_vg_s}\omega_t\bar{\xi}_1 \exp\left(-\frac{\bar{\xi}_1^2}{2g_s^2l_t^2}\right) + \frac{\omega_{p_1} + \omega_{p_2} + g_a\omega_{p_1}\omega_{p_2}}{g_ag_vg_s}\bar{\xi}_2$$

$$\dot{\bar{\psi}}_2 = -\omega_d\bar{\psi}_2 \quad (4.57d)$$

$$\dot{\bar{\psi}}_3 = (2\omega_m + \kappa\omega_t - \omega_d)\bar{\psi}_2 - (\omega_m + \kappa\omega_t)\bar{\psi}_3 - \frac{\omega_t}{g_s}\bar{\xi}_1 \exp\left(-\frac{\bar{\xi}_1^2}{2g_s^2l_t^2}\right) \quad (4.57e)$$

$$\dot{\bar{\psi}}_4 = \frac{\omega_{z_v} - \omega_{p_v}}{g_a\omega_{p_1}\omega_{p_2}}\bar{\psi}_1 + \frac{\kappa\omega_t}{g_ag_v}\bar{\psi}_2 - \frac{\kappa\omega_t}{g_ag_v}\bar{\psi}_3 \quad (4.57f)$$

$$+ \frac{-\omega_{p_1}(\omega_{p_v} + g_a\omega_{p_2}\omega_z - \omega_{z_v}) + \omega_{p_2}(\omega_{z_v} - \omega_{p_v})}{g_a\omega_{p_1}\omega_{p_2}}\bar{\psi}_4$$

$$- \frac{\omega_t}{g_ag_vg_s}\bar{\xi}_1 \exp\left(-\frac{\bar{\xi}_1^2}{2g_s^2l_t^2}\right) - \frac{1}{g_ag_vg_s}\bar{\xi}_2,$$

Next, the stability of the internal state is studied and this leads to the concept of zero dynamics. Zero dynamics are intrinsic properties of nonlinear systems (analogous to transfer function zeros of linear systems) that characterizes the stability of the internal state [50]. The internal states are stable if the zero dynamics are minimum phase. The zero dynamics are defined as the internal states when the system output is held identically at zero [50]. The system output is identically zero by applying the state feedback,

$$u = -\frac{\beta(0, \bar{\psi})}{\alpha(0, \bar{\psi})}, \quad (4.58)$$

resulting in the zero dynamics being described by

$$\dot{\bar{\psi}} = \delta(0, \bar{\psi}) = A_\psi\bar{\psi}, \quad (4.59)$$

and constrained on the four-dimensional manifold  $M$ ,

$$M = \{\bar{x} : h(\bar{x}) = L_f h(\bar{x}) = 0\}. \quad (4.60)$$

The stability of the zero dynamics are characterized by the eigenvalues of  $A_\psi$ ,

$$\lambda_1 = -\omega_d \quad (4.61a)$$

$$\lambda_2 = -\omega_{z_v} \quad (4.61b)$$

$$\lambda_3 = -\omega_z \quad (4.61c)$$

$$\lambda_4 = -\kappa\omega_t - \omega_m. \quad (4.61d)$$

All the eigenvalues have a negative real part and this fact implies the zero dynamics are exponentially stable. The internal state is bounded by BIBO stability because the state  $\bar{\xi}$  is bounded as the result of the application of equation 4.47. The proof for BIBO stability will be given for the case when the system output is the tracking error.

These definitions are now applied to the optical trap system when its output is the tracking error. The change in system output does not effect the analysis of the system relative degree, the state transformation  $T(\bar{x})$ , or the zero dynamics. However, the change does affect the state definition in the input-output map and the state feedback used to linearize the input-output map. The new state in the input-output map is the tracking error  $\check{\xi}$ , defined as

$$\check{\xi} = \xi_r - \bar{\xi}, \quad \text{with} \quad \xi_r = [r, \dot{r}]^T, \quad (4.62)$$

where  $\xi_r$  is the reference signal vector and  $r$  is the reference signal. Then, the optical trap system is transformed into normal form,

$$\dot{\check{\xi}} = A_\xi \check{\xi} + B_\xi (\ddot{r} - L_f^2 h(\bar{x}) - L_{B_u} L_f h(\bar{x}) u) \quad (4.63a)$$

$$\dot{\check{\psi}} = \delta(\xi_r - \check{\xi}, \bar{\psi}) \quad (4.63b)$$

There are two differences in the normal form as expressed in equation 4.63 to that in equation 4.52:

1. In equation 4.63, the input-output map depends on the second time derivative of the reference signal. Thus, the state feedback must contain information about the reference signal to linearize the input-output map. The reference signal has two constraints:  $r \in C^2$  and  $\ddot{r} \neq 0, \forall t \geq 0$ . Choosing the state feedback

$$u = -\frac{1}{L_{B_u} L_f h(\bar{x})} (L_f^2 h(\bar{x}) - \ddot{r} + v), \quad (4.64)$$

and substituting it into equation 4.63 results in the linearized input-output map

$$\ddot{\xi} = v.$$

2. The internal state is driven by two virtual inputs: the controllable state  $\check{\xi}$  and the reference signal  $\xi_r$ . The internal state is bounded by BIBO stability because the zero dynamics are exponentially stable, and the virtual inputs are bounded.

The following theorem states the internal states are uniformly ultimately bounded.

**Theorem 1** (Internal states in tracking problems). *[103] The optical trap system as expressed in normal form via equation 4.63 is well-behaved during the application of the state feedback in equation 4.64. The zero dynamics are exponentially stable, reference signal is chosen such that it remains bounded and its derivatives are bounded, and the tracking error is bounded by the application of equation 4.64. Assume there are positive constants  $b_1, b_2, b_3, b_4$ , and  $b_5$ , then the internal states are BIBO stable with the uniformly ultimate bound*

$$\|\bar{\psi}\| \leq \sqrt{\frac{b_2}{b_1 b_3 b_4}} b_5. \quad (4.65)$$

*Proof.* The following assumptions are used:

**Assumption 1.** *The internal states are Lipschitz in the reference signal and the tracking error state. There exists a positive constant  $l_1$  such that*

$$\left\| \delta(\xi_r - \check{\xi}, \bar{\psi}) - \delta(0, \bar{\psi}) \right\| \leq l_1 \left\| \xi_r + \check{\xi} \right\|. \quad (4.66)$$

**Assumption 2.** *Assuming a matrix  $A_\psi$  is Hurwitz and a matrix  $Q_\psi$  is positive definite and symmetric, then there exists a positive definite and symmetric matrix  $P_\psi$  satisfying*

$$A_\psi^T P_\psi + P_\psi A_\psi = -Q_\psi. \quad (4.67)$$

The internal state dynamics via equation 4.63 are equal to

$$\dot{\bar{\psi}} = \delta(\xi_r - \check{\xi}, \bar{\psi}) + \delta(0, \bar{\psi}) - \delta(0, \bar{\psi}) = A_\psi \bar{\psi} + \delta(\xi_r - \check{\xi}, \bar{\psi}) - \delta(0, \bar{\psi}). \quad (4.68)$$

The Lyapunov function candidate is

$$W = \bar{\psi}^T P_\psi \bar{\psi}, \quad (4.69)$$

and this candidate is positive definite and decrescent because the function can be lower and upper bounded with class  $K$  functions,

$$b_1 \|\bar{\psi}\|^2 \leq W \leq b_2 \|\bar{\psi}\|^2, \quad (4.70)$$

where  $b_1 = \lambda_{\min}(P_\psi)$  and  $b_2 = \lambda_{\max}(P_\psi)$ . Its time deviative is

$$\dot{W} = \dot{\bar{\psi}}^T P_\psi \bar{\psi} + \bar{\psi}^T P_\psi \dot{\bar{\psi}}, \quad (4.71)$$

and substituting in equation 4.68 yields

$$\dot{W} = \bar{\psi}^T (A_\psi^T P_\psi + P_\psi A_\psi) \bar{\psi} + 2\bar{\psi}^T P_\psi \left( \delta(\xi_r - \check{\xi}, \bar{\psi}) - \delta(0, \bar{\psi}) \right). \quad (4.72)$$

Applying assumptions 1 and 2 to equation 4.72 yields

$$\dot{W} \leq -\bar{\psi}^T Q_\psi \bar{\psi} + 2l_1 \|\bar{\psi}\| \|P_\psi\| \left\| \xi_r + \check{\xi} \right\|. \quad (4.73)$$

Equation 4.73 can be further bounded using a property of positive definite matrices to yield

$$\dot{W} \leq -b_3 \|\bar{\psi}\|^2 - b_4 \|\bar{\psi}\|^2 + 2b_5 \|\bar{\psi}\|, \quad (4.74)$$

where  $b_3, b_4, b_5$  are such that  $b_3 + b_4 = \lambda_{\min}(Q_\psi)$  and  $b_5 = l_1 \|P_\psi\| \left\| \xi_r + \check{\xi} \right\|$ . Applying nonlinear damping (completing the squares) to the last two terms in equation 4.74 yields

$$\dot{W} \leq -b_3 \|\bar{\psi}\|^2 + \frac{b_5^2}{b_4} - b_4 \left( \|\bar{\psi}\| - \frac{b_5}{b_4} \right)^2. \quad (4.75)$$

The term  $-b_4 \left( \|\bar{\psi}\| - \frac{b_5}{b_4} \right)^2$  is always negative. Showing the stability case of uniformly ultimately bounded requires the term  $-b_3 \|\bar{\psi}\|^2$  be expressed in terms of the Lyapunov

function. The term  $-b_3 \|\bar{\psi}\|^2$  is bounded (made less negative) in terms of  $W$  by using equation 4.70 to relate  $\|\bar{\psi}\|^2$  to  $W$ . Equation 4.74 is bounded by

$$\dot{W} \leq -\frac{b_3}{b_2}W + \frac{b_5^2}{b_4}, \quad (4.76)$$

and has the solution

$$W(t) \leq W(0) \exp\left(-\frac{b_3}{b_2}t\right) + \frac{b_2}{b_3 b_4} b_5^2 \left(1 - \exp\left(-\frac{b_3}{b_2}t\right)\right). \quad (4.77)$$

At steady state, the Lyapunov function converges to the value  $W(\infty) = \frac{b_2}{b_3 b_4} b_5^2$ . The steady-state value  $W(\infty)$  is related to the bound on  $\psi$  through equation 4.70. The bound on  $\bar{\psi}$  is

$$\|\bar{\psi}\| \leq \sqrt{\frac{b_2}{b_1 b_3 b_4} b_5}, \quad (4.78)$$

which shows the internal states are BIBO stable. □

The implementation of the control law in equation 4.64 is challenging because not all of the states are available for measurement. One may ask, can the measurement be used to obtain information on the remaining states? The answer leads to the concept of observability. Observability is a system property that implies the initial system state can be uniquely determined from the output [104]. An observable system allows the use of a state observer to reconstruct/estimate the system state based on its output.

#### 4.5.2 Observability Condition

A system is called observable if for any two initial states:  $x_0, x_1 \in M$  and a control input  $v \in V$ , the corresponding system outputs  $h(x_0, v)$  and  $h(x_1, v)$  can be distinguished [105, 106]. Observability for nonlinear systems is a local property and the property needs to be satisfied at each point in the admissible state space. A system is observable if the matrix

$$O = \left[ \nabla h, \nabla L_f h(x), \dots, \nabla L_f^{n-1} h(x) \right]^T, \quad \forall x \in M \quad (4.79)$$

is full rank.

Applying the optical trap system to the observability condition results in the matrix  $O$  being full rank, which is  $\text{rank}(O) = 6, \forall x \in M$ . The optical trap system being observable allows for a state observer to reconstruct/estimate its states.

### 4.5.3 Separation Principle

The ability to manipulate the dielectric bead via feedback control requires two different feedback problems be simultaneously addressed. The two feedback problems are an estimation problem and a control problem. The estimation problem reconstructs/estimates the system state based on noisy measurements and the control input. The control problem finds the state feedback that drives the expected value of the tracking error to zero. The challenge of simultaneously solving the feedback problems can be alleviated by the noise characteristics, which the noise is additive and contributes a small effect on the system response compared to the system nonlinearities. The noise characteristics turns the problem of simultaneously addressing both feedback problems into two separate feedback problems. The estimation and control problems can be solved independently, then the solutions can be combined. The ability to solve the estimation and control problems independently, then combine their solutions, is called the separation principle.

The separation principle is possible for stochastic systems being driven by additive process white noise with additive white noisy measurements. The noise terms are additive and contribute a small effect on the system response compared to the system nonlinearities. The system response can be described as the sum of a nominal control system response and a small perturbed control system response (neighboring control solution). The perturbed control response is due to the noisy measurements and the state estimates. In this research, the perturbed system dynamics can be described by a first-degree expansion, and the corresponding variational functional can be described by a quadratic functional in the state and control, then the estimation and control problems can be designed independently.

## 5.0 LINEAR DESIGN

Typically, optical traps are operated within their linear range and this fact has allowed linear controllers to yield satisfactory closed-loop performance. A popular control choice is linear integral control because of its ability to increase the system type, reject constant disturbances, and reduce the effects of the Brownian noise. The closed-loop advantages of linear integral control can also be achieved using LQG control. LQG control addresses the estimation and the control problems with a similar architecture to the architecture of the nonlinear control designs. The similar architecture between the LQG and the nonlinear control designs allow for the improvement in the closed-loop performance of the optical trap be quantified when considering the system nonlinearities in the control design.

This chapter discusses the design and the performance of the LQG design. The Kalman filter is a recursive Bayesian approach for state estimation by minimizing the mean-squared estimation error. The state estimate is then used in an input-output feedback type architecture with an LQ structure to find the suboptimal state feedback that drives the tracking error to zero. In order to assess the effectiveness of the LQG control on the quality of the measurements, statistical analyzes are made on the resulting open-loop and closed-loop systems to quantify its effects on the system bandwidth and the state statistical properties. These statistical quantities affect the quality of the nominal molecular force estimate, and these effects are studied by deriving a theoretical expression for its SNR. Finally, the performance of the LQG design is compared to that of linear integral control.

## 5.1 LINEARIZED OPTICAL TRAP SYSTEM

When designing linear controllers, it is convenient to use the linearized system dynamics. The optical trap system in equation 4.37 is linearized about the equilibrium point  $x = 0$  with a first order Taylor series approximation to yield

$$\dot{x} = Ax + B_u u + B_w \tilde{w} \quad (5.1a)$$

$$y = Cx + \tilde{n}. \quad (5.1b)$$

The linearized optical trap system has the state matrix  $A$  and the output matrix  $C$ . These matrices are given by

$$A = \left. \frac{\partial f(x)}{\partial x} \right|_{x=0} = \begin{bmatrix} -\omega_t & -\kappa\omega_t & -g_v(\omega_{z_v} - \omega_{p_v}) & -g_v g_a \omega_z & -g_v g_a & 0 \\ -\omega_t & -\kappa\omega_t - \omega_m & 0 & 0 & 0 & \omega_m \\ 0 & 0 & -\omega_{p_v} & g_a \omega_z & g_a & 0 \\ 0 & 0 & 0 & 0 & 1 & 0 \\ 0 & 0 & 0 & -\omega_{p_1} \omega_{p_2} & -\omega_{p_1} - \omega_{p_2} & 0 \\ 0 & 0 & 0 & 0 & 0 & -\omega_d \end{bmatrix} \quad (5.2a)$$

$$C = \left. \frac{\partial h(x)}{\partial x} \right|_{x=0} = [g_s \ 0 \ 0 \ 0 \ 0 \ 0]. \quad (5.2b)$$

The linearized optical trap system satisfies the observability and output controllability conditions because equation 4.79 is full rank and equation 5.1 can be expressed in normal form.

## 5.2 STATE ESTIMATION WITH A KALMAN FILTER

The state estimation problem is addressed with a Kalman filter by using the linearized system in a Luenberger observer structure to find the observer gains that minimizes the mean-squared estimation error [100]. Such observer gains are found when the optical trap system is subjected to process noise  $\tilde{w} = [\tilde{d}, \tilde{d}_m, \tilde{d}_d]$ , and measurement noise  $\tilde{n}$ . These noise sources are Gaussian white noise with the following statistical properties:

1. The process noise  $w$  is described by

$$E[\tilde{w}(t)] = 0 \quad \text{and} \quad E[\tilde{w}(t)\tilde{w}^T(t+\tau)] = S_w\delta(t), \quad (5.3)$$

where the spectral density matrix  $S_w$  is

$$S_w = \begin{bmatrix} S_d & 0 & 0 \\ 0 & S_m & 0 \\ 0 & 0 & S_d \end{bmatrix}. \quad (5.4)$$

2. The measurement noise  $\tilde{n}$  is described by

$$E[\tilde{n}(t)] = 0 \quad \text{and} \quad E[\tilde{n}(t)\tilde{n}^T(t+\tau)] = S_n\delta(t), \quad (5.5)$$

3. The process noise and the measurement noise are orthogonal

$$E[\tilde{n}(t)\tilde{w}^T(t+\tau)] = 0. \quad (5.6)$$

The Kalman filter is a recursive Bayesian estimation approach that provides the conditional expectation of the state  $x$  based on the measurements,

$$\hat{x}(t) = E[x(t)|y(\tau)], \quad \tau \in [0, t], \quad (5.7)$$

by minimizing the square of the estimation error [100, 107]. The estimation error is defined as

$$\check{x} = x - \hat{x}. \quad (5.8)$$

The state estimate dynamics are expressed in a Luenberger state observer structure and described by

$$\dot{\hat{x}} = A\hat{x} + B_u u + J[y - C\hat{x}], \quad (5.9)$$

where  $J \in \mathbb{R}^6$  is the observer (Kalman) gain. The last term  $J[y - C\hat{x}]$  is the correction term. The correction term drives the state estimate dynamics because as new measurements arrive, the measurement error  $y - C\hat{x}$  is weighted by the observer gain to affect the state estimate dynamics.

The Kalman filter finds the observer gain  $J$  to ensure the state matrix  $A - JC$  is stable and to minimize the mean-squared estimation error. The dynamics for the estimation error is described by

$$\dot{\check{x}} = (A - JC)\check{x} + B_w\tilde{w} - J\tilde{n}, \quad (5.10)$$

which characterizes a linear system driven by the process noise and the measurement noise. The observer gain  $J$  depends on the estimation error covariance matrix  $P$ ,

$$P = E [\check{x}\check{x}^T],$$

a symmetric and positive semidefinite matrix. The estimation error covariance matrix is the solution to the differential Riccati equation,

$$\dot{P} = PA^T + AP + B_wS_wB_w^T - PC^TS_n^{-1}CP. \quad (5.11)$$

The Riccati equation is model dependent and driven by the spectral densities of the process noise  $S_w$  and the measurement noise  $S_n$ . Its solution can be calculated off-line. The Kalman filter is going to operate longer than its time constant and this fact allows the solution to the differential Riccati equation to be simplified by only considering its steady-state solution ( $\dot{P} = 0$ ). The differential Riccati equation is turned into an algebraic Riccati equation,

$$0 = PA^T + AP + B_wS_wB_w^T - PC^TS_n^{-1}CP, \quad (5.12)$$

which has one solution such that the eigenvalues of the closed-loop estimation problem are the stabilizing eigenvalues of the Hamiltonian matrix [108]

$$H = \begin{bmatrix} A & -C^TS_n^{-1}C \\ -B_wS_wB_w^T & -A^T \end{bmatrix}. \quad (5.13)$$

The Riccati solution determines the observer gains through

$$J = PC^TS_n^{-1} = [j_1 \ j_2 \ j_3 \ j_4 \ j_5 \ j_6]^T. \quad (5.14)$$

Next, we qualitatively discuss the effects the magnitude of the process noise and measurement noise has on the Riccati solution and the observer gains. When the spectral density of the process noise is smaller than the measurement noise, there are small values for both the

Riccati solution and the observer gains. Small observer gains imply the system model is trusted more than the measurements. On the other hand, when the spectral density of the process noise is larger than the measurement noise, there are large values for both the Riccati solution and the observer gains. Large observer gains imply the system model is trusted less than the measurements.

It is insightful to assess the effectiveness the Kalman filter has on the quality of the state estimate by quantifying the estimation bandwidth, estimation bias, and estimation variance. These statistical quantities are crucial because the state estimate is used to estimate the molecule characteristics. The quality of the molecule characteristics is quantified by deriving the expression for the SNR of the nominal molecular force.

### 5.3 STATISTICAL ANALYSIS OF KALMAN FILTER

The effectiveness of the Kalman filter is assessed by quantifying the estimation bias, the estimation bandwidth, and the estimation variance. These statistical properties are then used to derive the expression for the SNR of the nominal molecular force estimate.

These statistical properties depend on the operating conditions of the optical trap system. The operating conditions change when there is a change in the laser power or the molecule's end-to-end extension. The laser power is related to the optical stiffness  $k_t$ , which affects  $\omega_t = k_t/\gamma$  and the linear operating range. An increase/decrease in the laser power results in an increase/decrease in the optical stiffness and the linear operating range. The molecule's end-to-end extension is related to the molecule's stiffness; an increase/decrease to the molecule's end-to-end distance results in an increase/decrease in the molecule's stiffness  $k_m$ . Thus, for each pair of  $k_t$  and  $k_m$  (or  $\kappa = k_m/k_t$ , the dimensionless stiffness), a Kalman filter is designed. Let us quantify the statistical properties for the different operating conditions using numerical methods.

The following assumption is used in the analysis.

**Assumption 3.** *The actuator dynamics are not driven by white noise. The Kalman gains associated with these states are small, such that  $\|j_i\| \ll 1$ , compared to the other Kalman gains.*

The estimation bandwidth and the estimation bias are found from the expected value of the estimation error dynamics  $\bar{\tilde{x}} = E[\tilde{x}]$  of equation 5.10,

$$\frac{d}{dt}\bar{\tilde{x}} = (A - JC)\bar{\tilde{x}}. \quad (5.15)$$

**Estimation Bias** The accuracy of the Kalman filter is quantified by studying the estimation bias at steady-state. The steady-state response of equation 5.15 converges to zero (no bias) if all the eigenvalues of  $A - JC$  have negative real parts (or stable). The eigenvalues of  $A - JC$  are stable because these eigenvalues are the stable eigenvalues of the Hamiltonian matrix in equation 5.13.

**Estimation Bandwidth** The estimation bandwidth provides how fast the Kalman filter produces the state estimate. It can be characterized by the slowest eigenvalue of the estimation error dynamics. The estimation bandwidth is shown in figure 23. For a given  $\kappa$ , as  $k_t$  is increased, the estimation bandwidth has an initial high slope, then the slope changes and becomes small in the same direction. For a given  $k_t$ , increasing  $\kappa$  (the molecule becomes stiffer) results in the estimation bandwidth increasing.

**State Variances** The open-loop composite system (the combination of the optical trap system and the Kalman filter) fluctuates at steady-state due to process noise (Brownian noise and molecule noise), and the measurement noise. Recall that the optical trap (same as in equation 5.1 but with no control) is

$$\dot{x} = Ax + B_w \tilde{w},$$

and the Kalman filter (same as in equation 5.9 but with no control) is

$$\dot{\hat{x}} = A\hat{x} + J[y - C\hat{x}].$$

The system fluctuations are simplified by using the fact that the noise inputs only drive the states describing the bead and the molecule; then assumption 3 is used to imply that measurement noise only affects the state estimates describing the bead and the molecule. In this research, the fluctuations are characterized by performing a linear noise analysis about the expected value at steady-state.

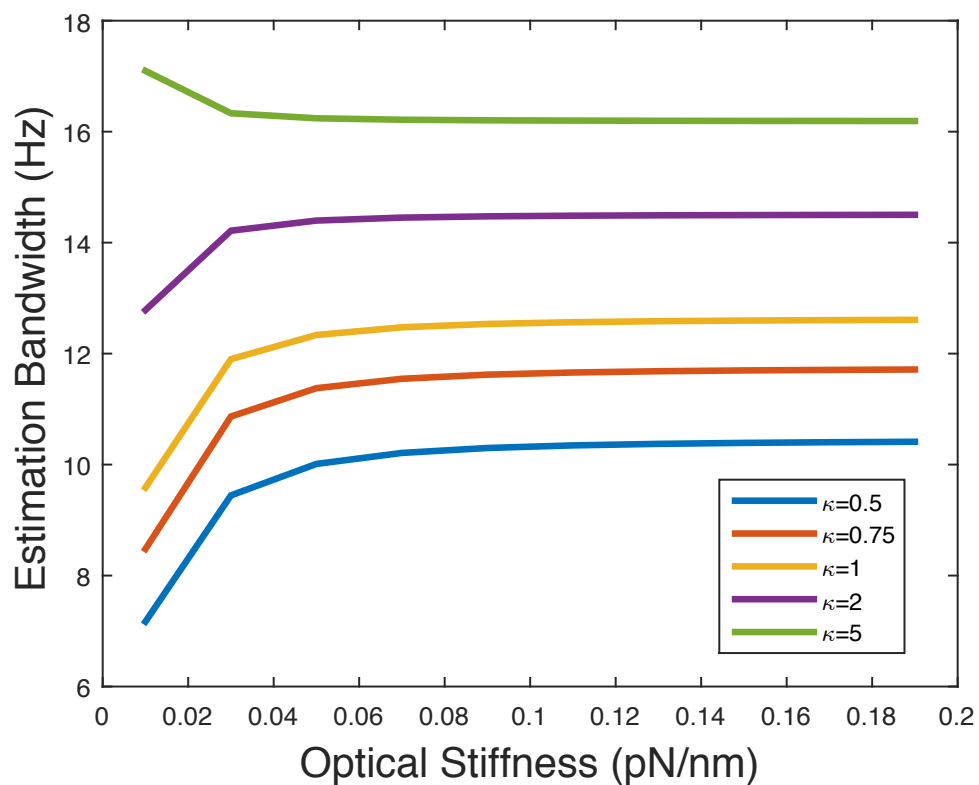


Figure 23: A schematic of the estimation bandwidth obtained using a Kalman filter. For a given  $\kappa$ , as  $k_t$  is increased, the estimation bandwidth has an initial high slope, then the slope changes and becomes small in the same direction. For a given  $k_t$ , increasing  $\kappa$  (the molecule is becoming stiffer) results in the estimation bandwidth increasing.

The fluctuations are determined by first describing the composite system and its expected value. The dynamics for the composite system  $x_o$  are described by

$$\dot{x}_o = A_o x_o + B_o \tilde{w}_o, \quad \text{with} \quad x_o = [z, d_m, \hat{z}, \hat{d}_m, \hat{d}_d]^T, \quad \text{and} \quad \tilde{w}_o = [\tilde{d}, \tilde{d}_m, \tilde{n}]^T, \quad (5.16)$$

and its expected value  $\bar{x}_o = E[x_o]$  has dynamics of

$$\dot{\bar{x}}_o = A_o \bar{x}_o. \quad (5.17)$$

The system fluctuations are described by the noise  $\tilde{x}_o = x_o - \bar{x}_o$  and its dynamics are

$$\dot{\tilde{x}}_o = A_o(\tilde{x}_o + \bar{x}_o) + B_o \tilde{w}_o - A_o \bar{x}_o, \quad (5.18a)$$

$$= A_o \tilde{x}_o + B_o \tilde{w}_o, \quad (5.18b)$$

where the matrices  $A_o$  and  $B_o$  being

$$A_o = \begin{bmatrix} -\omega_t & \kappa\omega_t & 0 & 0 & 0 \\ -\omega_t & -\kappa\omega_t - \omega_m & 0 & 0 & 0 \\ j_1 g_s & 0 & -\omega_t - j_1 g_s & -\kappa\omega_t & 0 \\ j_2 g_s & 0 & -\omega_t - j_2 g_s & -\kappa\omega_t - \omega_m & \omega_m \\ j_6 g_s & 0 & -j_6 g_s & 0 & -\omega_d \end{bmatrix} \quad B_o = \begin{bmatrix} \omega_t & 0 & 0 \\ \omega_t & \omega_m & 0 \\ 0 & 0 & j_1 \\ 0 & 0 & j_2 \\ 0 & 0 & j_6 \end{bmatrix}. \quad (5.19)$$

The state variances are characterized by the steady-state state covariance matrix  $X_o = E[\tilde{x}_o \tilde{x}_o^T]$ , which is the solution to the Lyapunov equation

$$A_o X_o + X_o A_o^T + B_o S_o B_o^T = 0 \quad \text{where} \quad S_o = \begin{bmatrix} S_d & 0 & 0 \\ 0 & S_m & 0 \\ 0 & 0 & S_n \end{bmatrix}. \quad (5.20)$$

The variance for the bead deflection and its estimate are shown in figure 24; the variance of the molecule extension and its estimate are shown in figure 25. For a given  $\kappa$ , increasing  $k_t$  (also  $k_m$  is increased to maintain a constant  $\kappa$ ) results in a decrease in the variance for the states and their estimates; a stiffer optical trap and molecule reduces the variance. Then, for a given  $k_t$ , an increase in  $\kappa$  (a stiffer molecule) results in an decrease in the variance for the state, the variance decreases for the estimated molecule extension, and the variance increases for the estimated bead deflection when  $k_t \geq 0.07$  pN/nm. The variance for the estimated

disturbance is shown in figure 26. Figure 26 shows that, for a given  $\kappa$ , an increase in  $k_t$  ( $k_m$  is also increased to maintain  $\kappa$ ) initially reduces the variance quickly, then the variance decreases slowly. Then, for a constant  $k_t$ , an increase in  $\kappa$  (the molecule becoming stiffer) reduces the variance.

These statistical quantities affect the quality of the estimated force disturbance and the effect is quantified by studying its SNR.

**SNR For Molecule Force Estimate** The statistical quantities of the estimated force disturbance are proportional to that of the disturbance estimate because  $\hat{f}_d = k_m \hat{d}_d$ . At steady-state, the expected value for the estimated force disturbance is

$$E[\hat{f}_d] = k_m E[\hat{d}_d]. \quad (5.21)$$

The variance of the estimated force disturbance is described by

$$\text{Var}(\hat{f}_d) = k_m^2 \text{Var}(\hat{d}_d). \quad (5.22)$$

The SNR for the estimated force disturbance is

$$\text{SNR} = \frac{1}{\sqrt{\text{Var}(\hat{f}_d)}} E[\hat{f}_d]. \quad (5.23)$$

Its value is numerically evaluated for each operating condition (each pair of  $k_t$  and  $\kappa$ ), as shown in figure 27. For a given  $\kappa$ , increasing  $k_t$  results in a decrease in the SNR.

A second advantage with the Kalman filter is that the state estimate can be implemented in the controller to study the molecule. The state estimate is used in the controller to achieve disturbance rejection and the state estimate contains less noise than the actual state.

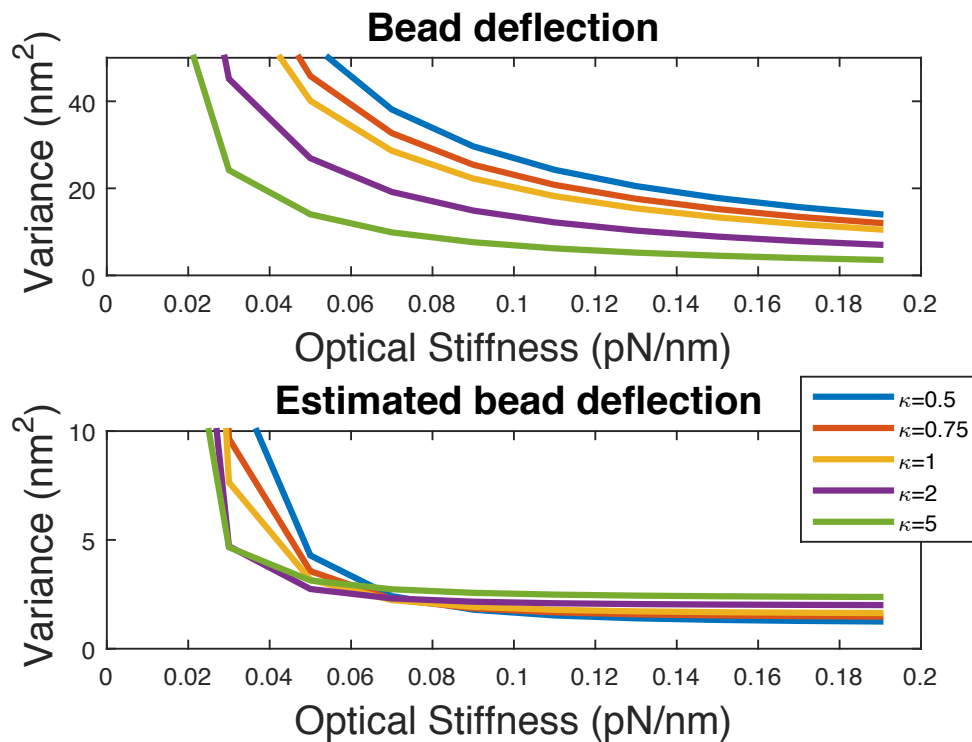


Figure 24: A schematic for the variance of the bead deflection and its estimate obtained using a Kalman filter. For a given  $\kappa$ , increasing  $k_t$  (also  $k_m$  is increased to maintain a constant  $\kappa$ ) results in a decrease in the variance for the state and estimated state; a stiffer optical trap and molecule reduces the variance. Then, for a given  $k_t$ , an increase in  $\kappa$  (a stiffer molecule) results in an decrease in the variance for the state and an increase in variance for the estimated state.

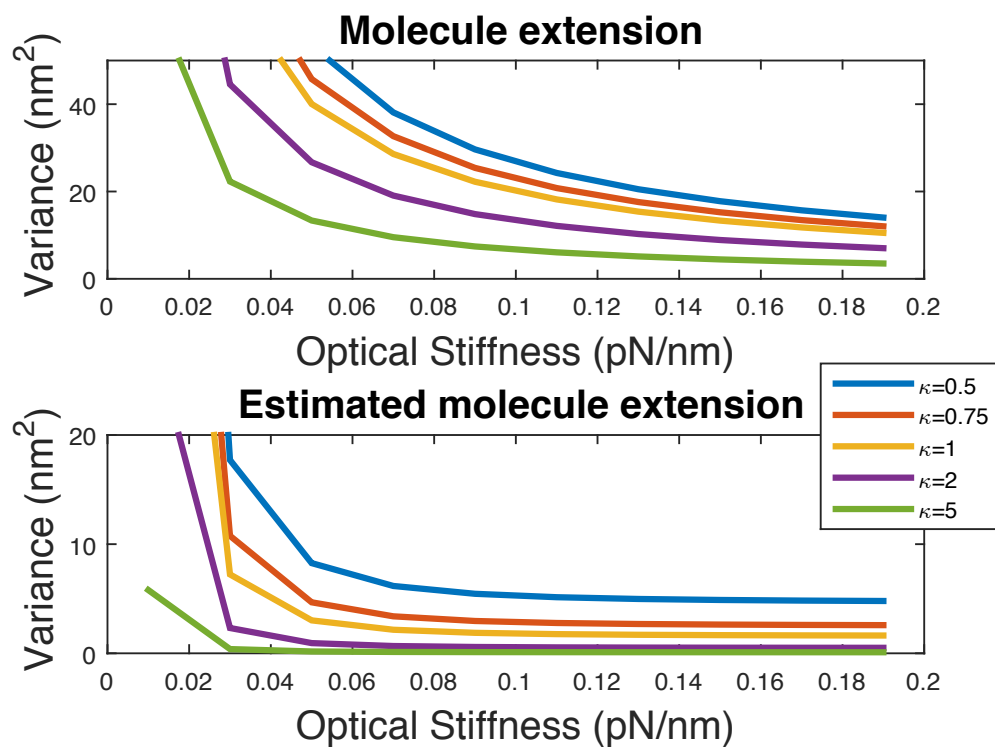


Figure 25: A schematic for the variance of the molecule extension and its estimate obtained using a Kalman filter. For a given  $\kappa$ , increasing  $k_t$  (also  $k_m$  is increased to maintain a constant  $\kappa$ ) results in a decrease in the variance for the states and their estimates; a stiffer optical trap and molecule reduces the variance. Then, for a given  $k_t$ , an increase in  $\kappa$  (a stiffer molecule) results in an decrease in the variance for the state and estimated state.

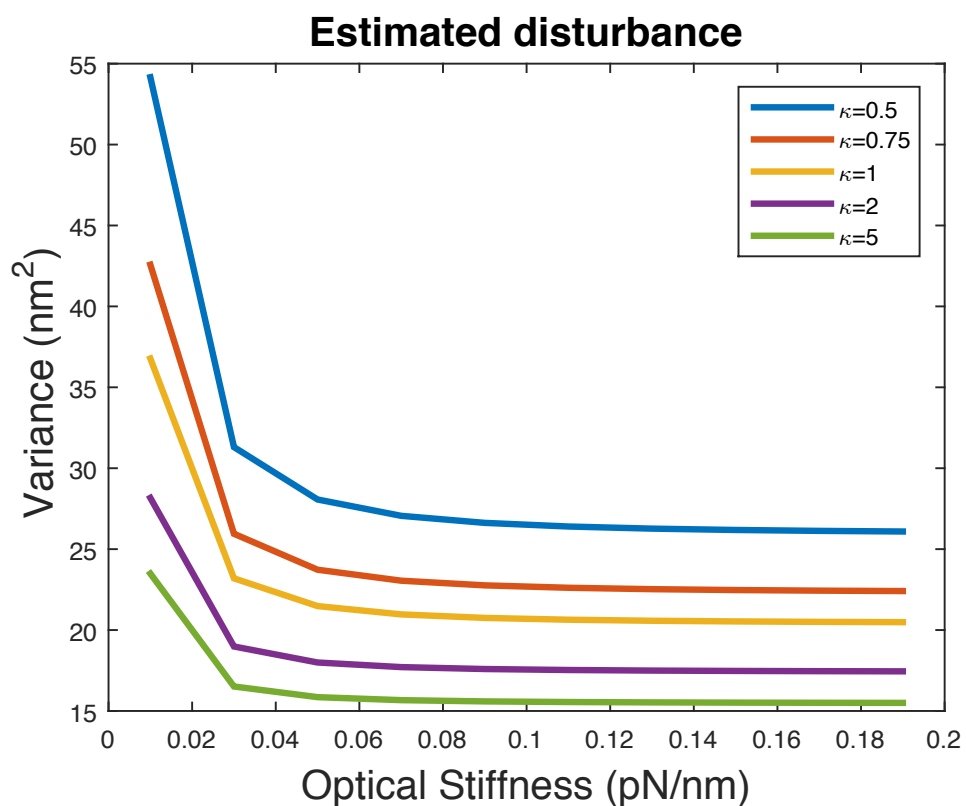


Figure 26: A schematic for the variance of the estimated disturbance obtained using a Kalman filter. For a given  $\kappa$ , an increase in  $k_t$  ( $k_m$  is also increased to maintain  $\kappa$ ) initially reduces the variance quickly, then the variance decreases slowly. Then, for a constant  $k_t$ , an increase in  $\kappa$  (the molecule becoming stiffer) reduces the variance.

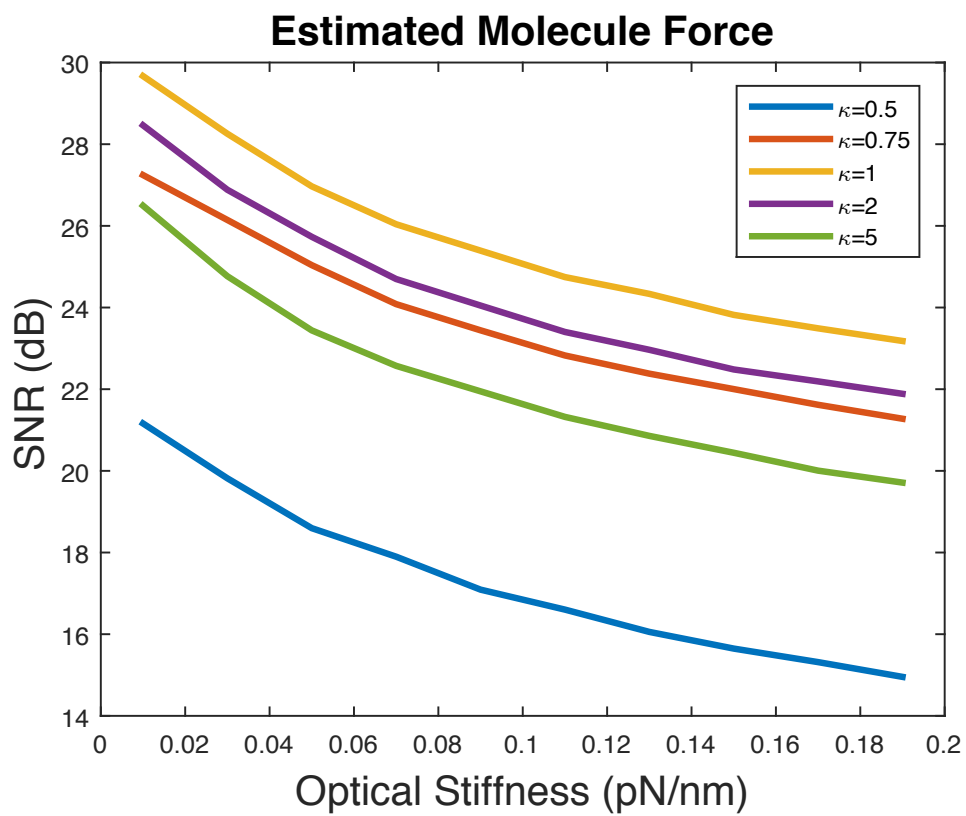


Figure 27: A schematic for the SNR of the estimated force disturbance obtained using a Kalman filter. For a given  $\kappa$ , increasing  $k_t$  results in a decrease in the SNR.

## 5.4 CONTROL STRUCTURE

The molecule is studied by having the expected value of the bead deflection track a reference signal. The tracking control problem is turned into a regulation control problem with the new control objective being design the control to drive the expected value of the tracking error to zero. Recall that the expected value of the tracking error  $\check{\xi}$  is defined in equation 4.62 in

$$\check{\xi}(\bar{x}) = \xi_r - \xi(x) = \begin{bmatrix} r - Cx \\ \dot{r} - CAx \end{bmatrix},$$

where  $r$  is the reference signal. The tracking error is driven to zero by a combination of an input-output feedback with LQ control architecture, as shown in the block diagram in figure 28. The control structure has two feedback loops: the linearization loop (loop 1) and the tracking loop (loop 2). The linearization loop transforms the optical trap system such that the input-output map is in controllable canonical form by state feedback. The tracking loop uses the controllable canonical state equation in an LQ optimal control algorithm to find the state feedback that drives the tracking error to zero.

The linearization loop transforms the optical trap system with the tracking error as its output into normal form (according to the procedure given in section 4.5.1),

$$\frac{d}{dt}\check{\xi} = A_\xi\check{\xi}(x) + B_\xi[\ddot{r} - CA^2x - CAB_uu] \quad (5.24a)$$

$$\dot{\psi} = \delta(\xi_r - \check{\xi}, \psi). \quad (5.24b)$$

The normal form describes the input-output map between the control input  $u$  and the tracking error  $\check{\xi}$ . Choosing the state feedback to be

$$u(\hat{x}) = -\frac{1}{CAB_u} [CA^2\hat{x} - \ddot{r} + v], \quad (5.25)$$

with  $v$  being the auxiliary control input, transforms the input-output map to controllable canonical form,

$$\frac{d}{dt}\check{\xi} = A_\xi\check{\xi}(x) + B_\xi v - B_\xi CA^2\check{x}, \quad (5.26)$$

where  $\check{x} = x - \hat{x}$  is the state estimation error. Equation 5.26 describes the controllable canonical state equation  $\frac{d}{dt}\check{\xi} = A_\xi\check{\xi}(x) + B_\xi v$  being driven by the perturbation  $-B_\xi CA^2\check{x}$ .

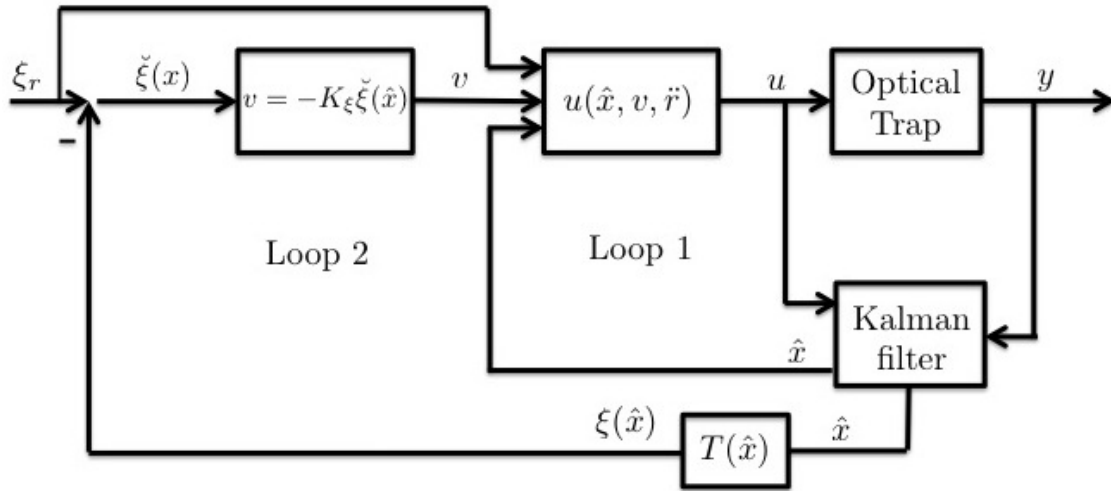


Figure 28: The schematic of the block diagram for the closed-loop system. The block diagram has two feedback loops. The linearization loop (loop 1) transforms the optical trap system into normal form such that the input-output map is transformed to controllable canonical form by state feedback  $u(\hat{x}, v, \ddot{r})$ . The tracking loop (loop 2) uses the controllable canonical state equation in an LQ optimal algorithm to find the state feedback  $v = -K_\xi \check{\xi}(\hat{x})$  that drives the tracking error to zero.

The perturbation  $-B_\xi C A^2 \check{x}$  results from the estimation error (mismatch) in the input-output feedback due to the state estimation process.

The tracking loop uses controllable canonical state equation

$$\frac{d}{dt}\check{\xi} = A_\xi \check{\xi}(x) + B_\xi v$$

in an LQ optimal control algorithm to find the state feedback  $v(\hat{x}) = -K_\xi \check{\xi}(\hat{x})$  (where  $K_\xi$  is the state feedback matrix) that drives the tracking error to zero. The LQ control algorithm assumes the state  $x$  is available to find the state feedback  $v(x)$ , then the state feedback is implemented using the state estimate. The dynamics for the closed-loop tracking error are characterized by the eigenvalues of  $A_\xi - B_\xi K_\xi$  and its bandwidth is described by a frequency equal to the slowest eigenvalue. The slowest eigenvalue of  $A_\xi - B_\xi K_\xi$  can be made arbitrarily fast by choosing large values for  $K_\xi$ , which requires higher signal energy in the auxiliary control  $v$ . High control signal may not be practical due to actuator saturation. Clearly, there is a tradeoff between the system's convergence speed and the control energy. This tradeoff motivates the use of LQ methods to find the state feedback by minimizing a quadratic functional that reflects the desired closed-loop performance. The LQ control problem is a constrained minimization problem described by

$$\begin{aligned} \text{minimize } J &= \frac{1}{2} \int_0^\infty [\check{\xi}^T(x) Q_\xi \check{\xi}(x) + R_\xi v^2] d\tau \text{ with } Q_\xi = \begin{bmatrix} q_1 & 0 \\ 0 & q_2 \end{bmatrix} \\ \text{subject to } \dot{\check{\xi}} &= A_\xi \check{\xi}(x) + B_\xi v \end{aligned} \quad (5.27)$$

where  $Q_\xi = Q_\xi^T > 0$  is a weighted matrix placed on the tracking error and  $R_\xi > 0$  is the weight placed on the auxiliary control [109]. The constrained minimization problem results from the the tracking error and the auxiliary control being dependent because to solve the controllable canonical state equation. The dependency is addressed by turning the constrained minimization problem into a unconstrained minimization problem with higher dimension by introducing Lagrange mulitpliers (costates) [109]. The costates are chosen to have the tracking error be independent of the auxiliary control. The unconstrained problem minimizes the Hamiltonian function,

$$H(\check{\xi}(x), \lambda, v) = \frac{1}{2} \check{\xi}^T(x) Q_\xi \check{\xi}(x) + \frac{1}{2} R_\xi v^2 + \lambda^T (A_\xi \check{\xi}(x) + B_\xi v) \quad (5.28)$$

where  $\lambda$  is the costate. The Hamiltonian function is minimized when its gradient  $\nabla H = 0$ , which is equivalent to the optimality conditions satisfying

$$\dot{\check{\xi}} = \frac{\partial H}{\partial \lambda} = A_\xi \check{\xi}(x) + B_\xi v \quad (5.29a)$$

$$\dot{\lambda} = -\frac{\partial H}{\partial \check{\xi}} = -Q_\xi \check{\xi}(x) - A_\xi^T \lambda \quad (5.29b)$$

$$0 = \frac{\partial H}{\partial v} = R_\xi v + B_\xi^T \lambda. \quad (5.29c)$$

The auxiliary control depends on the costate via  $v(x) = -R_\xi^{-1} B_\xi^T \lambda(x)$ . To implement state feedback, the auxiliary control needs to be expressed in the tracking error not the costate. The auxiliary control can be expressed in the tracking error by relating the costate to the tracking error via a standard optimal control assumption  $\lambda(x) = P_\xi \check{\xi}(x), \forall t$ , where  $P_\xi = P_\xi^T \geq 0$ . The matrix  $P_\xi$  is the solution to the differential Riccati equation [109]

$$\dot{P}_\xi = -A_\xi^T P_\xi - P_\xi A_\xi - Q + P_\xi B_\xi R_\xi^{-1} B_\xi^T P_\xi, \quad \text{with} \quad P_\xi = \begin{bmatrix} p_1 & p_2 \\ p_2 & p_3 \end{bmatrix}. \quad (5.30)$$

The Riccati equation is model dependent and driven by the weights  $Q_\xi$  and  $R_\xi$ . Its solution can be calculated off-line. The LQ controller is going to operate longer than its time constant and this fact allows the solution to the differential Riccati equation to be simplified by only considering its steady-state solution ( $\dot{P}_\xi = 0$ ). The differential Riccati equation is turned into an algebraic Riccati equation,

$$0 = A_\xi^T P_\xi + P_\xi A_\xi + Q_\xi - P_\xi B_\xi R_\xi^{-1} B_\xi^T P_\xi, \quad (5.31)$$

which has one solution such that the eigenvalues of the closed-loop system are the stabilizing eigenvalues of the Hamiltonian matrix [108],

$$H = \begin{bmatrix} A_\xi & -B_\xi R_\xi^{-1} B_\xi^T \\ -Q_\xi & -A_\xi^T \end{bmatrix} \quad (5.32)$$

The Riccati solution relates the auxiliary control to the tracking error via  $\lambda(x) = P_\xi \check{\xi}(x)$  to yield

$$v(\check{\xi}(x)) = -R_\xi^{-1} B_\xi^T P_\xi \check{\xi}(x) = -K_\xi \check{\xi}(x), \quad (5.33)$$

where  $K_\xi = R_\xi^{-1}B_\xi^T P_\xi = [k_1 \ k_2]$  is the state feedback matrix. The implementation of the auxiliary control uses the state estimate to yield

$$v(\check{\xi}(\hat{x})) = -R_\xi^{-1}B_\xi^T P_\xi \check{\xi}(\hat{x}) = -K_\xi \check{\xi}(\hat{x}). \quad (5.34)$$

The dynamics for the closed-loop tracking error are obtained by substituting equation 5.34 into equation 5.26, and adding and subtracting the term  $B_\xi v(x)$  to equation 5.26 to yield

$$\begin{aligned} \frac{d}{dt}\check{\xi} &= A_\xi \check{\xi}(x) + B_\xi v(\check{\xi}(\hat{x})) - B_\xi \left( v(\check{\xi}(x)) - v(\check{\xi}(\hat{x})) \right) - B_\xi C A^2 \check{x} \\ &= \left( A_\xi - B_\xi R_\xi^{-1} B_\xi^T P_\xi \right) \check{\xi}(x) + B_\xi R_\xi^{-1} B_\xi^T P_\xi \left( \check{\xi}(x) - \check{\xi}(\hat{x}) \right) - B_\xi C A^2 \check{x}. \end{aligned} \quad (5.35)$$

Equation 6.42 describes the nominal closed-loop tracking error dynamics

$\frac{d}{dt}\check{\xi} = (A_\xi - B_\xi R_\xi^{-1} B_\xi^T P_\xi) \check{\xi}(x)$  being driven by two perturbations. The first perturbation  $-B_\xi C A^2 \check{x}$  results from the estimation error in the input-output feedback due to the state estimation process; the second perturbation  $B_\xi R_\xi^{-1} B_\xi^T P_\xi (\check{\xi}(x) - \check{\xi}(\hat{x}))$  results from the pseudo estimation error of the tracking error definition due to the state estimation process.

It is insightful to assess the effectiveness the control has on the closed-loop composite system by quantifying the state bias and state variance of the composite system.

## 5.5 STATISTICAL ANALYSIS ON CLOSED-LOOP COMPOSITE SYSTEM

These statistical properties depend on the operating conditions of the optical trap system. The operating conditions change when there is a change in the laser power or the molecule's end-to-end extension. The laser power is related to the optical stiffness  $k_t$ , which affects  $\omega_t = k_t/\gamma$  and the linear operating range. An increase/decrease in the laser power results in an increase/decrease in the optical stiffness and the linear operating range. The molecule's end-to-end extension is related to the molecule's stiffness; an increase/decrease to the molecule's end-to-end distance results in an increase/decrease in the molecule's stiffness  $k_m$ . Thus, for each pair of  $k_t$  and  $k_m$  (or  $\kappa = k_m/k_t$ , the dimensionless stiffness), a Kalman filter is designed.

Let us quantify the statistical properties for the different operating conditions by performing Lyapunov stability analysis for the bias and numerical methods for the variances.

The dynamics for the closed-loop composite system is composed of

1. The dynamics for the closed-loop tracking error in equation 5.35,

$$\frac{d}{dt}\check{\xi} = \left( A_\xi - B_\xi R_\xi^{-1} B_\xi^T P_\xi \right) \check{\xi}(x) + B_\xi R_\xi^{-1} B_\xi^T P_\xi \left( \check{\xi}(x) - \check{\xi}(\hat{x}) \right) - B_\xi C A^2 \check{x}$$

2. The dynamics for the internal states in equation 5.24,

$$\dot{\psi} = \delta(\xi_r - \check{\xi}, \psi)$$

3. The dynamics for the closed-loop state-estimation error in equation 5.10

$$\dot{\check{x}} = (A - JC)\check{x} + B_w \tilde{w} - J\tilde{n}.$$

**Closed-loop bias** A Lyapunov stability analysis is performed to quantify the bias of the expected value of the closed-loop composite system. The expected value for the closed-loop composite system is described by

1. The expected value of the dynamics for the closed-loop tracking error is obtained by taking the expected value of equation 5.35,

$$\frac{d}{dt}\bar{\xi} = \left( A_\xi - B_\xi R_\xi^{-1} B_\xi^T P_\xi \right) \bar{\xi}(\bar{x}) + B_\xi R_\xi^{-1} B_\xi^T P_\xi \left( \bar{\xi}(\bar{x}) - \bar{\xi}(\bar{\hat{x}}) \right) - B_\xi C A^2 \bar{x}. \quad (5.36)$$

2. The expected value of the dynamics for the internal states is obtained by taking the expected value of equation 5.24,

$$\dot{\bar{\psi}} = \delta(\xi_r - \bar{\xi}, \bar{\psi}) \quad (5.37)$$

3. The expected value of the dynamics for the closed-loop state-estimation error is obtained by taking the expected value of equation 5.10,

$$\frac{d}{dt}\bar{\check{x}} = (A - JC)\bar{\check{x}}. \quad (5.38)$$

The following assumptions are used:

**Assumption 4.** *The tracking error is Lipschitz. The Lipschitz condition implies there exists a positive constant  $l_2$  such that*

$$\left\| \check{\xi}(\bar{x}) - \check{\xi}(\bar{\hat{x}}) \right\| \leq l_2 \|\bar{\check{x}}\|, \quad (5.39)$$

where  $\bar{\check{x}} = \bar{x} - \bar{\hat{x}}$  is the expected value of the state estimation error.

**Assumption 5.** *Assuming the matrix  $A - JC$  is Hurwitz and a matrix  $Q_x$  is a positive definite and symmetric, then there exists a positive and definite matrix  $P_x$  satisfying the Lyapunov equation*

$$(A - JC)^T P_x + P_x (A - JC) = -Q_x. \quad (5.40)$$

**Theorem 2.** *Assume there are positive constants  $b_3$ ,  $b_4$ ,  $b_5$  and  $b_6$ . When these constants satisfy*

$$b_6 = \min\{b_4 - b_3, b_5 - b_3\},$$

*the closed-loop composite system yielding exponential stability for the expected value of the tracking error and the expected value state estimation error. The exponential stability result implies there is no bias in the tracking error or the state estimation error. The boundedness of the tracking error and the reference signal implies the internal states are bounded by BIBO stability according to theorem 1.*

*Proof.* The Lyapunov function candidate is

$$W = \check{\xi}^T(\bar{x}) P_\xi \check{\xi}(\bar{x}) + \bar{\check{x}}^T P_x \bar{\check{x}}, \quad (5.41)$$

and this candidate is positive definite and decrescent because the function can be lower and upper bounded with class  $K$  functions

$$b_1 (\|\check{\xi}\|^2 + \|\bar{\check{x}}\|^2) \leq W \leq b_2 (\|\check{\xi}\|^2 + \|\bar{\check{x}}\|^2) \quad (5.42)$$

where  $b_1 = \min\{\lambda_{\min}(P_\xi), \lambda_{\min}(P_x)\}$  and  $b_2 = \max\{\lambda_{\max}(P_\xi), \lambda_{\max}(P_x)\}$ . Taking the time derivative of equation 5.41,

$$\dot{W} = \frac{d}{dt} \check{\xi}^T P_\xi \check{\xi} + \check{\xi}^T P_\xi \frac{d}{dt} \check{\xi} + \frac{d}{dt} \bar{\check{x}}^T P_x \bar{\check{x}} + \bar{\check{x}}^T P_x \frac{d}{dt} \bar{\check{x}}, \quad (5.43)$$

substituting in the expressions for the closed-loop state estimation error and the tracking error, and rearranging terms yield

$$\begin{aligned}
\dot{W} &= \check{\xi}^T(\bar{x}) \left( A_\xi^T P_\xi + P_\xi A_\xi - P_\xi B_\xi R_\xi^{-1} B_\xi^T P_\xi \right) \check{\xi}(\bar{x}) - \check{\xi}^T(\bar{x}) P_\xi B_\xi R_\xi^{-1} B_\xi^T P_\xi \check{\xi}(\bar{x}) \\
&\quad + 2\check{\xi}^T(\bar{x}) P_\xi B_\xi R_\xi^{-1} B_\xi^T P_\xi \left( \check{\xi}^T(\bar{x}) - \check{\xi}^T(\hat{x}) \right) + 2\check{\xi}^T(\bar{x}) B_\xi C A^2 \bar{x} \\
&\quad + \bar{x}^T \left( (A - JC)^T P_x + P_x (A - JC) \right) \bar{x}
\end{aligned} \tag{5.44}$$

Applying assumption 5 to the last term in equation 5.44 and using the fact  $-\check{\xi}^T(\bar{x}) P_\xi B_\xi R_\xi^{-1} B_\xi^T P_\xi \check{\xi}(\bar{x}) \leq 0$  yields

$$\begin{aligned}
\dot{W} &\leq \check{\xi}^T(\bar{x}) \left( A_\xi^T P_\xi + P_\xi A_\xi - P_\xi B_\xi R_\xi^{-1} B_\xi^T P_\xi \right) \check{\xi}(\bar{x}) - \bar{x}^T Q_x \bar{x} \\
&\quad + 2\check{\xi}^T(\bar{x}) P_\xi B_\xi R_\xi^{-1} B_\xi^T P_\xi \left( \check{\xi}^T(\bar{x}) - \check{\xi}^T(\hat{x}) \right) + 2\check{\xi}^T(\bar{x}) B_\xi C A^2 \bar{x}
\end{aligned} \tag{5.45}$$

The first term is simplified by applying the steady-state algebraic Riccati equation (as shown in equation 5.31)

$$A_\xi^T P_\xi + P_\xi A_\xi + Q_\xi - P_\xi B_\xi R_\xi^{-1} B_\xi^T P_\xi = 0$$

with  $Q_\xi$  being positive negative. Applying equation 5.31 to equation 5.45 yields

$$\begin{aligned}
\dot{W} &= -\check{\xi}^T(\bar{x}) Q_\xi \check{\xi}(\bar{x}) - \bar{x}^T Q_x \bar{x} + 2\check{\xi}^T(\bar{x}) P_\xi B_\xi R_\xi^{-1} B_\xi^T P_\xi \left( \check{\xi}^T(\bar{x}) - \check{\xi}^T(\hat{x}) \right) + 2\check{\xi}^T(\bar{x}) B_\xi C A^2 \bar{x}
\end{aligned} \tag{5.46}$$

Equation 5.46 is further bounded by applying the properties of positive definite matrices to the first two terms, and taking the norm of the last two terms to yield

$$\begin{aligned}
\dot{W} &\leq -b_3 \left\| \check{\xi}(\bar{x}) \right\|^2 - b_4 \left\| \bar{x} \right\|^2 \\
&\quad + \left\| 2\check{\xi}^T(\bar{x}) P_\xi B_\xi R_\xi^{-1} B_\xi^T P_\xi \left( \check{\xi}^T(\bar{x}) - \check{\xi}^T(\hat{x}) \right) \right\| + \left\| 2\check{\xi}^T(\bar{x}) B_\xi C A^2 \bar{x} \right\|
\end{aligned} \tag{5.47}$$

where  $b_3 = \lambda_{\min}(Q_\xi)$  and  $b_4 = \lambda_{\min}(Q_x)$ . Next, the norm of the last two terms are bounded in terms of  $\left\| \check{\xi}(\bar{x}) \right\|^2$  and  $\left\| \bar{x} \right\|^2$ . The norm  $\left\| 2\check{\xi}^T(\bar{x}) P_\xi B_\xi R_\xi^{-1} B_\xi^T P_\xi \left( \check{\xi}^T(\bar{x}) - \check{\xi}^T(\hat{x}) \right) \right\|$  is bounded

using assumption 4, which implies the tracking error  $\check{\xi}(\bar{x})$  is Lipschitz. Then, the norms of the last two terms are bounded by

$$\left\| 2\check{\xi}^T(\bar{x})P_\xi B_\xi R_\xi^{-1} B_\xi^T P_\xi \left( \check{\xi}^T(\bar{x}) - \check{\xi}^T(\hat{x}) \right) \right\| + \left\| 2\check{\xi}^T(\bar{x})B_\xi C A^2 \bar{x} \right\| \leq b_5 2 \left\| \check{\xi}(\bar{x}) \right\| \left\| \bar{x} \right\| \quad (5.48)$$

where  $b_5 = l_2 \left\| P_\xi B_\xi R_\xi^{-1} B_\xi^T P_\xi \right\| + \left\| B_\xi C A^2 \right\|$ . The norm  $2 \left\| \check{\xi}(\bar{x}) \right\| \left\| \bar{x} \right\|$  is further bounded using Young's inequality to yield

$$2 \left\| \check{\xi}(\bar{x}) \right\| \left\| \bar{x} \right\| \leq \left\| \check{\xi}(\bar{x}) \right\|^2 + \left\| \bar{x} \right\|^2.$$

Then, equation 5.48 is bounded by

$$\left\| 2\check{\xi}^T(\bar{x})P_\xi B_\xi R_\xi^{-1} B_\xi^T P_\xi \left( \check{\xi}^T(\bar{x}) - \check{\xi}^T(\hat{x}) \right) \right\| + \left\| 2\check{\xi}^T(\bar{x})B_\xi C A^2 \bar{x} \right\| \leq b_5 \left\| \check{\xi}(\bar{x}) \right\|^2 + b_5 \left\| \bar{x} \right\|. \quad (5.49)$$

Substituting equation 5.49 into equation 5.47 yields

$$\begin{aligned} \dot{W} &\leq -(b_3 - b_5) \left\| \check{\xi}(\bar{x}) \right\|^2 - (b_4 - b_5) \left\| \bar{x} \right\|^2 \\ &\leq -b_6 \left( \left\| \check{\xi}(\bar{x}) \right\|^2 + \left\| \bar{x} \right\|^2 \right), \end{aligned} \quad (5.50)$$

where  $b_6 = \min\{b_3 - b_5, b_4 - b_5\}$ . Equation 5.50 is negative definite, which implies that the estimation error dynamics and the tracking error dynamics are asymptotically stable. A stronger stability condition of exponential stability is now shown. Exponential stability requires bounding equation 5.50 (becomes less negative) in terms of the Lyapunov function  $W$  by expressing the term  $\left\| \check{\xi} \right\|^2 + \left\| \bar{x} \right\|^2$  in terms of  $W$  using equation 5.42. Equation 5.50 is bounded by

$$\dot{W} \leq -\frac{b_6}{b_2} W, \quad (5.51)$$

and its solution is

$$W(t) \leq W(0) \exp \left( -\frac{b_6}{b_2} t \right). \quad (5.52)$$

This results in the Lyapunov function  $W$  being exponentially stable, which implies the tracking error and the state estimation error are exponentially stable. The boundedness of the tracking error and the reference signal  $\xi_r$  allows for the internal states to remain bounded by BIBO stability according to theorem 1 because the undriven internal states are exponentially stable.  $\square$

**Control State Variance** The closed-loop composite system (the combination of the optical trap system, the Kalman filter, and the controller) fluctuates at steady-state due to process noise (Brownian noise and molecule noise), and the measurement noise. Recall that the optical trap (same as in equation 5.1) is

$$\dot{x} = Ax + B_u u + B_w \tilde{w},$$

the nonlinear Kalman filter (same as in equation 5.9 ) is

$$\dot{\hat{x}} = Ax + B_u u + J[y - c\hat{x}],$$

and the controller is

$$u(\hat{x}) = \frac{1}{CAB_u} \left[ (CA^2 + k_1C + k_2CA)\hat{x} - k_1r - k_2\dot{r} - \ddot{r} \right].$$

The system fluctuations are simplified by using the fact that the noise inputs only drive the states describing the bead and the molecule; then assumption 3 is used to imply that measurement noise only affects the state estimates describing the bead and the molecule. The control signal is considered by including the actuator state whose dynamics explicitly depends on the control signal. In this research, the fluctuations are characterized by performing a linear noise analysis about the expected value at steady-state. The fluctuations are determined by first describing the composite system and its expected value. The dynamics for the composite system  $x_c$  are described by

$$\dot{x}_c = A_c x_c + B_c \tilde{w}_c, \quad \text{with} \quad x_c = [z, d_m, a_3, \hat{z}, \hat{d}_m, \hat{a}_3, \hat{d}_d]^T, \quad \text{and} \quad \tilde{w}_c = [\tilde{d}, \tilde{d}_m, \tilde{n}]^T, \quad (5.53)$$

and its expected value  $\bar{x}_c = E[x_c]$  has dynamics of

$$\dot{\bar{x}}_c = A_c \bar{x}_c. \quad (5.54)$$

The system fluctuations are described by the noise  $\tilde{x}_c = x_c - \bar{x}_c$  and its dynamics are

$$\dot{\tilde{x}}_c = A_c(\tilde{x}_c + \bar{x}_c) + B_c \tilde{w}_c - A_c \bar{x}_c, \quad (5.55a)$$

$$= A_c \tilde{x}_c + B_c \tilde{w}_c. \quad (5.55b)$$

The state matrix  $A_c$  and the input matrix  $B_c$  are partitioned and described by

$$A_c = \begin{bmatrix} A_p & -B_p(CA^2 + c_1C + c_2CA) \\ JC_p & A - JC - B_v(CA^2 + c_1C + c_2CA) \end{bmatrix} \quad (5.56)$$

where the state matrices  $A_p$  and  $A$  are

$$A_p = \begin{bmatrix} -\omega_t & -\kappa\omega_t & -g_v g_a \\ -\omega_t & -\kappa\omega_t - \omega_m & 0 \\ 0 & 0 & -\omega_{p1} - \omega_{p2} \end{bmatrix}, \quad (5.57)$$

$$A = \begin{bmatrix} -\omega_t & -\kappa\omega_t & -g_v g_a & 0 \\ -\omega_t & -\kappa\omega_t - \omega_m & 0 & \omega_m \\ 0 & 0 & -\omega_{p1} - \omega_{p2} & 0 \\ 0 & 0 & 0 & -\omega_d \end{bmatrix}; \quad (5.58)$$

the input matrices  $B_p$  and  $B$  are

$$B_p = \begin{bmatrix} 0 & 0 & 1 \end{bmatrix}^T, \quad \text{and} \quad B = \begin{bmatrix} 0 & 0 & 1 & 0 \end{bmatrix}^T; \quad (5.59)$$

the output matrices  $C_p$  and  $C$  are

$$C_p = \begin{bmatrix} g_s & 0 & 0 \end{bmatrix}^T, \quad \text{and} \quad C = \begin{bmatrix} g_s & 0 & 0 & 0 \end{bmatrix}^T. \quad (5.60)$$

The state variances are characterized by the steady-state state covariance matrix

$X_c = E [\tilde{x}_c \tilde{x}_c^T]$ , which is the solution to the Lyapunov equation

$$A_c X_c + X_c A_c^T + B_c S_c B_c^T = 0 \quad \text{where} \quad S_c = \begin{bmatrix} S_d & 0 & 0 \\ 0 & S_m & 0 \\ 0 & 0 & S_n \end{bmatrix}. \quad (5.61)$$

The variance for the bead deflection and its estimate are shown in figure 29; the variance of the molecule extension and its estimate are shown in figure 30. For a given  $\kappa$ , increasing  $k_t$  (also  $k_m$  is increased to maintain a constant  $\kappa$ ) results in a decrease in the variance for the states and their estimates; a stiffer optical trap and molecule reduces the variance. Then, for a given  $k_t$ , an increase in  $\kappa$  (a stiffer molecule) results in an decrease in the variance for the states and the variance. The control has minimal effect on the variance of the actual

state when compared to the open-loop case; the control reduces the variance of the estimated states when compared to the open-loop case. The variance for the estimated disturbance and its description are the same its variance in the open-loop case and its description as given in section 5.3. The SNR analysis for the estimated force disturbance and its description are the same as given in section 5.3.

The closed-loop performance with LQG control drives the expected value of the tracking error to zero, provides a real-time unbiased estimate of the molecule force, and reduces the noise effects. The same statistical characteristics of the estimated molecule force can be obtained using linear integral control, a feedback method used in practice by biophysicists. The statistical characteristics being equivalent for both feedback methods is crucial because the statistical characteristics obtained using a controller in practice can be compared to the statistical characteristics obtained using the nonlinear feedback methods. The comparison is then performed with the LQG design because the LQG design has a similar architecture of the proposed nonlinear feedback designs to address the estimation and controls. First, we must show the statistical characteristics obtained with the LQG design are equivalent to that obtained with linear integral control.

## 5.6 LINEAR INTEGRAL CONTROL

Linear integral control is a fixed-gain design that must be designed for each operating condition (each pair  $k_t$  and  $\kappa$ ). Its closed-loop performance is studied using a transfer function approach. The transfer function approach requires the optical trap system in equation 5.1 be expressed into a transfer function matrix to relate each system input to the system output. The optical trap system is driven by the control input, and three disturbance inputs: the disturbance extension, the molecule noise, and the Brownian noise. The resulting transfer function matrix  $G(s) = C(sI - A)^{-1}B + D$  describes the three transfer functions:

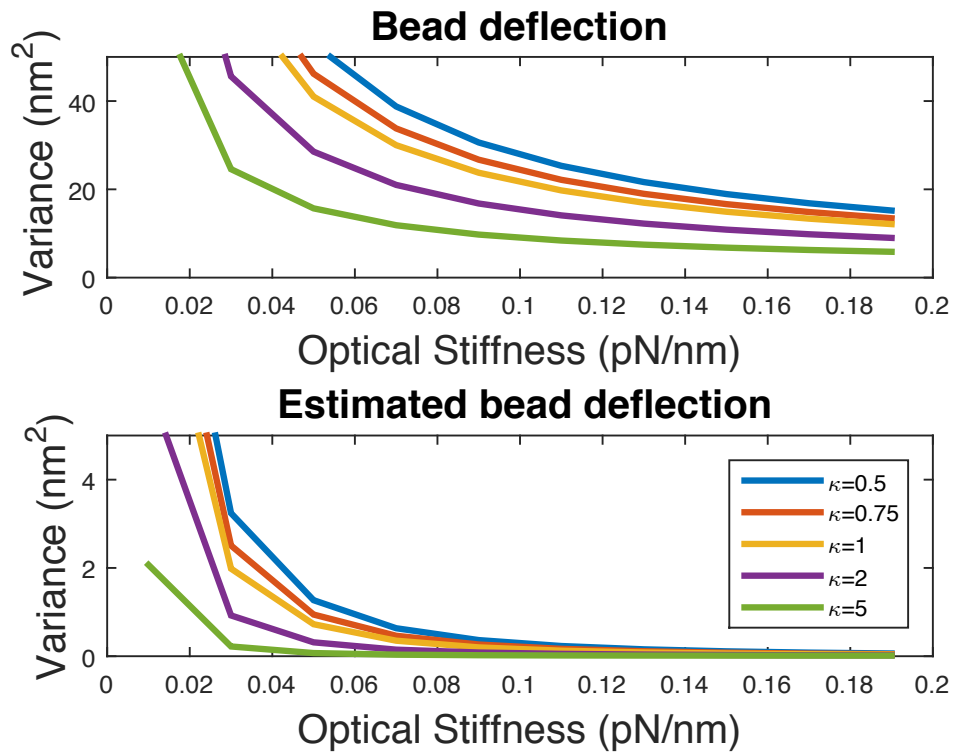


Figure 29: A schematic for the variance of the bead deflection and its estimate obtained using LQG control. For a given  $\kappa$ , increasing  $k_t$  (also  $k_m$  is increased to maintain a constant  $\kappa$ ) results in a decrease in the variance for the states and their estimates; a stiffer optical trap and a stiffer molecule reduces the variance. Then, for a given  $k_t$ , an increase in  $\kappa$  (a stiffer molecule) results in an decrease in the variance for the states and the variance.

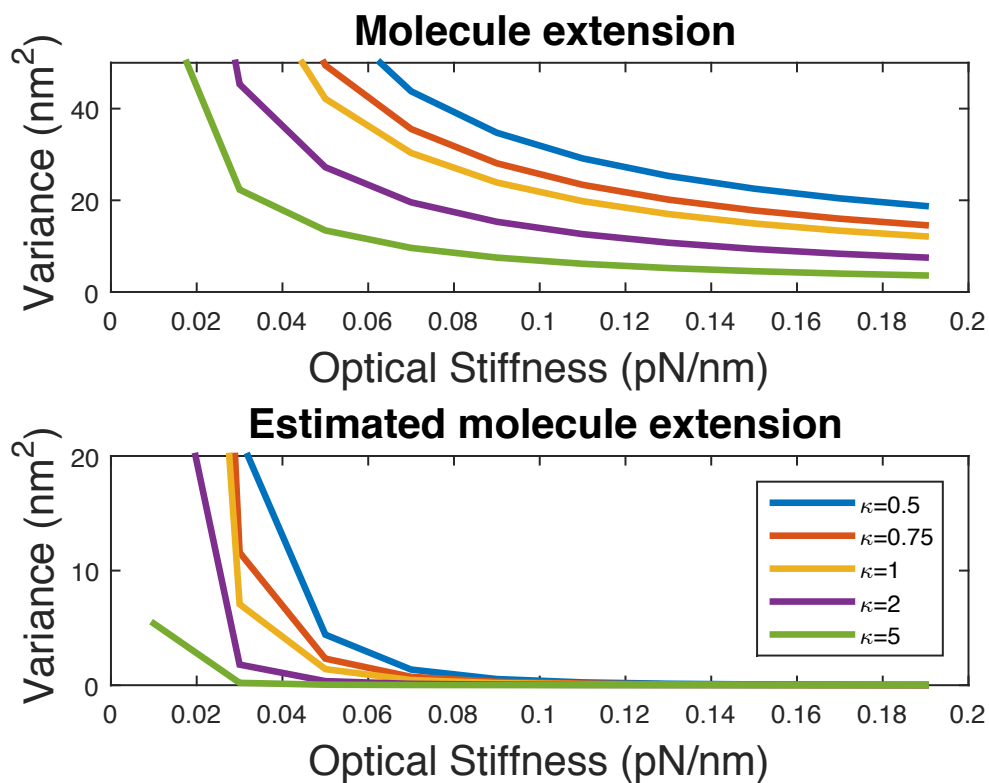


Figure 30: A schematic for the variance of the molecule extension and its estimate obtained using LQG control. For a given  $\kappa$ , increasing  $k_t$  (also  $k_m$  is increased to maintain a constant  $\kappa$ ) results in a decrease in the variance for the states and their estimates; a stiffer optical trap and a stiffer molecule reduces the variance. Then, for a given  $k_t$ , an increase in  $\kappa$  (a stiffer molecule) results in an decrease in the variance for the states and the variance.

1. The control input affects the system output through the cascaded system of the actuator and the optical trap dynamics. This cascaded system is described by

$$\begin{aligned}
G_1(s) &= \frac{z(s)}{u(s)} \\
&= - \left( \frac{g\omega_{p_1}\omega_{p_2}\omega_{p_v}}{\omega_z\omega_{z_v}} \right) \frac{(s + \omega_z)(s + \omega_{z_v})(s + \omega_m + \kappa\omega_t)}{(s + \omega_{p_1})(s + \omega_{p_2})(s + \omega_{p_v})(s^2 + (\omega_m + \omega_t + \kappa\omega_t)s + \omega_m\omega_t)}
\end{aligned} \tag{5.62}$$

2. The disturbance extension and the molecule noise affect the the system output by

$$G_2(s) = \frac{z(s)}{d_d(s) + \tilde{d}_m(s)} = - \frac{g_s\kappa\omega_m\omega_t}{s^2 + (\omega_m + \omega_t + \kappa\omega_t)s + \omega_m\omega_t}. \tag{5.63}$$

3. The Brownian noise affects the system output by

$$G_3(s) = \frac{z(s)}{\tilde{d}(s)} = \frac{g_s\omega_t(s + \omega_m)}{s^2 + (\omega_m + \omega_t + \kappa\omega_t)s + \omega_m\omega_t}. \tag{5.64}$$

The objective is to manipulate the system output in the presence of disturbances, which is a servocontrol problem. The servocontrol problem (e.g., disturbance rejection and tracking problem) is described with the block diagram, as shown in figure 31. The error,  $e$ , the difference between the reference signal and the system output (the measured bead deflection), is fed into the controller,  $K$ , to create the control signal,  $u$ . For servocontrol, the control objective is to minimize the error. The closed-loop error is described by

$$e = Sr - SG_2(d_d + \tilde{d}_m) - SG_3\tilde{d} + T\tilde{n} \tag{5.65}$$

where  $S$  and  $T$  are the sensitivity function and the complimentary sensitivity function respectively,

$$S = \frac{1}{1 + L} \quad \text{and} \quad T = \frac{L}{1 + L} = 1 - S, \tag{5.66}$$

with  $L = G_1K$  being the loop gain. Of interest is the expected value of the steady-state error, and its performance is characterized by the loop-gain characteristics. The loop-gain should be large (equivalent to the sensitivity being small) for disturbance rejection and tracking. However, analytic constraints, placed on the closed-loop system, prevent the sensitivity function being small for all frequencies. Attenuating the sensitivity function by a factor

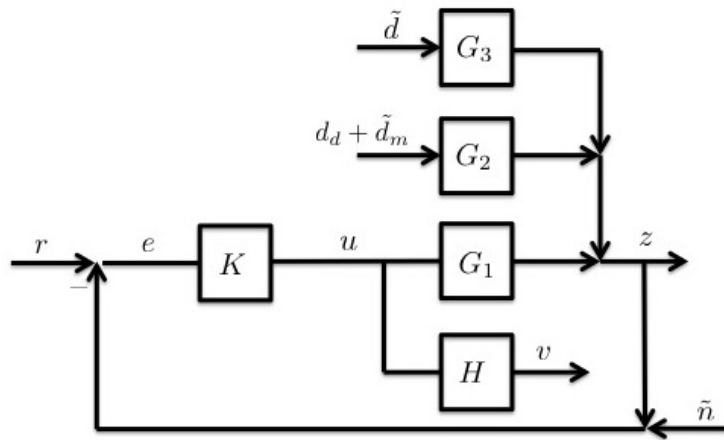


Figure 31: The block diagram schematic of the closed-loop optical trap with integral control. In the diagram, the plant is  $G_1$ , the controller is  $K$ , the molecule disturbances are filtered by  $G_2$ , the Brownian disturbance is filtered by  $G_3$ , and the control  $u$  is filtered by a phase-lead compensation filter  $H$  to form  $v$ . The other signals are the reference signal  $r$  and the error  $e$ .

of  $P$  over the bandwidth  $w_b$  can cause the sensitivity function to be magnified elsewhere according to the waterbed effect and the Bode Sensitivity Integral [51].

The closed-loop error is minimized in the presence of process noise (Brownian noise and molecule noise), disturbance extensions (constant disturbances), and a constant reference signal for the bead deflection (equivalent to applying a constant optical force). The constant inputs are modeled with step inputs. Zero steady-state error for step inputs is achieved with type 1 systems. A type 1 system has its loop gain with a pole located at the origin, or equivalently, its sensitivity function having a zero at the origin.

The system  $G_1$  is Hurwitz, minimum phase, and a type 0 system. Its pole-zero map is shown in figure 32, and shows that a zero is located at  $-0.1$ , which is the zero in the phase-lead compensation filter to approximate the laser's velocity. The zero is troublesome because its location cannot be changed with linear integral control, and its bandwidth provides an upper limit on the bandwidth of the closed-loop system.

The controller must have one pole at the origin for the loop-gain to be type 1. The controller chosen is

$$K(s) = -\frac{\omega_k}{s}, \quad \text{with } \omega_k < \omega_t, \quad (5.67)$$

with  $\omega_k$  being the control gain. The loop gain, sensitivity function, and the complimentary sensitivity function are shown in figure 33. Figure 33 shows that  $T = 1$  for DC frequencies and  $T \approx 1$  within the system bandwidth, and results in the broadband measurement noise being directly fed through to the error.

Next, the bias of the closed-loop error is quantified by applying the final value theorem to its expected value. The expected value of the closed-loop error is  $\bar{e} = E[e]$ . Taking the expected value of equation 5.65 and applying the final value theorem yields.

$$\bar{e}_{ss} = \lim_{t \rightarrow \infty} E[e(t)] = \lim_{s \rightarrow 0} sE[e(s)] = \lim_{s \rightarrow 0} \left( sS(s) \frac{E[r]}{s} - sS(s)G_2(s) \frac{E[d_d]}{s} \right) = 0. \quad (5.68)$$

Integral control ensuring perfect disturbance rejection and zero tracking error for step inputs or DC frequencies. The perfect disturbance rejection is an apparent problem with integral control because our proxy for the measurement of  $d_d$  is now forced to zero.

A second advantage with integral control is disturbance estimation, in this case, an estimate the disturbance extension (force). Disturbance estimation is possible by analyzing

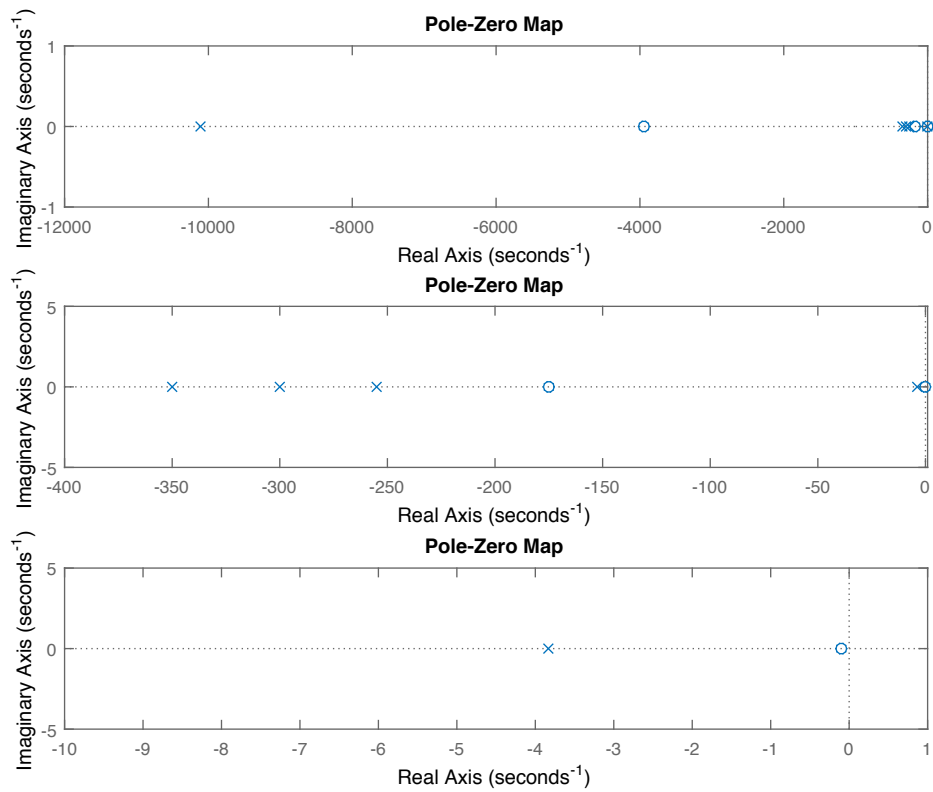


Figure 32: A schematic of the pole-map for the plant  $G_1(s)$ .

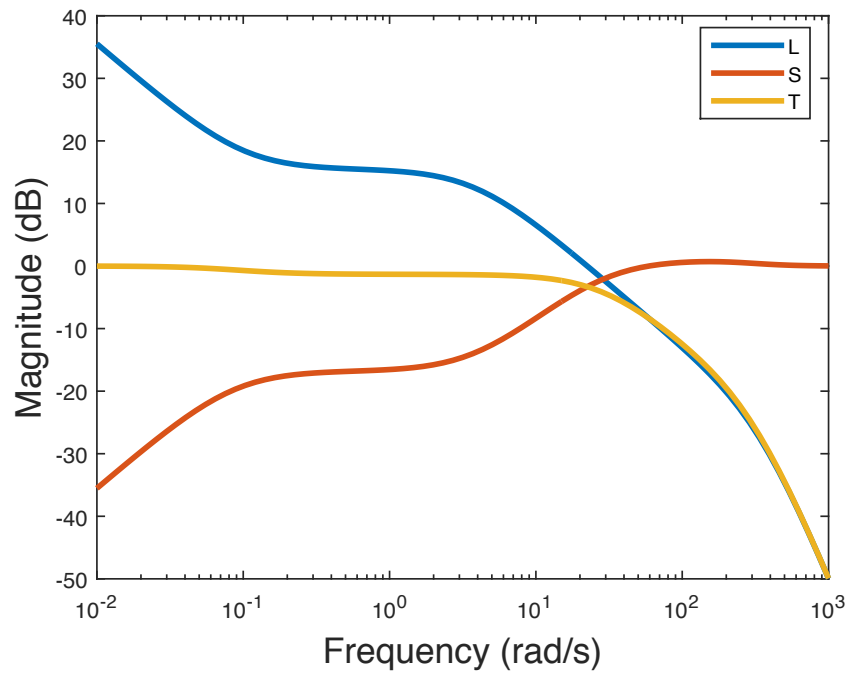


Figure 33: A schematic of the loop gain, sensitivity function, and the complementary sensitivity function obtained using linear integral control.

the control, in particular the filtered control ( $v=Hu$ ), where  $H$  is a phase-lead compensation filter,

$$H(s) = \frac{\omega_{p_h}}{\omega_{z_h}} \left( \frac{s + \omega_{z_h}}{s + \omega_{p_h}} \right) \quad \text{with} \quad \omega_{z_h} < \omega_{p_h}, \quad (5.69)$$

where  $\omega_{z_h}$  describes the bandwidth of the closed-loop system with integral control and  $\omega_{p_h}$  describes the bandwidth of the closed-loop system with the LQG design.

The closed-loop filtered control is described by

$$v = Hu = HKSr - HKSG_2(d_d + \tilde{d}_m) - HKSG_3\tilde{d} - HKSn, \quad (5.70)$$

as shown in the block diagram in figure 31. The filtered control and not the control is used for disturbance estimation to address the estimation bandwidth associated with the control. The control has a bandwidth that is equal to  $\omega_{z_h} < 0.1$  Hz. One consequence of having inadequate bandwidth is missed molecular characteristics. The inadequate bandwidth is addressed by feeding the control through the filter  $H$  to improve the estimation bandwidth.

For disturbance estimation, we are interested in the expected value of the steady-state filtered control  $\bar{v} = E[v]$ . Taking the expected value of equation 5.70 ,

$$\bar{v} = HKSr - HKSG_2d_d, \quad (5.71)$$

then applying the final value theorem yields

$$\bar{v}_{ss} = \lim_{s \rightarrow 0} sE[v(s)] = H(0)K(0)S(0)E[r] - H(0)K(0)S(0)G_2(0)E[d_d]. \quad (5.72)$$

The steady-state filtered control depends on the reference signal and the disturbance extension. This fact is used to obtain an unbiased estimate of the disturbance extension,

$$E[\hat{d}_d] = \frac{1}{H(0)K(0)S(0)G_2(0)} (H(0)K(0)S(0)E[r] - \bar{v}_{ss}), \quad (5.73)$$

then the unbiased estimate of the force disturbance is

$$E[\hat{f}_d] = k_m E[\hat{d}_d] = \frac{k_m}{H(0)K(0)S(0)G_2(0)} (H(0)K(0)S(0)E[r] - \bar{v}_{ss}). \quad (5.74)$$

The estimated force disturbance fluctuates at steady-state due to the Brownian noise, the molecular noise, and the measurement noise. These fluctuations are characterized by its variance, which is related to the variance of the filtered control by equation 5.71 to yield

$$\text{Var}(\hat{f}_d) = \left( \frac{k_m}{H(0)K(0)S(0)G_2(0)} \right)^2 \text{Var}(v). \quad (5.75)$$

The variance of the filtered control is found by taking its inverse Fourier transform of its PSD in equation 5.70 to yield

$$\begin{aligned} \text{Var}(v) &= \frac{1}{2\pi} \int_{-\infty}^{\infty} |H(j\omega)K(j\omega)S(j\omega)G_2(j\omega)|^2 S_m d\omega \\ &+ \frac{1}{2\pi} \int_{-\infty}^{\infty} |H(j\omega)K(j\omega)S(j\omega)G_3(j\omega)|^2 S_m d\omega \\ &+ \frac{1}{2\pi} \int_{-\infty}^{\infty} |H(j\omega)K(j\omega)S(j\omega)|^2 S_n d\omega. \end{aligned} \quad (5.76)$$

The SNR for the estimated force disturbance is

$$\text{SNR} = \frac{1}{\sqrt{\text{Var}(\hat{f}_d)}} E[\hat{f}_d]. \quad (5.77)$$

The statistical characteristics of the estimated force disturbance can be numerically solved. Next, the statistical characteristics of the estimated force disturbance obtained with linear integral control is compared with the statistical characteristics obtained with the LQG design.

Table 5: A comparison of the statistical characteristics of the estimated force disturbance obtained with the LQG design and the linear integral controller. The operating condition is  $k_t = 0.1$  pN/nmnd  $\kappa = 0.6384$  The molecule is stretched until its force reaches 6 pN

Controller	Estimation bandwidth (Hz)	$E[\hat{f}_d]$ (pN)	$\text{Var}(\hat{f}_d)$ (pN <sup>2</sup> )	SNR (dB)
LQG	11.21	6	0.09795	25.63
Integral	11.21	6	0.09772	25.66

### 5.6.1 Comparison of the Linear Controllers

The statistical characteristics of the estimated force disturbances obtained using the linear I control and the LQG design are compared. The comparison is performed at one operating condition (a pair of  $k_t$  and  $\kappa$ ). The molecule is initially at zero extension, then the molecule is stretched until its force reaches 6 pN. The integral control gain  $\omega_k$  is tuned until the statistical characteristics of the estimated force disturbance are equal to that obtained with the LQG design, as shown in table 5. Then, it is straightforward to see that for each operating condition, the integral control gain can be tuned such that the statistical characteristics of the estimated force disturbance are equal to that obtained with the LQG design. The statistical characteristics being equivalent for both feedback methods is crucial because the statistical characteristics obtained using a controller in practice can be compared to the statistical characteristics obtained using the nonlinear feedback methods. The comparison is then performed with the LQG design because the LQG design has a similar architecture of the proposed nonlinear feedback designs to address the estimation and controls.

## 6.0 NONLINEAR DESIGNS

Linear controllers yield satisfactory closed-loop performance when the optical forces are small. The limited operating range presents a challenge when the optical trap needs to produce higher optical forces. Higher optical forces are necessary when studying, for example, the stall force of viral packaging motors, DNA hysteresis, and RNA backstepping [8, 9, 43]. The higher optical forces can be produced within the entire operating range by considering the system nonlinearities in the control design. The advantage is lower laser power can be used, which can reduce the photodamage; the disadvantage is the bead deflection becomes large, which causes stability issues due to the decreasing optical stiffness and difficulties in estimating the molecule force. These issues are addressed with nonlinear feedback methods.

This chapter discusses the design and performance of the nominal nonlinear design to address the estimation and control problem, and the nonlinear PI design. The nominal design is a combination of a Luenberger observer with input-output feedback linearization and LQ structure. The estimation problem is addressed with a Luenberger state observer to provide a recursive state estimate. The state estimate is then used in the input-output feedback linearization with LQ structure to find the optimal state feedback that drives the tracking error to zero. In order to assess the effectiveness of this control approach on the quality of the measurements, statistical analyses are made on the resulting open-loop and closed-loop systems to quantify the effects of the nominal controller on the system bandwidth and the state statistical properties. These statistical quantities affect the quality of the nominal molecule force estimate, and these effects are studied by deriving a theoretical expression for its SNR.

## 6.1 NONLINEAR KALMAN FILTER

The estimation problem is addressed with a Kalman filter that uses the optical trap system, equation 4.37, in a state observer architecture to find the state-dependent observer gains. The problem of finding the state-dependent observer gain is turned into a problem of finding a state transformation to ensure that the expected value of the transformed estimation error exhibit linear dynamic behavior and to minimize the mean-squared estimation error. The state-dependent observer gains can be found when the optical trap system is subjected to process noise and measurement noise. These noise sources are Gaussian white noise and have the same statistical properties given in section 5.2.

The Kalman filter provides the conditional expectation of the state  $x$  based on the past and current measurements,

$$\hat{x}(t) = E[x(t)|y(\tau)], \quad \tau \in [0, t], \quad (6.1)$$

and minimizes the mean-squared estimation error. The state estimate dynamics can be described by

$$\dot{\hat{x}} = f(\hat{x}) + B_u u + G(\hat{x}) [m(h(x) + \tilde{n}) - m(h(\hat{x}))] \quad (6.2)$$

where  $G(\hat{x})$  is a state-dependent observer gain, and  $m : \mathbb{R} \rightarrow \mathbb{R}^n$  with  $m(0) = 0$  is a pseudo-measurement to be chosen later. A pseudo-measurement  $m(h(x))$  is used to expand the operating range of linear dynamics behavior for the transformed estimation error [110]. The correction term  $G(\hat{x}) [m(h(x) + \tilde{n}) - m(h(\hat{x}))]$  drives the state estimate dynamics because as new measurements arrive, the pseudo-measurement error  $m(h(x) + \tilde{n}) - m(h(\hat{x}))$  is weighted by  $G(\hat{x})$ .

The problem of finding  $G$  and  $m$  is turned into a problem of finding a state transformation  $p(x)$ . The state transformation is chosen to satisfy [111, 110]

$$\frac{\partial p(x)}{\partial x} f(x) = A_x p(x) + m(h(x)), \quad p(0) = 0, \quad (6.3)$$

where  $A_x$  is a Hurwitz matrix chosen such that the pair  $(A_x, \frac{\partial h(0)}{\partial x})$  is observable and the pair  $(A_x, \frac{\partial m(0)}{\partial x})$  is controllable.

For this research, there is a convenient choice for the state transformation,

$$p(x) = x, \quad (6.4)$$

and this choice is possible because the system dynamics is affine in the system nonlinearity, which depends on the measured state. The identity transformation  $p(x) = x$  is chosen to cancel the effects of the control input on the state estimation error dynamics as shown in the following analysis. The state estimation error dynamics is obtained by first expressing the dynamics for the optical trap system (same as equation 4.37)

$$\dot{x} = f(x) + B_u u + B_w \tilde{w},$$

and the state estimate in equation 6.2 in the transformed state. In the transformed state, the optical trap system is described by

$$\dot{p}(x) = \frac{\partial p(x)}{\partial x} \dot{x} = \frac{\partial p(x)}{\partial x} \left( f(x) + B_u u + B_w \tilde{w} \right), \quad (6.5a)$$

$$= A_x p(x) + m(h(x)) + \frac{\partial p(x)}{\partial x} \left( B_u u + B_w \tilde{w} \right). \quad (6.5b)$$

and the state estimate is described by

$$\dot{p}(\hat{x}) = \frac{\partial p(\hat{x})}{\partial \hat{x}} \dot{\hat{x}} = \frac{\partial p(\hat{x})}{\partial \hat{x}} \left( f(\hat{x}) + B_u u + G(\hat{x}) [m(h(x) + \tilde{n}) - m(h(\hat{x}))] \right), \quad (6.6a)$$

$$= A_x p(\hat{x}) + m(h(\hat{x})) + \frac{\partial p(\hat{x})}{\partial \hat{x}} \left( B_u u + G(\hat{x}) [m(h(x) + \tilde{n}) - m(h(\hat{x}))] \right). \quad (6.6b)$$

On the transformed state, the state estimation error is

$$\check{x} = p(x) - p(\hat{x}), \quad (6.7)$$

and its dynamics is described by

$$\begin{aligned} \dot{\check{x}} &= A_x \check{x} + \frac{\partial p(x)}{\partial x} B_w \tilde{w} + \left( \frac{\partial p(x)}{\partial x} - \frac{\partial p(\hat{x})}{\partial \hat{x}} \right) B_u u \\ &\quad + m(h(x)) - m(h(\hat{x})) - \frac{\partial p(\hat{x})}{\partial \hat{x}} G(\hat{x}) \left( m(h(x) + \tilde{n}) - m(h(\hat{x})) \right). \end{aligned} \quad (6.8)$$

Next, we show the control input  $u$  has zero effect on  $\bar{x}$  by studying the expected value of the transformed state estimation error  $\bar{x} = E[\check{x}]$ . Taking the expected value of equation 6.8 yields

$$\begin{aligned} \frac{d}{dt}\bar{x} &= A_x\bar{x} + \left( \frac{\partial p(x)}{\partial x} - \frac{\partial p(\hat{x})}{\partial \hat{x}} \right) B_u u \\ &\quad + m(h(x)) - m(h(\hat{x})) - \frac{\partial p(\hat{x})}{\partial \hat{x}} G(\hat{x}) \left( m(h(x)) - m(h(\hat{x})) \right). \end{aligned} \quad (6.9)$$

Choosing  $G(\hat{x})$  to be

$$G(\hat{x}) = \left[ \frac{\partial p(\hat{x})}{\partial \hat{x}} \right]^{-1}, \quad (6.10)$$

and substituting it into equation 6.9 yields

$$\frac{d}{dt}\bar{x} = A_x\bar{x} + \left( \frac{\partial p(x)}{\partial x} - \frac{\partial p(\hat{x})}{\partial \hat{x}} \right) B_u u. \quad (6.11)$$

The control input effects the dynamics of  $\bar{x}$  through the difference of the tangent manifolds,  $\frac{\partial p(x)}{\partial x} - \frac{\partial p(\hat{x})}{\partial \hat{x}}$ . These effects are neglected when using the identity transformation  $p(x) = x$  and  $\frac{\partial p}{\partial x} = I$ . Substituting the identity transformation  $p(x) = x$  into equation 6.11,

$$\frac{d}{dt}\bar{x} = A_x\bar{x}, \quad (6.12)$$

yields  $\bar{x}$  exhibiting linear dynamic behavior, and is guaranteed to exponentially converge to zero if all  $\lambda(A_x) < 0$ .

The next step is to choose the matrix  $A_x$  and the pseudo-measurement  $m$  that satisfies equation 6.3, ensures  $A_x$  is Hurwitz, and minimizes the mean-squared state estimation error. First, let us simplify equation 6.3 by substituting in the identity transformation  $p(x) = x$  to yield

$$f(x) = A_x x + m(h(x)). \quad (6.13)$$

The matrix  $A_x$  and the pseudo-measurement  $m$  are chosen by solving equation 6.13 with a Taylor series approach and equating the coefficients at each degree. The system dynamics  $f$  and the pseudo-measurement  $m$  are expressed in a Taylor series about  $x = 0$ ,

$$f(x) = Ax + f^2(x) + f^3(x) + \dots \quad (6.14a)$$

$$m(x) = JCx + m^2(h(x)) + m^3(h(x)) + \dots \quad (6.14b)$$

where  $f^d(x)$  describes the  $d$ th degree term in the Taylor series. Substituting equation 6.14 into equation 6.13 yields the following conditions:

1. For degree  $d = 1$ :

$$A_x = A - JC, \quad (6.15)$$

where  $C$  is the linearized output matrix for the optical trap system given in section 5.1 and  $J \in \mathbb{R}^6$  is defined later.

2. For degree  $d \geq 2$ :

$$m^d(x) = f^d(x). \quad (6.16)$$

The higher order terms of the pseudo-measurements can be equated to the higher order terms of the system dynamics because the system dynamics is affine in the system nonlinearity that depends on the measured state. The higher order terms of the pseudo-measurements are considered to expand the operating range where the state estimation error exhibits linear dynamic behavior. The linear constraint in equation 6.15 exists and unique when the matrix  $A_x$  satisfies a nonresonant condition. The nonresonant condition is now given.

**Definition 3** (Nonresonant Condition). *Given the eigenvalues of  $F \in \mathbb{R}^{n \times n}$ ,  $\lambda(F) = (\lambda_1, \dots, \lambda_n)$ , and a nonnegative vector  $c = (c_1, \dots, c_n)$  whose elements are all not zero, then a complex number  $\mu$  is nonresonant with  $\lambda(F)$  if*

$$\mu \neq \sum_{i=1}^n c_i \lambda_i. \quad (6.17)$$

The nonresonant condition requires  $\lambda(F)$  (where  $F$  is defined in definition 3) does not contain zero in its convex hull. The vector  $c$  is nonnegative to ensure the real part of  $\mu$  has the same sign as  $\lambda(F)$ . Now, definition 3 is applied to equation 6.15. Equation 6.15 has a solution that exists and is unique when the matrix  $A_x$  is chosen such that each element of  $\lambda(A_x)$  is nonresonant with  $\lambda(A)$ .

Next, the term  $J$  is chosen to have  $A_x$  satisfy the nonresonant condition, ensure the pair  $(A, JC)$  is controllable, and minimize the mean-squared estimation error. It is easy to choose  $J$  to satisfy the nonresonant and controllability conditions; however, choosing  $J$  to minimize the mean-squared state estimation error also requires the consideration of the state estimation error dynamics in equation 6.8. The state estimation error dynamics are

simplified by substituting the state transformation  $p(x) = x$ , the matrix  $A_x = A - JC$ , and  $G(x)$  into equation 6.8 yields

$$\frac{d}{dt}\check{x} = (A - JC)\check{x} + B_w\tilde{w} + m(h(x)) - m(h(x) + \tilde{n}). \quad (6.18)$$

The state estimation error dynamics are driven by the process noise  $\tilde{w}$  and the measurement noise through the pseudo-measurement error  $m(h(x)) - m(h(x) + \tilde{n})$ . In this research, we are interested in minimizing the mean-squared estimation error locally about the expected value of the bead deflection (the measurement). The local effects of the measurement noise are determined by expanding the pseudo-measurement error  $m(h(x)) - m(h(x) + \tilde{n})$  in a first order Taylor series about  $y = h(x)$  to yield

$$m(h(x)) - m(h(x) + \tilde{n}) \approx -\frac{\partial m}{\partial y}(y)\tilde{n}. \quad (6.19)$$

The localized state estimation error dynamics are obtained by substituting equation 6.19 into equation 6.18 to yield

$$\frac{d}{dt}\check{x} = (A - JC)\check{x} + B_w\tilde{w} - \frac{\partial m}{\partial y}(y)\tilde{n}, \quad (6.20)$$

which has the same structure as the estimation error dynamics given in section 5.2. Equation 6.20 is considered the estimation error dynamics for the following linear system

$$\dot{x} = Ax + B_w\tilde{w}, \quad (6.21a)$$

$$y = Cx + \frac{\partial m}{\partial y}(y)\tilde{n}. \quad (6.21b)$$

The term  $J$  is an observer gain. The system in equation 6.21 is placed in a Kalman filter structure to find  $J$  that minimizes the mean-squared estimation error. The Kalman filter analysis is the same as given in section 5.2.

The final expressions for the matrix  $A_x$  and the pseudo-measurement  $m$  are

$$A_x = \begin{bmatrix} -\omega_t - j_1 g_s & -\kappa \omega_t & -g_v(\omega_{z_v} - \omega_{p_v}) & -g_v g_a \omega_z & -g_v g_a & 0 \\ -\omega_t - j_2 g_s & -\kappa \omega_t - \omega_m & 0 & 0 & 0 & \omega_m \\ -j_3 g_s & 0 & -\omega_{p_v} & g_a \omega_z & g_a & 0 \\ -j_4 g_s & 0 & 0 & 0 & 1 & 0 \\ -j_5 g_s & 0 & 0 & -\omega_{p_1} \omega_{p_2} & -\omega_{p_1} - \omega_{p_2} & 0 \\ -j_6 g_s & 0 & 0 & 0 & 0 & -\omega_d \end{bmatrix} \quad (6.22)$$

$$m(y) = \begin{bmatrix} j_1 y + \frac{\omega_t}{g_s} y - \frac{\omega_t}{g_s} y \exp\left(-\frac{y^2}{2g_s^2 l_t^2}\right) \\ j_2 y + \frac{\omega_t}{g_s} y - \frac{\omega_t}{g_s} y \exp\left(-\frac{y^2}{2g_s^2 l_t^2}\right) \\ j_3 y \\ j_4 y \\ j_5 y \\ j_6 y \end{bmatrix} \quad (6.23)$$

The Kalman filter provides a state estimate. It is insightful to assess the effectiveness that the Kalman filter has on the quality of the state estimate by quantifying the estimation bandwidth, estimation bias, and estimation variance. These statistical quantities are used to obtain information about the molecule characteristics. The molecule characteristics are determined by using the statistical properties of the state estimate to derive an expression for the SNR of the nominal molecular force.

## 6.2 STATISTICAL ANALYSIS ON NONLINEAR KALMAN FILTER

The effectiveness of the Kalman filter is assessed by quantifying the estimation bias, the estimation bandwidth, and the estimation variance. These statistical properties are then used to derive the an expression for the SNR of the nominal molecular force estimate.

These statistical properties depend on the operating conditions of the optical trap system. The operating conditions change when there is a change in the laser power or the molecule's end-to-end extension. The laser power is related to the optical stiffness  $k_t$ , which affects  $\omega_t =$

$k_t/\gamma$  and the linear operating range. An increase/decrease in the laser power results in an increase/decrease in the optical stiffness and the linear operating range. The molecule's end-to-end extension is related to the molecule's stiffness; an increase/decrease to the molecule's end-to-end distance results in an increase/decrease in the molecule's stiffness  $k_m$ . Thus, for each pair of  $k_t$  and  $k_m$  (or  $\kappa = k_m/k_t$ , the dimensionless stiffness), a Kalman filter is designed. Let us quantify the statistical properties for the different operating conditions using numerical methods.

**Estimation bias** The accuracy of the Kalman filter is quantified by studying the estimation bias at steady-state. The steady-state response of equation 6.12 converges to zero (no bias) if all the eigenvalues of  $A_x$  have negative real parts (or stable). All the eigenvalues of  $A_x = A - JC$  are stable as discussed in section 5.2.

**Estimation bandwidth** The estimation bandwidth provides how fast the Kalman filter produces the state estimate. It can be characterized by the slowest eigenvalue of the estimation error dynamics. The estimation bandwidth is shown in figure 34. The bandwidth increases with increasing  $\kappa$  and is independent of the value of  $k_t$ .

**Estimation Variance** The open-loop composite system (the combination of the optical trap system and the nonlinear Kalman filter) fluctuates at steady-state due to process noise (Brownian noise and molecule noise), and the measurement noise. Recall that the optical trap (same as in equation 4.37 but with no control) is

$$\dot{x} = f(x) + B_w \tilde{w},$$

and the nonlinear Kalman filter (same as in equation 6.2 but with no control) is

$$\dot{\hat{x}} = f(\hat{x}) + B_u u + G(\hat{x})[m(h(x) + \tilde{n}) - m(h(\hat{x}))].$$

The system fluctuations are simplified by using the fact that the noise inputs only drive the states describing the bead and the molecule; then assumption 3 is used to imply that measurement noise only affects the state estimates describing the bead and the molecule. In this research, the fluctuations are characterized by performing a linear noise analysis about the expected value at steady-state. The fluctuations are determined by first describing the

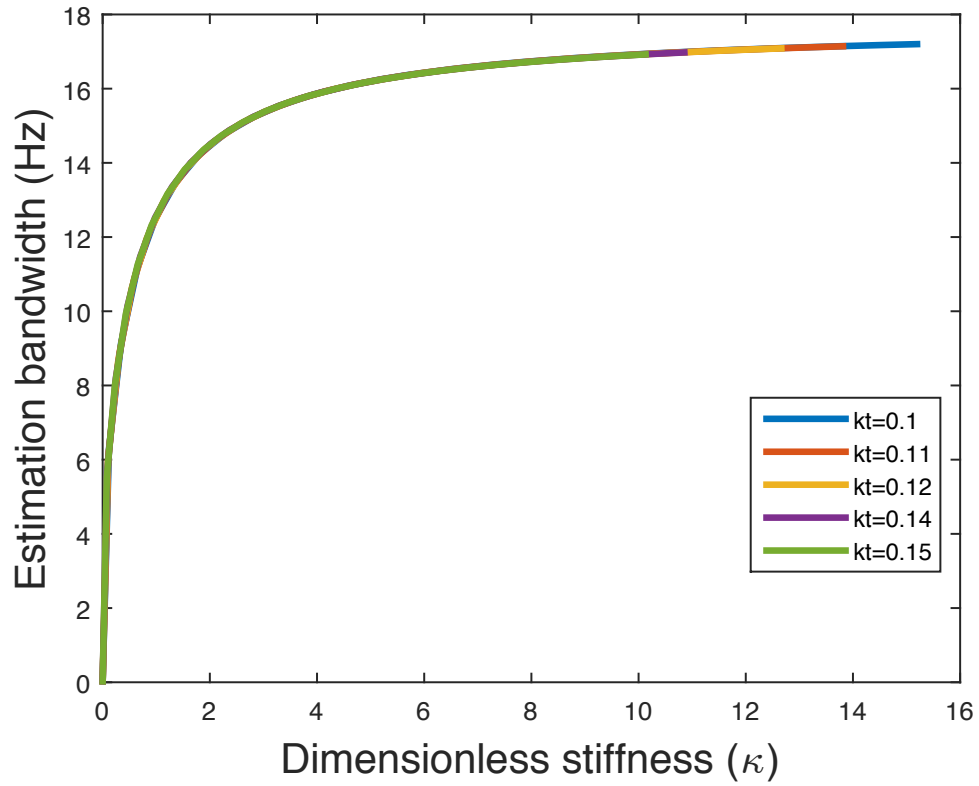


Figure 34: A schematic of the estimation bandwidth obtained using the nonlinear Kalman filter. The bandwidth increases with increasing  $\kappa$  and is independent of the value of  $k_t$ .

composite system and its expected value. The dynamics for the composite system  $x_c$  are described by

$$\dot{x}_o = f_o(x_o, \tilde{w}_o), \quad \text{with} \quad x_o = [z, d_m, \hat{z}, \hat{d}_m, \hat{d}_d]^T, \quad \text{and} \quad \tilde{w}_o = [\tilde{d}, \tilde{d}_m, \tilde{n}]^T, \quad (6.24)$$

and its expected value  $\bar{x}_o = E[x_o]$  has dynamics of

$$\dot{\bar{x}}_o = f_o(\bar{x}_o, 0). \quad (6.25)$$

The system fluctuations are described by the noise  $\tilde{x}_o = x_o - \bar{x}_o$  and its dynamics are

$$\dot{\tilde{x}}_o = f_o(\tilde{x}_o + \bar{x}_o, \tilde{w}_o) - f_o(\bar{x}_o, 0). \quad (6.26)$$

The linear noise analysis requires the linearization of equation 6.26. The linearization is performed by expressed the term  $f_o(\tilde{x}_o + \bar{x}_o, \tilde{w}_o)$  in a first-order Taylor series in two variables,

$$f_o(\tilde{x}_o + \bar{x}_o, \tilde{w}_o) \approx f_o(\bar{x}_o, 0) + \left. \frac{\partial f(x, y)}{\partial x} \right|_{x=\bar{x}_o, y=0} \tilde{x}_o + \left. \frac{\partial f(x, y)}{\partial y} \right|_{x=\bar{x}_o, y=0} \tilde{w}_o \quad (6.27a)$$

$$= f_o(\bar{x}_o, 0) + A_o \tilde{x}_o + B_o \tilde{w}_o \quad (6.27b)$$

with the matrices  $A_o$  and  $B_o$  being

$$A_o = \left. \frac{\partial f(x, y)}{\partial x} \right|_{x=\bar{x}_o, y=0} \quad \text{and} \quad B_o = \left. \frac{\partial f(x, y)}{\partial y} \right|_{x=\bar{x}_o, y=0}. \quad (6.28)$$

Substituting equation 6.27 into equation 6.26 yields

$$\dot{\tilde{x}}_o = A_o \tilde{x}_o + B_o \tilde{w}_o, \quad (6.29)$$

where

$$A_o = \begin{bmatrix} -\bar{\omega}_t & -\kappa\omega_t & 0 & 0 & 0 \\ -\bar{\omega}_t & -\kappa\omega_t - \omega_m & 0 & 0 & 0 \\ j_1g_s + \omega_t - \bar{\omega}_t & 0 & -\omega_t - j_1g_s & -\kappa\omega_t & 0 \\ j_2g_s + \omega_t - \bar{\omega}_t & 0 & -\omega_t - j_2g_s & -\kappa\omega_t - \omega_m & \omega_m \\ j_6g_s & 0 & -j_6g_s & 0 & -\omega_d \end{bmatrix} \quad (6.30a)$$

$$B_o = \begin{bmatrix} \omega_t & 0 & 0 \\ \omega_t & \omega_m & 0 \\ 0 & 0 & j_1 + \frac{1}{g_s}\omega_t - \frac{1}{g_s}\bar{\omega}_t \\ 0 & 0 & j_2 + \frac{1}{g_s}\omega_t - \frac{1}{g_s}\bar{\omega}_t \\ 0 & 0 & j_6 \end{bmatrix}, \quad (6.30b)$$

and  $\bar{\omega}_t = \omega_t \left(1 - \frac{\bar{z}^2}{l_o^2}\right) \exp\left(-\frac{\bar{z}^2}{l_o^2}\right)$ . The matrices  $A_o$  and  $B_o$  are features worth mentioning that are the result of the state observer. In the matrix  $A_o$ , the dynamics describing the fluctuations of the bead deflection and the molecule extension are affected by the bead deflection through  $\bar{\omega}_t$ . The value of  $\bar{\omega}_t$  decreases as the bead deflection increases (the molecule is extended). The dynamics describing the fluctuations of the estimated bead deflection and the estimated molecule extension are affected by the estimated bead deflection through  $\omega_t$  not  $\bar{\omega}_t$  such that  $\omega_t = \bar{\omega}_t$  when  $z = 0$  and  $\omega_t > \bar{\omega}_t$  when  $z > 0$ . Thus, as the bead deflection increases (the molecule is extended), the dynamics describing the fluctuations of the bead deflection and the molecule extension experience less effect of the bead deflection than that of their estimated dynamics due to the estimated bead deflection. In the matrix  $B_o$ , the dynamics for the fluctuations of the estimated bead deflection and the molecule extension are affected by the sensor noise through  $j_1 + \frac{1}{g_s}\omega_t - \frac{1}{g_s}\bar{\omega}_t$  and  $j_2 + \frac{1}{g_s}\omega_t - \frac{1}{g_s}\bar{\omega}_t$  respectively. The term  $\frac{1}{g_s}\omega_t - \frac{1}{g_s}\bar{\omega}_t$  increases with increasing bead deflection (molecule is extended), as shown in figure 35, and results in the estimated states experiencing a greater effect from the sensor noise. These features are inherent to the state observer because its correction term depends on the difference of nonlinear pseudo measurements to yield linear observer error dynamics.

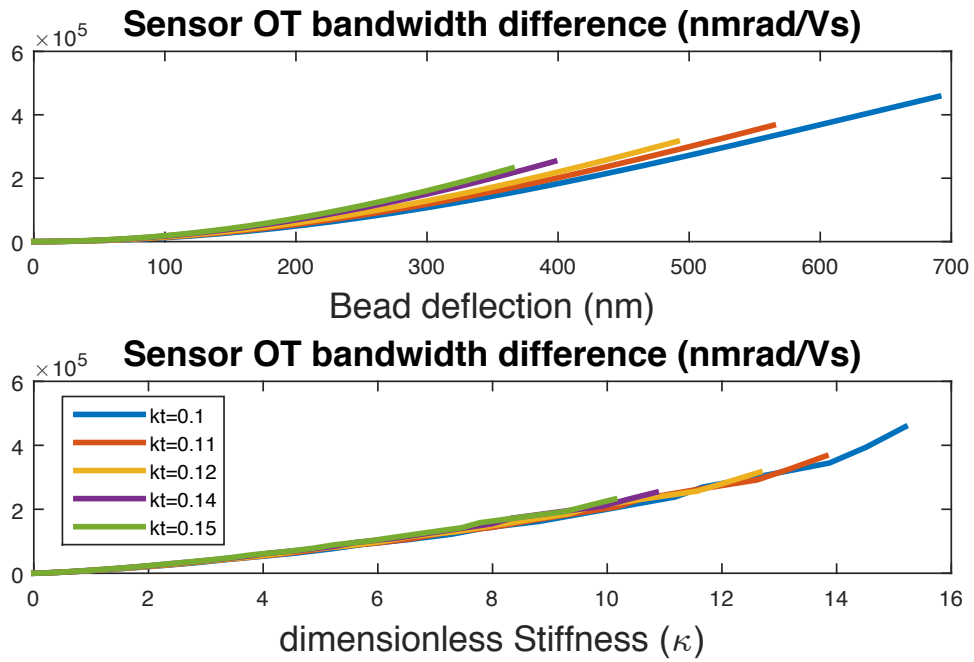


Figure 35: A schematic of the sensor gain optical bandwidth difference  $\frac{1}{g_s} (\omega_t - \bar{\omega}_t)$ . The optical bandwidth difference is the additional effect the sensor noise has on the estimated bead deflection and the estimated molecule extension as the bead deflection increases. The difference is the result of the nonlinear state observer because nonlinear pseudo measurements are used to yield linear observer error dynamics.

The state variances are characterized by the steady-state state covariance matrix  $X_o = E[\tilde{x}_o \tilde{x}_o^T]$ , which is the solution to the Lyapunov equation

$$A_o X_o + X_o A_o^T + B_o S_o B_o^T = 0 \quad \text{where} \quad S_o = \begin{bmatrix} S_d & 0 & 0 \\ 0 & S_m & 0 \\ 0 & 0 & S_n \end{bmatrix}. \quad (6.31)$$

The variance for the bead deflection and its estimate are shown in figure 36; the variance of the molecule extension and its estimate are shown in figure 38. For a given  $k_t$ , increasing  $\kappa$  (a stiffer molecule), the variance of the state decreases, while the variance for the state estimate increases. The variance decreases for the state because the molecule becomes stiffer as its extended and is able to suppress the fluctuations. The variance increases for the state estimate because the state estimate experiences a greater effect from the sensor noise as  $\kappa$  increases, and this effect is a feature of the state observer. The increase effect of the sensor noise on the state estimates in a feature of the state observer because a nonlinear pseudo measurements are used in the correction term to yield linear observer error dynamics. For a given  $\kappa$ , increasing  $k_t$  results in the variance decreases for the molecule extension and the estimated molecule extension. A stiffer optical trap has a larger linear operating range and able to help suppress the fluctuations. The variance of the estimated disturbance is shown in figure 24. For a given  $k_t$ , the variance of the estimated disturbance decreases as  $\kappa$  is increased (the molecule is extended), and the variance is independent of the value of  $k_t$ .

These statistical quantities effect the quality of the estimated force disturbance and their effect is quantified by studying its SNR.

**SNR For Molecule Force Estimate** The statistical quantities of the estimated force disturbance are proportional to that of the disturbance estimate because  $\hat{f}_d = k_m \hat{d}_d$ . At steady-state, the expected value for the estimated force disturbance is

$$E[\hat{f}_d] = k_m E[\hat{d}_d]. \quad (6.32)$$

The variance of the estimated force disturbance is described by

$$\text{Var}(\hat{f}_d) = k_m^2 \text{Var}(\hat{d}_d). \quad (6.33)$$

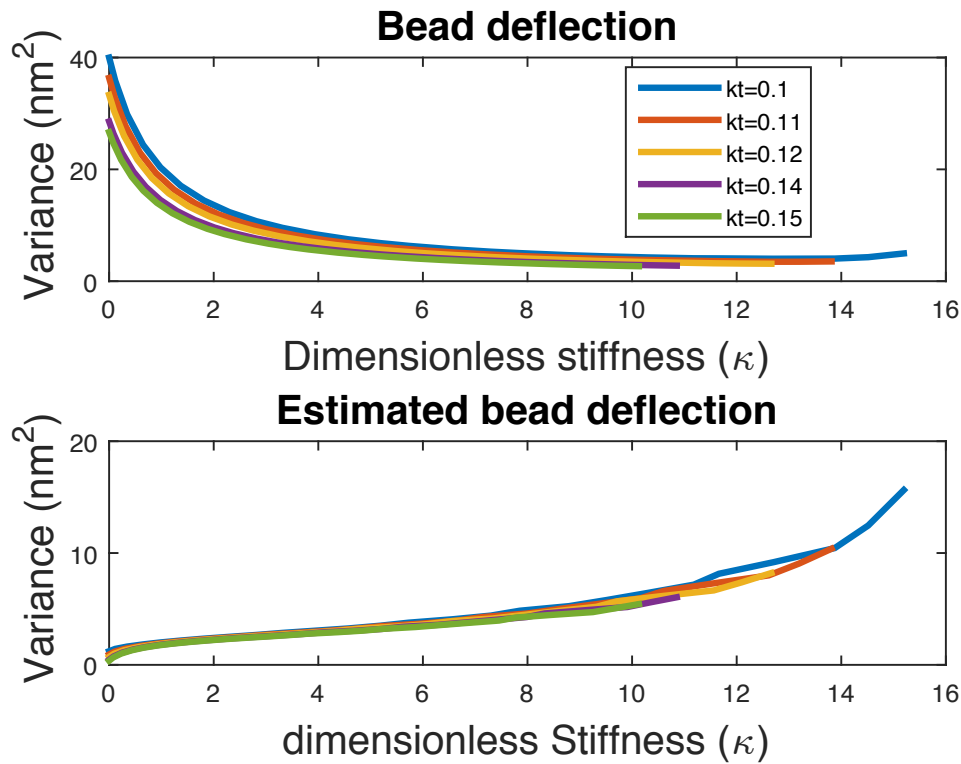


Figure 36: A schematic for the variance of the bead deflection and its estimate obtained using a nonlinear Kalman filter. For a given  $k_t$ , increasing  $\kappa$  (a stiffer molecule), the variance of the bead deflection decreases, while the variance for the estimated bead deflection increases. The variance decreases for the bead deflection because the molecule becomes stiffer as it is extended and able to suppress the fluctuations. The variance increases for the estimated bead deflection because the estimated bead deflection experiences a greater effect from the sensor noise as  $\kappa$  increases, and this effect is a feature of the state observer. For a given  $\kappa$ , increasing  $k_t$  results in the variance decreases for the bead deflection and the estimated bead deflection. A stiffer optical trap has a larger linear operating range and is able to help suppress the fluctuations.

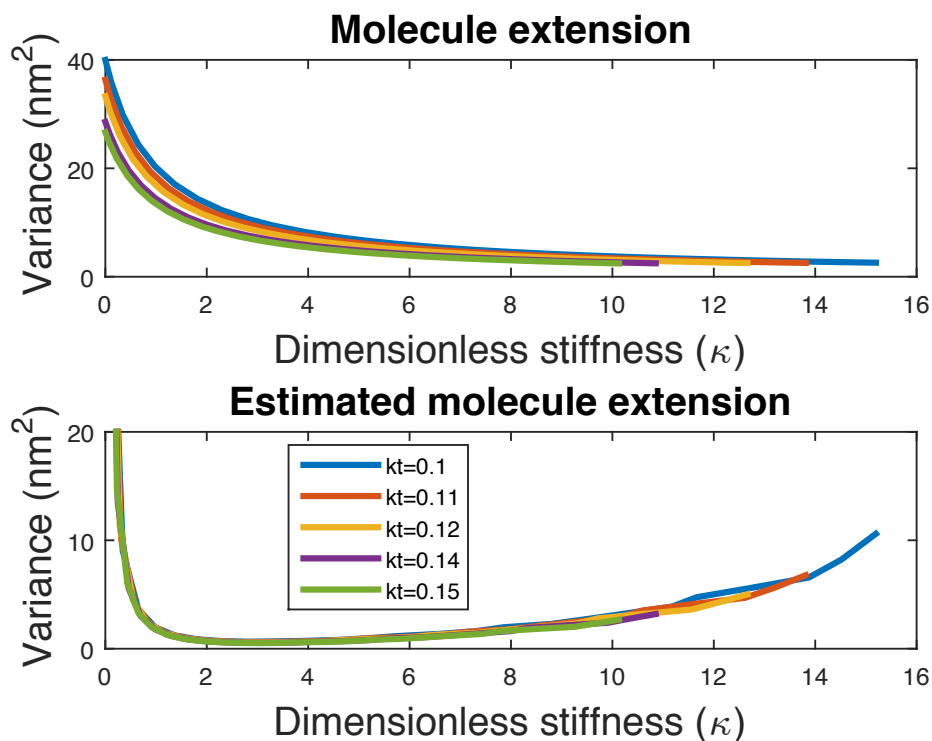


Figure 37: A schematic for the variance of the molecule extension and its estimate obtained using a nonlinear Kalman filter. For a given  $k_t$ , increasing  $\kappa$  (a stiffer molecule), the variance of the molecule extension decreases, while the variance for the estimated molecule extension increases. The variance decreases for the molecule extension because the molecule becomes stiffer as it is extended and is able to suppress the fluctuations. The variance increases for the estimated molecule extension because the estimated molecule extension experiences a greater effect from the sensor noise as  $\kappa$  increases, and this effect is a feature of the state observer. For a given  $\kappa$ , increasing  $k_t$  results in the variance decreases for the molecule extension and the estimated molecule extension. A stiffer optical trap has a larger linear operating range and is able to help suppress the fluctuations.

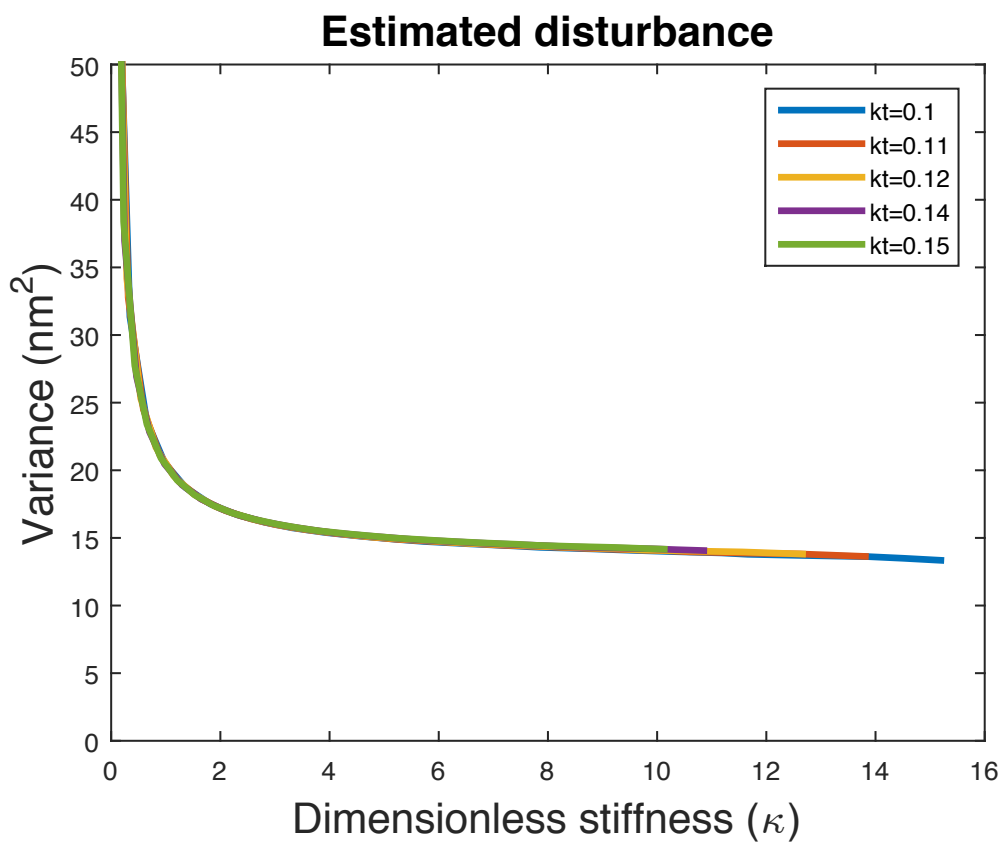


Figure 38: A schematic for the variance of the estimated disturbance obtained using a nonlinear Kalman filter. For a given  $k_t$ , the variance of the estimated disturbance decreases as  $\kappa$  is increased (the molecule is extended), and the variance is independent of the value of  $k_t$ .

The SNR for the estimated force disturbance is

$$\text{SNR} = \frac{1}{\sqrt{\text{Var}(\hat{f}_d)}} E[\hat{f}_d]. \quad (6.34)$$

Its value is numerically evaluated for each operating condition (each pair of  $k_t$  and  $\kappa$ ), as shown in figure 39. For a given  $k_t$ , increasing  $\kappa$  results in a decrease in the SNR; for a given  $\kappa$ , increasing  $k_t$  results in the SNR decreasing.

A second advantage to using a Luenberger observer is that the state estimate is used in a control structure to study the molecule characteristics. The state estimate is used in the control because the state estimate contains less noise and disturbance rejection is achieved.

### 6.3 CONTROL STRUCTURE

The molecule is studied by having the expected value of the bead deflection track a reference signal. The tracking control problem is turned into a regulation control problem with the new control objective being to design the control to drive the expected value of the tracking error to zero. Recall that the expected value of the tracking error  $\check{\xi}$  as defined in equation 4.62 is

$$\check{\xi}(x) = \xi_r - \xi(x) = \begin{bmatrix} r - h(x) \\ \dot{r} - L_f h(x) \end{bmatrix},$$

where  $r$  is the reference signal. The tracking error is driven to zero by a combination of an input-output feedback linearization with an LQ structure, as shown in the block diagram in figure 40. The control structure has two feedback loops: the linearization loop (loop 1) and the tracking loop (loop 2). The linearization loop transforms the optical trap system into normal form such that the input-output map is linearized via state feedback. The tracking loop uses the linearized input-output map in an LQ control algorithm to find the state feedback that drives the tracking error to zero.

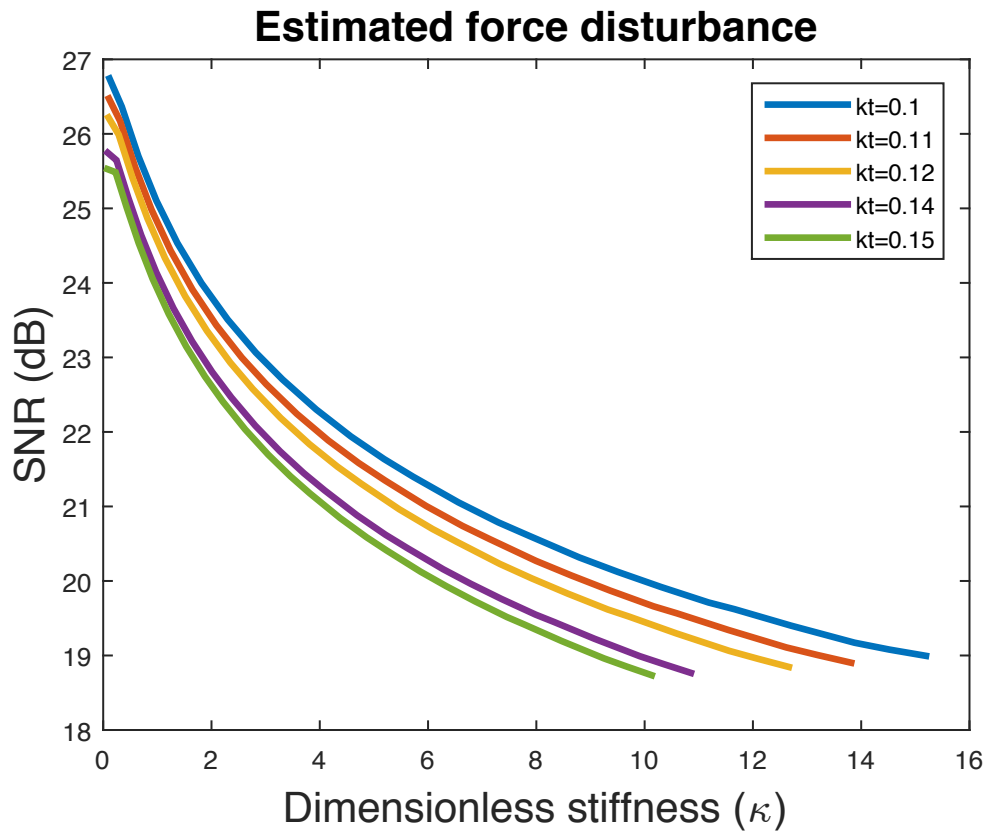


Figure 39: A schematic for the SNR of the estimated force disturbance obtained using the nonlinear Kalman filter. For a given  $k_t$ , increasing  $\kappa$  results in a decrease in the SNR; for a given  $\kappa$ , increasing  $k_t$  results in the SNR decreasing.

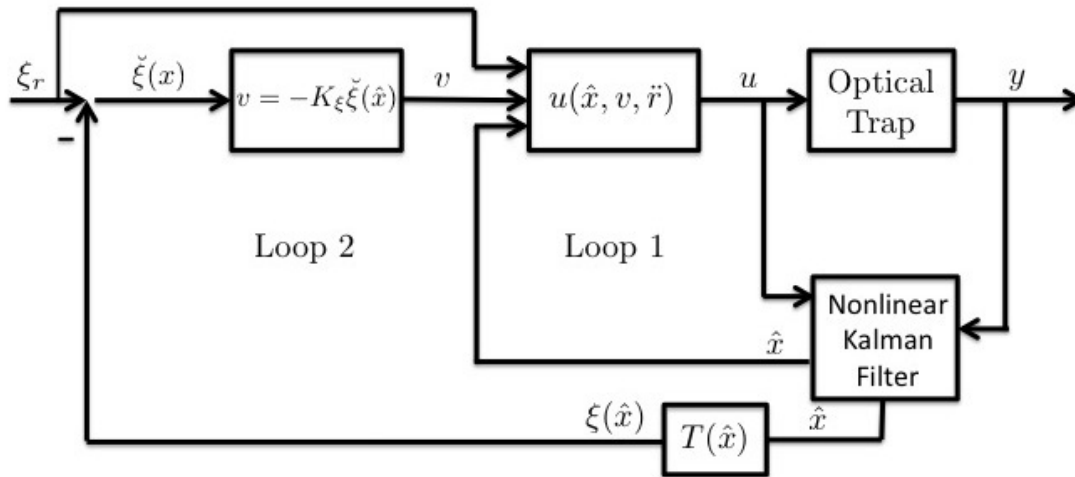


Figure 40: The schematic of the block diagram for the closed-loop system. The block diagram has two feedback loops. The linearization loop (loop 1) transforms the optical trap system into normal form such that the input-output map can be linearized using state feedback. The tracking loop (loop 2) uses the linearized input-output map in an LQ optimal algorithm to find the state feedback to drive the tracking error to zero.

The linearization feedback loop transforms the optical trap system with the tracking error as its output into normal form (according to the procedure given in section 4.5.1),

$$\frac{d}{dt}\check{\xi} = A_\xi\check{\xi}(x) + B_\xi [\ddot{r} - L_f^2 h(x) - L_{B_u} L_f h(x)u], \quad (6.35a)$$

$$\dot{\psi} = \delta(\xi_r - \check{\xi}(x), \psi). \quad (6.35b)$$

The normal form describes the input-output map between the control input  $u$  and the tracking error  $\check{\xi}$ . Choosing the state feedback to be

$$u(\hat{x}) = -\frac{1}{L_{B_u} L_f h(x)} [L_f^2 h(\hat{x}) - \ddot{r} + v], \quad (6.36)$$

with  $v$  being the auxiliary control input, linearizes the input-output map,

$$\frac{d}{dt}\check{\xi} = A_\xi\check{\xi}(x) + B_\xi v - B_\xi (L_f^2 h(x) - L_f^2 h(\hat{x})). \quad (6.37)$$

Equation 6.37 describes the nominal linearized input-output map  $\frac{d}{dt}\check{\xi} = A_\xi\check{\xi}(x) + B_\xi v$  being driven by the perturbation  $-B_\xi(L_f^2 h(x) - L_f^2 h(\hat{x}))$ . The perturbation  $-B_\xi(L_f^2 h(x) - L_f^2 h(\hat{x}))$  results from the pseudo estimation error in the input-output feedback due to the state estimation process.

The tracking loop uses the nominal linearized input-output map

$$\frac{d}{dt}\check{\xi} = A_\xi\check{\xi}(x) + B_\xi v$$

in an LQ control algorithm to find the state feedback  $v(\hat{x}) = -K_\xi\check{\xi}(\hat{x})$  (where  $K_\xi$  is the state feedback matrix) that drives the tracking error to zero. The LQ control problem is a minimization problem that is described by

$$\begin{aligned} \text{minimize } J &= \frac{1}{2} \int_0^\infty [\check{\xi}(x)^T Q_\xi \check{\xi}(x) + R_\xi v^2] d_T \text{ with } Q = \begin{bmatrix} q_1 & 0 \\ 0 & q_2 \end{bmatrix}, \\ \text{subject to } \frac{d}{dt}\check{\xi} &= A_\xi\check{\xi}(x) + B_\xi v, \end{aligned} \quad (6.38)$$

where  $Q_\xi = Q_\xi^T > 0$  is a weighted matrix placed on the tracking error and  $R > 0$  is the weight placed on the auxiliary control [109]. The functional  $J$  is minimized to find the state

feedback using the same method as discussed in section 5.4. Then, the algebraic Riccati equation and the auxiliary control are

$$A_\xi^T P_\xi + P_\xi A_\xi + Q_\xi - P_\xi B_\xi R_\xi^{-1} B_\xi^T P_\xi = 0, \quad (6.39)$$

$$v(\check{\xi}(x)) = -R_\xi^{-1} B_\xi^T P_\xi \check{\xi}(x) = -K_\xi \check{\xi}(x), \quad (6.40)$$

where  $K_\xi = R_\xi^{-1} B_\xi^T P_\xi = [k_1 \ k_2]^T$  is the state feedback gain. The implementation of the auxiliary control using the state estimate to yield

$$v(\check{\xi}(\hat{x})) = -R_\xi^{-1} B_\xi^T P_\xi \check{\xi}(\hat{x}) = -K_\xi \check{\xi}(\hat{x}), \quad (6.41)$$

The dynamics for the closed-loop tracking error is obtained by substituting equation 6.41 into equation 6.37, and adding and subtracting the term  $B_\xi v(\check{\xi}(x))$  to yield

$$\begin{aligned} \frac{d}{dt} \check{\xi} &= A_\xi \check{\xi}(x) + B_\xi (\check{\xi}(x)) - B_\xi \left( v(\check{\xi}(x)) - v(\check{\xi}(\hat{x})) \right) - B_\xi \left( L_f^2 h(x) - L_f^2 h(\hat{x}) \right), \\ &= \left( A_\xi - B_\xi R_\xi^{-1} B_\xi^T P_\xi \right) \check{\xi}(x) + B_\xi R_\xi^{-1} B_\xi^T P_\xi \left( \check{\xi}(x) - \check{\xi}(\hat{x}) \right) - B_\xi \left( L_f^2 h(x) - L_f^2 h(\hat{x}) \right). \end{aligned} \quad (6.42)$$

Equation 6.42 describes the nominal closed-loop tracking error dynamics

$\frac{d}{dt} \check{\xi} = (A_\xi - B_\xi R_\xi^{-1} B_\xi^T P_\xi) \check{\xi}(x)$  being driven by two perturbations. The first perturbation  $-B_\xi (L_f^2 h(x) - L_f^2 h(\hat{x}))$  results from the pseudo estimation error in the input-output feedback due to the state estimation process; the second perturbation  $B_\xi R_\xi^{-1} B_\xi^T P_\xi (\check{\xi}(x) - \check{\xi}(\hat{x}))$  results from the pseudo estimation error of the tracking error definition due to the state estimation process.

It is insightful to assess the effectiveness the control has on the closed-loop system by quantifying the state bias and state variance of the composite system.

## 6.4 STATISTICAL ANALYSIS ON NONLINEAR CONTROL

The dynamics for the closed-loop composite system is composed of:

1. The closed-loop tracking error in equation 6.42,

$$\begin{aligned} \frac{d}{dt}\check{\xi} = & \left( A_\xi - B_\xi R_\xi^{-1} B_\xi^T P_\xi \right) \check{\xi}(x) + B_\xi R_\xi^{-1} B_\xi^T P_\xi \left( \check{\xi}(x) - \check{\xi}(\hat{x}) \right) \\ & - B_\xi \left( L_f^2 h(x) - L_f^2 h(\hat{x}) \right). \end{aligned}$$

2. The internal states in equation 6.35,

$$\dot{\psi} = \delta(\xi_r - \check{\xi}(x), \psi).$$

3. The closed-loop estimation error in equation 6.18,

$$\frac{d}{dt}\check{x} = (A - JC)\check{x} + B_w \tilde{w} + m(h(x)) - m(h(\hat{x}) + \tilde{n}).$$

**Closed-loop bias** A Lyapunov stability analysis is performed to quantify the bias of the expected value of the closed-loop composite system. The expected value for the closed-loop system is described by:

1. The expected value for the dynamics of the closed-loop tracking error is obtained by taking the expected value of equation 6.42,

$$\begin{aligned} \frac{d}{dt}\check{\xi}(\bar{x}) = & \left( A_\xi - B_\xi R_\xi^{-1} B_\xi^T P_\xi \right) \check{\xi}(\bar{x}) + B_\xi R_\xi^{-1} B_\xi^T P_\xi \left( \check{\xi}(\bar{x}) - \check{\xi}(\hat{\bar{x}}) \right) \\ & - B_\xi \left( L_f^2 h(\bar{x}) - L_f^2 h(\hat{\bar{x}}) \right). \end{aligned} \tag{6.43}$$

2. The expected value for the dynamics of the internal states is obtained by taking the expected value of equation 6.35,

$$\frac{d}{dt}\bar{\psi} = \delta(\xi_r - \check{\xi}(\bar{x}), \bar{\psi}). \tag{6.44}$$

3. The expected value for the dynamics of the estimation error is obtained by taking the expected value of equation 6.18,

$$\frac{d}{dt}\bar{\check{x}} = (A - JC)\bar{\check{x}}. \tag{6.45}$$

The following assumptions are used:

**Assumption 6.** *The tracking error is Lipschitz. The Lipschitz condition implies there exists a positive constant  $l_1$  such that*

$$\left| \left| \check{\xi}(\bar{x}) - \check{\xi}(\hat{x}) \right| \right| \leq l_1 \|\check{x}\|. \quad (6.46)$$

**Assumption 7.** *The Lie derivative is Lipschitz. The Lipschitz condition implies there exists a positive constant  $l_2$  such that*

$$\left| \left| L_f^2(\bar{x}) - L_f^2 h(\hat{x}) \right| \right| \leq l_2 \|\check{x}\|, \quad (6.47)$$

**Assumption 8.** *Assuming the matrix  $A - JC$  is Hurwitz and a matrix  $Q_x$  is a positive definite and symmetric, then there exists a positive and definite matrix  $P_x$  satisfying the Lyapunov equation*

$$(A - JC)^T P_x + P_x (A - JC) = -Q_x. \quad (6.48)$$

**Theorem 3.** *Assume there are positive constants  $b_3$ ,  $b_4$ ,  $b_5$  and  $b_6$ . When these constants satisfy*

$$b_6 = \min\{b_3 - b_5, b_3 - b_5\},$$

*the closed-loop composite system yields exponential stability for the expected value of the tracking error and the state estimation error. The exponential stability implies there is no bias in either the tracking error or the state estimation error. The boundedness of the tracking error and the reference signal vector implies the internal states are bounded by BIBO stability according to theorem 1.*

*Proof.* The proof is essentially the same as Theorem 2. □

**Control State Variance** The closed-loop composite system (the combination of the optical trap system, the nonlinear Kalman filter, and the controller) fluctuates at steady-state due to process noise (Brownian noise and molecule noise), and the measurement noise. Recall that the optical trap (same as in equation 4.37) is

$$\dot{x} = f(x) + B_u u + B_w \tilde{w},$$

the nonlinear Kalman filter (same as in equation 6.2) is

$$\dot{\hat{x}} = f(\hat{x}) + B_u u + G(\hat{x})[m(h(x) + \tilde{n} - m(h(\hat{x}))),$$

and the controller (the combination of equation 6.36 and equation 6.41) is

$$u(\hat{x}) = -\frac{1}{L_{B_u} L_f h(\hat{x})} [L_f^2 h(\hat{x}) + k_1 h(\hat{x}) + k_2 L_f h(\hat{x}) - k_1 r - k_2 \dot{r} - \ddot{r}].$$

The system fluctuations are simplified by using the fact that the noise inputs only drive the states describing the bead and the molecule; then assumption 3 is used to imply that measurement noise only affects the state estimates describing the bead and the molecule. The control signal is considered by including the actuator state whose dynamics explicitly depends on the control signal. In this research, the fluctuations are characterized by performing a linear noise analysis about the expected value at steady-state. The fluctuations are determined by first describing the composite system and its expected value. The dynamics for the composite system  $x_c$  are described by

$$\dot{x}_c = f_c(x_c, \tilde{w}_c), \quad \text{with} \quad x_c = [z, d_m, a_3, \hat{z}, \hat{d}_m, \hat{a}_3, \hat{d}_d]^T, \quad \text{and} \quad \tilde{w}_c = [\tilde{d}, \tilde{d}_m, \tilde{n}]^T, \quad (6.49)$$

and its expected value  $\bar{x}_c = E[x_c]$  has dynamics of

$$\dot{\bar{x}}_c = f_c(\bar{x}_c, 0). \quad (6.50)$$

The system fluctuations are described by the noise  $\tilde{x}_c = x_c - \bar{x}_c$  and its dynamics are

$$\dot{\tilde{x}}_c = f_c(\tilde{x}_c + \bar{x}_c, \tilde{w}_c) - f_c(\bar{x}_c, 0). \quad (6.51)$$

The linear noise analysis requires the linearization of equation 6.51. The linearization is performed by expressed the term  $f_c(\tilde{x}_c + \bar{x}_c, \tilde{w})$  in a first-order Taylor series in two variables,

$$f_c(\tilde{x}_c + \bar{x}_c, \tilde{w}_c) \approx f_c(\bar{x}_c, 0) + \left. \frac{\partial f(x, y)}{\partial x} \right|_{x=\bar{x}_c, y=0} \tilde{x}_c + \left. \frac{\partial f(x, y)}{\partial y} \right|_{x=\bar{x}_c, y=0} \tilde{w}_c \quad (6.52a)$$

$$= f_c(\bar{x}_c, 0) + A_c \tilde{x}_c + B_c \tilde{w}_c \quad (6.52b)$$

with the matrices  $A_c$  and  $B_c$  being

$$A_c = \left. \frac{\partial f(x, y)}{\partial x} \right|_{x=\bar{x}_c, y=0} \quad \text{and} \quad B_c = \left. \frac{\partial f(x, y)}{\partial y} \right|_{x=\bar{x}_c, y=0}. \quad (6.53)$$

Substituting equation 6.52 into equation 6.51 yields

$$\dot{\tilde{x}}_c = A_c \tilde{x}_c + B_c \tilde{w}_c. \quad (6.54)$$

The state variances are characterized by the steady-state state covariance matrix  $X_c = E[\tilde{x}_c \tilde{x}_c^T]$ , which is the solution to the Lyapunov equation

$$A_c X_c + X_c A_c^T + B_c S_c B_c^T = 0 \quad \text{where} \quad S_c = \begin{bmatrix} S_d & 0 & 0 \\ 0 & S_m & 0 \\ 0 & 0 & S_n \end{bmatrix}. \quad (6.55)$$

The variance for the bead deflection and its estimate are shown in figure 41; the variance of the molecule extension and its estimate are shown in figure 42. For a given  $k_t$ , increasing  $\kappa$  (a stiffer molecule), the variance of the state decreases, while the variance for the state estimate increases. The variance decreases for the state because the molecule becomes stiffer as its extended and is able to suppress the fluctuations. The variance increases for the state estimate because the state estimate experiences a greater effect from the sensor noise as  $\kappa$  increases, and this effect is a feature of the state observer. The increase effect of the sensor noise on the state estimates in a feature of the state observer because a nonlinear pseudo measurements are used in the correction term to yield linear observer error dynamics. For a given  $\kappa$ , increasing  $k_t$  results in the variance decreases for the molecule extension and the estimated molecule extension. A stiffer optical trap has a larger linear operating range and able to help suppress the fluctuations. The control reduces the variance of the estimated state when compared to that of the open-loop case.

The nominal nonlinear controller yields satisfactory closed-loop performance and estimates of the molecule characteristics. It is insightful to compare the statistical properties of the nominal nonlinear control to the statistical properties of another nonlinear controller used in practice. The nonlinear controller chosen is a nonlinear PI controller [49].

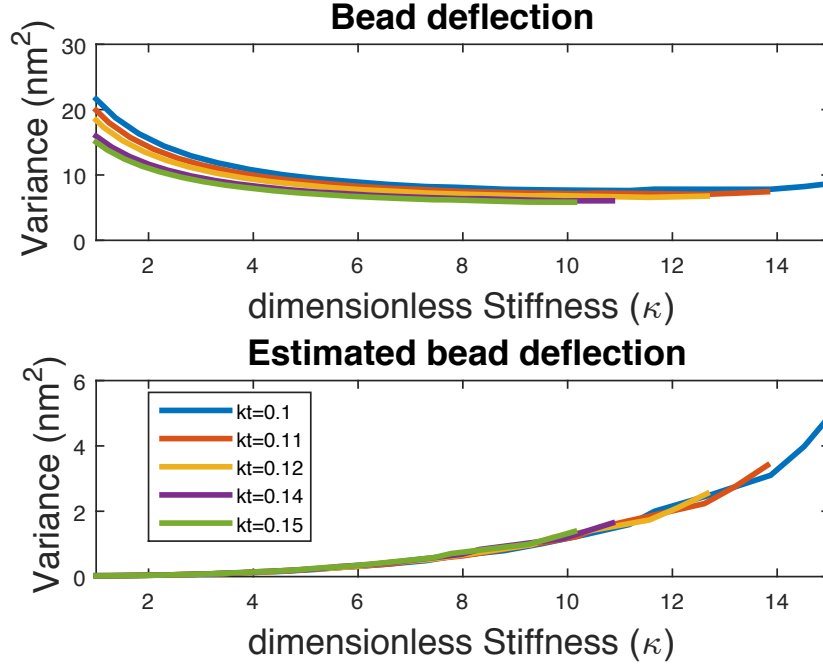


Figure 41: A schematic for the variance of the bead deflection and its estimate obtained using the closed-loop nominal nonlinear design. For a given  $k_t$ , increasing  $\kappa$  (a stiffer molecule), the variance of the bead deflection decreases, while the variance for the estimated bead deflection increases. The variance decreases for the bead deflection because the molecule becomes stiffer as its extended and able to suppress the fluctuations. The variance increases for the estimated bead deflection because the estimated bead deflection experiences a greater effect from the sensor noise as  $\kappa$  increases, and this effect is a feature of the state observer. For a given  $\kappa$ , increasing  $k_t$  results in the variance decreases for the bead deflection and the estimated bead deflection. A stiffer optical trap has a larger linear operating range and able to help suppress the fluctuations. The control reduces the variance of the estimated state when compared to that of the open-loop case.

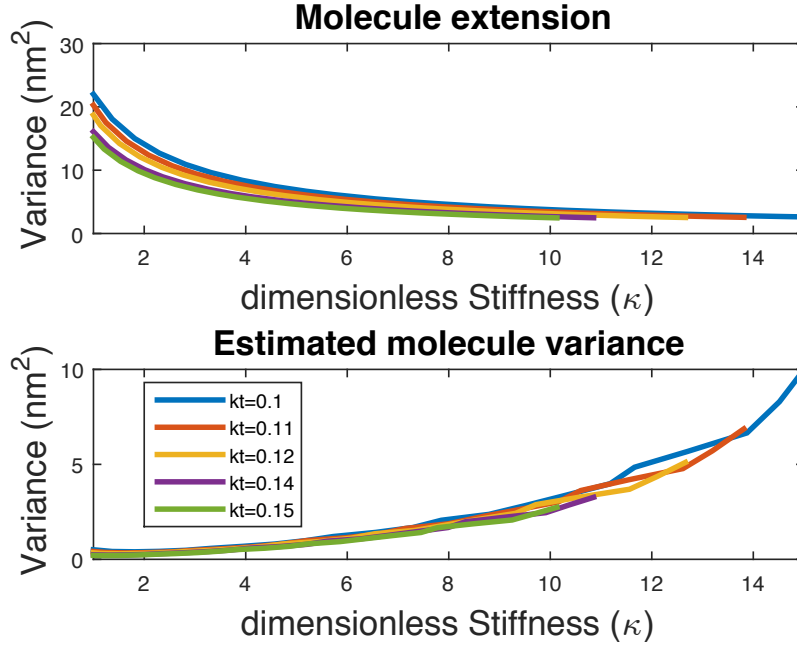


Figure 42: A schematic for the variance of the molecule extension and its estimate obtained using the closed-loop nominal nonlinear design. For a given  $k_t$ , increasing  $\kappa$  (a stiffer molecule), the variance of the molecule extension decreases, while the variance for the estimated molecule extension increases. The variance decreases for the molecule extension because the molecule becomes stiffer as its extended and is able to suppress the fluctuations. The variance increases for the estimated molecule extension because the estimated molecule extension experiences a greater effect from the sensor noise as  $\kappa$  increases, and this effect is a feature of the state observer. For a given  $\kappa$ , increasing  $k_t$  results in the variance decreases for the molecule extension and the estimated molecule extension. A stiffer optical trap has a larger linear operating range and able to help suppress the fluctuations. The control reduces the variance of the estimated state when compared to that of the open-loop case.

## 6.5 NONLINEAR PI CONTROLLER

The nonlinear PI is designed for a simplified version of the optical trap system to be consistent with the literature. The simplified dynamics ignores the actuator, sensor, and the molecule. Then, the simplified optical trap system consists only of the bead deflection that is driven by Brownian noise and a molecule force. The dynamics for the bead deflection are (the dynamics are similar to the dynamics given in equation 4.6)

$$\dot{z} = \frac{1}{\eta} f_t(z) - u - \frac{1}{\eta} f_m + \frac{1}{\eta} \tilde{f} \quad (6.56)$$

where  $u$  is the trap's velocity (control signal). The control objective is to manipulate the trap's velocity to have the bead deflection track a reference signal. The control design is based on the architecture presented in [112]. The nonlinear PI controller has the following criteria:

1. The controller is first order to limit controller complexity and to facilitate design. The criteria is achieved by choosing two feedback gains and results in the closed-loop system being second order.
2. The controller possess integral action. Integral action is necessary to drive the tracking error to zero at steady-state.
3. The system dynamics in equation 6.56 are input-to-state feedback linearizable to yield linear closed-loop dynamics. A linear closed-loop system is easier to quantify performance metrics.

The control criteria is satisfied with the following controller,

$$\frac{d}{dt} \hat{z} = k_1(z_r - z), \quad (6.57a)$$

$$u = -k_1(z_r - z) - k_2(\hat{z} - z) + \frac{1}{\eta} f_t(z), \quad (6.57b)$$

with the feedback gains being  $k_1$  and  $k_2$ , and the reference signal being  $z_r$ . Substituting the controller in equation 6.57 into equation 6.56 yields the closed-loop dynamics

$$\frac{d}{dt} \begin{bmatrix} z \\ \hat{z} \end{bmatrix} = \begin{bmatrix} -(k_1 + k_2) & k_2 \\ -k_1 & 0 \end{bmatrix} \begin{bmatrix} z \\ \hat{z} \end{bmatrix} + \begin{bmatrix} k_1 \\ k_1 \end{bmatrix} z_r - \begin{bmatrix} \frac{1}{\eta} \\ 0 \end{bmatrix} f_m + \begin{bmatrix} \frac{1}{\eta} \\ 0 \end{bmatrix} \tilde{f} \quad (6.58)$$

The closed-loop system has second-order linear dynamics that is characterized by the characteristic equation

$$s^2 + (k_1 + k_2)s + k_1k_2 = 0, \quad (6.59)$$

and the eigenvalues are  $\lambda_{1,2} = \{-k_1, -k_2\}$ . Thus, the closed-loop system is characterized by the two time constants,  $\tau_1 = \frac{1}{k_1}$  and  $\tau_2 = \frac{1}{k_2}$ .

The closed-loop behavior of  $\hat{z}$  is studied when the exogenous forces are zero,  $f_m = \tilde{f} = 0$ , and defining the estimation error  $z - \hat{z}$ . The dynamics for the estimation error is

$$\frac{d}{dt}(z - \hat{z}) = -k_2(z - \hat{z}), \quad (6.60)$$

which implies that  $\hat{z}$  approaches  $z$  with time constant  $\tau_2$ . The control law has  $\hat{z}$  track  $z$  so that the closed-loop dynamics are linear and first order. For  $t \gg \tau_2$ ,  $\hat{z} \approx z$ , the closed-loop dynamics for the bead deflection is

$$\frac{d}{dt}z = k_1(z_r - z) \quad \text{for } t \gg \tau_2, \quad (6.61)$$

which has  $z$  track  $z_r$  with the time constant  $\tau_1$ . Notice that equation 6.61 has the same dynamics as  $\hat{z}$  that is given in equation 6.57. Comparing the dynamics in equation 6.61 and equation 6.57, shows that once the estimator  $\hat{z}$  reaches steady-state,  $\hat{z}$  represents a precalculated estimate of  $z$  in closed-loop.

Next, the dynamics for the closed-loop system is studied when considering  $f_m$  and  $\tilde{f}$ . For sufficiently long time  $t \gg \tau_2$ , the expected value of the steady-state response is

$$E[z] = z_r, \quad (6.62)$$

$$E[\hat{z}] = z_r + \frac{1}{\eta k_2} E[f_m]. \quad (6.63)$$

The controller has  $z$  track  $z_r$ , and  $z$  experiences no effect from the molecule force. Disturbance rejection is one of the advantages to using integral control. In addition, we see that  $E[\hat{z}]$  depends on  $E[f_m]$ , then this map allows use to use  $\hat{z}$  to estimate the molecule force

$$\hat{f}_m = \eta k_2(\hat{z} - z_r). \quad (6.64)$$

The results in equation 6.63 shows that

$$E[\hat{f}_m] = \eta k_2 (E[\hat{z}] - z_r) = E[f_m], \quad (6.65)$$

which makes this an unbiased estimate of the molecule force.

The force estimate  $\hat{f}_m$  fluctuates about its expected value due to Brownian noise acting on the system. These fluctuations are characterized by its variance

$$\text{Var}(\hat{f}_m) = (\eta k_2)^2 \text{Var}(\hat{z}). \quad (6.66)$$

The variance  $\text{Var}(\hat{z})$  is found by performing a linear noise analysis on the linear closed-loop dynamics when  $z_r = 0$  and  $f_m = 0$ , so that the closed-loop system is only driven by Brownian noise. The Brownian noise is modeled by zero mean Gaussian white noise with a spectral density of  $S_f = 2\gamma k_B T$ . The state variances of the closed-loop system are characterized by the steady-state covariance matrix  $X$ , which is the solution to the Lyapunov equation

$$AX + XA^T + BB^T S_f = 0, \quad (6.67)$$

where

$$A = \begin{bmatrix} -(k_1 + k_2) & k_2 \\ -k_1 & 0 \end{bmatrix}, \quad B = \begin{bmatrix} -\frac{1}{\eta} \\ 0 \end{bmatrix}, \quad X = \begin{bmatrix} \text{Var}(z) & \text{Cov}(z, \hat{z}) \\ \text{Cov}(z, \hat{z}) & \text{Var}(\hat{z}) \end{bmatrix}. \quad (6.68)$$

The state variances are

$$\text{Var}(z) = \frac{1}{k_1 + k_2} \left( \frac{k_B T}{\eta} \right), \quad \text{Var}(\hat{z}) = \frac{k_1}{k_2(k_1 + k_2)} \left( \frac{k_B T}{\eta} \right), \quad \text{Cov}(z, \hat{z}) = 0. \quad (6.69)$$

Then, the variance for the force estimate is

$$\text{Var}(f_m) = (\eta k_2)^2 \text{Var}(\hat{z}) = \frac{k_1 k_2}{k_1 + k_2} \eta k_B T \approx k_1 \eta k_B T, \quad (6.70)$$

with the approximation being valid for  $k_1 \ll k_2$ . When the approximation holds, the variance  $\text{Var}(f_{est})$  is proportional to  $k_1$ . The effect of decreasing  $k_1$  to decrease the variance has a similar effect of applying a low-pass filter and reducing its bandwidth. However, the advantage to using feedback control is the additional ability of controlling the bead deflection to track a reference signal. Since bead deflections are related to optical forces, we have precise control over the forces applied to single-molecules. Note that the variance is constant

throughout the operating range of the optical trap. The constant variance is from the system dynamics being input-to-state feedback linearizable with state feedback to yield linear closed-loop dynamics.

The SNR for the force estimate is

$$\text{SNR} = \frac{1}{\sqrt{\text{Var}(\hat{f}_m)}} E[\hat{f}_m] = \frac{E[\hat{f}_m]}{\sqrt{\eta k_B T}} \left( \frac{1}{k_1} + \frac{1}{k_2} \right)^{1/2} \approx \frac{E[\hat{f}_m]}{\sqrt{k_1 \eta k_B T}}. \quad (6.71)$$

When ensuring  $k_1 \ll k_2$ , the SNR is proportional to  $k_1^{-1/2}$  and  $E[\hat{f}_m]$ . A decrease in  $k_1$  results in an increase of the SNR and a decrease in the time constant  $\tau_1$ . The SNR increases as  $E[\hat{f}_m]$  increases (equivalent to the molecule being further stretched).

## 7.0 ADAPTIVE NONLINEAR DESIGN

Model based feedback methods yield satisfactory closed-loop performance for the estimation and control problem when the feedback methods are based on exact model knowledge. Exact model knowledge is a bad assumption because of parameter uncertainty. In optical trap studies, parameter uncertainty occurs due to the medium's viscosity changing per experiment. The viscosity affects other parameters because many calibration methods use Stokes drag as a reference force [28]. Parameter uncertainty introduces robustness effects into the estimation and control problems when using feedback methods based on exact model knowledge. In addition, the operating condition changes per experiment because the laser power can be changed and the molecule becomes stiffer as it is stretched. A consequence is that users are spending an enormous amount of time during instrument calibration and control design, causing the users to divert their time away from the biophysics. As a result, there is a need and interest to create an automated optical trap that can perform parameter identification and control the bead deflection. The need is addressed by using adaptive feedback methods to solve the estimation and control problems. The estimation problem is addressed with an adaptive Luenberger type state observer to simultaneously provide a state and parameter estimate when a persistent exciting condition is satisfied. The state and parameter estimates are then used in an adaptive feedback linearization and LQ structure to find the optimal state feedback gains for each experiment. The result is an automated self-tuning optical trap that can probe molecules to obtain information about their characteristics.

This chapter discusses the system parameters that can change, the robustness effects being quantified from implementing the nominal nonlinear controller on the perturbed estimation and the control problems, and finally the design and analysis of the adaptive nonlinear design.

## 7.1 ROBUSTNESS CHARACTERISTICS OF NOMINAL DESIGN

Parameter uncertainty introduces robustness effects into the estimation and the control problems. The robustness effects are quantified by:

1. first determining the system parameters that can change,
2. expressing the optical trap system in terms of the parameter uncertainty to define the perturbed optical trap system,
3. implementing the nominal nonlinear design on the perturbed optical trap system to quantify its closed-loop performance.

In this research, the following parameters can change per experiment, the optical stiffness and the dimensionless stiffness (the molecule stiffness). The optical stiffness changes accordingly to the laser power setting. An increase/decrease in the laser power results in an increase/decrease in the laser power. The molecule becomes stiffer as it is stretched. Then, for a given optical stiffness, the dimensionless stiffness increases as the molecule is stretched. The optical trap system contains the product of these parameters; it is convenient to consider the product as one parameter. The true parameter is  $\theta = [\omega_t, \kappa\omega_t]^T$ , and is defined as

$$\theta = \bar{\theta} + \tilde{\theta}, \quad (7.1)$$

where  $\bar{\theta}$  is the nominal parameter value and  $\tilde{\theta}$  is the parameter perturbation (noise) about the nominal value.

The optical trap system is expressed in terms of the true parameter to form the perturbed optical trap system. First, recall the expression for the optical trap system (same as given in equation 4.37 but expressed explicitly in the nominal parameter)

$$\dot{x} = f(x, \bar{\theta}) + B_u u + B_w \tilde{w}.$$

Then, substituting the true parameter into the optical trap system yields the perturbed optical trap system,

$$\dot{x} = f(x, \bar{\theta}) + f_1(x)\tilde{\theta} + B_u u + B_w w. \quad (7.2)$$

The parameter perturbation is expressed in linear parametric form. The vector fields  $f : \mathbb{R}^{6 \times 2} \rightarrow \mathbb{R}^6$  and  $f_1 : \mathbb{R}^2 \rightarrow \mathbb{R}^6$  describes the nominal system dynamics and the regression vector respectively.

Next, the robustness effects on the closed-loop perturbed optical trap system are quantified by implementing the nominal nonlinear design on equation 7.2.

**Estimation problem:** The robustness effects are quantified by implementing the nonlinear Kalman filter as discussed in section 6.1. It is straightforward to show that the expected value for the estimation error dynamics is

$$\frac{d}{dt}E[\check{x}] = A_x E[\check{x}] + f_1(\bar{x})\tilde{\theta}, \quad (7.3)$$

which results in a steady-state estimation bias,

$$E[\check{x}] = -A_x^{-1} f_1(\bar{x})\tilde{\theta}. \quad (7.4)$$

The estimation bias has two effects: the first effect is the state estimate now contains inaccurate information about the molecule characteristics; the second effect is the estimation bias propagates through the closed-loop system because the state estimate is used in state feedback.

**Control problem:** The robustness effects are quantified by implementing the input-output feedback linearization and LQ structure as discussed in section 6.3. The analysis assumes the state  $x$  is available (all states are measurable) to separate the robustness effects due to the control implementation from the robustness effects due to the propagation of the estimation bias.

First, the perturbed optical trap system with the tracking error as its output is transformed into normal form (according to the procedure given in section 4.5.1)

$$\begin{aligned} \check{\xi} = & A_\xi \check{\xi} + B_\xi \left[ \ddot{r} - L_f^2 h(x) - L_{B_u} L_f h(x) u \right] \\ & - B_\xi \left[ L_{f_1 \tilde{\theta}} L_f h(x) + L_f L_{f_1 \tilde{\theta}} h(x) + L_{f_1 \tilde{\theta}}^2 h(x) + L_{B_u} L_{f_1 \tilde{\theta}} h(x) u \right] \end{aligned} \quad (7.5)$$

Equation 7.5 describes the input-output map between the control input  $u$  and the tracking error  $\check{\xi}$ . The input-output map has three terms on the right hand side. The first two

terms represent the nominal input-output map (equivalent input-output map when using the nominal parameters); the third term is the perturbation due to parameter uncertainty.

The input-output map in equation 7.5 is linearized with state feedback (same as given in equation 6.36 but with actual states)

$$u(x) = -\frac{1}{L_{B_u}L_f h(x)} \left[ L_f^2 h(x) - \ddot{r} - K_\xi \check{\xi} \right]$$

to yield

$$\begin{aligned} \dot{\check{\xi}} = & (A_\xi - B_\xi K_\xi) \check{\xi} - B_\xi \left[ L_{f_1 \bar{\theta}} L_f h(x) + L_f L_{f_1 \bar{\theta}} h(x) \right] \\ & - B_t \left[ L_{f_1 \bar{\theta}}^2 h(x) - \frac{L_{B_u} L_{f_1 \bar{\theta}} h(x)}{L_{B_u} L_f h(x)} \left( L_f^2 h(x) - \ddot{r} - K_\xi \check{\xi} \right) \right]. \end{aligned} \quad (7.6)$$

The input-output map has three terms on the right side. The first term is the closed-loop state matrix when using the nominal parameters; the last two terms are perturbations due to parameter uncertainty. Parameter uncertainty in the control problem results in tracking bias.

The robustness effects must be addressed to improve the closed-loop performance. In this research, the robustness effects are addressed by using adaptive feedback methods to solve the estimation and control problems. The estimation problem is addressed with an adaptive Luenberger type state observer to simultaneously estimate the state and parameter when a persistently exciting condition is satisfied. The control problem is addressed with the state and parameter estimates being used the controller using the certainty equivalence principle, and expressing the control gains in terms of the parameter estimate. This control design approach creates an automated self-tuning optical trap.

## 7.2 ADAPTIVE STATE OBSERVER

The estimation problem is addressed by using an adaptive state observer to simultaneously estimate the state and parameter. Many methods exist to implement adaptive state observers for nonlinear systems. The first method uses a global transformation to express the system into adaptive observable canonical form [113, 114], which is in linear parametric form and the nonlinearities depend only on the measurements and the control inputs. The simultaneous estimation of the state and parameters were obtained by using an auxiliary state, a time-varying linear combination of the state and the parameter, also known as a filter transformation. The true state estimate/reconstruction requires a persistent excitation condition be satisfied. The use of the auxiliary state has allowed for further contributions in adaptive state observers. Adaptive state observer have been designed for MIMO systems when the auxiliary state is the linear combination of the state estimation error and the parameter estimation error [115]. The auxiliary state being a function of the estimation errors allowed for adaptive state observers be designed for systems in nonlinear parametric form [116, 117].

The second method partitions the state space into two groups: measured states and unmeasured states. The unknown parameters can only appear in either the dynamics for the measured state [118, 119] or the unmeasured states [120]. Both cases contain the product of the unmeasured state and the unknown parameter. When the unknown parameters appear in the measured state, the system is expressed in a modified form of higher dimension to facilitate the design of the reduced-order adaptive state observer. The system is expressed in higher dimension to account for the non-zero off-diagonal entries in the product of the unmeasured state and the unknown product. The reduced order state observer provides an estimate of the unmeasured state and the parameters, and its stability is shown with a parameter-dependent Lyapunov function. For the case when the parameters appears in the unmeasured states, an auxiliary state (the combination of the measured state and the unmeasured state) is formed, and its stability requires a parameter-dependent Lyapunov function and a persistent excitation condition be satisfied.

The third method uses a high-gain adaptive state observer with two correction terms [117, 121]. The correction terms are the traditional Luenberger correction term that depends

on the measurement error, and the second correction term is a scaled version of the parameter estimation dynamics [115, 116, 117]. Its implementation requires the system be transformable to observable canonical form with the regression matrix being in column triangular form. Its stability analysis requires the use of an auxiliary state and a parameter-dependent Lyapunov function with the time-varying parameter adaptation gain to show asymptotic stability for high-gain values. The idea of using two correction terms in the state estimation dynamics allowed for additional contributions in adaptive state observer design for nonlinear systems when the system is in linear parametric form [122] and nonlinear parametric form [116].

In this research, the adaptive state observer architecture has a similar architecture to the high-gain adaptive state observers by M. Farza and his colleagues [117, 121]. The state observer architecture is chosen to address the fact that the dynamics of the optical trap system contain the product of unmeasured states and an unknown parameter in both the measured and a unmeasured state. Its implementation requires the optical trap system be transformed with a parameter independent state transformation to observable canonical form with the regression vector in column triangular form. The optical trap system (as given in equation 4.37) is rearranged to

$$\dot{x} = f(x) + f_1(x)\theta + B_u u + B_w \tilde{w}, \quad (7.7a)$$

$$y = h(x), \quad (7.7b)$$

where  $f : \mathbb{R}^6 \rightarrow \mathbb{R}^6$  is the parameter-independent system dynamics,  $f_1 : \mathbb{R}^6 \rightarrow \mathbb{R}^{6 \times 3}$  is the regression vector and  $\theta \in \mathbb{R}^3$  is the unknown parameter vector. Equation 7.7 is transformable with a parameter-independent state transformation when the parameter-independent system dynamics  $f$  and output function  $h$  satisfies the observability condition [113],

$$\text{rank} \begin{bmatrix} \nabla h(x) & \nabla L_f h(x) & \dots & \nabla L_f^5 h(x) \end{bmatrix} = 6, \forall x \in M. \quad (7.8)$$

The observability condition is satisfied by modifying the optical trap system. The system is modified by adding and subtracting the term  $\omega_p(z + d_m)$  to the first two state equations, where  $\omega_p$  is a bandwidth chosen by the user. The negative term  $-\omega_p(z + d_m)$  is added to

the system dynamics  $f$ , while the positive term  $\omega_p(z + d_m)$  is added to  $f_1(x)\theta$  with  $\omega_p$  being treated as an unknown parameter. Then, the unknown parameter  $\theta$  is defined as

$$\theta = [\omega_t, \kappa\omega_t, \omega_p]^T. \quad (7.9)$$

The vector field  $f$  and the regression vector  $f_1$  are defined as

$$f(x) = \begin{bmatrix} -\omega_p z - \omega_p d_m - g_v(\omega_{z_v} - \omega_{p_v})a_1 - g_v g_a \omega_z a_2 - g_v g_a a_3 \\ -\omega_p z - (\omega_p + \omega_m)d_m + \omega_m \bar{d}_m \\ -\omega_{p_v} a_1 + g_a \omega_z a_2 + g_a a_3 \\ a_3 \\ -\omega_{p_1} \omega_{p_2} a_2 - (\omega_{p_1} + \omega_{p_2})a_3 \\ -\omega_d \bar{d}_m \end{bmatrix} \quad (7.10a)$$

$$f_1(x) = \begin{bmatrix} -z \exp\left(-\frac{z^2}{2l_t^2}\right) & -d_m & z + d_m \\ -z \exp\left(-\frac{z^2}{2l_t^2}\right) & -d_m & z + d_m \\ 0 & 0 & 0 \\ 0 & 0 & 0 \\ 0 & 0 & 0 \\ 0 & 0 & 0 \end{bmatrix}. \quad (7.10b)$$

The optical trap system in equation 7.7 are transformed with the parameter-independent state transformation  $m(x)$ ,

$$m(x) = [h(x), L_f h(x), \dots, L_f^5 h(x)]^T, \quad (7.11)$$

a linear state transformation because  $f$  and  $h$  are linear in  $x$ , that satisfies

$$\frac{\partial m(x)}{\partial x} f(x) = A_m m(x) + b_1(m). \quad (7.12)$$

The state matrix  $A_m(i, j) = \delta_{i, j-1}$  (where  $i$  and  $j$  are the matrix indices and  $\delta$  is the Dirac delta function). The vector field  $b_1 : \mathbb{R}^6 \rightarrow \mathbb{R}^6$  is smooth and Lipschitz, and defined as

$$b_1(m) = \begin{bmatrix} 0_{5 \times 1} \\ L_f^6 h(m) \end{bmatrix},$$

and expressed in terms of  $m = m(x)$  because of the one-to-one map between the state  $x$  and the state  $m$ . Applying the state transformation in equation 7.11 to the optical trap system in equation 7.7 yields

$$\dot{m} = A_m m + b_1(m) + b_2(m)\theta + \frac{\partial m(x)}{\partial x} B_u u + \frac{\partial m(x)}{\partial x} B_w \tilde{w}, \quad \text{with } b_2(m(x)) = \frac{\partial m(x)}{\partial x} f_1(x), \quad (7.13a)$$

$$y = C_m m + \tilde{n} = m_1 + \tilde{n} \quad (7.13b)$$

where the output matrix  $C_m = [1, 0, 0, 0, 0, 0]$ . Notice that  $\frac{\partial m(x)}{\partial x} B_u$  is a constant matrix because the system dynamics  $f$  is linear. The regression matrix  $b_2(m)$  is expressed in column triangular form and depends on the unmeasured states. The fact that  $b_2$  depends on an unmeasured state presents a challenge in the estimation problem because the regression vector usually depends on available signals. The challenge is addressed by using the state estimate in the regression vector.

The transformed optical trap system in equation 7.13 is expressed in the structure for the implementation of the adaptive state observer. First, some math notations and definitions are given, then followed by the architecture of the adaptive state observer. The math notations are:

1. A symmetric and positive definite matrix  $S \in \mathbb{R}^{6 \times 6}$  satisfies the Lyapunov equation [123],

$$S + A_m^T S + S A_m - C_m^T C_m = 0, \quad (7.14)$$

and has the solution

$$S_{ij} = (-1)^{i+j} \alpha_{i+j-2}^{j-1}, \quad 1 \leq i, j \leq 6, \quad \text{where } \alpha_n^p = \frac{n!}{(n-p)!p!}. \quad (7.15)$$

The matrix  $S$  ensures that the matrix  $A_m - S^{-1} C_m^T C_m$  is Hurwitz.

2. For a positive constant  $\lambda$ , the diagonal matrix  $\Lambda \in \mathbb{R}^{6 \times 6}$  is defined as

$$\Lambda = \text{diag} \left[ 1, \frac{1}{\lambda}, \dots, \frac{1}{\lambda^5} \right]. \quad (7.16)$$

The matrix  $\Lambda$  satisfies the following identities [117]:

$$\Lambda A_m \Lambda^{-1} = \lambda A_m \quad \text{and} \quad C_m \Lambda^{-1} = C_m. \quad (7.17)$$

3. A function  $j : \mathbb{R} \rightarrow \mathbb{R}$  satisfies [117]

$$y^T j(y) \geq y^T y, \quad \forall y \in \mathbb{R}. \quad (7.18)$$

4. Each of the unknown parameters  $\theta_j$  (for  $j = 1, 2, 3$ ) has a characteristic index  $c_j$ . The characteristic index  $c_j$  is equal to the smallest positive constant  $i$  that corresponds to the state  $m_i$  (for  $i = 1, \dots, 6$ ) whose state dynamics  $\dot{m}_i$  contains the first appearance of the parameter  $\theta_j$ . The characteristic index  $c_j$  is described by

$$\frac{\partial \dot{m}_i}{\partial \theta_j} = 0 \quad \text{for } i = 1, \dots, c_j - 1, \quad \text{and} \quad \frac{\partial \dot{m}_{c_j}}{\partial \theta_j} \neq 0. \quad (7.19)$$

In this research, each parameter  $\theta_j$  has a characteristic index of one. Then, for a positive definite  $\lambda$ , and the characteristic indices, a diagonal matrix  $\Omega \in \mathbb{R}^{3 \times 3}$  is defined as

$$\Omega = \text{diag} \left[ \frac{1}{\lambda}, \frac{1}{\lambda}, \frac{1}{\lambda} \right]. \quad (7.20)$$

The matrix  $\Omega$  satisfies the following identity [121]:

$$\Lambda b_2(m) \Omega^{-1} = \lambda M(m) + R(m, \frac{1}{\lambda}), \quad (7.21)$$

with the matrices  $M \in \mathbb{R}^{6 \times 3}$  and  $R \in \mathbb{R}^{6 \times 3}$  being defined as

$$M_i^j(m) = 0 \quad \text{if } i \neq c_j, \quad \text{and} \quad M_{c_j}^j(m) = b_{2,c_j}^j(m) \quad (7.22a)$$

$$R_i^j(m, \frac{1}{\lambda}) = 0 \quad \text{if } i \leq c_j \quad \text{and} \quad R_i^j(m, \frac{1}{\lambda}) = \left( \frac{1}{\lambda} \right)^{i-1-c_j} b_{2,i}^j(m) \quad \text{otherwise}, \quad (7.22b)$$

where the notation  $M_i^j$  denotes the  $i$ th row and the  $j$ th column of the matrix  $M$ . The matrix  $M$  is a submatrix of the regression matrix  $b_2$  because  $M$  accounts only for the first instance the parameter  $\theta_j$  appears in the state equation. Notice that the matrix  $M(m)$  is independent of the positive constant  $\lambda$ , while the matrix  $R$  depends on  $\lambda$  through non-positive powers. Then, given the definitions for  $M$  and  $R$  in equation 7.22, the following properties hold [121]:

$$\begin{aligned} \Lambda M(m) \Omega &= \lambda M(m) \\ R_i^j(m, \frac{1}{\lambda}) &= 0 \quad \text{for } j = 1, 2, 3. \end{aligned} \quad (7.23)$$

The importance of  $M$  being independent of  $\lambda$  is that the persistent excitation condition to be given is bounded with lower and upper bounds independent of  $\lambda$ .

The architecture for the adaptive state observer is defined as

$$\frac{d}{dt}\hat{m} = A_m\hat{m} + b_1(\hat{m}) + \frac{\partial m(x)}{\partial x}B_u u + b_2(\hat{m})\hat{\theta} + \lambda\Lambda^{-1}S^{-1}C_m^T j(C_m\check{m}) + \Lambda^{-1}N\Omega\frac{d}{dt}\hat{\theta} \quad (7.24a)$$

$$\frac{d}{dt}\hat{\theta} = -\frac{d}{dt}\check{\theta} = \lambda\Omega^{-1}P_\theta N^T C_m^T j(C_m\check{m}) \quad (7.24b)$$

$$\dot{N} = \lambda(A_m - S^{-1}C_m^T C_m)N + \lambda M(\hat{m}), \quad \text{with } N(0) = 0 \quad (7.24c)$$

$$\dot{P}_\theta = -\lambda P_\theta N^T C_m^T C_m N P_\theta + \lambda P_\theta, \quad \text{with } P_\theta(0) = P_\theta(0)^T > 0, \quad (7.24d)$$

where  $\hat{m} = m(\hat{x})$  is the state estimate and  $\check{m} = m(x) - m(\hat{x})$  defines the state estimation error, and  $\check{\theta} = \theta - \hat{\theta}$  defines the parameter estimation error. The adaptive state observer has several features:

1. The dynamics for the state estimate in equation 7.24a has two correction terms: the first term is  $\lambda\Lambda^{-1}S^{-1}C_m^T j(C_m\check{m})$  and the second term is  $\Lambda^{-1}N\Omega\frac{d}{dt}\hat{\theta}$ . The first correction term is the traditional Luenberger correction term depending on the measurement error. The second correction term depends on the parameter estimate dynamics.
2. Parameter estimation is achieved using recursive least squares that is combined with exponential forgetting and a time-varying adaptation gain. The dynamics for the parameter estimate, as given in equation 7.24b, depends on the measurement error and the time-varying adaptation gain matrix  $P_\theta = P_\theta^T > 0$ , which is governed by equation 7.24d.
3. The matrix  $N$  is used in the auxiliary state to form the linear combination of the state estimation error and the parameter estimation error. Let us show that  $N$  has lower and upper bounds independent of  $\lambda$  by performing a time scale change by setting  $\tau = \frac{t}{\lambda}$  and let  $\bar{N}(\tau) = N(\frac{t}{\lambda})$ . Then, equation 7.24c becomes

$$\frac{d}{d\tau}\bar{N} = (A_m - S^{-1}C_m^T C_m)\bar{N} + M(\hat{m}). \quad (7.25)$$

The matrix  $\bar{N}$  is bounded with lower and upper bounded independent of  $\lambda$  because the matrix  $(A_m - S^{-1}C_m^T C_m)$  is Hurwitz and  $M(\hat{m})$  is bounded with lower and upper bounds independent of  $\lambda$ .

4. State and parameter estimation are possible when a persistent excitation condition is satisfied. The persistent excitation condition is satisfied when there exists positive constants  $\delta_1$ ,  $\delta_2$ , and  $T$  (each being independent of  $\lambda$ ) such that

$$\delta_1 I_3 \leq \int_t^{t+T} N(\tau)^T C_m^T C_m N(\tau) d\tau \leq \delta_2 I_3. \quad (7.26)$$

The persistent excitation condition is made on the state estimate not known inputs and measurements because the dynamics for  $N$  are driven by a function of the state estimate  $M(\hat{m})$ . As a result, the persistent excitation condition can be checked on-line by computing the eigenvalues of the symmetric matrix  $\int_t^{t+T} N(\tau)^T C_m^T C_m N(\tau) d\tau$  [121]. If the condition is not satisfied with the inherent noise (process noise and sensor noise) in the system, then a perturbation signal of Gaussian white noise is added to the control input and its power spectral density is increased until the persistent excitation condition is satisfied. Caution needs to be taken when adding a perturbing white noise signal to the system because the system performance may degrade as a result. A second potential issue with the persistent excitation condition is that it depends on  $N$ , a filtered version of the regression matrix  $b_2$ , more specifically its submatrix matrix  $M$  by introducing the concept of characteristic indices. One may ask if dynamics being ignored by using the matrix  $M$ . The answer is given by substituting the dynamics of  $N$  by the dynamics for the matrix  $Z$  [121],

$$\dot{Z} = \lambda(A_m - S^{-1}C_m^T C_m)Z + \Lambda b_2(\hat{m})\Omega^{-1} \quad (7.27)$$

Notice that the  $Z$  dynamics depends on the regression matrix  $b_2(\hat{m})$ . We show that the dynamics for  $Z$  converges uniformly with respect to time to the dynamics for  $N$  when  $\lambda \rightarrow \infty$ . Performing a time scale change  $\bar{Z}(\tau) = Z(\frac{t}{\lambda})$  yields

$$\dot{\bar{Z}} = (A_m - S^{-1}C_m^T C_m)\bar{Z} + \frac{1}{\lambda}\Lambda b_2(\hat{m})\Omega^{-1}, \quad (7.28)$$

and applying the identity in equation 7.21 yields

$$\dot{\bar{Z}} = (A_m - S^{-1}C_m^T C_m)\bar{Z} + M(\hat{m} + \frac{1}{\lambda}R(\hat{m}, \frac{1}{\lambda})). \quad (7.29)$$

Since the entries in  $R$  are polynomial in  $\frac{1}{\lambda}$ , the matrix  $\frac{1}{\lambda}R(\hat{m}, \frac{1}{\lambda}) \rightarrow 0$  as  $\lambda \rightarrow \infty$ , and the dynamics for the matrix  $\bar{Z}$  converges to the dynamics for the matrix  $\bar{N}$ .

It is insightful to provide the state estimate dynamics given in equation 7.24a in the original state  $x$ . Applying the inverse of the state transformation  $m = m(x)$  to equation 7.24a yields the dynamics of the state estimate being

$$\dot{\hat{x}} = f(\hat{x}) + f_1(\hat{x})\hat{\theta} + B_u u + \left( \frac{\partial m(\hat{x})}{\partial \hat{x}} \right)^{-1} \left( \lambda \Lambda S^{-1} C_m^T j(C_m \check{m}) + \Lambda N \Omega \frac{d}{dt} \hat{\theta} \right). \quad (7.30)$$

Before the theorem and proof for the adaptive state observer are given, the following assumptions are used:

**Assumption 9.** *The state  $m$ , the control input  $u$ , and the parameters  $\theta$  are bounded for all time. This assumption is standard for high-gain adaptive state observers [117, 121].*

**Assumption 10.** *The vector field  $b_1(m)$  is continuous and Lipschitz in  $m$  uniformly in  $u$ . The Lipschitz condition implies there exists a positive constant  $l_1$  such that*

$$\|b_1(m) - b_1(\hat{m})\| \leq l_1 \|\check{m}\|. \quad (7.31)$$

**Assumption 11.** *The vector field  $b_2(m)$  is continuous and Lipschitz. The Lipschitz condition implies there exists a positive constant  $l_2$  such that*

$$\|b_2(m) - b_2(\hat{m})\| \leq l_2 \|\check{m}\|. \quad (7.32)$$

**Theorem 4** (Adaptive State Observer). *Assume the expected value of the system given in equation 7.13 (with  $w = 0$ ) satisfies assumption 9, assumption 10, and assumption 11. Then, for every bounded input that satisfies the persistent excitation condition in equation 7.26, there exists a positive constant  $\lambda_o$ , such that for every positive constant  $\lambda > \lambda_o$ , the adaptive state observer in equation 7.24, for the system in equation 7.13 (with  $w = 0$ ), yields exponential error convergence to the origin for high values of  $\lambda$ .*

*Proof.* In this proof, the state estimation error dynamics are first manipulated to a desired form, the auxiliary state is given, then a Lyapunov stability analysis is performed.

The dynamics for the state estimation error  $\check{m} = m - \hat{m}$  are

$$\begin{aligned} \frac{d}{dt}\check{m} &= A_m\check{m} - \lambda\Lambda^{-1}S^{-1}C_m^T j(C_m\check{m}) - \Lambda^{-1}N\Omega\frac{d}{dt}\hat{\theta} \\ &+ b_1(m) - b_1(\hat{m}) + b_2(m)\theta - b_2(\hat{m})\hat{\theta}, \end{aligned} \quad (7.33)$$

and is independent of the control input. Equation 7.33 needs to depend on the parameter estimation error  $\check{\theta}$  and its dynamics  $\frac{d}{dt}\check{\theta}$ . Adding and subtracting the term  $b_2(\hat{m})\theta$  and applying  $\frac{d}{dt}\hat{\theta} = -\frac{d}{dt}\check{\theta}$  to equation 7.33 yields

$$\begin{aligned} \frac{d}{dt}\check{m} &= A_m\check{m} - \lambda\Lambda^{-1}S^{-1}C_m^T j(C_m\check{m}) + \Lambda^{-1}N\Omega\frac{d}{dt}\check{\theta} \\ &+ b_1(m) - b_1(\hat{m}) + (b_2(m) - b_2(\hat{m}))\theta + b_2(\hat{m})\check{\theta}. \end{aligned} \quad (7.34)$$

Equation 7.34 is driven by two pseudo-state estimation errors. The first pseudo state-estimation error  $b_1(m) - b_1(\hat{m})$  results from using the state estimate in the vector field  $b_1$ ; the second pseudo error  $(b_2(m) - b_2(\hat{m}))\theta$  results from using the state estimate in the regression vector  $b_2$ .

Next, the auxiliary state is defined by forming a linear combination of a scaled version of the state estimation error and a scaled version of the parameter estimation error. First, the state estimation error  $\check{m}$  and the parameter estimation error  $\check{\theta}$  are scaled by the matrices  $\Lambda$  and  $\Omega$  respectively. The scaled state estimation error  $\acute{m}$  and the scaled parameter estimation error  $\acute{\theta}$  are

$$\acute{m} = \Lambda\check{m} \quad \text{and} \quad \frac{d}{dt}\acute{m} = \Lambda\frac{d}{dt}\check{m}, \quad (7.35)$$

$$\acute{\theta} = \Omega\check{\theta} \quad \text{and} \quad \frac{d}{dt}\acute{\theta} = \Omega\frac{d}{dt}\check{\theta}. \quad (7.36)$$

Then, the dynamics for the scaled state dynamics error and the scaled parameter estimation error are obtained by:

1. applying the scaling relationships given in equation 7.35 and equation 7.36 to the dynamics for the state estimation error in equation 7.34 and the parameter estimation error in equation 7.24b,

2. applying the identities  $\Lambda A_m \Lambda^{-1} = \lambda A_m$  and  $C_m \Lambda^{-1} = C_m$  given in equation 7.17.

The dynamics for the scaled state estimation error is

$$\begin{aligned} \frac{d}{dt} \hat{m} &= \lambda A_m \hat{m} - \lambda S^{-1} C_m^T j(C_m \hat{m}) + N \frac{d}{dt} \hat{\theta} \\ &+ \Lambda(b_1(m) - b_1(\hat{m})) + \Lambda(b_2(m) - b_2(\hat{m}))\theta + \Lambda b_2(\hat{m})\Omega^{-1} \hat{\theta}, \end{aligned} \quad (7.37)$$

while the dynamics for the scaled parameter estimation error is

$$\frac{d}{dt} \hat{\theta} = -\lambda P_\theta N^T C_m^T j(C_m \hat{m}). \quad (7.38)$$

The auxiliary state  $\hat{q}$  is defined as

$$\hat{q} = \hat{m} - N \hat{\theta} \quad (7.39)$$

Its dynamics are obtained by:

1. taking the time derivative of equation 7.39,
2. applying the dynamics for the scaled state estimation error in equation 7.37 and the scaled parameter estimation error in equation 7.38,
3. imposing  $\dot{\hat{m}} = \dot{\hat{q}} + N \dot{\hat{\theta}}$  from equation 7.39.

The dynamics for the auxiliary state are then

$$\begin{aligned} \frac{d}{dt} \hat{q} &= \frac{d}{dt} \hat{m} - \dot{N} \hat{\theta} - N \frac{d}{dt} \hat{\theta} \\ &= \lambda A_m \hat{q} - \lambda S^{-1} C_m^T j(C_m \hat{m}) + \Lambda(b_1(m) - b_1(\hat{m})) \\ &+ \Lambda(b_2(m) - b_2(\hat{m}))\theta + \left( \lambda A_m N + \Lambda b_2(\hat{m})\Omega^{-1} - \dot{N} \right) \hat{\theta}. \end{aligned} \quad (7.40)$$

The last term contains  $\hat{\theta}$  and this term is eliminated by choosing an update law for  $N$  such that  $\hat{\theta}$  is multiplied by zero. First, apply the identity in equation 7.21 ( $\Lambda b_2(\hat{m})\Omega^{-1} = \lambda M(\hat{m}) + R(\hat{m}, \frac{1}{\lambda})$  with  $R(\hat{m}, \frac{1}{\lambda}) = 0$ ), then add and subtract the term  $\lambda S^{-1} C_m^T C_m N \hat{\theta}$  to equation 7.40 to yield

$$\begin{aligned} \frac{d}{dt} \hat{q} &= \lambda A_m \hat{q} + \lambda S^{-1} C_m^T C_m N \hat{\theta} - \lambda S^{-1} C_m^T j(C_m \hat{m}) + \Lambda(b_1(m) - b_1(\hat{m})) \\ &+ \Lambda(b_2(m) - b_2(\hat{m}))\theta + \left( \lambda(A_m - S^{-1} C_m^T C_m)N + \lambda M(\hat{m}) - \dot{N} \right) \hat{\theta} \end{aligned} \quad (7.41)$$

Choosing the update for the  $N$  (equivalent to applying equation 7.24c)

$$\dot{N} = \lambda(A_m - S^{-1}C_m^T C_m)N + \lambda M(\hat{m})$$

and substituting back into equation 7.41 yields

$$\begin{aligned} \frac{d}{dt}\dot{q} &= \lambda A_m \dot{q} + \lambda S^{-1}C_m^T C_m N \dot{\theta} - \lambda S^{-1}C_m^T j(C_m \dot{m}) \\ &+ \Lambda(b_1(m) - b_1(\hat{m})) + \Lambda(b_2(m) - b_2(\hat{m}))\theta. \end{aligned} \quad (7.42)$$

Next, a stability analysis is performed on the auxiliary state  $\dot{q}$  and the scaled parameter estimation error  $\dot{\theta}$ . The Lyapunov function candidate is

$$W(\dot{q}, \dot{\theta}) = W_1(\dot{q}) + W_2(\dot{\theta}) = \dot{q}^T S \dot{q} + \dot{\theta}^T P_\theta^{-1} \dot{\theta}, \quad (7.43)$$

and each term is lower and upper bounded with class K functions by

$$\lambda_{\min}(S) \|\dot{q}\|^2 \leq W_1(\dot{q}) \leq \lambda_{\max}(S) \|\dot{q}\|^2, \quad (7.44a)$$

$$\lambda_{\min}(P_\theta) \|\dot{\theta}\|^2 \leq W_2(\dot{\theta}) \leq \lambda_{\max}(P_\theta) \|\dot{\theta}\|^2. \quad (7.44b)$$

Taking the time derivative of equation 7.43 yields

$$\dot{W} = \frac{d}{dt}\dot{q}^T S \dot{q} + \dot{q}^T S \frac{d}{dt}\dot{q} + 2\dot{\theta}^T P_\theta^{-1} \frac{d}{dt}\dot{\theta} - \dot{\theta}^T P_\theta^{-1} \dot{P}_\theta P_\theta^{-1} \dot{\theta}. \quad (7.45)$$

Substituting in equation 7.42 for  $\frac{d}{dt}\dot{q}$  yields

$$\begin{aligned} \dot{W} &= \lambda \dot{q}^T (A_m^T S + S A_m) \dot{q} + 2\lambda \dot{q}^T C_m^T C_m N \dot{\theta} - 2\lambda \dot{q}^T C_m^T j(C_m \dot{m}) \\ &+ 2\dot{\theta}^T P_\theta^{-1} \frac{d}{dt}\dot{\theta} - \dot{\theta}^T P_\theta^{-1} \dot{P}_\theta P_\theta^{-1} \dot{\theta} \\ &+ 2\dot{q}^T S \Lambda (b_1(m) - b_1(\hat{m})) + 2\dot{q}^T S \Lambda (b_2(m) - b_2(\hat{m})) \theta. \end{aligned} \quad (7.46)$$

The first term  $\lambda \dot{q}^T (A_m^T S + S A_m) \dot{q}$  is expressed in terms of the Lyapunov function  $W_1$ . Equation 7.46 is modified by adding and subtracting the term  $\lambda \dot{q}^T C_m^T C_m \dot{q}$ , applying the Lyapunov equation (same as given in equation 7.14),

$$S + A_m^T S + S A_m - C_m^T C_m = 0,$$

and imposing  $\dot{q}^T S \dot{q} = W_1$  from equation 7.43 to yield

$$\begin{aligned} \dot{W} &= -\lambda W_1 + \lambda \dot{q}^T C_m^T C_m \dot{q} + 2\lambda \dot{q}^T C_m^T C_m N \dot{\theta} - 2\lambda \dot{q}^T C_m^T j(C_m \dot{m}) \\ &\quad + 2\dot{\theta}^T P_\theta^{-1} \frac{d}{dt} \dot{\theta} - \dot{\theta}^T P_\theta^{-1} \dot{P}_\theta P_\theta^{-1} \dot{\theta} \\ &\quad + 2\dot{q}^T S \Lambda (g_1(m, u) - g_1(\hat{m}, u)) + 2\dot{q}^T S \Lambda (g_2(m) - g_2(\hat{m})) \theta. \end{aligned} \quad (7.47)$$

Equation 7.47 is further bounded by taking the norm of the last two terms to yield

$$\begin{aligned} \dot{W} &\leq -\lambda W_1 + \lambda \dot{q}^T C_m^T C_m \dot{q} + 2\lambda \dot{q}^T C_m^T C_m N \dot{\theta} - 2\lambda \dot{q}^T C_m^T j(C_m \dot{m}) \\ &\quad + 2\dot{\theta}^T P_\theta^{-1} \frac{d}{dt} \dot{\theta} - \dot{\theta}^T P_\theta^{-1} \dot{P}_\theta P_\theta^{-1} \dot{\theta} \\ &\quad + \left\| 2\dot{q}^T S \Lambda (b_1(m) - b_1(\hat{m})) \right\| + \left\| 2\dot{q}^T S \Lambda (b_2(m) - b_2(\hat{m})) \theta \right\|. \end{aligned} \quad (7.48)$$

Next, the norms  $\left\| 2\dot{q}^T S \Lambda (b_1(m) - b_1(\hat{m})) \right\|$  and  $\left\| 2\dot{q}^T S \Lambda (b_2(m) - b_2(\hat{m})) \theta \right\|$  are bounded in terms of  $\|\dot{q}\|^2$  and  $\left\| \dot{\theta} \right\|^2$ . These norms are bounded using assumption 10 and assumption 11, which implies the vector fields  $b_1(m)$  and  $b_2(m)$  are Lipschitz in  $m$ . The same procedure is used to bound both norms. The procedure is given to bound the norm  $\left\| 2\dot{q}^T S \Lambda (b_1(m) - b_1(\hat{m})) \right\|$ , then the bound for the norm  $\left\| 2\dot{q}^T S \Lambda (b_2(m) - b_2(\hat{m})) \theta \right\|$  is given. First, the norm  $\Lambda (b_1(m) - b_1(\hat{m}))$  is bounded in terms of  $\|\dot{m}\|$  by using the mean value theorem, applying assumption 10, and using equation 7.35 ( $\check{m} = \Lambda^{-1} \dot{m}$ ) to yield

$$\left\| \Lambda (b_1(m) - b_1(\hat{m})) \right\| \leq \left\| \Lambda \frac{\partial b_1}{\partial m} \Lambda^{-1} \right\| \|\dot{m}\| \leq \beta_1 \|\dot{m}\|.$$

The vector field  $g_1$  being in lower triangular structure enables  $\left\| \Lambda \frac{\partial b_1}{\partial m} \Lambda^{-1} \right\|$  to be bounded by a positive constant  $\beta_1$ , which is independent of  $\lambda$  for  $\lambda \geq 1$  [117]. The norm  $\dot{m}$  is bounded in terms of  $\dot{q}$  and  $\dot{\theta}$  by using equation 7.39 ( $\dot{m} = \dot{q} + N\dot{\theta}$ ) to yield

$$\left\| \Lambda (b_1(m) - b_1(\hat{m})) \right\| \leq \beta_1 \|\dot{m}\| \leq \beta_1 \left( \|\dot{q}\| + \|N\| \left\| \dot{\theta} \right\| \right) \quad (7.49)$$

Then, the norm  $\left\| 2\dot{q}^T S \Lambda (b_1(m) - b_1(\hat{m})) \right\|$  is bounded by

$$\left\| 2\dot{q}^T S \Lambda (b_1(m) - b_1(\hat{m})) \right\| \leq \beta_1 \|S\| \left( 2\|\dot{q}\|^2 + \|N\| 2\|\dot{q}\| \left\| \dot{\theta} \right\| \right) \quad (7.50)$$

The norm  $2\|\dot{q}\| \left\| \dot{\theta} \right\|$  is bounded by Young's inequality to yield

$$2\|\dot{q}\| \left\| \dot{\theta} \right\| \leq \|\dot{q}\|^2 + \left\| \dot{\theta} \right\|^2,$$

then equation 7.50 is bounded by

$$\|2\dot{q}^T S \Lambda (b_1(m) - b_1(\hat{m}))\| \leq \beta_1 \|S\| \left( (2 + \|N\|) \|\dot{q}\|^2 + \|N\| \|\dot{\theta}\|^2 \right). \quad (7.51)$$

The norms  $\|\dot{q}\|^2$  and  $\|\dot{\theta}\|^2$  are bounded in the Lyapunov functions  $W_1$  and  $W_2$  by using equation 7.44 to yield

$$\|\dot{q}\|^2 \leq \frac{1}{\lambda_{\min}(S)} W_1 \quad \text{and} \quad \|\dot{\theta}\|^2 \leq \frac{1}{\lambda_{\min}(P^{-1})} W_2.$$

Then equation 7.51 is bounded by

$$\|2\dot{q}^T S \Lambda (b_1(m) - b_1(\hat{m}))\| \leq \frac{(2 + \|N\|)\beta_1 \|S\|}{\lambda_{\min}(S)} W_1 + \frac{\beta_1 \|S\| \|N\|}{\lambda_{\min}(P^{-1})} W_2 \quad (7.52)$$

The norm of  $2\dot{q}^T S \Lambda (b_2(m) - b_2(\hat{m})) \theta$  is obtained using the same procedure. It is straight-forward to show its bound is

$$\|2\dot{q}^T S \Lambda (b_2(m) - b_2(\hat{m})) \theta\| \leq \frac{(2 + \|N\|)\beta_2 \|\theta\| \|S\|}{\lambda_{\min}(S)} W_1 + \frac{\beta_2 \|\theta\| \|S\| \|N\|}{\lambda_{\min}(P^{-1})} W_2, \quad (7.53)$$

where the positive constant  $\beta_2$  is defined as  $\|\Lambda \frac{\partial b_2}{\partial m} \Lambda^{-1}\| \leq \beta_2$  with  $\beta_2$  being independent of  $\lambda$  for  $\lambda \geq 1$ . It is convenient to add the norms of equation 7.52 and equation 7.53 to yield

$$\begin{aligned} & \|2\dot{q}^T S \Lambda (b_1(m) - b_1(\hat{m})) \theta\| + \|2\dot{q}^T S \Lambda (b_2(m) - b_2(\hat{m})) \theta\| \\ & \leq \eta_1 W_1 + \eta_2 W_2, \end{aligned} \quad (7.54)$$

where the positive constants  $\eta_1$  and  $\eta_2$  are defined as

$$\eta_1 = \frac{(2 + \|N\|)(\beta_1 + \beta_2 \|\theta\|) \|S\|}{\lambda_{\min}(S)} \quad \text{and} \quad \eta_2 = \frac{(\beta_1 + \beta_2 \|\theta\|) \|S\| \|N\|}{\lambda_{\min}(P^{-1})}. \quad (7.55)$$

Equation 7.54 is substituted back into  $\dot{W}$  in equation 7.48 to yield

$$\begin{aligned} \dot{W} = & -(\lambda - \eta_1)W_1 + \eta_2 W_2 + 2\dot{\theta}^T P_\theta^{-1} \frac{d}{dt} \theta - \dot{\theta}^T P_\theta^{-1} \dot{P}_\theta P_\theta^{-1} \theta \\ & + \lambda \dot{q}^T C_m^T C_m \dot{q} + 2\lambda \dot{q}^T C_m^T C_m N \dot{\theta} - 2\lambda \dot{q}^T C_m^T j(C_m \hat{m}). \end{aligned} \quad (7.56)$$

Next, the update laws for  $\dot{\theta}$  and  $P_\theta$  are chosen. These update laws are chosen by first manipulating the last three terms in equation 7.56. The last three terms are expressed in terms of  $\dot{m}$  and  $\dot{\theta}$  by imposing  $\dot{q} = \dot{m} - N\dot{\theta}$  from equation 7.39 to yield

$$\lambda \dot{q}^T C_m^T C_m \dot{q} = \lambda \dot{m}^T C_m^T C_m \dot{m} - 2\lambda \dot{\theta}^T N^T C_m^T C_m \dot{m} + \lambda \dot{\theta}^T M^T C_m^T C_m M \dot{\theta}, \quad (7.57a)$$

$$2\lambda \dot{q}^T C_m^T C_m N \dot{\theta} = 2\lambda \dot{\theta}^T N^T C_m^T C_m \dot{m} - 2\lambda \dot{\theta}^T N^T C_m^T C_m N \dot{\theta}, \quad (7.57b)$$

$$-2\lambda \dot{q}^T C_m^T j(C_m \dot{m}) = -2\lambda \dot{m}^T C_m^T j(C_m \dot{m}) + 2\lambda \dot{\theta}^T N^T C_m^T j(C_m \dot{m}). \quad (7.57c)$$

Substituting equation 7.57 into equation 7.56 and rearranging the terms yield

$$\begin{aligned} \dot{W} = & -(\lambda - \eta_1)W_1 + \eta_2 W_2 + \lambda \dot{m}^T C_m^T C_m \dot{m} - 2\lambda \dot{m}^T C_m^T j(C_m \dot{m}) \\ & - \dot{\theta}^T \left( P_\theta^{-1} \dot{P}_\theta P_\theta^{-1} + \lambda N^T C_m^T C_m N \right) \dot{\theta} + 2\dot{\theta}^T \left( P_\theta^{-1} \frac{d}{dt} \dot{\theta} + \lambda N^T C_m^T j(C_m \dot{m}) \right) \end{aligned} \quad (7.58)$$

Choosing the update laws for  $\dot{\theta}$  and  $P$  to be equation 7.38 and equation 7.24d respectively

$$\begin{aligned} \frac{d}{dt} \dot{\theta} &= -\lambda P_\theta N^T C_m^T j(C_m \dot{m}) \\ \dot{P}_\theta &= -\lambda P_\theta N^T C_m^T C_m N P_\theta + \lambda P_\theta \end{aligned}$$

yields

$$\dot{W} = -(\lambda - \eta_1)W_1 - \lambda \dot{\theta}^T P_\theta^{-1} \dot{\theta} + \eta_2 W_2 + \lambda \dot{m}^T C_m^T C_m \dot{m} - 2\lambda \dot{m}^T C_m^T j(C_m \dot{m}) \quad (7.59)$$

The term  $\lambda \dot{m}^T C_m^T C_m \dot{m}$  is always positive and is bounded by  $2\lambda \dot{m}^T C_m^T C_m \dot{m}$ . Also, impose  $\dot{\theta}^T P_\theta^{-1} \dot{\theta} = W_2$  using equation 7.43 to yield

$$\dot{W} \leq -(\lambda - \eta_1)W_1 - (\lambda - \eta_2)W_2 + 2\lambda \left( \dot{m}^T C_m^T C_m \dot{m} - \dot{m}^T C_m^T j(C_m \dot{m}) \right). \quad (7.60)$$

The term  $\dot{m}^T C_m^T C_m \dot{m} - \dot{m}^T C_m^T j(C_m \dot{m})$  is always negative because the function  $j$  is defined in equation 7.18 as  $y^T j(y) > y^T y$ . Then, equation 7.60 is bounded by

$$\begin{aligned} \dot{W} &\leq -(\lambda - \eta_1)W_1 - (\lambda - \eta_2)W_2, \\ &\leq -(\lambda - \lambda_o)(W_1 + W_2), \quad \text{where } \lambda_o = \max(\eta_1, \eta_2), \\ &= -(\lambda - \lambda_o)W. \end{aligned} \quad (7.61)$$

Equation 7.61 shows that the Lyapunov function  $W$  is exponentially converges to the origin. We can conclude that  $W \in L_\infty$  and  $W$  is exponentially stable. Signal tracing is now performed to show that the transformations do not affect the stability properties and that the signals are bounded.

1. The Lyapunov function is  $W \in L_\infty$  and exponentially stable, then equation 7.43 implies that  $\dot{q}, \dot{\theta} \in L_\infty$ , and  $q$  and  $\theta$  are exponentially stable.
2. The scaled parameter estimation error  $\dot{\theta} \in L_\infty$  and exponentially stable, and  $\Omega \in L_\infty$ , then equation 7.36 ( $\check{\theta} = \Omega\dot{\theta}$ ) implies  $\check{\theta} \in L_\infty$  and  $\check{\theta}$  exponentially stable.
3. The parameter estimation error  $\check{\theta} \in L_\infty$  and the true parameter  $\theta \in L_\infty$ , then from  $\check{\theta} = \theta - \hat{\theta}$  implies  $\hat{\theta} \in L_\infty$ .
4. The scaled estimation errors  $\dot{q}, \dot{\theta} \in L_\infty$  and exponentially stable, and  $\|N\| \in L_\infty$ , then equation 7.39 ( $\dot{q} = \dot{m} - N\dot{\theta}$ ) implies  $\dot{m} \in L_\infty$  and  $\dot{m}$  exponentially stable.
5. The scaled state estimation error  $\dot{m} \in L_\infty$  and  $\dot{m}$  exponentially stable, and  $\Lambda \in L_\infty$ , then equation 7.35 ( $\check{m} = \Lambda\dot{m}$ ) implies  $\check{m} \in L_\infty$  and  $\check{m}$  is exponentially stable.
6. The state estimation error and the state  $\check{m}, m \in L_\infty$ , then from  $\check{m} = m - \hat{m}$  implies  $\hat{m} \in L_\infty$ .
7. The state estimate  $\hat{m} \in L_\infty$  and using the one-to-one map between  $m$  and  $x$  implies  $\hat{x} \in L_\infty$ .

□

A second advantage to using an adaptive state observer is the state estimate and parameter estimate is implemented in a control structure to study the molecule characteristics. The state estimate is used in the control because the state estimate contains less noise and disturbance rejection is possible. The parameter estimate is used because to address the parameter uncertainty in the state feedback to linearize the input-output map and the tracking error state.

### 7.3 ADAPTIVE CONTROL STRUCTURE

The molecule is studied by having the bead deflection track a reference signal. The tracking control problem is turned into a regulation control problem with the new control objective being design the control to drive the tracking error to zero. The tracking error is driven

to zero by a combination of an adaptive input-output feedback linearization with an LQ structure, as shown in the block diagram in figure 43.

The control structure has three feedback loops: the linearization loop (loop 1), the tracking loop (loop 2), and the self tuning loop (loop 3). The linearization loop transforms the optical trap system into normal form such that the input-output map is linearized via state feedback. The state feedback is implemented with the parameter estimate because the input-output map depends on the system parameters. The tracking loop uses the linearized input-output map in an adaptive LQ control algorithm to find the state feedback that drives the tracking error to zero. The state feedback is obtained in the self-tuning loop that

1. performs online parameter identification on the linearized input-output map by using recursive least squares combined with exponential forgetting and the projection algorithm,
2. finds the mapping between the state feedback parameters and the system parameters,
3. implements the state feedback parameters with the parameter estimate by applying the certainty equivalence principle.

The control architecture uses adaptive self-tuning methods (indirect adaptive control) to address the parameter uncertainty in the feedback loops. The desired closed-loop performance is satisfied by adjusting the state feedback parameters indirectly through using the parameter estimation process [124]. Self-tuning methods use the certainty equivalence principle to have the parameter estimate be considered the true parameter during the control design process [124].

First, to ease the notation, changes are made to the definitions of the tracking error and the Lie derivative to account for these definitions depending explicitly on the system parameters. The Lie derivative definition given in definition 1 is modified as followed:

**Definition 4** (Lie derivative modification). *Given a state  $x \in \mathbb{R}^n$  and parameters  $\theta \in \mathbb{R}^p$ , smooth vector fields  $f : \mathbb{R}^n \times \mathbb{R}^p \rightarrow \mathbb{R}^n$  and  $g : \mathbb{R}^n \rightarrow \mathbb{R}^n$ , and a smooth scalar field  $h : \mathbb{R}^n \times \mathbb{R}^p \rightarrow \mathbb{R}$ , then the Lie derivative is defined as  $L_f h(x, \theta)$ , which is the gradient of the scalar field  $h$  along the directions of the vector field  $f$ . The following notation is used for the*

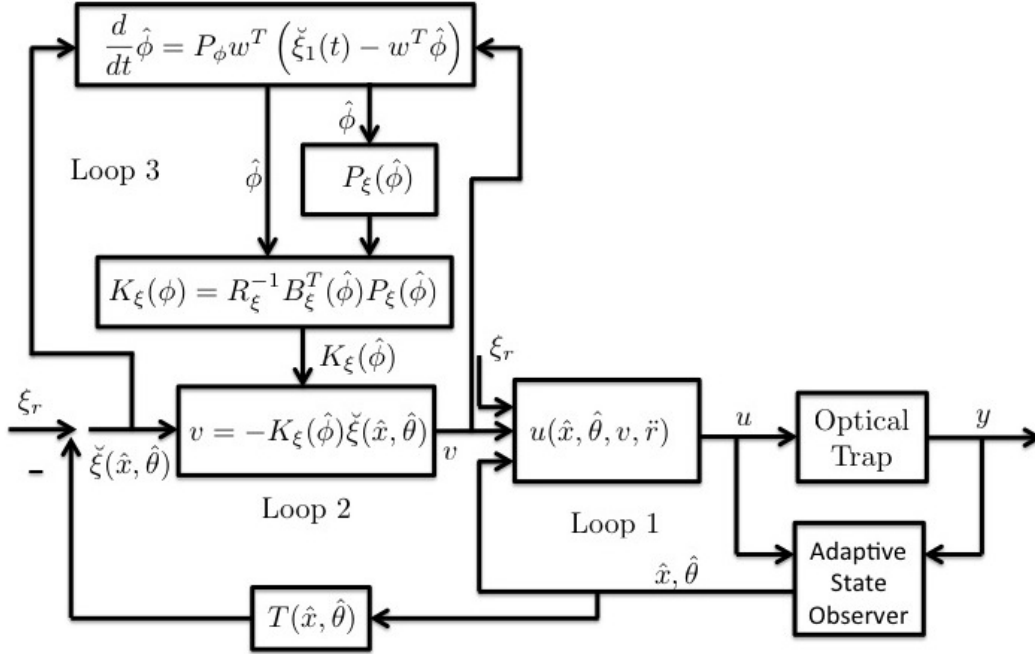


Figure 43: The schematic for the block diagram of the closed-loop block diagram. The block diagram has three feedback loops. The linearization loop (loop 1) transforms the optical trap system into normal form such that the input-output map can be linearized with state feedback. The tracking loop (loop 2) uses the linearized input-output map in an adaptive LQ optimal algorithm to find the state feedback to drive the tracking error to zero. The self-tuning loop (loop 3) performs the identification process and finds the online control solution.

Lie derivatives:

$$L_f^0 h(x, \theta) = h(x, \theta), \quad (7.62a)$$

$$L_f h(x, \theta) = \frac{\partial h(x, \theta)}{\partial x} f(x, \theta), \quad (7.62b)$$

$$L_f^2 h(x, \theta) = \frac{\partial L_f h(x, \theta)}{\partial x} f(x, \theta), \quad (7.62c)$$

$$L_g L_f h(x, \theta) = \frac{\partial L_f h(x, \theta)}{\partial x} g(x). \quad (7.62d)$$

The tracking error is defined in terms of the system parameters as

$$\check{\xi}(x, \theta) = \xi_r - \xi(x, \theta) = \begin{bmatrix} r - h(x, \theta) \\ \dot{r} - L_f h(x, \theta) \end{bmatrix}, \quad (7.63)$$

where  $r$  is the reference signal. Equation 7.63 is defined as the expected value of the tracking error and the bar accent notation is not used to simplify the notation.

The linearization loop transforms the optical trap system with the tracking error as its output into normal form (according to the procedure given in section 4.5.1),

$$\frac{d}{dt} \check{\xi}(x, \theta) = A_\xi(\phi) \check{\xi}(x, \theta) + B_\xi(\phi) [\ddot{r} - L_f^2 h(x, \theta) - L_{B_u} L_f h(x, \theta) u], \quad (7.64a)$$

$$\dot{\psi} = \delta(\xi_r - \check{\xi}(x, \theta), \psi) \quad (7.64b)$$

The input-output map describes the relationship between the control input  $u$  and the tracking error  $\check{\xi}$ . The matrices  $A_\xi(\phi)$  and  $B_\xi(\phi)$  are the state matrix and input matrix that result from transforming the optical trap system to normal form. These matrices are assumed to have unknown constant parameters and are described by

$$A_\xi(\phi) = \begin{bmatrix} 0 & 1 \\ -\phi_1 & -\phi_2 \end{bmatrix}, \quad \text{and} \quad B_\xi(\phi) = \begin{bmatrix} 0 \\ \phi_3 \end{bmatrix},$$

with the true parameters being  $\phi_1 = \phi_2 = 0$  and  $\phi_3 = 1$ . Equation 7.64 has the term  $L_f^2 h(x, \theta)$ , which depends on the system state and parameters, and the term  $L_{B_u} L_f h(x, \theta)$ , which is a constant. The input-output map is linearized using state feedback that depends on the state and parameter estimates. Choosing the state feedback to be

$$u(\hat{x}, \hat{\theta}) = -\frac{1}{L_{B_u} L_f h(x, \theta)} [L_f^2 h(\hat{x}, \hat{\theta}) - \ddot{r} + v], \quad (7.65)$$

with  $v$  being the auxiliary control input, and adding and subtracting the term  $B_\xi(\phi)L_f^2h(\hat{x}, \theta)$  results in the input-output map

$$\frac{d}{dt}\check{\xi} = A_\xi(\phi)\check{\xi}(x, \theta) + B_\xi(\phi)v - B_\xi(\phi) [L_f^2h(x, \theta) - L_f^2h(\hat{x}, \theta)] - B_\xi(\phi) [L_f^2h(\hat{x}, \theta) - L_f^2h(\hat{x}, \hat{\theta})]. \quad (7.66)$$

Equation 7.66 describes the nominal linearized input-output map  $\frac{d}{dt}\check{\xi} = A_\xi(\phi)\check{\xi}(x, \theta) + B_\xi(\phi)v$  being driven by two perturbations. The first perturbation  $-B_\xi(\phi) [L_f^2h(x, \theta) - L_f^2h(\hat{x}, \theta)]$  results from the pseudo estimation error in the input-output feedback due to the state estimation process; the second perturbation  $-B_\xi(\phi) [L_f^2h(\hat{x}, \theta) - L_f^2h(\hat{x}, \hat{\theta})]$  results from the pseudo estimation error in the input-output feedback due to the parameter estimation process.

The tracking loop uses the nominal linearized input-output map

$$\frac{d}{dt}\check{\xi} = A_\xi(\phi)\check{\xi}(x, \theta) + B_\xi(\phi)v,$$

in an adaptive LQ optimal control architecture. The adaptive LQ architecture finds the state feedback that drives the tracking error to zero. The state feedback is obtained in the self-tuning loop that

1. performs online parameter identification on the linearized input-output map,
2. finds the mapping between the state feedback parameters and the system parameters,
3. implements the state feedback parameters with the parameter estimate by applying the certainty equivalence principle.

Online parameter identification is performed by using recursive least squares combined with exponential forgetting and projection [124, 125]. Least squares provide the parameter estimate by curve fitting a mathematical model to observed data, and minimizing a quadratic cost function on the observation error, the difference between the observed value and the estimated value [124]. Exponential forgetting places more emphasis on new data by discarding old data. Projection uses prior knowledge of the parameter  $\phi$  to restrict the parameter search space to a bounded convex set  $\Phi$  such that  $\phi \in \Phi$ . The result is an online parameter identification process with parameter update laws in the constrained convex set. There are additional benefits to using projection in adaptive systems. Projection reduces

large transients in the parameter trajectories and ensures the estimated plant is controllable (well-posed) for all time [125]. The parameter identification approach is discussed as follows: first the parameter update laws are derived using recursive least squares with exponential forgetting, then the parameter update laws are combined with projection.

The implementation of recursive least squares require  $\frac{d}{dt}\check{\xi} = A_{\xi}(\phi)\check{\xi}(x, \theta) + B_{\xi}(\phi)v$  be expressed with a mathematical model in linear parametric form. The mathematical model is obtained by expressing  $\frac{d}{dt}\check{\xi} = A_{\xi}(\phi)\check{\xi}(x, \theta) + B_{\xi}(\phi)v$  in its second order differential input-output form, and taking its Laplace transform to yield

$$s^2\check{\xi}_1(x, \theta) = -\phi_1\check{\xi}_1(x, \theta) - \phi_2s\check{\xi}_1(x, \theta) + \phi_3v, \quad (7.67)$$

where  $\check{\xi}_1(x, \theta) = r - h(x, \theta)$  is the observed value and  $s$  is the Laplace domain variable. Equation 7.67 requires the the observed value and its first two derivatives be available. However, the derivatives are not available and measuring derivatives is bad due to noise amplification at high frequencies. The derivative measurements are obtained by low-pass filtering equation 7.67 with a second-order filter  $(s + \omega_{\phi})^2$ , where  $\omega_{\phi}$  is the frequency chosen by the user. Applying the low-pass filter to equation 7.67 yields

$$\check{\xi}_1 = \begin{bmatrix} \frac{1}{(s+\omega_{\phi})^2}\check{\xi}_1 & \frac{s}{(s+\omega_{\phi})^2}\check{\xi}_1 & \frac{1}{(s+\omega_{\phi})^2}v \end{bmatrix} \begin{bmatrix} \omega_{\phi}^2 - \phi_1 \\ 2\omega_{\phi} - \phi_2 \\ \phi_3 \end{bmatrix} = w^T\phi, \quad (7.68)$$

yields the observed value being described with a mathematical model in linear parametric form. The system parameter is  $\phi = [\omega_{\phi}^2 - \phi_1, 2\omega_{\phi} - \phi_2, \phi_3]^T$ . The regression vector  $w$  is the filtered version of the observed value  $\check{\xi}(x, \theta)$  and the input  $v$ . The observed value is then estimated using the mathematical value in equation 7.68 by  $\hat{\xi}_1 = w^T\hat{\phi}$ , where  $\hat{\phi}$  is the parameter estimate.

Parameter estimation with an unconstrained minimization problem described by

$$\begin{aligned} \text{minimize } & J = \int_0^t \exp(-\beta(t-\tau)) \left( \check{\xi}_1(\tau) - w^T(\tau)\hat{\phi}(t) \right)^2 d\tau, \\ \text{subject to } & \hat{\phi} \in \mathbb{R}^3, \end{aligned} \quad (7.69)$$

where  $\beta$  is a positive constant that describes the exponential forgetting factor. Taking its gradient yields the parameter estimate

$$\hat{\phi}(t) = \left( \int_0^t \exp(-\beta(t-\tau)) w(\tau)w^T(\tau)d\tau \right)^{-1} \int_0^t \exp(-\beta(t-\tau)) w(\tau)\check{\xi}_1(\tau)d\tau. \quad (7.70)$$

Defining the symmetric matrix  $P_\phi$  as

$$P_\phi(t) = \left( \int_0^t \exp(-\beta(t-\tau)) w(\tau)w^T(\tau)d\tau \right)^{-1}, \quad (7.71)$$

allows for the update laws in the parameter estimation to be described as [124],

$$\dot{P}_\phi = \beta P_\phi - P_\phi w w^T P_\phi, \quad \text{with } P_\phi(0) > 0, \quad (7.72a)$$

$$\dot{\hat{\phi}} = P_\phi w \epsilon, \quad (7.72b)$$

where  $\epsilon = \check{\xi}_1(t) - w^T(t)\hat{\phi}(t)$  is the observation error. The parameter estimate converges to the true parameter  $\hat{\phi} \rightarrow \phi$  when the matrix  $P_\phi$  is positive definite. The matrix  $P_\phi$  is positive definite when the regression vector  $w$  is persistently exciting. The persistent exciting condition is satisfied when there exists positive constants  $\delta_1$ ,  $\delta_2$ , and  $T$  such that

$$\delta_1 I_3 \leq \int_t^{t+T} w(\tau)w^T(\tau)d\tau \leq \delta_3 I_3. \quad (7.73)$$

The persistent excitation condition is made on the tracking error and the auxiliary control input. If the condition is not satisfied, then a perturbation signal of Gaussian white noise is added to the auxiliary control input and its power spectral density is increased until the condition is satisfied. Caution needs to be taken when adding a perturbing white noise signal to the system because the system performance may degrade as a result.

The parameter update laws in equation 7.72 has the following properties [125]:

1. The signals  $\check{\xi}(\hat{x}, \hat{\theta}), v \in L_\infty$  due to assumption 9 implies  $w, P, \hat{\phi}, \frac{d}{dt}\hat{\phi} \in L_\infty$ .
2. The signal  $\frac{d}{dt}\hat{\phi} \in L_2$
3. When the signal  $w \in L_\infty$  and  $w$  is PE, then  $\check{\phi} = \phi - \hat{\phi}$  converges exponentially to zero.

Equation 7.72 describes the parameter update laws for an unconstrained search algorithm because the parameter can be everywhere or  $\phi \in \mathbb{R}^3$ . The unconstrained search algorithm can lead to two problems: large transients in the parameter trajectories and the estimated plant may not being controllable or well-posed for all time. In this research, both problems are addressed by modifying the parameter update laws with projection. Projection uses prior knowledge of the system parameter to constrain the parameter search to the constrained convex set  $\Phi$  such that  $\phi \in \Phi \subset \mathbb{R}^3$ . The importance of embedding the true parameter in a convex set is to save the properties/features of the parameter update laws that were established in the unconstrained case when  $\phi \in \Phi$ ,  $\forall t \geq 0$  and  $\hat{\phi}(0) \in \Phi$  [125].

The combination of projection with the recursive least squares and exponential forgetting turns the parameter estimation problem into a constrained minimization problem. The constrained minimization problem is [125]

$$\begin{aligned} \text{minimize } J &= \int_0^t \exp(-\beta(t-\tau)) \left( \check{\xi}_1(\tau) - w^T(\tau)\hat{\phi}(t) \right)^2 d\tau, \\ \text{subject to } \hat{\phi} &\in \Phi, \end{aligned} \quad (7.74)$$

where  $\Phi$  is the constrained convex set that is defined by

$$\Phi = \{\phi \in \mathbb{R}^3 | g(\hat{\phi}) \leq 0\}, \quad \text{where } g(\hat{\phi}) = (\phi_0 - \hat{\phi})^T(\phi_0 - \hat{\phi}) - M_o^2, \quad (7.75)$$

and  $\phi_0$  describes the center of the convex set. The parameter update laws in equation 7.72 are modified by the projection algorithm and are described by

$$\dot{P}_\phi = \begin{cases} \beta P_\phi - P_\phi w w^T P_\phi, & \text{if } \hat{\phi} \in \Phi^o, \text{ or } \phi \in \partial\Phi \text{ and } (P_\phi w \epsilon)^T \nabla g \leq 0 \\ 0, & \text{otherwise,} \end{cases} \quad (7.76a)$$

$$\dot{\hat{\phi}} = \begin{cases} P_\phi w \epsilon, & \text{if } \hat{\phi} \in \Phi^o, \text{ or } \phi \in \partial\Phi \text{ and } (P_\phi w \epsilon)^T \nabla g \leq 0, \\ \left(1 - \frac{P \nabla g \nabla g^T}{\nabla g^T P \nabla g}\right) P_\phi w \epsilon, & \text{otherwise.} \end{cases} \quad (7.76b)$$

The modified parameter update laws have the following features [125]:

1. When  $\hat{\phi}(0) \in \Phi$  with  $\hat{\phi} \in \Phi$  and  $g(\hat{\phi}) < 0$ , the parameter update laws are that of the unconstrained parameter update laws in the absence of projection and guarantees  $\hat{\phi} \in \Phi$ .

2. When  $\hat{\phi} \in \partial\Phi$  (where  $\partial\Phi$  is the boundary of  $\Phi$ ) and the direction of the search is directed toward the interior of  $\Phi$  (equivalent to  $P_\phi w \epsilon \nabla g \leq 0$ ), then the update parameter laws are that of the unconstrained parameter update laws.
3. When  $\hat{\phi} \in \partial\Phi$  and the direction of the search is directed toward the exterior of  $\Phi$  (equivalent to  $P_\phi w \epsilon \nabla g > 0$ ), then the projection is used. In this case, a constant adaptation gain  $P_\phi$  is used and  $\frac{d}{dt}\hat{\phi}$  is modified by projecting the negative of the gradient of the cost function onto the constrained parameter set  $\Phi$ .

The second aspect of adaptive self-tuning controllers is to find the mapping between the plant parameters and the control parameters. The map is found by using  $\frac{d}{dt}\check{\xi} = A_\xi(\phi)\check{\xi}(x, \theta) + B_\xi(\phi)v$  in an LQ control algorithm and solving for the control parameters (state feedback gains) in terms of the plant parameters. The LQ control problem is a constrained minimization problem described by

$$\begin{aligned} \text{minimize } J &= \frac{1}{2} \int_0^\infty \left[ \check{\xi}^T(x, \theta) Q_\xi \check{\xi}(x, \theta) + R_\xi v^2 \right] d\tau, \text{ with } Q = \begin{bmatrix} q_1 & 0 \\ 0 & q_2 \end{bmatrix}, \\ \text{subject to } \frac{d}{dt}\check{\xi} &= A(\phi)\check{\xi}(x, \theta) + B_\xi(\phi)v, \end{aligned} \quad (7.77)$$

where  $Q_\xi = Q_\xi^T > 0$  is the weighted matrix on the tracking error and  $R_\xi > 0$  is the weight placed on the auxiliary control. The constrained minimization problem is turned into an unconstrained minimization problem of higher dimension with the new objective is to minimize the Hamiltonian function

$$H(\check{\xi}, \lambda, v) = \frac{1}{2} \check{\xi}^T(x, \theta) Q_\xi \check{\xi}(x, \theta) + \frac{1}{2} R_\xi v^2 + \lambda^T (A_\xi(\phi)\check{\xi}(x, \theta) + B_\xi(\phi)v). \quad (7.78)$$

The Hamiltonian function is minimized when its gradient  $\nabla H = 0$ , which is equivalent to the optimality conditions satisfying

$$\frac{d}{dt}\check{\xi} = \frac{\partial H}{\partial \lambda} = A_\xi(\phi)\check{\xi}(x, \theta) + B_\xi(\phi)v \quad (7.79a)$$

$$\dot{\lambda} = -\frac{\partial H}{\partial \check{\xi}} = -Q_\xi \check{\xi}(x, \theta) - A_\xi^T(\phi)\lambda \quad (7.79b)$$

$$0 = \frac{\partial H}{\partial v} = R_\xi v + B_\xi^T(\phi)\lambda. \quad (7.79c)$$

The auxiliary control depends on the costate by  $v = -R_\xi^{-1}B_\xi^T(\phi)\lambda$ . Its implementation requires the auxiliary control be explicitly expressed in the tracking error not the costate. The auxiliary control is expressed in the tracking error by relating the costate to the tracking error with a standard optimal control assumption  $\lambda = P_\xi(\phi)\check{\xi}(x, \theta), \forall t$ , where the matrix  $P_\xi(\phi)$  is  $P_\xi(\phi) = P_\xi^T(\phi) \geq 0$ . The matrix  $P_\xi$  is the solution to the differential Riccati equation [109]

$$\dot{P}_\xi = -P_\xi(\phi)A_\xi(\phi) - A_\xi^T(\phi)P_\xi(\phi) - Q_\xi + P_\xi(\phi)B_\xi(\phi)R_\xi^{-1}B_\xi^T(\phi)P_\xi(\phi), \quad (7.80)$$

where

$$P_\xi(\phi) = \begin{bmatrix} p_1(\phi) & p_2(\phi) \\ p_2(\phi) & p_3(\phi) \end{bmatrix}.$$

The differential Riccati equation is model equation and driven by the weights  $Q_\xi$  and  $R_\xi$ . The LQ controller is going to operate longer than its time constant and this fact allows the solution to the differential Riccati equation to be simplified by only considering its steady-state solution ( $\dot{P}_\xi = 0$ ). The differential Riccati equation is turned into an algebraic Riccati equation,

$$P_\xi(\phi)A_\xi(\phi) + A_\xi^T(\phi)P_\xi(\phi) + Q_\xi - P_\xi(\phi)B_\xi(\phi)R_\xi^{-1}B_\xi^T(\phi)P_\xi(\phi) = 0, \quad (7.81)$$

and its solution is

$$p_1(\phi) = -\frac{R\phi_1\phi_2}{\phi_3^2} + \frac{\phi_3^2}{R} \sqrt{\left(\frac{R\phi_1}{\phi_3^2}\right)^2 + \left(\frac{Rq_1}{\phi_3^2}\right)} \times \quad (7.82a)$$

$$\frac{\phi_3^2}{R} \sqrt{\left(\frac{R\phi_2}{\phi_3^2}\right)^2 + \frac{Rq_2}{\phi_3^2} - \frac{2R^2}{\phi_3^2} + \frac{2R}{\phi_3} \sqrt{\left(\frac{R\phi_1}{\phi_3^2}\right)^2 + \left(\frac{Rq_1}{\phi_3^2}\right)}}$$

$$p_2(\phi) = -\frac{R\phi_1}{\phi_3^2} + \sqrt{\left(\frac{R\phi_1}{\phi_3^2}\right)^2 + \left(\frac{Rq_1}{\phi_3^2}\right)} \quad (7.82b)$$

$$p_3(\phi) = -\frac{R\phi_2}{\phi_3^2} + \sqrt{\left(\frac{R\phi_2}{\phi_3^2}\right)^2 + \frac{Rq_2}{\phi_3^2} - \frac{2R^2}{\phi_3^2} + \frac{2R}{\phi_3} \sqrt{\left(\frac{R\phi_1}{\phi_3^2}\right)^2 + \left(\frac{Rq_1}{\phi_3^2}\right)}}. \quad (7.82c)$$

The Riccati solution relates the auxiliary control to the tracking error via  $\lambda = P_\xi(\phi)\check{\xi}(x, \theta)$  to yield the auxiliary control being

$$v(\check{\xi}(x, \theta), \phi) = -R_\xi^{-1}B_\xi^T(\phi)P_\xi(\phi)\check{\xi}(x, \theta) = -\begin{bmatrix} \frac{\phi_3 p_2(\phi)}{R_\xi} & \frac{\phi_3 p_3(\phi)}{R_\xi} \end{bmatrix} \check{\xi}(x, \theta) = -K_\xi(\phi)\check{\xi}(x, \theta), \quad (7.83)$$

with the state feedback gain  $K_\xi(\phi) = [k_1(\phi), k_2(\phi)]^T$  being

$$k_1(\phi) = \phi_3 p_2(\phi) = -\frac{\phi_1}{\phi_3} + \frac{\phi_3}{R} \sqrt{\left(\frac{R\phi_1}{\phi_3}\right)^2 + \frac{Rq_1}{\phi_3^2}} \quad (7.84a)$$

$$k_2(\phi) = \phi_3 p_3(\phi) = -\frac{\phi_2}{\phi_3} + \frac{\phi_3}{R} \sqrt{\left(\frac{R\phi_2}{\phi_3}\right)^2 + \frac{Rq_2}{\phi_3^2} - \frac{2R^2}{\phi_3^2} + \frac{2R}{\phi_3} \sqrt{\left(\frac{R\phi_1}{\phi_3}\right)^2 + \frac{Rq_1}{\phi_3^2}}}. \quad (7.84b)$$

The algebraic Riccati equation in equation 7.81 and the state feedback in equation 7.83 describes the mapping between the state feedback gains and the system parameters. The mapping is combined with the certainty equivalence principle to create a self-tuning adaptive LQ controller [124]. The certainty equivalence principle implies that the parameter estimate is used as true parameter for the plant, then the estimated plant is used in the LQ control algorithm, and the algebraic Riccati equation and state feedback are implemented with the state estimates. The result is the state feedback is updated indirectly based on the parameter estimation process. The implementation of the adaptive LQ controller, the algebraic Riccati equation and the state feedback, uses the state estimate and the parameter estimate to yield

$$P_\xi(\hat{\phi})A_\xi(\hat{\phi}) + A_\xi^T(\hat{\phi})P_\xi(\hat{\phi}) + Q_\xi - P_\xi(\hat{\phi})B_\xi(\hat{\phi})R_\xi^{-1}B_\xi^T(\hat{\phi})P_\xi(\hat{\phi}) = 0, \quad (7.85)$$

$$v(\check{\xi}(\hat{x}, \hat{\theta}), \hat{\phi}) = -R_\xi^{-1}B_\xi^T(\hat{\phi})P_\xi(\hat{\phi})\check{\xi}(\hat{x}, \hat{\theta}) \quad (7.86)$$

The certainty equivalence principle is implementable when the estimated plant with parameters  $\hat{\phi}$  is controllable or at least stabilizable for all time  $\forall t \geq 0$ . For the estimated plant to be controllable, a condition is placed on the parameter estimate  $\hat{\phi}_3$ , which is  $\hat{\phi}_3$  cannot be zero or change sign. This condition must hold for the estimated plant be controllable and for the existness and uniform boundedness of the solution to the Riccati equation  $P(\hat{\phi})$  and the state feedback  $K(\hat{\phi})$ . Therefore, satisfying the condition placed on  $\hat{\phi}_3$  is the motivating idea to implement the projection algorithm in the parameter estimation process.

The dynamics for the closed-loop tracking error are obtained by substituting the auxiliary control in equation 7.86 into equation 7.66, and adding and subtracting the term

$$A_\xi(\hat{\phi})\check{\xi}(x, \theta) + B_\xi(\hat{\phi})v(\check{\xi}(x, \theta), \hat{\phi}) + B_\xi(\phi)v(\check{\xi}(x, \theta), \hat{\phi}) + B_\xi(\phi)v(\check{\xi}(\hat{x}, \theta), \hat{\phi})$$

to equation 7.66. Then, the dynamics for the closed-loop tracking error is described by

$$\begin{aligned} \frac{d}{dt}\check{\xi} &= \left[ A_\xi(\hat{\phi}) - B_\xi(\hat{\phi})R_\xi^{-1}B_\xi^T(\hat{\phi})P_\xi \right] \check{\xi}(x, \theta) \\ &+ \left[ A_\xi(\phi) - A_\xi(\hat{\phi}) \right] \check{\xi}(x, \theta) + \left[ B_\xi(\phi) - B_\xi(\hat{\phi}) \right] v(\check{\xi}(x, \theta), \hat{\phi}) \\ &- B_\xi(\phi) \left[ L_f^2 h(x, \theta) - L_f^2 h(\hat{x}, \theta) \right] - B_\xi(\phi) \left[ L_f^2 h(\hat{x}, \theta) - L_f^2 h(\hat{x}, \hat{\theta}) \right] \\ &+ B_\xi(\phi)R_\xi^{-1}B_\xi^T(\hat{\phi})P_\xi(\hat{\phi}) \left[ \check{\xi}(x, \theta) - \check{\xi}(\hat{x}, \theta) \right] + B_\xi(\phi)R_\xi^{-1}B_\xi^T(\hat{\phi})P_\xi(\hat{\phi}) \left[ \check{\xi}(\hat{x}, \theta) - \check{\xi}(\hat{x}, \hat{\theta}) \right] \end{aligned} \quad (7.87)$$

The dynamics for the closed-loop tracking error is driven by five perturbation terms:

1. The perturbation  $-B_\xi(\phi) \left[ L_f^2 h(x, \theta) - L_f^2 h(\hat{x}, \theta) \right]$  results from the pseudo estimation error in the input-output linearization due to the state estimation process,
2. The perturbation  $-B_\xi(\phi) \left[ L_f^2 h(\hat{x}, \theta) - L_f^2 h(\hat{x}, \hat{\theta}) \right]$  results from the pseudo estimation error in the input-output linearization due to the parameter estimation process,
3. The perturbation  $B_\xi(\phi)R_\xi^{-1}B_\xi^T(\hat{\phi})P_\xi(\hat{\phi}) \left[ \check{\xi}(x, \theta) - \check{\xi}(\hat{x}, \theta) \right]$  results from the pseudo estimation error in the tracking error definition due to the state estimation process,
4. The perturbation  $B_\xi(\phi)R_\xi^{-1}B_\xi^T(\hat{\phi})P_\xi(\hat{\phi}) \left[ \check{\xi}(\hat{x}, \theta) - \check{\xi}(\hat{x}, \hat{\theta}) \right]$  results from the pseudo estimation error in the tracking error definition due to the parameter estimation process.
5. The perturbation  $\left[ A_\xi(\phi) - A_\xi(\hat{\phi}) \right] \check{\xi}(x, \theta) + \left[ B_\xi(\phi) - B_\xi(\hat{\phi}) \right] v(\check{\xi}(x, \theta), \hat{\phi})$  results from the parameter estimation process in the adaptive LQ architecture.

The perturbation  $\left[ A_\xi(\phi) - A_\xi(\hat{\phi}) \right] \check{\xi}(x, \theta) + \left[ B_\xi(\phi) - B_\xi(\hat{\phi}) \right] v(\check{\xi}(x, \theta), \hat{\phi})$  is

$$\begin{aligned} &\left[ A_\xi(\phi) - A_\xi(\hat{\phi}) \right] \check{\xi}(x, \theta) + \left[ B_\xi(\phi) - B_\xi(\hat{\phi}) \right] v(\check{\xi}(x, \theta), \hat{\phi}) \\ &= B_\phi \left[ -\check{\xi}_1(x, \theta) \quad -\frac{d}{dt}\check{\xi}_1(x, \theta) \quad v(\check{\xi}(x, \theta), \hat{\phi}) \right] \check{\phi}, \end{aligned} \quad (7.88)$$

where the matrix  $B_\phi = [0, 1]^T$  and the parameter estimation error is defined as  $\check{\phi} = \phi - \hat{\phi}$ . It is convenient to express the term  $B_\phi \left[ -\check{\xi}_1(x, \theta)\check{\phi}_1 - \frac{d}{dt}\check{\xi}_1(x, \theta)\check{\phi}_2 + v(\check{\xi}(x, \theta), \hat{\phi})\check{\phi}_3 \right]$  in terms

of the regression vector  $w$ , that was obtained from the adaptive LQ parameter estimation process. It is straightforward to show

$$B_\phi \left[ -\check{\xi}_1(x, \theta) \check{\phi}_1 - \frac{d}{dt} \check{\xi}_1(x, \theta) \check{\phi}_2 + v(\check{\xi}(x, \theta), \hat{\phi}) \check{\phi}_3 \right] = B_\phi [\ddot{w}^T + 2\omega_\phi \dot{w}^T + \omega_\phi^2 w^T] \check{\phi}. \quad (7.89)$$

Next, the dynamics for the closed-loop tracking error is expressed in terms of the regression vector  $w$  and the parameter estimation error  $\check{\phi}$  by substituting equation 7.88 and equation 7.89 into equation 7.87 to yield

$$\begin{aligned} \frac{d}{dt} \check{\xi} = & \left[ A_\xi(\hat{\phi}) - B_\xi(\hat{\phi}) R_\xi^{-1} B_\xi^T(\hat{\phi}) P_\xi \right] \check{\xi}(x, \theta) + B_\phi (\ddot{w}^T + 2\omega_\phi \dot{w}^T + \omega_\phi^2 w^T) \check{\phi} \\ & - B_\xi(\phi) [L_f^2 h(x, \theta) - L_f^2 h(\hat{x}, \theta)] - B_\xi(\phi) [L_f^2 h(\hat{x}, \theta) - L_f^2 h(\hat{x}, \hat{\theta})] \\ & + B_\xi(\phi) R_\xi^{-1} B_\xi^T(\hat{\phi}) P_\xi(\hat{\phi}) [\check{\xi}(x, \theta) - \check{\xi}(\hat{x}, \theta)] + B_\xi(\phi) R_\xi^{-1} B_\xi^T(\hat{\phi}) P_\xi(\hat{\phi}) [\check{\xi}(\hat{x}, \theta) - \check{\xi}(\hat{x}, \hat{\theta})] \end{aligned} \quad (7.90)$$

It is insightful to assess the effectiveness of the adaptive nonlinear design on the closed-loop system by quantifying the closed-loop bias.

## 7.4 STATISTICAL ANALYSIS ON THE CLOSED-LOOP COMPOSITE SYSTEM

The dynamics for the closed-loop composite system is:

1. The dynamics for the closed-loop tracking error in equation 7.90

$$\begin{aligned} \frac{d}{dt} \check{\xi} = & \left[ A_\xi(\hat{\phi}) - B_\xi(\hat{\phi}) R_\xi^{-1} B_\xi^T(\hat{\phi}) P_\xi \right] \check{\xi}(x, \theta) + B_\phi (\ddot{w}^T + 2\omega_\phi \dot{w}^T + \omega_\phi^2 w^T) \check{\phi} \\ & - B_\xi(\phi) [L_f^2 h(x, \theta) - L_f^2 h(\hat{x}, \theta)] - B_\xi(\phi) [L_f^2 h(\hat{x}, \theta) - L_f^2 h(\hat{x}, \hat{\theta})] \\ & + B_\xi(\phi) R_\xi^{-1} B_\xi^T(\hat{\phi}) P_\xi(\hat{\phi}) \left( [\check{\xi}(x, \theta) - \check{\xi}(\hat{x}, \theta)] + [\check{\xi}(\hat{x}, \theta) - \check{\xi}(\hat{x}, \hat{\theta})] \right). \end{aligned}$$

2. The dynamics for the internal states in equation 7.64

$$\dot{\psi} = \delta(\xi_r - \check{\xi}(x, \theta), \phi).$$

3. The dynamics for the parameter estimation in the adaptive LQ architecture are obtained by combining recursive least squares with exponential forgetting and projection as shown in equation 7.76

$$\dot{P}_\phi = \begin{cases} \beta P_\phi - P_\phi w w^T P_\phi, & \text{if } \hat{\phi} \in \Phi^o, \text{ or } \phi \in \partial\Phi \text{ and } (P_\phi w \epsilon)^T \nabla g \leq 0 \\ 0, & \text{otherwise,} \end{cases}$$

$$\dot{\hat{\phi}} = \begin{cases} P_\phi w \epsilon, & \text{if } \hat{\phi} \in \Phi^o, \text{ or } \phi \in \partial\Phi \text{ and } (P_\phi w \epsilon)^T \nabla g \leq 0, \\ \left(1 - \frac{P_\phi w \nabla g \nabla g^T}{\nabla g^T P_\phi \nabla g}\right) P_\phi w \epsilon, & \text{otherwise.} \end{cases}$$

4. The dynamics for the closed-loop adaptive state observer given in section 7.2,
- a. The dynamics for the auxiliary state in equation 7.42

$$\begin{aligned} \frac{d}{dt} \hat{q} &= \lambda A_m \hat{q} + \lambda S^{-1} C_m^T C_m N \hat{\theta} - \lambda S^{-1} C_m^T j(C_m \hat{m}) \\ &\quad + \Lambda(g_1(m, u) - g_1(\hat{m}, u)) + \Lambda(g_2(m) - g_2(\hat{m}))\theta. \end{aligned}$$

- b. The dynamics for the scaled parameter estimation error in equation 7.38

$$\frac{d}{dt} \hat{\theta} = -\lambda P N^T C_m^T j(C_m \hat{m}).$$

- c. The dynamics for the  $N$  dynamics in equation 7.24c

$$\dot{N} = \lambda(A_m - S^{-1} C_m^T C_m)N + \lambda \Psi(\hat{m}).$$

- d. The dynamics for the time-varying adaptive gain matrix  $P_\theta$  in equation 7.24d

$$\dot{P}_\theta = -\lambda P_\theta N^T C_m^T C_m N P_\theta + \lambda P_\theta.$$

The following assumptions are used:

**Assumption 12.** The Lie derivative  $L_f^2 h(x, \theta)$  is Lipschitz in both  $x$  and  $\theta$ . The Lipschitz condition implies there exists positive constants  $l_1$  and  $l_2$  such that

$$\|L_f^2 h(m, \theta) - L_f^2 h(\hat{m}, \theta)\| \leq l_1 \|\check{m}\| \quad (7.92a)$$

$$\|L_f^2 h(\hat{x}, \theta) - L_f^2 h(\hat{x}, \hat{\theta})\| \leq l_2 \|\check{\theta}\| \quad (7.92b)$$

The state  $x$  is related to the state  $m$  through a one-to-one mapping due to the state transformation  $m(x)$  in equation 7.11. The one-to-one map allows the term  $L_f^2 h(x, \theta)$  to be expressed as  $L_f^2 h(m, \theta)$ .

**Assumption 13.** The tracking error  $\check{\xi}(x, \theta)$  is Lipschitz in both  $x$  and  $\theta$ . The Lipschitz condition implies there exists positive constants  $l_3$  and  $l_4$  such that

$$\|\check{\xi}(m, \theta) - \check{\xi}(\hat{m}, \theta)\| \leq l_3 \|\check{m}\| \quad (7.93a)$$

$$\|\check{\xi}(\hat{m}, \theta) - \check{\xi}(\hat{m}, \hat{\theta})\| \leq l_4 \|\check{\theta}\| \quad (7.93b)$$

The state  $x$  is related to the state  $m$  through a one-to-one mapping due to the state transformation  $m(x)$  in equation 7.11. The one-to-one map allows the term  $\check{\xi}(x, \theta)$  to be expressed as  $\check{\xi}(m, \theta)$ .

**Assumption 14.** Assumption 9 states the state  $x$ , the input  $v$ , and the parameters  $\theta$  are bounded for all time. The use of assumption 9 implies the regression vector  $w$  and its first two derivatives are bounded for all time. Then, there exists a positive constant  $l_6$  such that

$$\|\ddot{w} + 2\omega_\phi \dot{w} + \omega_\phi^2 w\| \leq l_6, \quad \forall t \geq 0. \quad (7.94)$$

**Assumption 15.** The state  $m$ , the control input  $u$ , and the parameters  $\theta$  are bounded for all time. This assumption is standard for high-gain adaptive state observers [117, 121].

**Assumption 16.** The vector field  $b_1(m)$  is Lipschitz in  $m$ . The Lipschitz condition implies there exists a positive constant  $l_7$  such that

$$\|b_1(m) - b_1(\hat{m})\| \leq l_7 \|\check{m}\|. \quad (7.95)$$

**Assumption 17.** *The vector field  $b_2(m)$  is Lipschitz. The Lipschitz condition implies there exists a positive constant  $l_8$  such that*

$$\|b_2(m) - b_2(\hat{m})\| \leq l_8 \|\check{m}\|. \quad (7.96)$$

**Theorem 5** (Closed-loop Adaptive System). *The dynamics for the expected value of the closed-loop composite system are described by the tracking error in equation 7.90, the internal states in equation 7.64, and the parameter estimation for the adaptive LQ architecture in equation 7.76, and the adaptive state observer in section 7.2. Then, for every bounded input that satisfies the persistent excitation condition in equation 7.26 and equation 7.73, there exists a positive constant  $\lambda_o$ , such that for every positive constant  $\lambda > \lambda_o$ , the closed-loop composite system is uniformly ultimately bounded for high values of  $\lambda$ .*

*Proof.* The stability analysis is performed on the auxiliary state  $\dot{q}$ , the scaled parameter estimation error  $\dot{\theta}$ , the tracking error  $\check{\xi}(x, \theta)$ , and the parameter estimation error  $\check{\phi}$ . The Lyapunov function candidate is

$$\begin{aligned} W(\dot{q}, \dot{\theta}, \check{\xi}(x, \theta), \check{\phi}) &= W_1(\dot{q}) + W_2(\dot{\theta}) + W_3(\check{\xi}(x, \theta)) + W_4(\check{\phi}) \\ &= \dot{q}^T S \dot{q} + \dot{\theta}^T P_\theta^{-1} \dot{\theta} + \check{\xi}^T(x, \theta) P_\xi \check{\xi}(x, \theta) + \check{\phi}^T P_\phi^{-1} \check{\phi}, \end{aligned} \quad (7.97)$$

which is lower and upper bounded by

$$\Upsilon_1 \left( \|\dot{q}\|^2 + \|\dot{\theta}\|^2 + \|\check{\xi}(x, \theta)\|^2 \right) \leq W \leq \Upsilon_2 \left( \|\dot{q}\|^2 + \|\dot{\theta}\|^2 + \|\check{\xi}(x, \theta)\|^2 \right) + \Upsilon_3 M_o^2, \quad (7.98a)$$

where the  $\Upsilon_1, \Upsilon_2, \Upsilon_3$  are positive constants with  $\Upsilon_1$  and  $\Upsilon_2$  defined as

$$\Upsilon_1 \leq \min(\lambda_{\min}(S), \lambda_{\min}(P_\theta^{-1}), \lambda_{\min}(P_\xi)) \quad (7.99)$$

$$\Upsilon_2 \geq \max(\lambda_{\max}(S), \lambda_{\max}(P_\theta^{-1}), \lambda_{\max}(P_\xi)) \quad (7.100)$$

Taking the time derivative of equation 7.97 yields

$$\begin{aligned} \dot{W} &= \dot{W}_1 + \dot{W}_2 + \dot{W}_3 + \dot{W}_4 \\ &= \frac{d}{dt} \dot{q}^T S \dot{q} + \dot{q}^T S \frac{d}{dt} \dot{q} + \frac{d}{dt} \check{\xi}^T P_\xi \check{\xi} + \check{\xi}^T P_\xi \frac{d}{dt} \check{\xi} \\ &\quad + 2\dot{\theta}^T P_\theta^{-1} \frac{d}{dt} \dot{\theta} - \dot{\theta}^T P_\theta^{-1} \dot{P}_\theta P_\theta^{-1} \dot{\theta} + 2\check{\phi}^T P_\phi^{-1} \frac{d}{dt} \check{\phi} - \check{\phi}^T P_\phi^{-1} \dot{P}_\phi P_\phi^{-1} \check{\phi}. \end{aligned} \quad (7.101)$$

The stability analysis is simplified by grouping the terms in equation 7.101, finding the bound for each group, and combining the results of each group. Equation 7.101 is grouped as:

1. Adaptive state observer group:  $\dot{W}_1 + \dot{W}_2$
2. Tracking error group:  $\dot{W}_3$
3. Recursive least squares for control group:  $\dot{W}_4$

A stability analysis is performed for each group.

1. The adaptive state observer group is

$$\dot{W}_1 + \dot{W}_2 = \frac{d}{dt} \dot{q}^T S \dot{q} + \dot{q}^T S \frac{d}{dt} \dot{q} + 2\dot{\theta}^T P_\theta^{-1} \frac{d}{dt} \dot{\theta} - \dot{\theta}^T P_\theta^{-1} \dot{P}_\theta P_\theta^{-1} \dot{\theta}. \quad (7.102)$$

The analysis is the same as given in the proof of theorem 4 for the adaptive state observer. Equation 7.102 is bounded by

$$\dot{W}_1 + \dot{W}_2 \leq -(\lambda - \eta_1)W_1(\dot{q}) - (\lambda - \eta_1)W_2(\dot{\theta}). \quad (7.103)$$

The Lyapunov functions  $W_1(\dot{q})$  and  $W_2(\dot{\theta})$  are bounded in terms of  $\|\dot{q}\|^2$  and  $\|\dot{\theta}\|^2$  by using equation 7.98 to yield

$$\dot{W}_1 + \dot{W}_2 \leq -(\lambda - \eta_1)\lambda_{\min}(S)\|\dot{q}\|^2 - (\lambda - \eta_2)\lambda_{\min}(P_\theta)\|\dot{\theta}\|^2. \quad (7.104)$$

2. The tracking error group is

$$\dot{W}_3 = \frac{d}{dt} \check{\xi}^T P_\xi \check{\xi} + \check{\xi}^T P_\xi \frac{d}{dt} \check{\xi}. \quad (7.105)$$

Substitute the tracking error dynamics in equation 7.90 into equation 7.105 yields

$$\begin{aligned} \dot{W}_3 = & \check{\xi}^T(x, \theta) \left( A_\xi^T(\hat{\phi}) P_\xi(\hat{\phi}) + P_\xi(\hat{\phi}) A_\xi(\hat{\phi}) - P_\xi(\hat{\phi}) B_\xi(\hat{\phi}) R_\xi^{-1} B_\xi^T(\hat{\phi}) P_\xi(\hat{\phi}) \right) \check{\xi}(x, \theta) \\ & - \check{\xi}^T(x, \theta) P_\xi(\hat{\phi}) B_\xi(\hat{\phi}) R_\xi^{-1} B_\xi^T(\hat{\phi}) P_\xi(\hat{\phi}) \check{\xi}(x, \theta) \\ & + 2\check{\xi}^T(x, \theta) P_\xi(\hat{\phi}) B_\phi(\hat{\phi}) (\ddot{w}^T + 2\omega_\phi \dot{w}^T + \omega_\phi^2 w^T) \check{\phi} \\ & - 2\check{\xi}^T(x, \theta) P_\xi(\hat{\phi}) B_\xi(\hat{\phi}) \left( [L_f^2 h(x, \theta) - L_f^2 h(\hat{x}, \theta)] + [L_f^2 h(\hat{x}, \theta) - L_f^2 h(\hat{x}, \hat{\theta})] \right) \\ & + 2\check{\xi}^T(x, \theta) P_\xi(\hat{\phi}) B_\xi(\hat{\phi}) R_\xi^{-1} B_\xi^T(\hat{\phi}) P_\xi(\hat{\phi}) \left( [\check{\xi}(x, \theta) - \check{\xi}(\hat{x}, \theta)] + [\check{\xi}(\hat{x}, \theta) - \check{\xi}(\hat{x}, \hat{\theta})] \right) \end{aligned} \quad (7.106)$$

It is straightforward to show that the term  $-\check{\xi}^T(x, \theta)P_\xi(\hat{\phi})B_\xi(\hat{\phi})R_\xi^{-1}B_\xi^T(\hat{\phi})P_\xi(\hat{\phi})\check{\xi}(x, \theta)$  is bounded by

$$-\check{\xi}^T(x, \theta)P_\xi(\hat{\phi})B_\xi(\hat{\phi})R_\xi^{-1}B_\xi^T(\hat{\phi})P_\xi(\hat{\phi})\check{\xi}(x, \theta) \leq 0.$$

The first term in equation 7.106 is simplified by applying the Riccati equation (same as given in equation 7.85)

$$P_\xi(\hat{\phi})A_\xi(\hat{\phi}) + A_\xi^T(\hat{\phi})P_\xi(\hat{\phi}) + Q_\xi - P_\xi(\hat{\phi})B_\xi(\hat{\phi})R_\xi^{-1}B_\xi^T(\hat{\phi})P_\xi(\hat{\phi}) = 0.$$

The last four terms in equation 7.106 are expressed in the state  $x$ . For the stability analysis, it is convenient to express these terms in the state  $m$ . As discussed in section 7.2, a one-to-one map exists between the state  $x$  and the state  $m$ . The one-to-one map allows for the Lie derivative  $L_f^2 h(x, \theta)$  and the tracking error  $\check{\xi}(x, \theta)$  to be expressed equivalently as  $L_f^2 h(m, \theta)$  and  $\check{\xi}(m, \theta)$  respectively. Then, equation 7.106 is equal to

$$\begin{aligned} \dot{W}_3 \leq & -\check{\xi}^T(x, \theta)Q_\xi\check{\xi}(x, \theta) + 2\check{\xi}^T(x, \theta)P_\xi(\hat{\phi})B_\phi(\ddot{w}^T + 2\omega_\phi\dot{w}^T + \omega_\phi^2 w^T)\check{\phi} \\ & - 2\check{\xi}^T(x, \theta)P_\xi(\hat{\phi})B_\xi(\phi) \left( [L_f^2 h(m, \theta) - L_f^2 h(\hat{m}, \theta)] + [L_f^2 h(\hat{m}, \theta) - L_f^2 h(\hat{m}, \hat{\theta})] \right) \\ & + 2\check{\xi}^T(x, \theta)P_\xi(\hat{\phi})B_\xi(\phi)R_\xi^{-1}B_\xi^T(\hat{\phi})P_\xi(\hat{\phi}) \left( [\check{\xi}(m, \theta) - \check{\xi}(\hat{m}, \theta)] + [\check{\xi}(\hat{m}, \theta) - \check{\xi}(\hat{m}, \hat{\theta})] \right) \end{aligned} \quad (7.107)$$

Equation 7.107 is further bounded by taking the norm of the last five terms and applying the properties of positive definite matrices to the first term to yield

$$\begin{aligned} \dot{W}_3 \leq & -\lambda_{\min}(Q_\xi) \left\| \check{\xi}(x, \theta) \right\|^2 + \left\| 2\check{\xi}^T(x, \theta)P_\xi(\hat{\phi})B_\phi(\ddot{w}^T + 2\omega_\phi\dot{w}^T + \omega_\phi^2 w^T)\check{\phi} \right\| \\ & + \left\| 2\check{\xi}^T(x, \theta)P_\xi(\hat{\phi})B_\xi(\phi) [L_f^2 h(m, \theta) - L_f^2 h(\hat{m}, \theta)] \right\| \\ & + \left\| 2\check{\xi}^T(x, \theta)P_\xi(\hat{\phi})B_\xi(\phi) [L_f^2 h(\hat{m}, \theta) - L_f^2 h(\hat{m}, \hat{\theta})] \right\| \\ & + \left\| 2\check{\xi}^T(x, \theta)P_\xi(\hat{\phi})B_\xi(\phi)R_\xi^{-1}B_\xi^T(\hat{\phi})P_\xi(\hat{\phi}) [\check{\xi}(m, \theta) - \check{\xi}(\hat{m}, \theta)] \right\| \\ & + \left\| 2\check{\xi}^T(x, \theta)P_\xi(\hat{\phi})B_\xi(\phi)R_\xi^{-1}B_\xi^T(\hat{\phi})P_\xi(\hat{\phi}) [\check{\xi}(\hat{m}, \theta) - \check{\xi}(\hat{m}, \hat{\theta})] \right\| \end{aligned} \quad (7.108)$$

Next, the norm of the last five terms in equation 7.108 are bounded in terms of  $\|q\|^2$ ,  $\|\theta\|^2$ ,  $\|\check{\xi}(x, \theta)\|^2$ , and  $\|\check{\phi}\|^2$ . These terms are bounded as follows:

- a. The norm  $\left\| 2\check{\xi}^T(x, \theta)P_\xi(\hat{\phi})B_\phi(\ddot{w}^T + 2\omega_\phi\dot{w}^T + \omega_\phi^2w^T)\check{\phi} \right\|$  is bounded by using assumption 14, which implies the regression vector and its derivatives are bounded. Taking the norm of  $2\check{\xi}^T(x, \theta)P_\xi(\hat{\phi})B_\phi(\ddot{w}^T + 2\omega_\phi\dot{w}^T + \omega_\phi^2w^T)\check{\phi}$  yields the bound

$$\left\| 2\check{\xi}^T(x, \theta)P_\xi(\hat{\phi})B_\phi(\ddot{w}^T + 2\omega_\phi\dot{w}^T + \omega_\phi^2w^T)\check{\phi} \right\| \leq \eta_3 2 \left\| \check{\xi}(x, \theta) \right\| \left\| \check{\phi} \right\|, \quad (7.109)$$

where  $\eta_3 = l_6 \left\| P_\xi(\hat{\phi}) \right\| \left\| B_\phi \right\|$ . The term  $2 \left\| \check{\xi}(x, \theta) \right\| \left\| \check{\phi} \right\|$  is bounded using Young's inequality to yield

$$2 \left\| \check{\xi}(x, \theta) \right\| \left\| \check{\phi} \right\| \leq \left\| \check{\xi}(x, \theta) \right\|^2 + \left\| \check{\phi} \right\|^2.$$

Then, equation 7.109 is bounded by

$$\left\| 2\check{\xi}^T(x, \theta)P_\xi(\hat{\phi})B_\phi(\ddot{w}^T + 2\omega_\phi\dot{w}^T + \omega_\phi^2w^T)\check{\phi} \right\| \leq \eta_3 \left\| \check{\xi}(x, \theta) \right\|^2 + \eta_3 \left\| \check{\phi} \right\|^2. \quad (7.110)$$

- b. The norm  $\left\| 2\check{\xi}^T(x, \theta)P_\xi(\hat{\phi})B_\xi(\phi) \left[ L_f^2h(\hat{m}, \theta) - L_f^2h(\hat{m}, \hat{\theta}) \right] \right\|$  is bounded using assumption 12, which implies the Lie derivative  $L_f^2h(m, \theta)$  is Lipschitz in  $\theta$ . First, taking the norm of  $\left\| L_f^2h(\hat{m}, \theta) - L_f^2h(\hat{m}, \hat{\theta}) \right\|$  yields

$$\left\| L_f^2h(\hat{m}, \theta) - L_f^2h(\hat{m}, \hat{\theta}) \right\| \leq l_2 \left\| \check{\theta} \right\|.$$

The norm  $\left\| \check{\theta} \right\|$  is bounded in terms of  $\left\| \hat{\theta} \right\|$  by using equation 7.36 ( $\check{m} = \Omega^{-1}\hat{\theta}$ ) to yield

$$\left\| L_f^2h(\hat{m}, \theta) - L_f^2h(\hat{m}, \hat{\theta}) \right\| \leq l_2 \left\| \Omega^{-1} \right\| \left\| \hat{\theta} \right\|. \quad (7.111)$$

Then, the norm  $\left\| 2\check{\xi}^T(x, \theta)P_\xi(\hat{\phi})B_\xi(\phi) \left[ L_f^2h(\hat{m}, \theta) - L_f^2h(\hat{m}, \hat{\theta}) \right] \right\|$  is bounded using equation 7.111 to be

$$\left\| 2\check{\xi}^T(x, \theta)P_\xi(\hat{\phi})B_\xi(\phi) \left[ L_f^2h(\hat{m}, \theta) - L_f^2h(\hat{m}, \hat{\theta}) \right] \right\| \leq \eta_4 2 \left\| \check{\xi}(x, \theta) \right\| \left\| \hat{\theta} \right\|, \quad (7.112)$$

where  $\eta_4 = l_2 \left\| P_\xi(\hat{\phi}) \right\| \left\| B_\xi(\phi) \right\| \left\| \Omega^{-1} \right\|$ . The norm  $2 \left\| \check{\xi}(x, \theta) \right\| \left\| \hat{\theta} \right\|$  is bounded using Young's inequality to yield

$$2 \left\| \check{\xi}(x, \theta) \right\| \left\| \hat{\theta} \right\| \leq \left\| \check{\xi}(x, \theta) \right\|^2 + \left\| \hat{\theta} \right\|^2.$$

Then, equation 7.112 is bounded by

$$\left\| 2\check{\xi}^T(x, \theta)P_\xi(\hat{\phi})B_\xi(\phi) \left[ L_f^2h(\hat{m}, \theta) - L_f^2h(\hat{m}, \hat{\theta}) \right] \right\| \leq \eta_4 \left\| \check{\xi}(x, \theta) \right\|^2 + \eta_4 \left\| \hat{\theta} \right\|^2, \quad (7.113)$$

c. The norm  $\left\| 2\check{\xi}^T(x, \theta)P_\xi(\hat{\phi})B_\xi(\phi) [L_f^2h(m, \theta) - L_f^2h(\hat{m}, \theta)] \right\|$  is bounded using assumption 12, which implies the Lie derivative  $L_f^2h(m, \theta)$  is Lipschitz in  $m$ . First, the norm  $\|L_f^2h(m, \theta) - L_f^2h(\hat{m}, \theta)\|$  is bounded by

$$L_f^2h(m, \theta) - L_f^2h(\hat{m}, \theta) \leq l_1 \|\check{m}\|.$$

The norm  $\|\check{m}\|$  is bounded in terms of  $\|\check{q}\|$  and  $\|\check{\theta}\|$  by using equation 7.35 ( $\check{m} = \Lambda^{-1}\hat{m}$ ) and equation 7.39 ( $\hat{m} = \check{q} + N\check{\theta}$ ) to yield

$$\|L_f^2h(m, \theta) - L_f^2h(\hat{m}, \theta)\| \leq l_1 \|\check{m}\| \leq l_1 \|\Lambda^{-1}\| \left( \|\check{q}\| + \|N\| \|\check{\theta}\| \right). \quad (7.114)$$

Then, the norm  $\left\| 2\check{\xi}^T(x, \theta)P_\xi(\hat{\phi})B_\xi(\phi) [L_f^2h(m, \theta) - L_f^2h(\hat{m}, \theta)] \right\|$  is bounded using equation 7.114 to be

$$\begin{aligned} & \left\| 2\check{\xi}^T(x, \theta)P_\xi(\hat{\phi})B_\xi(\phi) [L_f^2h(m, \theta) - L_f^2h(\hat{m}, \theta)] \right\| \\ & \leq \eta_5 2 \left\| \check{\xi}(x, \theta) \right\| \|\check{q}\| + \eta_5 \|N\| 2 \left\| \check{\xi}(x, \theta) \right\| \|\check{\theta}\| \end{aligned} \quad (7.115)$$

where  $\eta_5 = l_1 \|P_\xi(\hat{\phi})\| \|B_\xi(\phi)\| \|\Lambda^{-1}\|$ . The norms  $2 \left\| \check{\xi}(x, \theta) \right\| \|\check{q}\|$  and  $2 \left\| \check{\xi}(x, \theta) \right\| \|\check{\theta}\|$  are bounded using Young's inequality to yield

$$2 \left\| \check{\xi}(x, \theta) \right\| \|\check{q}\| \leq \left\| \check{\xi}(x, \theta) \right\|^2 + \|\check{q}\|^2 \quad \text{and} \quad 2 \left\| \check{\xi}(x, \theta) \right\| \|\check{\theta}\| \leq \left\| \check{\xi}(x, \theta) \right\|^2 + \|\check{\theta}\|^2.$$

Then, equation 7.115 is bounded by

$$\begin{aligned} & \left\| 2\check{\xi}^T(x, \theta)P_\xi(\hat{\phi})B_\xi(\phi) [L_f^2h(m, \theta) - L_f^2h(\hat{m}, \theta)] \right\| \\ & \leq \eta_5(1 + \|N\|) \left\| \check{\xi}(x, \theta) \right\|^2 + \eta_5 \|\check{q}\|^2 + \eta_5 \|N\| \|\check{\theta}\|^2. \end{aligned} \quad (7.116)$$

d. The norm  $\left\| 2\check{\xi}(x, \theta)P_\xi(\hat{\phi})B_\xi(\phi)R_\xi^{-1}B_\xi(\hat{\phi})P_\xi(\hat{\phi}) \left[ \check{\xi}(\hat{m}, \theta) - \check{\xi}(\hat{m}, \hat{\theta}) \right] \right\|$  is bounded using assumption 13, which implies the tracking error  $\check{\xi}(m, \theta)$  is Lipschitz in  $\theta$ . First, the norm  $\left\| \check{\xi}(\hat{m}, \theta) - \check{\xi}(\hat{m}, \hat{\theta}) \right\|$  is bounded by

$$\left\| \check{\xi}(\hat{m}, \theta) - \check{\xi}(\hat{m}, \hat{\theta}) \right\| \leq l_4 \left\| \check{\theta} \right\|.$$

The norm  $\left\| \check{\theta} \right\|$  is bounded in terms of  $\left\| \hat{\theta} \right\|$  by using equation 7.36 ( $\check{\theta} = \Omega^{-1}\hat{\theta}$ ) to yield

$$\left\| \check{\xi}(\hat{m}, \theta) - \check{\xi}(\hat{m}, \hat{\theta}) \right\| \leq l_4 \left\| \Omega^{-1} \right\| \left\| \hat{\theta} \right\|. \quad (7.117)$$

Then, the norm  $\left\| 2\check{\xi}(x, \theta)P_\xi(\hat{\phi})B_\xi(\phi)R_\xi^{-1}B_\xi(\hat{\phi})P_\xi(\hat{\phi}) \left[ \check{\xi}(\hat{m}, \theta) - \check{\xi}(\hat{m}, \hat{\theta}) \right] \right\|$  is bounded using equation 7.117 to yield

$$\begin{aligned} & \left\| 2\check{\xi}(x, \theta)P_\xi(\hat{\phi})B_\xi(\phi)R_\xi^{-1}B_\xi(\hat{\phi})P_\xi(\hat{\phi}) \left[ \check{\xi}(\hat{m}, \theta) - \check{\xi}(\hat{m}, \hat{\theta}) \right] \right\| \\ & \leq \eta_6 2 \left\| \check{\xi}(x, \theta) \right\| \left\| \hat{\theta} \right\|, \end{aligned} \quad (7.118)$$

where  $\eta_6 = l_4 \left\| P_\xi(\hat{\phi}) \right\| \left\| B_\xi(\phi) \right\| \left\| R_\xi^{-1} \right\| \left\| B_\xi(\hat{\phi}) \right\| \left\| P_\xi(\hat{\phi}) \right\| \left\| \Omega^{-1} \right\|$ . The norm  $2 \left\| \check{\xi}(x, \theta) \right\| \left\| \hat{\theta} \right\|$  is bounded using Young's inequality to yield

$$2 \left\| \check{\xi}(x, \theta) \right\| \left\| \hat{\theta} \right\| \leq \left\| \check{\xi}(x, \theta) \right\|^2 + \left\| \hat{\theta} \right\|^2.$$

Then, equation 7.118 is bounded by

$$\begin{aligned} & \left\| 2\check{\xi}(x, \theta)P_\xi(\hat{\phi})B_\xi(\phi)R_\xi^{-1}B_\xi(\hat{\phi})P_\xi(\hat{\phi}) \left[ \check{\xi}(\hat{m}, \theta) - \check{\xi}(\hat{m}, \hat{\theta}) \right] \right\| \\ & \leq \eta_6 \left\| \check{\xi}(x, \theta) \right\|^2 + \eta_6 \left\| \hat{\theta} \right\|^2, \end{aligned} \quad (7.119)$$

e. The norm  $\left\| 2\check{\xi}(x, \theta)P_\xi(\hat{\phi})B_\xi(\phi)R_\xi^{-1}B_\xi(\hat{\phi})P_\xi(\hat{\phi}) \left[ \check{\xi}(m, \theta) - \check{\xi}(\hat{m}, \theta) \right] \right\|$  is bounded using assumption 13, which implies the tracking error  $\check{\xi}(m, \theta)$  is Lipschitz in  $m$ . First, the norm  $\left\| \check{\xi}(m, \theta) - \check{\xi}(\hat{m}, \theta) \right\|$  is bounded by

$$\left\| \check{\xi}(m, \theta) - \check{\xi}(\hat{m}, \theta) \right\| \leq l_3 \|\check{m}\|.$$

The norm  $\|\check{m}\|$  is bounded in terms of  $\|q\|$  and  $\|\theta\|$  by using equation 7.35 ( $\check{m} = \Lambda^{-1}\hat{m}$ ) and equation 7.39 ( $\hat{m} = \hat{q} + N\theta$ ) to yield

$$\left\| \check{\xi}(m, \theta) - \check{\xi}(\hat{m}, \theta) \right\| \leq l_3 \|\Lambda^{-1}\| \left( \|\hat{q}\| + \|N\| \|\theta\| \right). \quad (7.120)$$

Then, the norm  $\left\| 2\check{\xi}(x, \theta)P_\xi(\hat{\phi})B_\xi(\phi)R_\xi^{-1}B_\xi(\hat{\phi})P_\xi(\hat{\phi}) \left[ \check{\xi}(m, \theta) - \check{\xi}(\hat{m}, \theta) \right] \right\|$  is bounded using equation 7.120 to be

$$\begin{aligned} & \left\| 2\check{\xi}(x, \theta)P_\xi(\hat{\phi})B_\xi(\phi)R_\xi^{-1}B_\xi(\hat{\phi})P_\xi(\hat{\phi}) \left[ \check{\xi}(m, \theta) - \check{\xi}(\hat{m}, \theta) \right] \right\| \\ & \leq \eta_7 2 \left\| \check{\xi}(x, \theta) \right\| \|\hat{q}\| + \eta_7 \|N\| 2 \left\| \check{\xi}(x, \theta) \right\| \|\theta\|, \end{aligned} \quad (7.121)$$

where  $\eta_7 = l_3 \left\| P_\xi(\hat{\phi}) \right\| \left\| B_\xi(\phi) \right\| \left\| R_\xi^{-1} \right\| \left\| B_\xi(\hat{\phi}) \right\| \left\| P_\xi(\hat{\phi}) \right\| \|\Lambda\|$ . The norms  $2 \left\| \check{\xi}(x, \theta) \right\| \|\hat{q}\|$  and  $2 \left\| \check{\xi}(x, \theta) \right\| \|\theta\|$  are bounded using Young's inequality to yield

$$2 \left\| \check{\xi}(x, \theta) \right\| \|\hat{q}\| \leq \left\| \check{\xi}(x, \theta) \right\|^2 + \|\hat{q}\|^2 \quad \text{and} \quad 2 \left\| \check{\xi}(x, \theta) \right\| \|\theta\| \leq \left\| \check{\xi}(x, \theta) \right\|^2 + \|\theta\|^2.$$

Then, equation 7.121 is bounded by

$$\begin{aligned} & \left\| 2\check{\xi}(x, \theta)P_\xi(\hat{\phi})B_\xi(\phi)R_\xi^{-1}B_\xi(\hat{\phi})P_\xi(\hat{\phi}) \left[ \check{\xi}(m, \theta) - \check{\xi}(\hat{m}, \theta) \right] \right\| \\ & \leq \eta_7 (1 + \|N\|) \left\| \check{\xi}(x, \theta) \right\|^2 + \eta_7 \|\hat{q}\| + \eta_7 \|N\| \|\theta\|. \end{aligned} \quad (7.122)$$

The time derivative  $\dot{W}_3$  in equation 7.108 is further bounded by bounding the norm of the last five terms with equation 7.110, equation 7.113, equation 7.116, equation 7.119, and equation 7.122 to yield

$$\begin{aligned} \dot{W}_3 \leq & - \left( \lambda_{\min}(Q_\xi) - \eta_3 - \eta_4 - \eta_6 - (\eta_5 + \eta_7)(1 + \|N\|) \right) \left\| \check{\xi}(x, \theta) \right\|^2 \\ & + (\eta_5 + \eta_7) \|\hat{q}\|^2 + \eta_3 \|\check{\phi}\|^2 + \left( \eta_4 + \eta_6 + (\eta_5 + \eta_7) \|N\| \right) \|\theta\|^2. \end{aligned} \quad (7.123)$$

3. The recursive least squares for control group is

$$\dot{W}_4 = 2\check{\phi}^T P_\phi^{-1} \frac{d}{dt} \check{\phi} - \check{\phi}^T P_\phi^{-1} \dot{P}_\phi P_\phi^{-1} \check{\phi}. \quad (7.124)$$

Add and subtract the term  $\check{\phi}^T w w^T \check{\phi}$  to equation 7.124 yields

$$\dot{W}_4 = 2\check{\phi}^T P_\phi^{-1} \frac{d}{dt} \check{\phi} + \check{\phi}^T w w^T \check{\phi} - \check{\phi}^T \left( P_\phi^{-1} \dot{P}_\phi P_\phi^{-1} + w w^T \right) \check{\phi}. \quad (7.125)$$

The term  $\check{\phi}^T w w^T \check{\phi}$  is always positive and is bounded by  $2\check{\phi}^T w w^T \check{\phi}$ . Recall from the recursive least squares formulation, the observation error is defined as  $w^T \check{\phi} = \check{\xi}_1(t) - w^T(t) \hat{\phi}(t)$ . Then, equation 7.125 is bounded by

$$\dot{W}_4 \leq 2\check{\phi}^T \left( P_\phi^{-1} \frac{d}{dt} \check{\phi} + w \epsilon \right) - \check{\phi}^T \left( P_\phi^{-1} \dot{P}_\phi P_\phi^{-1} + w w^T \right) \check{\phi}. \quad (7.126)$$

The update laws for  $\check{\phi}$  and  $P_\phi$  are chosen to be equation 7.76,

$$\dot{P}_\phi = \begin{cases} \beta P_\phi - P_\phi w w^T P_\phi, & \text{if } \hat{\phi} \in \Phi^o, \text{ or } \phi \in \partial\Phi \text{ and } (P_\phi w \epsilon)^T \nabla g \leq 0 \\ 0, & \text{otherwise,} \end{cases}$$

$$\frac{d}{dt} \check{\phi} = -\frac{d}{dt} \hat{\phi} = \begin{cases} -P_\phi w \epsilon, & \text{if } \hat{\phi} \in \Phi^o, \text{ or } \phi \in \partial\Phi \text{ and } (P_\phi w \epsilon)^T \nabla g \leq 0, \\ -\left(1 - \frac{P_\phi \nabla g \nabla g^T}{\nabla g^T P_\phi \nabla g}\right) P_\phi w \epsilon, & \text{otherwise.} \end{cases}$$

Applying the update laws in equation 7.76 to equation 7.126 yields

$$\dot{W}_4 \leq \begin{cases} -\beta \check{\phi}^T P_\phi^{-1} \check{\phi}, & \text{if } \hat{\phi} \in \Phi^o, \text{ or } \phi \in \partial\Phi \text{ and } (P_\phi w \epsilon)^T \nabla g \leq 0 \\ -\check{\phi}^T w w^T \check{\phi} + 2 \frac{\check{\phi}^T \nabla g}{\nabla g^T P_\phi \nabla g} (\nabla g^T P_\phi w \epsilon), & \text{otherwise} \end{cases}. \quad (7.128)$$

We are interested in the effects that projection has on the stability analysis, and these effects are quantified by considering the “otherwise” case of  $\dot{W}_4$ . Then, equation 7.128 becomes

$$\dot{W}_4 \leq -\check{\phi}^T w w^T \check{\phi} + 2 \frac{\check{\phi}^T \nabla g}{\nabla g^T P_\phi \nabla g} (\nabla g^T P_\phi w \epsilon). \quad (7.129)$$

In the stability analysis, the last term  $\frac{2\check{\phi}^T \nabla g \nabla g^T P_\phi w \epsilon}{\nabla g^T P_\phi \nabla g}$  may cause a problem, so let us examine its sign. For this case,  $\check{\phi}^T \check{\phi} = M_o^2$  and  $\nabla g^T P_\phi w \epsilon > 0$ , then the sign  $\left(\frac{2\check{\phi}^T \nabla g \nabla g^T P_\phi w \epsilon}{\nabla g^T P_\phi \nabla g}\right)$  is equated to the sign  $\left(\check{\phi}^T \nabla g\right)$  [125]. The gradient of  $g$  is  $\nabla g = -\check{\phi}$ , which implies

$$\check{\phi}^T \nabla g = -M_o^2 < 0, \quad (7.130)$$

and shows that the sign  $\left(\frac{2\check{\phi}^T \nabla g \nabla g^T P_\phi w \epsilon}{\nabla g^T P_\phi \nabla g}\right)$  is always negative. We can conclude the effects of projection is to make  $\dot{W}_4$  more negative. Then, equation 7.129 is bounded by

$$\dot{W}_4 \leq -\check{\phi}^T w w^T \check{\phi}. \quad (7.131)$$

Recall that the time derivative of the Lyapunov function (same as described in equation 7.101)

$$\begin{aligned} \dot{W} &= \dot{W}_1 + \dot{W}_2 + \dot{W}_3 + \dot{W}_4 \\ &= \frac{d}{dt} \check{q}^T S \check{q} + \check{q}^T S \frac{d}{dt} \check{q} + \frac{d}{dt} \check{\xi}^T P_\xi \check{\xi} + \check{\xi}^T P_\xi \frac{d}{dt} \check{\xi} \\ &\quad + 2\check{\theta}^T P_\theta^{-1} \frac{d}{dt} \check{\theta} - \check{\theta}^T P_\theta^{-1} \dot{P}_\theta P_\theta^{-1} \check{\theta} + 2\check{\phi}^T P_\phi^{-1} \frac{d}{dt} \check{\phi} - \check{\phi}^T P_\phi^{-1} \dot{P}_\phi P_\phi^{-1} \check{\phi}. \end{aligned}$$

Equation 7.101 was grouped into three groups and each group was bounded. Substitute the bound for the adaptive state observer group  $\dot{W}_1 + \dot{W}_2$  (same as equation 7.104), the tracking group  $\dot{W}_3$  (same as equation 7.123), and the recursive least squares group  $\dot{W}_4$  (same as equation 7.131) into  $\dot{W}$  yields

$$\begin{aligned} \dot{W} &\leq - \left( (\lambda - \eta_1) \lambda_{\min}(S_q) - \eta_5 - \eta_7 \right) \|\check{q}\|^2 \\ &\quad - \left( (\lambda - \eta_1) \lambda_{\min}(P_\theta^{-1}) - \eta_4 \eta_6 - (\eta_5 + \eta_7)(1 + \|N\|) \right) \|\check{\theta}\|^2 \\ &\quad - \left( \lambda_{\min}(Q_\xi) - \eta_3 - \eta_4 - \eta_6 - (\eta_5 + \eta_7)(1 + \|N\|) \right) \|\check{\xi}(x, \theta)\|^2 \\ &\quad - \check{\phi}^T w w^T \check{\phi} + \eta_3 \|\check{\phi}\|^2. \end{aligned} \quad (7.132)$$

Defining a positive constant  $\Upsilon_4$  as

$$\begin{aligned} \Upsilon_4 &= \min \left( (\lambda - \eta_1) \lambda_{\min}(S_q) - \eta_5 - \eta_7, \right. \\ &\quad \left. (\lambda - \eta_1) \lambda_{\min}(P_\theta^{-1}) - \eta_4 \eta_6 - (\eta_5 + \eta_7)(1 + \|N\|), \right. \\ &\quad \left. \lambda_{\min}(Q_\xi) - \eta_3 - \eta_4 - \eta_6 - (\eta_5 + \eta_7)(1 + \|N\|) \right), \end{aligned} \quad (7.133)$$

then equation 7.101 is bounded by

$$\dot{W} \leq -\Upsilon_4 \left( \|\dot{q}\|^2 + \|\dot{\theta}\|^2 + \|\check{\xi}(x, \theta)\|^2 \right) + \eta_3 \|\check{\phi}\|^2 \quad (7.134)$$

Equation 7.134 is expressed in terms of  $W$  by using the upper bound of  $W$  (same as given in equation 7.98)

$$W \leq \Upsilon_2 \left( \|\dot{q}\|^2 + \|\dot{\theta}\|^2 + \|\check{\xi}(x, \theta)\|^2 \right) + \Upsilon_3 M_o^2,$$

and applying  $\|\check{\phi}\|^2 \leq M_o^2$  yields

$$\dot{W} \leq -\frac{\Upsilon_4}{\Upsilon_2} W + \Upsilon_5 M_o^2, \quad (7.135)$$

where the positive constant  $\Upsilon_4$  is defined by  $\Upsilon_5 = \frac{\Upsilon_3 \Upsilon_4}{\Upsilon_2} + \eta_3$ . The solution to equation 7.135 is

$$W(t) \leq W(0) \exp\left(-\frac{\Upsilon_4}{\Upsilon_2} t\right) + \Upsilon_5 M_o^2 \left(1 - \exp\left(-\frac{\Upsilon_4}{\Upsilon_2} t\right)\right). \quad (7.136)$$

The Lyapunov function  $W$  decays exponentially to its steady-state value of  $\Upsilon_5 M_o^2$ . Thus, we can conclude that  $W \in L_\infty$ . Signal tracing is now performed to show that the closed-loop system remains bounded.

1. The Lyapunov function is  $W \in L_\infty$ , then equation 7.97 implies  $\dot{q}, \dot{\theta}, \check{\xi}, \check{\phi} \in L_\infty$ .
2. The parameter estimation error and the true parameter are  $\phi, \check{\phi} \in L_\infty$ , then from  $\check{\phi} = \phi - \hat{\phi}$  and projection implies  $\hat{\phi} \in L_\infty$ .
3. The scaled parameter estimation error  $\check{\theta} \in L_\infty$  and  $\Omega \in L_\infty$ , then equation 7.36 ( $\check{\theta} = \Omega \dot{\theta}$ ) implies  $\dot{\theta} \in L_\infty$ .
4. The parameter estimation error  $\check{\theta} \in L_\infty$  and the true parameter  $\theta \in L_\infty$ , then from  $\check{\theta} = \theta - \hat{\theta}$  implies  $\hat{\theta} \in L_\infty$ .
5. The scaled estimation errors  $\dot{q}, \dot{\theta} \in L_\infty$  and  $\|N\| \in L_\infty$ , then from equation 7.39 ( $\dot{q} = \dot{m} - N\dot{\theta}$ ) implies  $\dot{m} \in L_\infty$ .
6. The scaled state estimation error  $\dot{m}$  and  $\Lambda \in L_\infty$ , then from equation 7.35 ( $\dot{m} = \Lambda \check{m}$ ) implies  $\check{m} \in L_\infty$ .
7. The state estimation error and the state  $\check{m}, m \in L_\infty$ , then from  $\check{m} = m - \hat{m}$  implies  $\hat{m} \in L_\infty$ .

8. The state estimate  $\hat{m} \in L_\infty$  and using the one-to-one map between  $m$  and  $x$  implies  $\hat{x} \in L_\infty$ .
9. The tracking error  $\check{\xi} \in L_\infty$ , the reference signal  $\xi_r \in L_\infty$ , the estimates  $\hat{x}, \hat{\theta} \in L_\infty$ , then from equation 7.63 implies  $\xi(\hat{x}, \theta\theta) \in L_\infty$ .

□

## 8.0 SIMULATIONS

Proof of concept is needed to demonstrate the closed-loop performance of the controllers in a single-molecule study. The single-molecule study chosen is the stretching of a DNA molecule to replicate its force-extension curve. The force-extension curve is nonlinear because the DNA molecule becomes stiffer the farther it is stretched [126, 97]. The study is performed with simulations to demonstrate and compare the closed-loop performance of the controllers. The two metrics to be quantified are:

1. The improvement in the closed-loop performance when considering the system nonlinearities in the controller design.
2. The closed-loop performance using adaptive self-tuning feedback compared to that using fixed-gain feedback methods. The comparison quantifies the effect of using an automated optical trap to minimize the user interaction to that of an optical trap that requires extensive user interaction with the instrument and control design.

This chapter discusses the simulation setup and results.

### 8.1 SIMULATION SETUP

The simulations are performed in Simulink with a fixed-step Dormand-Prince solver. The optical trap system is modeled according to its dynamics given in equation 4.37. The model of the optical trap system is used as the plant for the following controllers (LQG, nominal nonlinear design, and adaptive nonlinear design). The simplified model of the optical trap is used as the plant for the nonlinear PI controller as discussed in section 6.5. The process noise

(Brownian noise and molecule noise) and the sensor noise are modeled with band-limited white noise.

For the LQG design, the nominal nonlinear design, and the adaptive nonlinear design, the force-extension curve of the DNA molecule is replicated by mimicking the molecule being stretched in the following way:

1. Initially, the molecule as zero extension. The molecule is then stretched to have its force (force disturbance) be increased in increments of 2 pN every 2 s.
2. The molecule's extension is stretched by having the bead deflection track a reference signal. The reference signal is increased to have the resulting optical force be increased in increments by 2 pN every 2 s. The optical force is increased between 0 to 50 pN.
3. For each increment the molecule force is increased, the estimated value of the estimated disturbance  $\hat{d}_d$  is related to the estimated molecule's extension  $\hat{x}_m$  through the one-to-one map (same as given in equation 4.32),

$$\left(\frac{\hat{x}_m}{l_m}\right)^4 - \left(\frac{13}{4} + \frac{\hat{d}_d}{l_m}\right) \left(\frac{\hat{x}_m}{l_m}\right)^3 + \left(\frac{15}{4} + \frac{3\hat{d}_d}{l_m}\right) \left(\frac{\hat{x}_m}{l_m}\right)^2 - \left(\frac{3}{2} + \frac{3\hat{d}_d}{l_m}\right) \left(\frac{\hat{x}_m}{l_m}\right) + \frac{3\hat{d}_d}{2l_m} = 0.$$

The contour length of the DNA molecule is chosen to be  $l_m = 9.5$  kb.

4. The estimated molecule's extension is then used to provide information on the molecule's stiffness using equation 4.12,

$$k_m = \frac{k_B T}{l_m l_p} \left[ \frac{1}{2} \left( 1 - \frac{\hat{x}_m}{l_m} \right)^{-3} + 1 \right].$$

5. The estimated disturbance and the molecule's stiffness is then used to provide an estimate of the molecule's force.

For the nonlinear PI design, the force-extension curve of the DNA molecule is replicated by mimicking the molecule being stretched in the following way:

1. Initially, the molecule as zero extension. The molecule is then stretched to have its force (force disturbance) be increased in increments of 2 pN every 2 s.
2. The molecule's extension is stretched by having the bead deflection track a reference signal. The reference signal is increased to have the resulting optical force be increased in increments by 2 pN every 2 s. The optical force is increased between 0 to 50 pN.

Table 6: The values of the dimensionless stiffness  $\kappa$  for each instance the molecule force is increased by 2 pN. Each pair of  $\kappa$  and  $k_t$  describes an operating condition.

Force (pN)	$\kappa$						
0	0.00037	14	2.2984	28	6.5612	42	11.66
2	0.11637	16	2.817	30	7.2987	44	12.704
4	0.34324	18	3.313	32	7.8528	46	13.875
6	0.64877	20	3.9327	34	8.7941	48	14.516
8	0.98181	22	4.5727	36	9.5068	50	15.196
10	1.3691	24	5.1884	38	10.299		
12	1.81147	26	5.7247	40	11.181		

3. The signal  $\hat{z}$  is used to estimate the molecule force through equation 6.64

$$\hat{f}_m = \eta k_2 (\hat{z} - z_r).$$

4. The force estimate is then used with the WLC model to relate the force to extension because the WLC model is a one-to-one map between force and extension.

## 8.2 LQG RESULTS

The LQG design is a fixed gain linear controller that needs to be designed for each operating condition. The operating condition (each pair of  $\kappa$  and  $k_t$ ) changes at each instance the molecule's extension is extended because the molecule stiffness increases (equal to the value of  $\kappa$  increasing because the optical stiffness is constant). At each instance the molecule is extended to have its force increase by 2 pN, the corresponding values for the dimensionless stiffness  $\kappa$  are shown in table 6. Therefore, for each operating condition for the optical trap system, a Kalman filter and the input-output feedback with LQ structure are designed.

The LQG design uses high values for the weight placed on the tracking error in the LQ control algorithm. High values are used because for each instance the molecule is stretched, large initial transients are present in the response of the bead deflection and its estimate as shown in figure 44. The large transients are bad because the molecule is stretched farther beyond its intended extension and the molecule can enter a different physical regime than intended. An example occurs when the DNA is nearly stretched to its contour length because large transient can lead to DNA entering a new regime called B-DNA and the DNA experiencing hysteresis behavior [9]. Large values are used for the weight on the tracking error in the LQ algorithm to prevent the large transients.

The results of the estimated disturbance  $\hat{d}_d$  is shown in figure 45. The estimated disturbance has an initial expected value of zero. For the first incremental increase, the expected value of the steady-state estimated disturbance converges to its maximum value, then for every incremental increase, the expected value of the steady-state estimated disturbance converges to a lesser value. The estimated disturbance has this behavior because the estimated disturbance is the force disturbance normalized by the molecule stiffness and as the molecule becomes stiffer the farther it is stretched.

Next, for each incremental value, the estimated disturbance is related to the estimated molecule's extension and the molecule's stiffness. The estimated disturbance is at steady-state for the last 1.5 s of each increment, and the last second of each increment is used to calculate its expected value. The expected value for the estimated disturbance is related to the molecule's extension through equation 4.32. The molecule's extension is then related to the molecule's stiffness using equation 4.12. The results for the expected value of the estimated disturbance, the molecule extension, and the molecule stiffness are shown in table 7.

For each increment, the expected value of the estimated force disturbance is  $E[\hat{f}_d] = k_m E[\hat{d}_d]$ . The expected value of the estimated force disturbance is plotted versus the molecule's extension to obtain the estimated force-extension curve. The estimated force-extension curve is compared with the force-extension curve obtained using the WLC model to quantify the estimation error. Figure 46 shows the estimation force-extension curve and the estimation error. As the molecule is stretched between the dimensionless extensions of

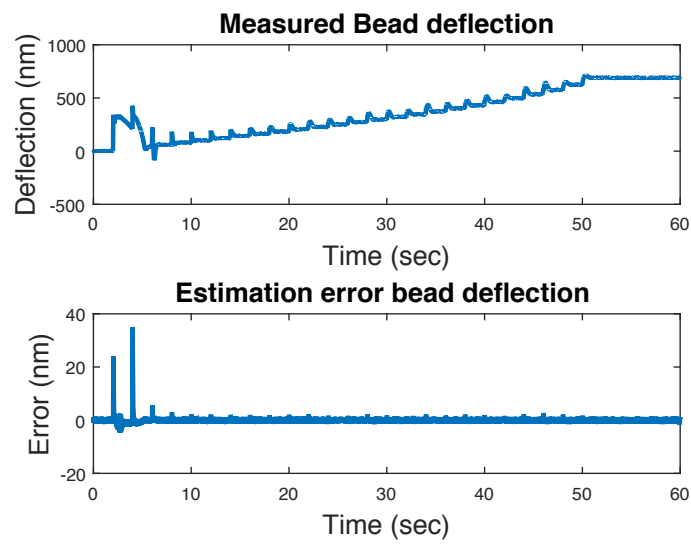


Figure 44: A schematic of the bead deflection and its estimate using the LQG design. Small values are used for the weight on the tracking error in the LQ control algorithm. The result is large transients each instance the molecule is stretched.

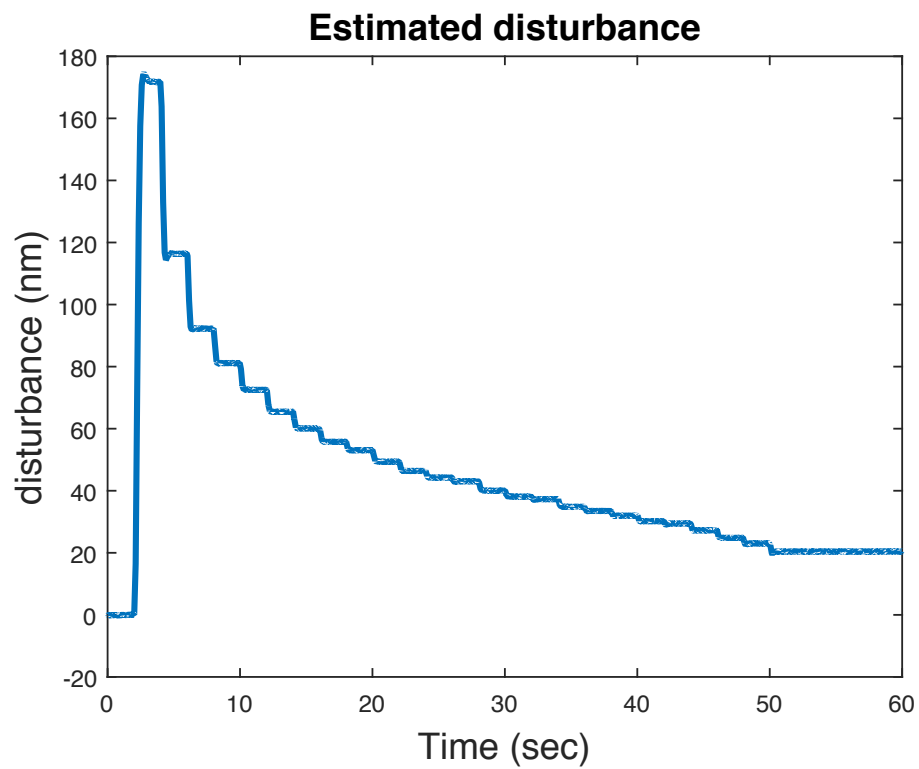


Figure 45: A schematic of the estimated disturbance obtained using the LQG controller. The DNA molecule is extended to have its force increase in increments of 2 pN every 2 s.

Table 7: The values of the expected value of the estimated disturbance, molecule extension, and the molecule stiffness for each increment that are obtained using the LQG design.

$E[\hat{d}_d]$ (nm)	$x_m$ (nm)	$k_m$ (pN/nm)	$E[\hat{d}_d]$ (nm)	$x_m$ (nm)	$k_m$ (pN/nm)
0.00918	0.00918	0.000037152	43.048	3144.1	0.65788
171.81	2894.9	0.011119	40.027	3150.1	0.81774
116.39	3000.2	0.03442	38.114	3153.9	0.94666
92.242	3047.1	0.068204	37.291	3155.5	1.0105
81.12	3068.8	0.09973	34.82	3160.5	1.2406
72.528	3085.7	0.139	33.49	3163.1	1.394
65.462	3099.7	0.18849	31.953	3166.2	1.6044
60.069	3110.3	0.24346	30.185	3169.7	1.9024
55.764	3118.8	0.30385	29.464	3171.1	2.0453
53.049	3124.2	0.3526	27.222	3175.6	2.5925
49.37	3131.5	0.43694	24.812	3180.4	3.4221
46.384	3137.4	0.5264	23.03	3184	4.2484
44.24	3141.7	0.60633	20.405	3189.2	6.1482

0 and 0.96, the absolute of the maximum estimation error is 0.62 pN. Also, as the molecule is further stretched closer to its contour length (the dimensionless extension  $\frac{x_m}{l_m} \rightarrow 1$ ), the estimation error increases to an absolute value of 75 pN. We can conclude that as the molecule is stretched such that its force is beyond that of the maximum linear optical force, the LQG design produces a poor estimate of the force-extension curve.

Next, the tracking error and the estimation error between the measured bead deflection and the estimated bead deflection are quantified. The response of the tracking error is shown in figure 47. At each instance the reference signal is increased, the tracking error has an initial bias that converges to zero at steady-state. A question to ask is, why is linear control yielding zero bias in the tracking error at steady-state throughout the entire operating range. The reason is the high values chosen for the weight on the tracking error in the LQ algorithm that the effects of the system nonlinearities in the input-output feedback are suppressed with linear state feedback. The estimation error between the measured bead deflection and the bead deflection is shown in figure 48. At each instance the measured bead deflection is increased, the estimation error has an initial bias that converges to zero at steady-state. One possible explanation for the zero estimation error is the high gain control characteristics that suppresses the effects of the system nonlinearities.

### 8.3 NOMINAL NONLINEAR DESIGN RESULTS

The nominal nonlinear design is a fixed gain nonlinear controller that needs to be designed for each operating condition. The operating condition (each pair of  $\kappa$  and  $k_t$ ) changes at each instance the molecule's extension is extended because  $\kappa$  increases (the molecule becomes stiffer). At each instance the molecule is extended to have its force increase by 2 pN, the corresponding values for the dimensionless stiffness  $\kappa$  are shown in table 6.

The results of the estimated disturbance  $\hat{d}_d$  is shown in figure 49. The estimated disturbance has an initial expected value of zero. For the first incremental increase, the expected value of the steady-state estimated disturbance converges to its maximum value, then for every incremental increase, the expected value of the steady-state estimated disturbance con-

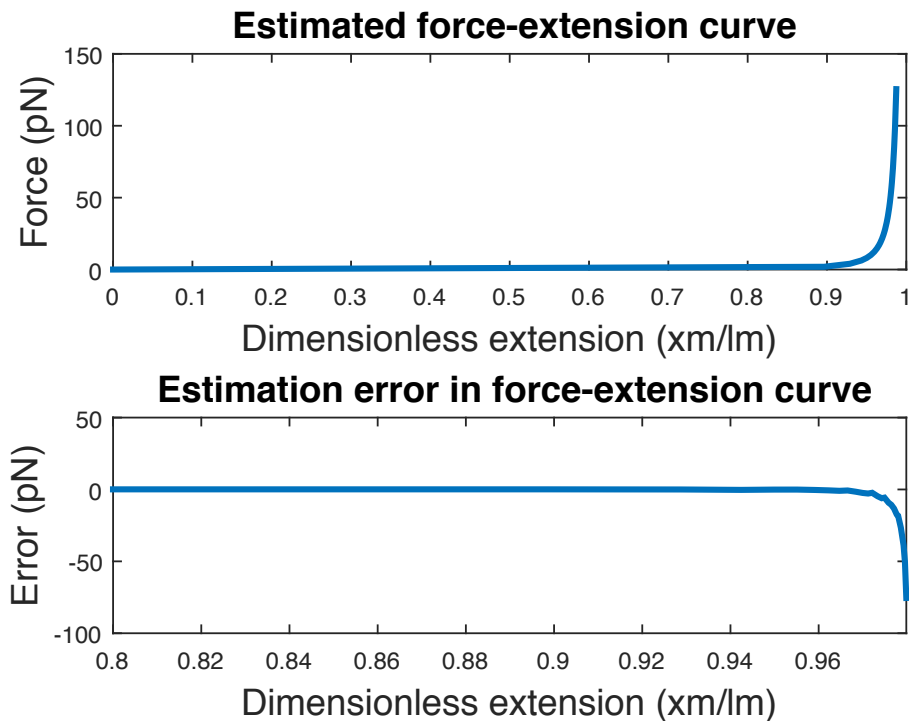


Figure 46: A schematic showing the estimation force-extension curve and the estimation error of the force-extension curve obtained using the LQG controller. As the molecule is stretched between the dimensionless extensions of 0 and 0.96, the absolute of the maximum estimation error is 0.62 pN. Also, as the molecule is further stretched closer to its contour length (the dimensionless extension  $\frac{x_m}{l_m} \rightarrow 1$ ), the estimation error increases to an absolute value of 75 pN.

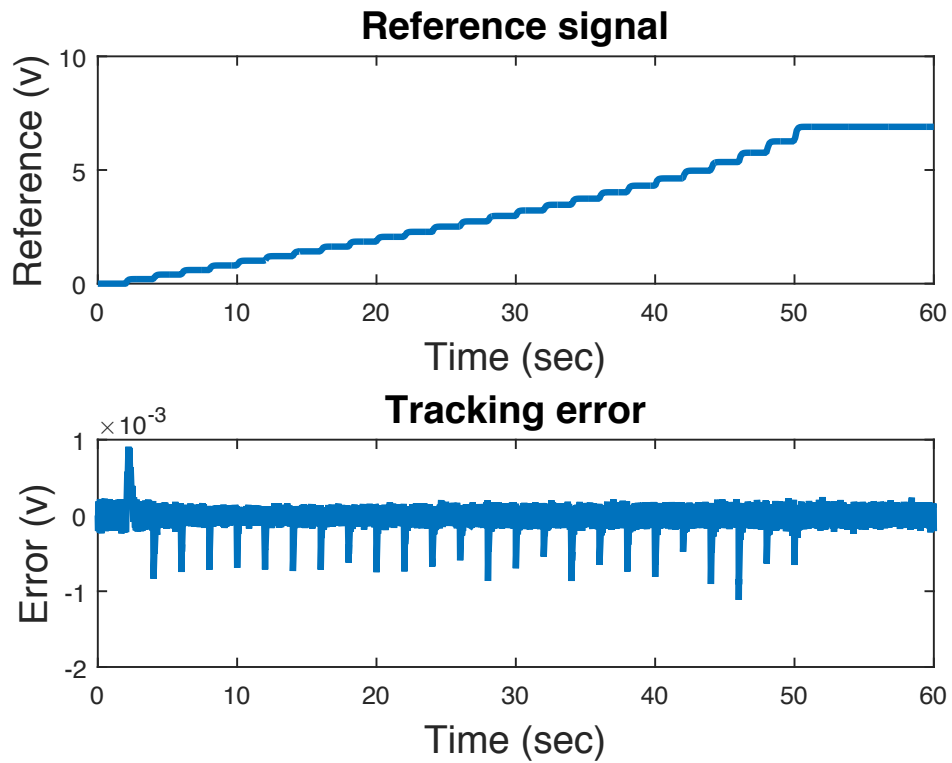


Figure 47: The response of the tracking error using LQG design. At each instance the reference signal is increased, the tracking error has an initial bias that converges to zero at steady-state.

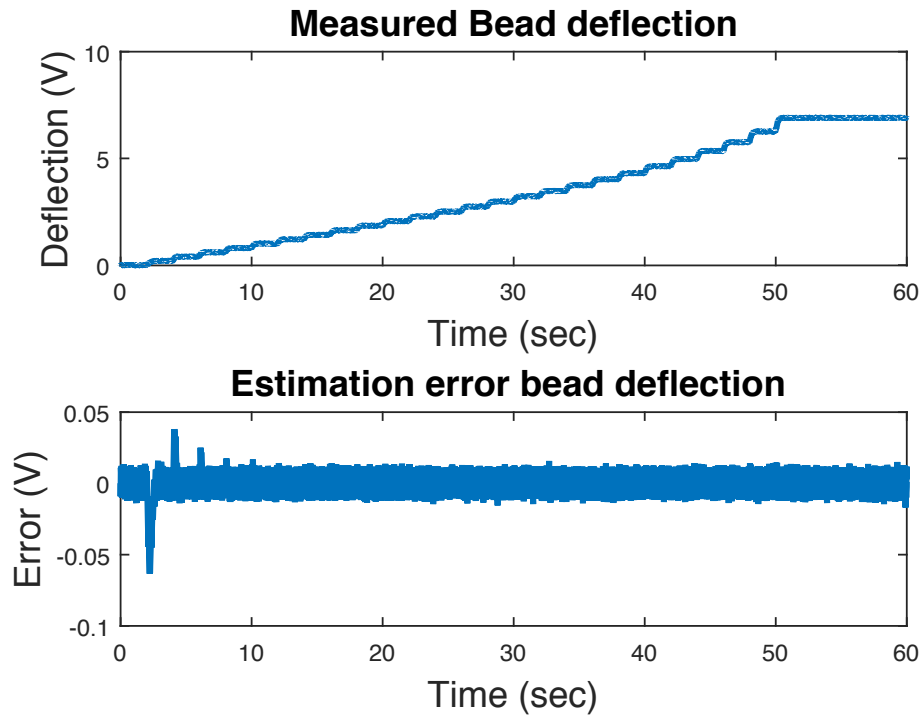


Figure 48: The response of the measured bead deflection and the estimation error between the measured bead deflection and the estimated bead deflection using the LQG design. At each instance the measured bead deflection is increased, the estimation error has an initial bias that converges to zero at steady-state.

verges to a lesser value. The estimated disturbance has this behavior because the estimated disturbance is the force disturbance normalized by the molecule stiffness and as the molecule becomes stiffer the farther it is stretched.

Next, for each incremental value, the estimated disturbance is related to the estimated molecule's extension and the molecule's stiffness. The estimated disturbance is at steady-state for the last 1.5 s of each increment, and the last second of each increment is used to calculate its expected value. The estimated value for the estimated disturbance is related to the molecule's extension through equation 4.32. The molecule's extension is then related to the molecule's stiffness using equation 4.12. The results for the expected value of the estimated disturbance, the molecule extension, and the molecule stiffness are shown in table 8.

For each increment, the expected value of the estimated force disturbance is  $E[\hat{f}_d] = k_m E[\hat{d}_d]$ . The expected value of the estimated force disturbance is plotted versus the molecule's extension to obtain the estimated force-extension curve. The estimated force-extension curve is compared with the force-extension curve obtained using the WLC model to quantify the estimation error. Figure 50 shows the estimation force-extension curve and the estimation error. As the molecule is stretched between the dimensionless extensions of 0 and 0.96, the absolute of the maximum estimation error is 0.23 pN. Then, as the molecule is further stretched closer to its contour length (the dimensionless extension  $\frac{x_m}{l_m} \rightarrow 1$ ), the estimation error increases to an absolute value of 1.63 pN. We can conclude that as the molecule is stretched such that its force is beyond that of the maximum linear optical force, the nominal nonlinear design provides a satisfactory estimate of the force-estimate curve. The improvement in the estimated force-extension curve using the nominal nonlinear design to that obtained with the LQG design, shows the advantages of considering the system nonlinearities in the control design.

Next, the tracking error and the estimation error between the measured bead deflection and the estimated bead deflection are quantified. The response of the tracking error is shown in figure 51. At each instance the reference signal is increased, the tracking error has an initial bias that converges to zero at steady-state. The variance of the tracking error increases as the reference signal increases and this phenomenon is due to the state observer. Recall that

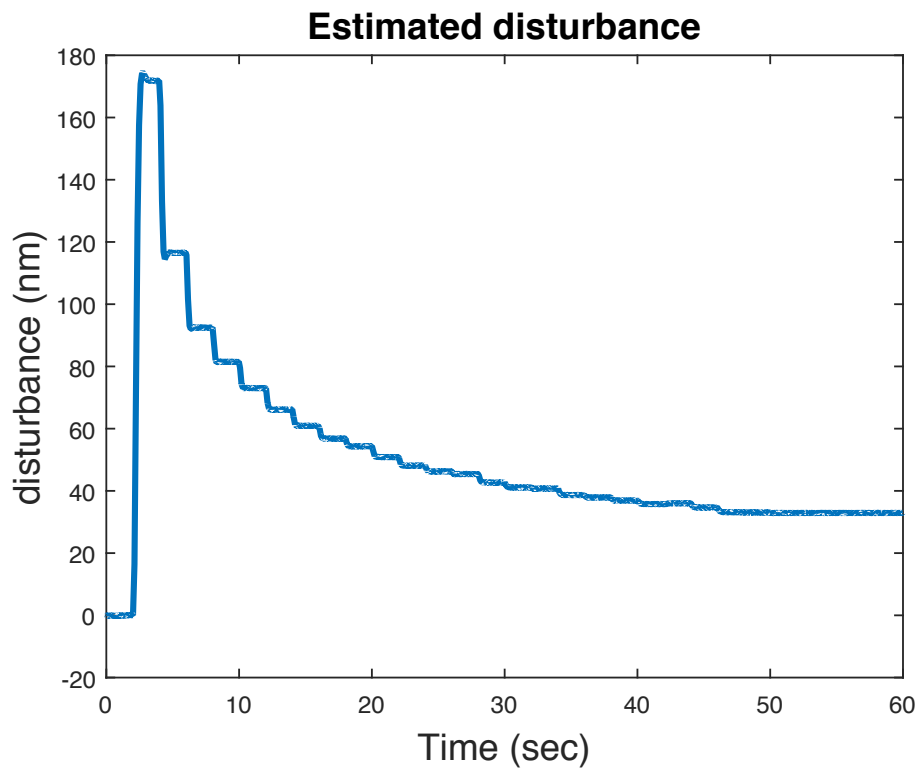


Figure 49: A schematic of the estimated disturbance obtained using the nominal nonlinear controller. The DNA molecule is extended to have its force increase in increments of 2 pN every 2 s.

Table 8: The values of the expected value of the estimated disturbance, molecule extension, and the molecule stiffness for each increment that are obtained using the nominal nonlinear design.

$E[\hat{d}_d]$ (nm)	$x_m$ (nm)	$k_m$ (pN/nm)	$E[\hat{d}_d]$ (nm)	$x_m$ (nm)	$k_m$ (pN/nm)
0.00918	0.00918	0.000037152	45.417	3139.4	0.5606
171.85	2894.9	0.011111	42.673	3144.8	0.67532
116.51	3000	0.034311	41.1	3148	0.75552
92.467	3046.6	0.067715	40.745	3148.7	0.77538
81.472	3068.2	0.09846	38.657	3152.8	0.90746
73.035	3084.7	0.13615	37.866	3154.4	0.96536
66.119	3098.4	0.18298	36.891	3156.3	1.0436
60.906	3108.7	0.23364	35.771	3158.6	1.1445
56.794	3116.8	0.28772	36.018	3158.1	1.1211
54.326	3121.7	0.32845	34.63	3160.8	1.2611
50.851	3128.6	0.40004	33.152	3163.8	1.4369
48.105	3134	0.47212	33.066	3163.9	1.4482
46.257	3137.7	0.53073	32.9	3164.3	1.4701

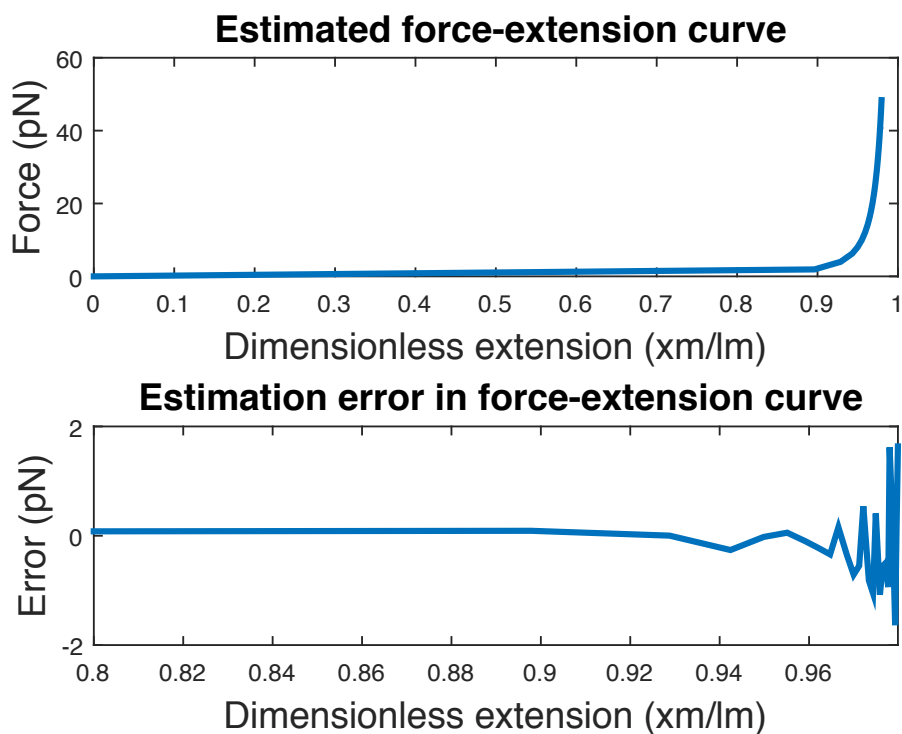


Figure 50: A schematic showing the estimation force-extension curve and the estimation error of the force-extension curve obtained using the nominal nonlinear controller. As the molecule is extended between the dimensionless extensions of 0 and 0.96, the absolute of the maximum estimation error is 0.22 pN. Then, as the molecule is further extended close to its contour length (the dimensionless extension  $\frac{x_m}{l_m} \rightarrow 1$ ), the estimation error increases to an estimation error with absolute value of 1.63 pN.

the state observer results in the estimated bead deflection experiencing a greater effect from the sensor noise as the bead deflection increases. The estimation error between the measured bead deflection and the bead deflection is shown in figure 52. At each instance the measured bead deflection is increased, the estimation error has an initial bias that converges to zero at steady-state.

## 8.4 NONLINEAR PI CONTROL RESULTS

The response of the reference signal and tracking error are shown in figure 53. The tracking error has zero bias for each instance the reference signal is increased. Also, the tracking error has a constant variance throughout the optical trap operating range, which is expected because of the controller linearized the input-to-state map.

The response of  $\hat{z}$  is shown in figure 54. The variable  $\hat{z}$  converges to a new steady-state value each instance the reference signal is increased. The advantage with the nonlinear PI controller is that  $\hat{z}$  is used to obtain an estimate of the molecule force using equation 6.64. The estimated molecule force is shown in figure 55. For each incremental value, the estimated molecule force is at steady-state for the last 1.5s of each increment, and the last second of each increment is used to calculate its expected value. The expected value of the molecule force is related to the molecule extension using the WLC model. The results for the expected value of the estimated molecule force and the molecule's extension are shown in table 9. The expected value of the estimated force disturbance is plotted verses the molecule's extension to obtain the estimated force-extension curve. The estimated force-extension curve is compared with the force-extension curve obtained using the WLC model to quantify the estimation error. Figure 56 shows the estimation force-extension curve and the estimation error.

### 8.4.1 Comparison Between the Nonlinear Control Methods

Both the nominal nonlinear control and the nonlinear PI control yields zero bias in the expected value of the tracking error at steady-state for incremental increases in the reference

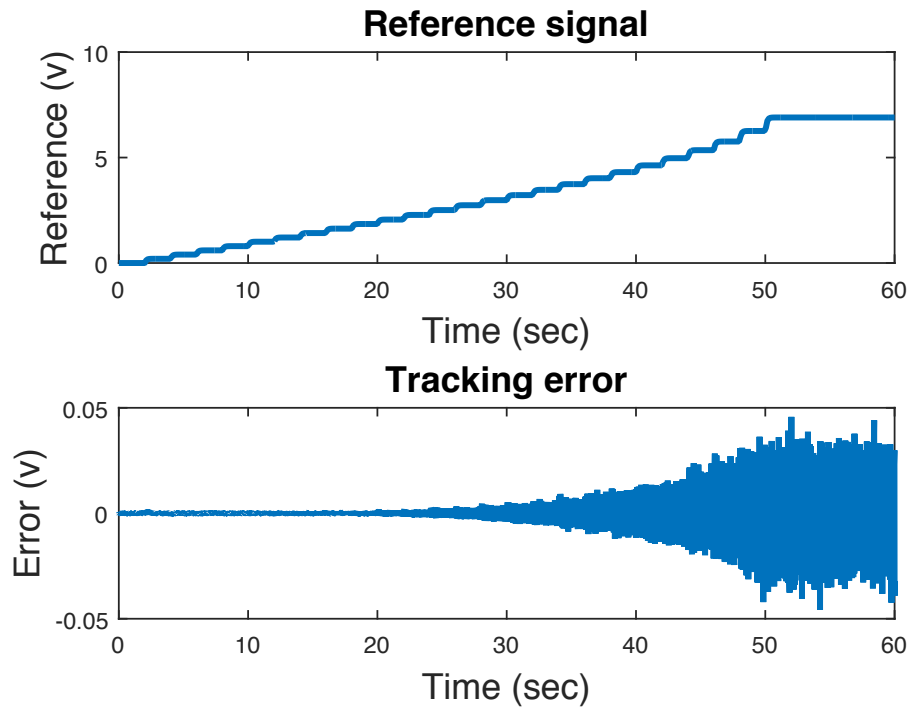


Figure 51: The response of the tracking error using the nominal nonlinear design. At each instance the reference signal is increased, the tracking error has an initial bias that converges to zero at steady-state.

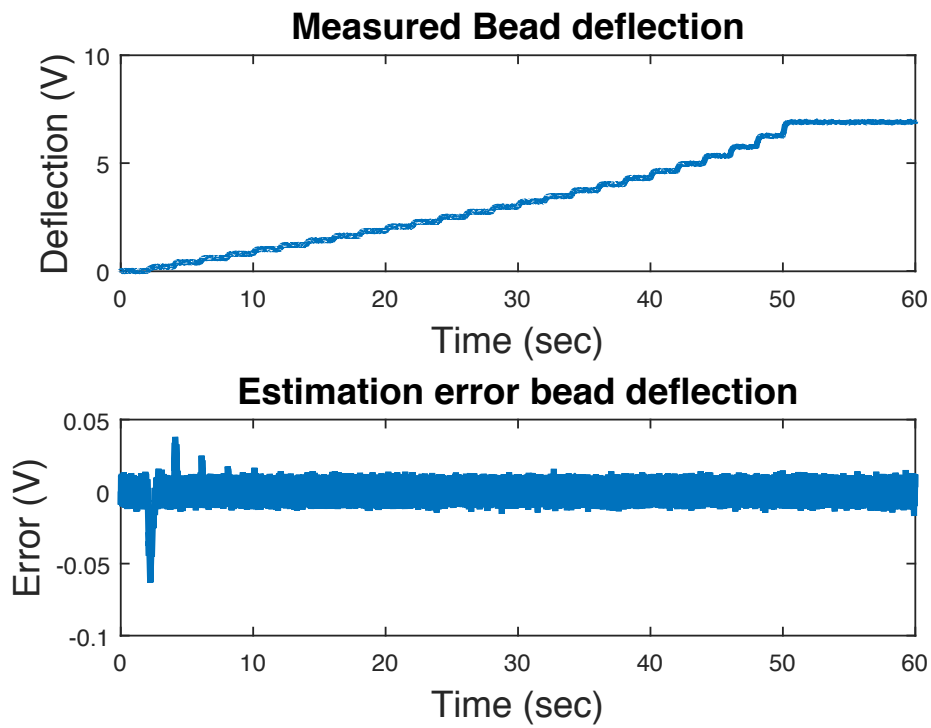


Figure 52: The response of the measured bead deflection and the estimation error between the measured bead deflection and the estimated bead deflection using the nominal nonlinear design. At each instance the measured bead deflection is increased, the estimation error has an initial bias that converges to zero at steady-state.

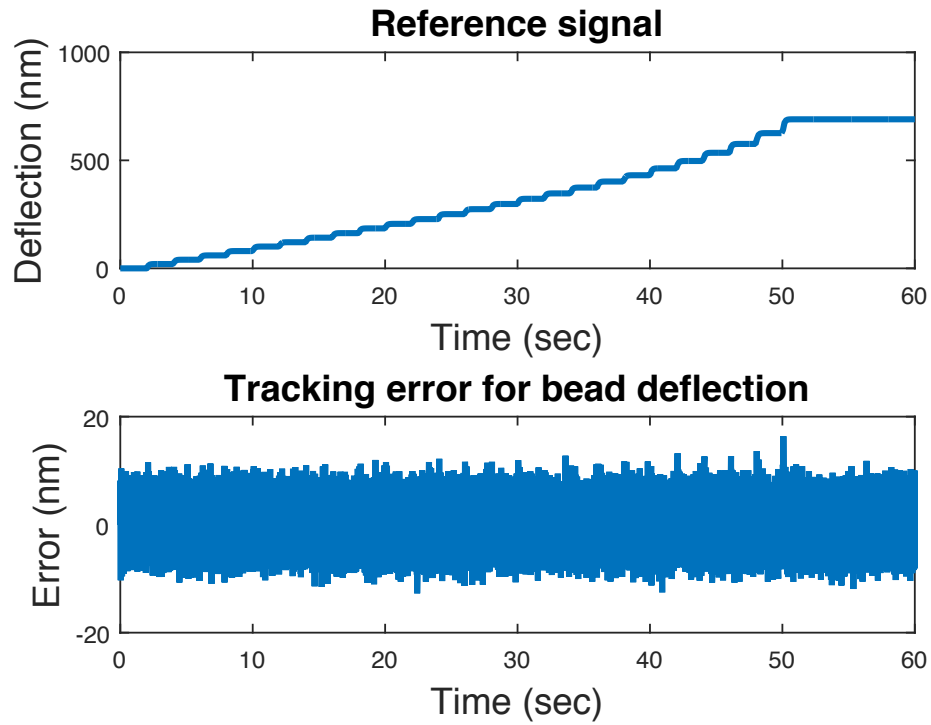


Figure 53: The response of the reference signal and the tracking error using the nonlinear PI controller. The tracking error has zero bias for each instance the reference signal is increased. Also, the tracking error has a constant variance throughout the optical trap operating range, which is expected because of the controller linearized the input-to-state map.

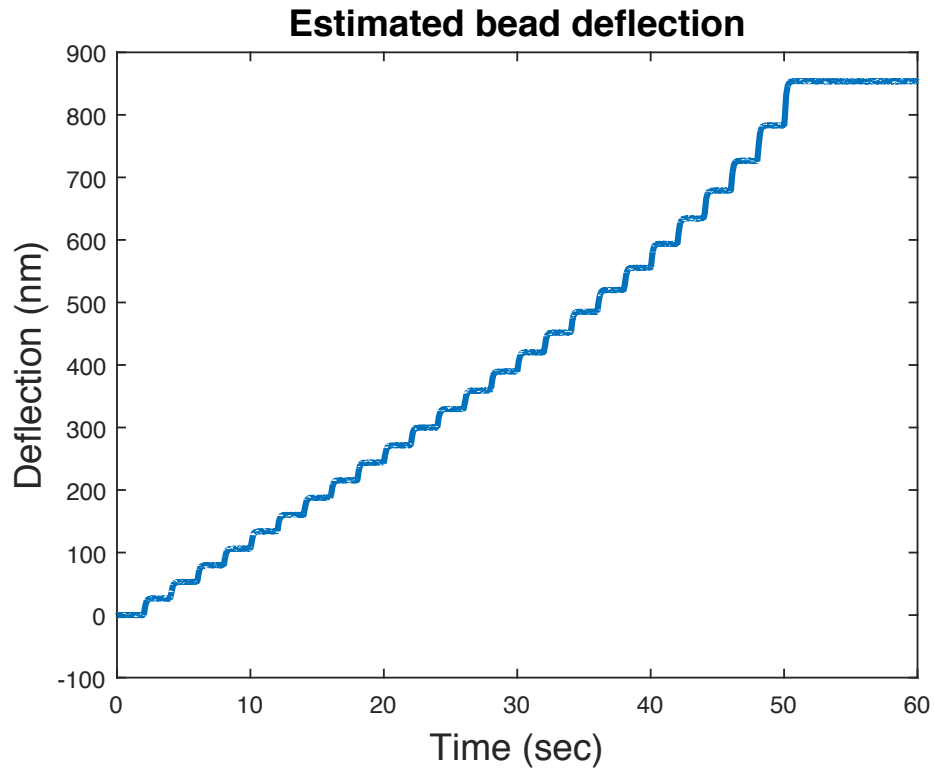


Figure 54: The response of  $\hat{z}$  using the nonlinear PI controller. The variable  $\hat{z}$  converges to a new steady-state value each instance the reference signal is increased.

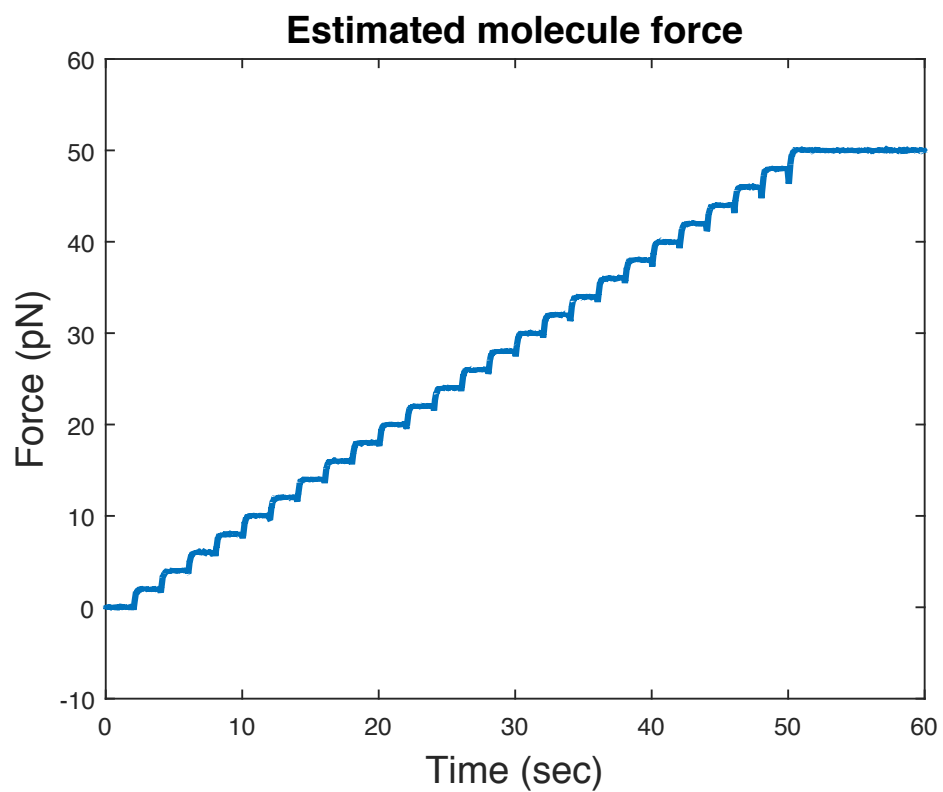


Figure 55: The response of the estimated molecule force using the nonlinear PI controller

Table 9: The values of the expected value of the  $\hat{z}$ ,  $f_d$ , and the molecule's for each increment that are obtained using the nonlinear PI design.

$E[\hat{z}]$ (nm)	$E[\hat{f}_d]$ (pN)	$x_m$ (nm)	$E[\hat{z}]$ (nm)	$E[\hat{f}_d]$ (pN)	$x_m$ (nm)
-0.02	-0.01	0	359.06	25.99	3140
26.52	1.99	2900	389.68	28.01	3144
53.07	3.99	3000	420.11	29.98	3147
79.61	5.99	3044	451.74	32.00	3149
106.18	7.99	3068	485.22	33.98	3152
133.78	10.02	3085	519.78	35.99	3154
160.25	11.99	3098	555.34	37.99	3156
187.84	14.01	3108	593.87	39.99	3158
215.35	15.99	3116	634.46	42.00	3159
243.89	17.99	3122	678.98	43.99	3161
271.45	19.99	3128	726.55	46.00	3163
300.07	22.02	3133	783.08	47.99	3164
329.62	24.02	3137	853.61	49.99	3165

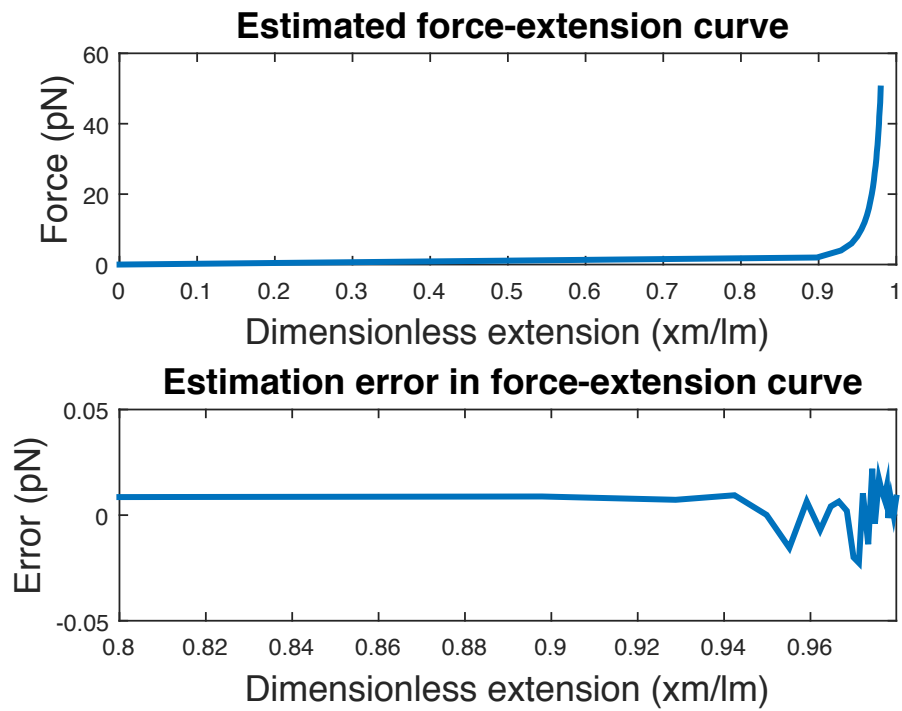


Figure 56: A schematic of the estimation force-extension curve and the estimation curve using the nonlinear PI controller.

signal and the molecule force. The difference in the methods is in the variance of the tracking error. The nonlinear PI control linearizes the state equation and the result is a constant variance in the tracking error throughout the operating range of the optical trap. The nominal nonlinear control uses a state observer with nonlinear pseudo-measurements to yield linear observer error dynamics. The tradeoff with the state observer is that the estimated bead deflection experiences a greater effect from the sensor noise as the bead deflection increases.

Both the nominal nonlinear control and the nonlinear PI control yield satisfactory estimates of the force-extension curve. The nonlinear PI control yields a maximum absolute error of 0.023 pN, while the nominal nonlinear control yields a maximum absolute error of 1.63 pN. Even though the nonlinear PI control yields less absolute error and is more easily implementable than the nominal nonlinear design, the nonlinear PI controller has a disadvantage that would be hard to satisfy in an experiment. The disadvantage is the nonlinear PI control requires the system be input-to-state feedback linearizable. In an experiment when the dynamics of the actuator, sensor, and molecule are considered, input-to-state feedback linearizable requires the system state be measurable or available to use in the state feedback to linearize the system dynamics. In the optical trap system, the system state is not measurable, so state observers are used to estimate/reconstruct the system state. The state observers also provide disturbance estimation. Thus, the nominal nonlinear design is a better control design when considering the whole dynamics of the optical trap system.

## 8.5 ADAPTIVE NONLINEAR DESIGN RESULTS

The response of the adaptive nonlinear design yielded many numerical issues in Simulink because of the adaptive state observer. Potential causes include the persistent excitation condition not being satisfied and the use of the characteristic indices that reduces the filtered version of the regression matrix to a filtered version of its submatrix. It is interesting to note that the same numerical issues arise for a simplified version of the optical trap dynamics. The simplified dynamics neglect the dynamics for the actuator, laser derivative state, and the

molecule relaxation state are neglected. Then, the simplified dynamics for the optical trap consists only of the bead deflection the disturbance. In what follows, the numerical issues are easier to explain with the simplified version of the optical trap system. The dynamics for the simplified optical trap system are

$$\frac{d}{dt} \begin{bmatrix} z \\ d_d \end{bmatrix} = \begin{bmatrix} -\omega_p & -\omega_p \\ 0 & -\omega_d \end{bmatrix} \begin{bmatrix} z \\ d_d \end{bmatrix} + \begin{bmatrix} -z \exp\left(-\frac{z^2}{2l_t^2}\right) & -d_d & z + d_d \\ 0 & 0 & 0 \end{bmatrix} \begin{bmatrix} \omega_t \\ \kappa\omega_t \\ \omega_p \end{bmatrix} \quad (8.1a)$$

$$+ \begin{bmatrix} -1 \\ 0 \end{bmatrix} u + \begin{bmatrix} \omega_t & 0 \\ 0 & \omega_e \end{bmatrix} \begin{bmatrix} \tilde{d} \\ \tilde{d}_d \end{bmatrix}$$

$$y = \begin{bmatrix} g_s & 0 \end{bmatrix} \begin{bmatrix} z \\ d_d \end{bmatrix} + \tilde{n}. \quad (8.1b)$$

and in shorthand notation as

$$\dot{x} = A_x x + f_1(x)\theta + B_u u + B_w \tilde{w} \quad (8.2)$$

$$y = C_x x + \tilde{n}. \quad (8.3)$$

The dynamics are expressed in the structure for the adaptive state observer by using the transformation

$$m = M_x x = \begin{bmatrix} C_x \\ C_x A_x \end{bmatrix} x, \quad (8.4)$$

where  $m = [m_1, m_2]^T$ , to yield the dynamics in the transformed state,

$$\dot{m} = A_m m + \begin{bmatrix} 0 \\ 1 \end{bmatrix} C_x A_x^2 M_x^{-1} m + M_x f_1(x)\theta + M_x B_w \tilde{w}, \quad (8.5)$$

where  $A_m = \delta_{i,j-1}$ . The term

$$\begin{bmatrix} 0 \\ 1 \end{bmatrix} C_x A_x^2 M_x^{-1} m$$

is in triangular structure in the  $m$  state. It is straightforward to express the regression matrix  $M_x f_1(x)$  in terms of the  $m$  state as

$$M_x f_1(m) = \begin{bmatrix} -m_1 \exp\left(-\frac{m_1^2}{2g_s^2 l_t^2}\right) & m_1 + \frac{1}{\omega_p} m_2 & -\frac{m_2}{\omega_p} \\ \omega_p m_1 \exp\left(-\frac{m_1^2}{2g_s^2 l_t^2}\right) & -\omega_p m_1 - m_2 & m_2 \end{bmatrix}, \quad (8.6)$$

which is expressed in column triangular form with respect to the state  $m$ . Each parameter has a characteristic index of one. Then, the regression matrix is expressed by the identity (as given in equation 7.21)

$$\Lambda M_x f_1(m) \Omega^{-1} = \lambda M(m) + R(m, \frac{1}{\lambda}).$$

The submatrices  $M$  and  $R$  are

$$M(m) = \begin{bmatrix} -m_1 \exp\left(-\frac{m_1^2}{2g_s^2 l_t^2}\right) & m_1 + \frac{1}{\omega_p} m_2 & -\frac{m_2}{\omega_p} \\ 0 & 0 & 0 \end{bmatrix}, \quad (8.7)$$

$$R(m, \frac{1}{\lambda}) = \begin{bmatrix} 0 & 0 & 0 \\ \omega_p m_1 \exp\left(-\frac{m_1^2}{2g_s^2 l_t^2}\right) & -\omega_p m_1 - m_2 & m_2 \end{bmatrix}. \quad (8.8)$$

The  $M$  matrix is independent of  $\lambda$  as expected. The adaptive state observer is designed for the simplified dynamics. The architecture of the adaptive state observer requires a scalar function  $j$  is chosen such that  $y^T j(y) \geq y^T y \forall y \in \mathbb{R}$  as given in equation 7.18. Several functions of  $j$  were chosen, which were

$$j(y) = k_1 y, \quad (8.9)$$

$$j(y) = k_2 \tanh(k_3 y), \quad (8.10)$$

where  $k_i$  (for  $i = 1, 2, 3$ ) are positive constants.

Let us look at the potential causes for the numerical issues with the dynamics for the simplified optical trap system. For this analysis, the molecule is stretched such that its force is increased from 0 pN to 18 pN. The same  $j$  function and the same perturbing signal of Gaussian white noise are used in the analysis.

1. Persistent excitation condition not being satisfied. The response for the parameter estimates with different values for  $\lambda$  are shown in figure 57, figure 58, and figure 59. These figures show that increasing the value of  $\lambda$  leads to a numerical singularity being introduced quicker into the system. Approaches to address the issue include
  - a. adding a perturbing signal of Gaussian white noise and increasing its power spectral density, the maximum value of the noise level chosen was 50,
  - b. applying the projection algorithm,

- c. choosing the initial value for the estimated parameter to be the true parameter value.
  - d. rescaling the problem to reduce the parameter search space,
  - e. changing the value for the frequency  $\omega_p$ , that is used to have the parameter independent system dynamics be observable,
  - f. decreasing the sampling period,
  - g. implementing different fixed-step numerical solvers,
  - h. choosing different scalar functions  $j$ ,
- and none of these approaches were successful.
2. The use of characteristic indices required a high value for  $\lambda$  be chosen to have the filtered response of the regression matrix converge uniformly with respect to time to the filtered response of the submatrix of the regression matrix. However, high values for  $\lambda$  cannot be chosen due to the numerical singularities, and results in the filtered response for the regression matrix not converging to the filtered response for the submatrix of the regression matrix. Therefore, the implementation of the adaptive state observer does not describe the system dynamics when using small value for  $\lambda$ .

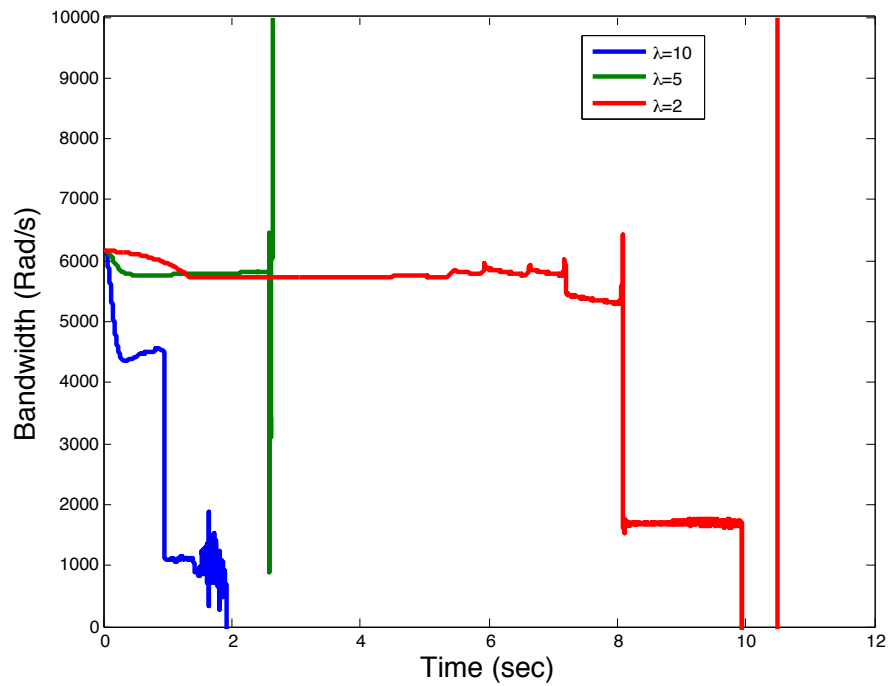


Figure 57: The response of the estimated optical bandwidth  $\omega_t$  for different values of  $\lambda$ . Increasing the value of  $\lambda$  leads to a numerical singularity being approached quicker. The actual value for  $\omega_t$  is  $6189 \text{ rad s}^{-1}$ .

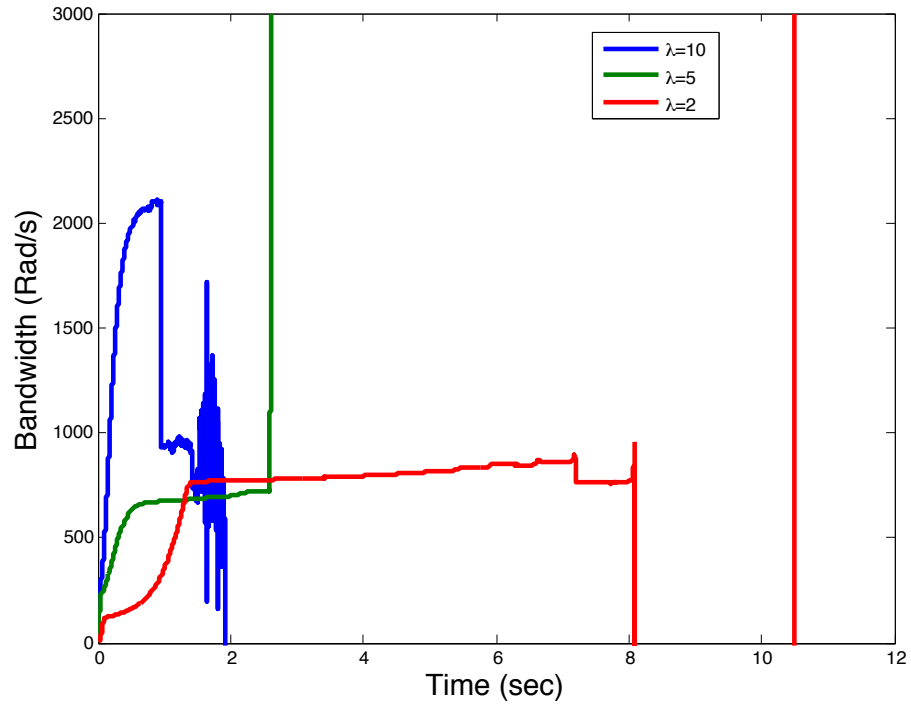


Figure 58: The response of the estimated optical bandwidth  $\kappa\omega_t$  for different values of  $\lambda$ . Increasing the value of  $\lambda$  leads to a numerical singularity being approached quicker. The actual value for  $\omega_t$  is  $6189 \text{ rad s}^{-1}$ .

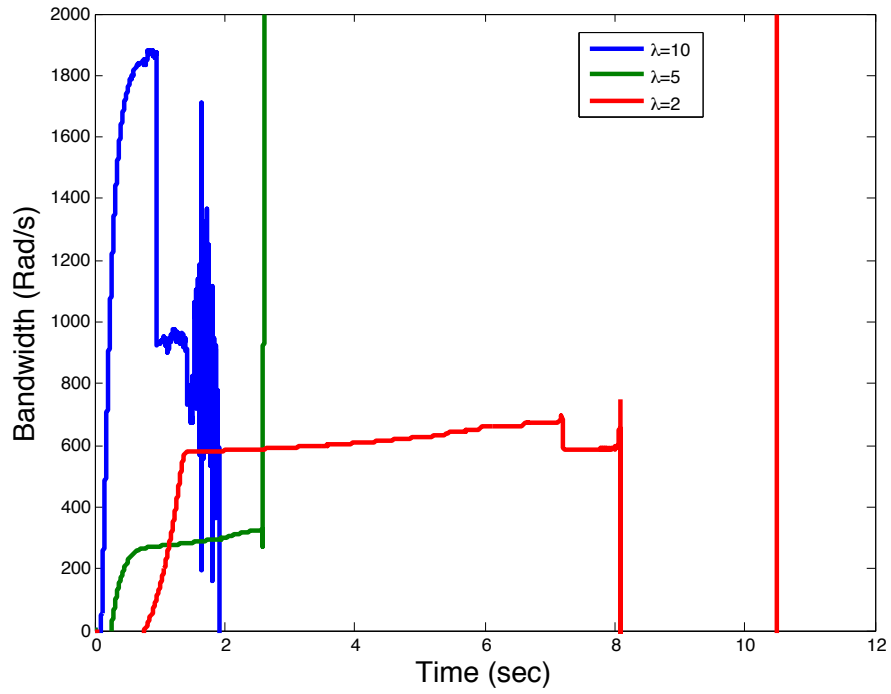


Figure 59: The response of the estimated optical bandwidth  $\omega_p$  for different values of  $\lambda$ . Increasing the value of  $\lambda$  leads to a numerical singularity being approached quicker. The actual value for  $\omega_t$  is  $10 \text{ rad s}^{-1}$ .

## 9.0 CONCLUSION

An optical trap uses radiation pressure of light to manipulate microscopic objects. The interaction between the light and the microscopic objects result in the objects experiencing optical forces. These forces are on the same order of magnitude as biological forces (typically 0.1 to 100 pN) and this feature makes optical traps appropriate for single-molecule studies. Currently, there is a growing need to create an automated optical trap that uses the entire operating range of the optical trap to study the biological forces. Spatial nonlinearities in the optical force and parameter uncertainty complicate feedback control for optical traps. A consequence is that users are spending an enormous amount of time calibrating the instrument and designing a controller, and this diverts their time away from studying the biophysics. This research explores the use of nonlinear and adaptive feedback methods to create an automated optical trap.

This research created a sensitive and automated optical trap for single-molecule applications. The effort produced the following contributions to the field of optical trapping:

1. An enhanced description of the optical trap system was derived by including a model of the molecule dynamics. The molecule experiences relaxation when stretched and thermal fluctuations due to Brownian noise, and these phenomena effect the optical trap performance. Combining the dynamics of the molecule and the optical trap results in a more accurate model of the optical trap system. Then, incorporating feedback control with the optical trap system results in better closed-loop performance and more accurate information about the molecule characteristics.

2. Statistical analyses were performed to quantify the effects of different feedback methods has on the closed-loop system and the estimate of the molecular characteristics. The optical trap system changes for each experiment depending on the stiffness of the optical trap and the molecule. For each operating condition, a fixed-gain controller needs to be designed. For each operating condition, statistical analyses were performed to quantify the effects the controller has on the closed-loop system and the estimate of the molecule characteristics.
3. The molecule characteristics were studied using the entire operating range of the optical trap. The advantages are lower laser power is used and photodamage is minimized. The tradeoff is the bead deflection becomes large, which causes stability issues, and difficulties in estimating the molecule force. These issues were addressed with nonlinear control methods that considering the system nonlinearities in the control design. The two nonlinear feedback methods considered were nonlinear PI control and the nominal nonlinear design (nonlinear Kalman filter combined with a input-output feedback and LQ structure).
4. A theoretical analysis showed that adaptive self-tuning control methods created an automated optical trap. The benefit is that the user interaction is minimized with the instrument calibration and control design. Currently, users are implementing fixed-gain control methods to improve the closed-loop performance of the optical trap. Fixed-gain control methods yield satisfactory closed-loop performance with considerable user interaction with the control design and calibration processes. A consequence is that users are diverting their time away from studying biological phenomena. This problem was addressed with adaptive self-tuning feedback methods. Adaptive self-tuning feedback methods address the parameter uncertainty by simultaneously providing parameter estimation, finding the mapping between the state feedback gains and the system parameters, and implementing the control law using the parameter estimate by applying the certainty equivalence principle.

In single-molecule studies, the trapping object is a dielectric bead that is attached to the molecule. On average, the molecule force estimate balances the optical force once the bead deflection reaches steady state. The molecule force estimate fluctuates at steady-state

because of Brownian noise. One particular interest is studying the molecule characteristics by detecting local changes in the molecular force at steady state. The force changes are measured by detecting changes in the bead deflection, then using Hooke's law to relate the position change to force change. However, the presence of Brownian noise presents a challenge in detecting local changes in the bead deflection. Controlling the bead deflection in the presence of Brownian noise is a servo control problem. Improving the servo control problem leads to better information about the molecule characteristics.

In this research, a more accurate description the optical trap system was provided by including a model of the molecule dynamics. The optical trap system was manipulated with the FSM (actuator) and the bead deflection was measured with the QPD (sensor). A complete outline for building the optical trap system was presented along with calibration methods. This experimental setup used the same laser simultaneously for sensing and actuation. The advantage of this setup over other setups is that the system is intrinsically aligned since a second laser for position sensing is not necessary.

The different feedback methods used were the LQG design, the nominal nonlinear design, nonlinear PI control, and the adaptive nonlinear design. LQG design yielded satisfactory closed-loop performance and estimates of the force-extension curve as the molecule was stretched within the linear operating range of the optical trap. As the molecule was stretched beyond the linear range, the LQG design provided poor estimates of the force-extension. The nonlinear control methods yielded satisfactory closed-loop performance and estimates of the force-extension as the molecule was stretched throughout the entire operating range of the optical trap. Nonlinear PI control yielded less absolute error in the force-extension curve than the nominal nonlinear design. However, nonlinear PI control requires the system dynamics be input-to-state feedback linearizable. The requirement would be hard to satisfy in an actual experiment because the system state is not entirely available for measurement. The entire state can be estimated with a state observer that must include disturbance estimation. Therefore, the nominal nonlinear design would be the nonlinear feedback method researchers use because the feedback method is ready to be implemented in an experiment and the resulting estimated force-extension curve yielded satisfactory results. The adaptive nonlinear design analytical work shows that the adaptive state observer yields exponential stability in

the state estimation error and the parameter estimation error. Its closed-loop analysis shows that the tracking error is driven to zero. However, numerical issues in the simulation prevent its demonstration.

## 9.1 FUTURE WORK

This research provides the foundation for an automated self-tuning optical trap capable of applying forces within its entire operating range. The research can be expanded in several ways:

1. Performing a robustness analysis on the fixed-gain controllers,
2. Expanding the control designs for a multi-input multi-output problem,
3. Incorporating the control designs into a magnetic trap,
4. Demonstrating the closed-loop performance of the controllers on an actual experiment.

### 9.1.1 Fixed gain robustness analysis

In this research, the linear design and the nominal nonlinear design are fixed-gain controllers based on the nominal values of the parameters. Fixed-gain control designs yield satisfactory closed-loop performance when assuming exact model knowledge (using the nominal value of the parameters). However, exact model knowledge is not a practical assumption, and the optical trap system is operating at off-nominal values of the parameters. The result is the closed-loop performance degradation in the linear design and the nominal nonlinear design. It is insightful to quantify the performance degradation (robustness effects) for the linear design and the nominal nonlinear design when the optical trap system is operating at an off-nominal value of the parameters, and to quantify the robustness effects on the estimate of the molecule characteristics.

### 9.1.2 MIMO control problem

The optical trap system uses the fast steering mirror (actuator) and the quadrant photodiode (sensor) to manipulate and sense the bead deflection. The optical trap system is configured

for the fast steering mirror and the quadrant photodiode manipulates and sensing in one dimension of two orthogonal dimensions. In this configuration, the estimation and control problems have been posed as a single-input single-output (SISO) problem. For the SISO problems, the proposed nonlinear and adaptive control designs yield satisfactory closed-loop performance. However, using only one dimension of the FSM and QPD may be restrictive. It is insightful to use both dimensions of the FSM and QPD to manipulate and sense the bead deflection. To manipulate and sense in two dimensions, the estimation and control problems must be reposed as multi-input multi-output (MIMO) problem. The MIMO problem can be formulated by modeling the dynamics for the optical trap system in two dimensions, then calibrating the sensor, actuator dynamics, and the optical stiffness in two dimensions. Luckily, both dimensions in the optical trap system are uncoupled because the FSM and the QPD can manipulate and sense in one dimensions independent of the other dimension. The dynamics for the optical trap system can be described by

$$\frac{d}{dt} \begin{bmatrix} \dot{x}_1 \\ \dot{x}_2 \end{bmatrix} = \begin{bmatrix} f_1(x_1) \\ f_2(x_2) \end{bmatrix} + \begin{bmatrix} B_{v1} & 0 \\ 0 & B_{v2} \end{bmatrix} \begin{bmatrix} v_1 \\ v_2 \end{bmatrix} + \begin{bmatrix} B_w \\ B_w \end{bmatrix} w, \quad (9.1a)$$

$$\begin{bmatrix} y_1 \\ y_2 \end{bmatrix} = \begin{bmatrix} h_1(x_1) \\ h_2(x_2) \end{bmatrix} + \begin{bmatrix} n_1 \\ n_2 \end{bmatrix}, \quad (9.1b)$$

where  $x_i \in \mathbb{R}^6$  are the states for each dimension,  $f_i(x_i)$  is the state-dependent vector field,  $B_{vi}$  is the input matrix for each input  $v_i$ , and  $h_i(x_i)$  is a scalar field describing the measurements for each dimension.

Equation 9.1 can then be posed into a MIMO estimation problem and a MIMO control problem. Both the MIMO estimation and control problems can be turned into two SISO problems, one SISO problem for each dimension. Therefore, the MIMO estimation and control problems can be addressed by solving a SISO problem for each dimension using the proposed nonlinear and adaptive control methods presented in this research.

### 9.1.3 Magnetic Traps

Optical traps have inherent spatial nonlinearities and parameter uncertainty. In this research, the nonlinearities and parameter uncertainty have been considered in the control

design via nonlinear and adaptive feedback methods. The proposed feedback methods can be incorporated into another single-molecule manipulator to account for its inherent nonlinearities and parameter uncertainty. The other manipulator is a magnetic trap, which uses magnetic fields to manipulate microscopic objects. Magnetic traps are able to produce forces over a large range of magnitudes, selective because only magnetic objects are manipulated, and noninvasive since the force field can be applied external to the environment. Several designs exist for magnetic traps, permanent and electromagnet, and we would be interested in the electromagnet design. For electromagnet magnetic traps, the forces are produced via the magnetic field and high field gradient. The high field gradients are producing by shaping the magnetic cores, while the field's strength and orientation are controlled via the current flow in the electromagnet. The result is a nonlinear relationship between the force produced and the current. In addition to nonlinearities, a magnetic trap contains parameter uncertainties due to the the viscous forces and magnetic characteristics of an individual bead are unknown. Viscous forces acting on the bead depends on its depth due to wall effects. The magnetic characteristics of an individual bead are unknown due to uncertainties in the manufacturing process. One approach to improve the closed-loop performance of a magnetic trap is to implement the proposed nonlinear and adaptive feedback methods to address the inherent nonlinearities and parameter uncertainty.

#### **9.1.4 Proof of Concept Demonstration**

Proof of concept is needed to demonstrate the closed-loop performance of these controllers in an actual single molecule experiment. The experiment chosen is the stretching of DNA to replicate its force-extension curve. The force-extension curve is nonlinear because DNA becomes stiffer the farther the molecule is stretched [126, 97]. The experiment is performed in a single-gradient optical trap configuration that requires the one end of the DNA be attached to the flow cell and the other end of DNA be attached to the dielectric bead. This experiment enables the closed-loop performance of each controller to be quantified and compared. The two metrics to be quantified are:

1. The improvement in the closed-loop performance when considering the system nonlinearities in the controller design.
2. The total time saved when using adaptive self-tuning control methods instead of fixed-gain control methods.

This section discusses the experimental setup, and the materials and methods needed for the sample preparation.

**9.1.4.1 Experimental Setup** The optical trap was built according to section 2.3 using an inverted microscope (Zeiss Axiovert 200) and an infrared laser (Nd:YAG at 1064 nm). The actuation method uses a fast steering mirror (FSM) to control the laser's position at the specimen plane. The FSM provides more than adequate bandwidth according to the actuator's Bode plot as shown in figure 21. The sensing method uses a quadrant photodiode (QPD) to measure the bead deflection. The optical system is intrinsically aligned because the same laser is used for trapping and sensing. The experimental setup operated in a single-beam optical trap configuration. The bead deflection is digitized using a dSpace data-acquisition board. The controllers were built using Matlab's Simulink environment and numerically implemented using the dSpace ControlDesk environment. The implementation was done using a one-step solver (fourth order Runge-Kutta) with a sampling frequency of 10 kHz.

**9.1.4.2 Materials and Methods** The experiment required a custom-made DNA sample be compatible with the single-beam optical trap configuration. The sample includes the flow cell chamber (flow cell), linear DNA differentially labeled at either end, and modified surfaces to attach the DNA. The sample was created by slightly modifying the protocol given by Schlingman [5].

It is first necessary to attach the DNA to the flow cell and the dielectric bead. The attachment methods affect the cleaning process of the flow cell and also the DNA labeling process. First, consider the attachment between the DNA and dielectric bead. The attachment method chosen is a streptavidin-biotin bond by having a biotin labeled end of the DNA

Table 10: The lifetime of different bonds as a function of force. Source [5].

Force (pN)	Lifetime (s)
Streptavidin-Biotin	
10	18.000
20	5.500
30	1.7000
60	46
90	1.3
Digoxigenin - Antidigoxigenin	
10	4
20	0.24
30	0.015

react with streptavidin coated dielectric beads [19, 16, 127]. The streptavidin-biotin bond is chosen because it is a high affinity bond between a protein and a ligand, and is the strongest noncovalent bond [128].

The second attachment method considered is the attachment between the DNA and the flow cell. Many methods are used to attach the DNA to the flow cell [5], and these methods include using a second streptavidin-biotin bond or a digoxigenin-antidigoxigenin bond [127]. A second streptavidin-biotin bond is not used because both ends of the DNA need different types of non-covalent bonds to allow consistent binding of the DNA to both the bead and the flow cell, and weak attachment forces. These attachment methods have a lifetime (time needed to rupture) that is force dependent [5]. Table 10 lists the lifetime of the digoxigenin-antidigoxigenin bond and the streptavidin-biotin bond at several forces. Weak attachment bonds like the digoxigenin-antidigoxigenin bond can rupture if the experiment requires high forces to probe molecules. For example, experiments requiring high forces to probe molecules include greater than ( $>20$  pN) for polymerases [129] and ( $>13$  pN) for

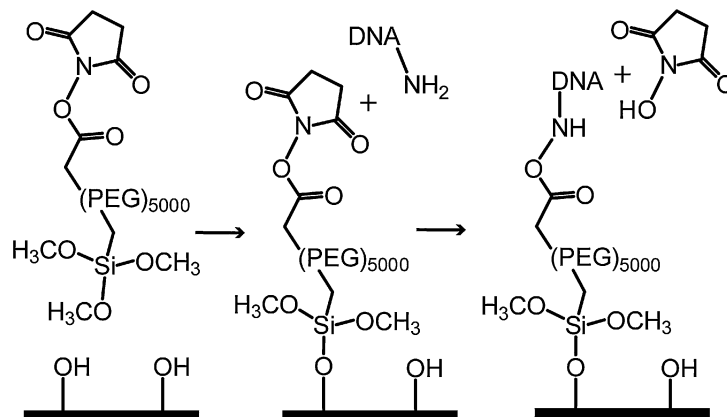


Figure 60: The surface chemistry of attaching DNA to a glass surface. The glass is first cleaned with “piranha solution” to remove any dirt and to increase hydroxylation. The OH groups react with the silane attach the silane-PEG-NHS to the glass surface. The NHS group then reacts with the amino-allyl labeled end of DNA to attach DNA to the surface. Source [5].

hairpins [130]. Therefore, strong attachment bonds are needed when the experiment require high forces and also the binding must be different than the streptavidin-biotin bond.

In this research, DNA is attached to the flow cell through the reaction between a N-hydroxysuccinimide (NHS) group on the flow cell with a amino-allyl labeled end of the DNA. This attachment method involves the flow cell be coated with silane polyethylene glycol N-hydroxysuccinimide, silane PEG-NHS (Nanocs); the NHS group on the PEG reacts with a amino-allyl labeled end of the DNA [5, 131]. PEG is chosen because it is a polymer that reduces protein absorption on the surface. This surface attachment method has specific binding between the NHS group and the amino-labeled end of the DNA, and a strong bond for pulling experiments. The surface chemistry for this attachment has two steps, as shown in figure 60. The first step requires a clean surface with hydroxyl groups (OH). The hydroxyl groups react to the silane to attach the silane-PEG-NHS to the surface. The second step creates the covalent attachment between the amino-allyl labeled end of the DNA with the NHS group.

The sample preparation protocol is given in the following subsections. The protocol includes the flow cell creation, attaching the silane PEG-NHS to the surface, labeling the DNA, and attaching the DNA to the flow cell and the dielectric bead.

**Flow Cell Chamber:** The flow cell chamber is created with the following materials:

1. Glass coverslips (Corning, Number 1.5, 25 mm<sup>2</sup>)
2. Glass microscope slides (VWR micro slides, 1 mm thick, Area is 25 mm by 75 mm)
3. Double sided sticky tape (3M)
4. Sulfuric Acid
5. 30% Hydrogen peroxide
6. Double distilled water ddH<sub>2</sub>O

The glass coverslips are cleaned by immersion in “piranha solution”, a solution of 3:1 concentrated sulfuric acid to 30% hydrogen peroxide for 15 min. The piranha solution removes any dirt and debris from the glass coverslips and increases hydroxylation. The coverslips are then rinsed thoroughly in ddH<sub>2</sub>O to remove any remaining piranha solution. The microscope slides are also rinsed in ddH<sub>2</sub>O. Both the coverslips and the microscope slides are then air dried at room temperature. Finally the coverslip is attached to the microscope slides via the 2 pieces of double sided sticky tape that are placed 20 mm apart.

**Applying the Silane PEG-NHS to Surface:** The application of the silane PEG-NHS to the flow cell required the following material:

1. Silane PEG-NHS (Nanocs, 5000 molecular weight)
2. Dimethyl Sulfoxide DMSO (Sigma-Aldrich, anhydrous  $\geq 99\%$ )
3. ddH<sub>2</sub>O
4. PBS solution at pH 7.3

The silane PEG-NHS is dissolved in DMSO at a concentration of 1% weight per volume. The DMSO provides an anhydrous environment to minimize the hydrolysis of NHS. The solution of silane PEG-NHS with DMSO is flowed into the flow chamber and held there for 1 h to allow the reaction between the silane and the hydroxyl groups to complete. After an hour, the flow cell is rinsed with ddH<sub>2</sub>O. A second rinse is performed with PBS solution at pH 7.3. This pH level is chosen to minimize NHS hydrolysis.

**DNA Preparation:** The DNA chosen was pTol2 Dual-fucci (P027.2) that was originally configured in a circular strand or plasmid. The plasmid needed to be reconfigured into a linear strand to allow its ends be labeled for the attachments. The reconfiguration required the use of restriction enzymes. Restriction enzymes look for a particular sequence of nucleobases, then cut the DNA at that location. DNA is composed of a sequence of four nucleobases: Adenine (A), Thymine (T), Guanine (G), and Cytosine (C). The DNA labeling procedure used is shown in figure 61 and outlined as follows:

1. A 10 kb plasmid was cut with the restriction enzyme Apa1 to yield a linear piece of DNA.
2. Biotin label both ends of the DNA. The biotin labeling allows for the biotin labeled end of DNA to attach to the streptavidin coated dielectric bead via the reaction between streptavidin and biotin.
3. The biotin-labeled DNA was cut with the restriction enzyme Sph1 to yield two linear pieces of DNA, a 9.5 kb piece and a 0.5 kb piece. Each DNA piece is biotin labeled on one end and its other end is unmodified.
4. The unmodified ends of DNA are labeled with amino-allyl. This amino-allyl labeling allows for the amino-allyl labeled end of DNA to attach to the flow cell via the reaction between amino-allyl and the NHS group.

The DNA labeling procedure is detailed below. Each step was verified by simultaneously running the procedure on a second type of DNA, pCS2+ mSA-eGFP (P087), and comparing the results.

The first step required the restriction enzyme Apa1 (New England Biolabs). Apa1 cut the plasmid at the nucleobase sequence GGGCCC (5' to 3' direction) and left a 3' overhang. The restriction digest occurred in a 100  $\mu$ l sample and required the material listed in table 11. The restriction digest incubated overnight in a water bath at 37 °C. The digests were taken out of the water bath and cleaned using the PCR clean-up Gel extraction kit from Macherey-Nagal. Note that the P027 sample contained too much DNA to follow the procedure given in the PCR clean-up Gel extraction kit. The P027 sample was separated into two equal samples (labeled P027A and P027B), and cleaned with the PCR clean-up Gel extraction kit.

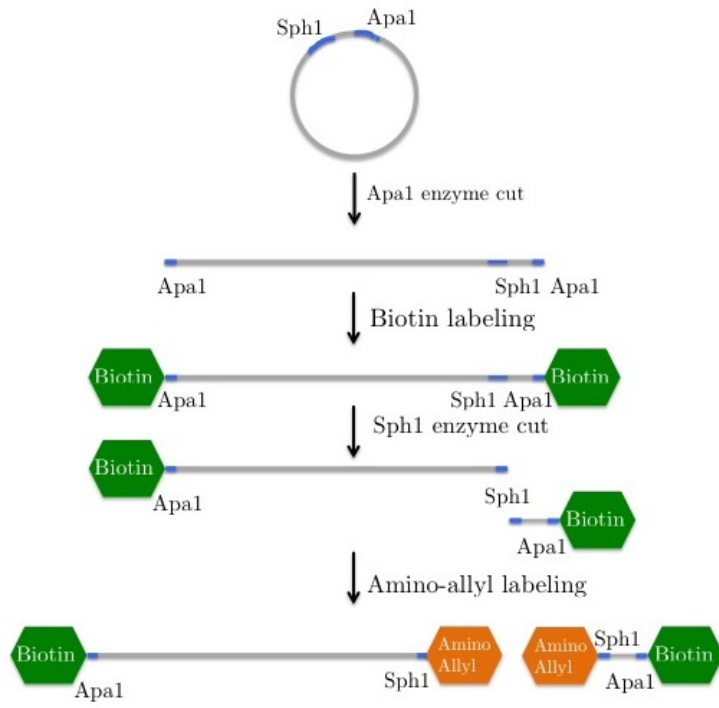


Figure 61: A schematic of the DNA preparation process. The DNA (grey) is a plasmid, or circularly configured. The first step used the restriction enzyme *Apa1* (blue) to cut the plasmid to yield a linear piece of DNA with 3' overhangs. The 3' overhangs were labeled with biotin (green). A second restriction enzyme *Sph1* (blue) cuts the biotin-labeled DNA into two pieces with 3' overhangs. Finally, the 3' overhangs were labeled with aminoallyl (orange).

Table 11: Material used for the *Apa1* restriction digest.

Material	P027	P087
DNA	30 $\mu$ l	10 $\mu$ l
10x CutSmart Buffer	10 $\mu$ l	10 $\mu$ l
<i>Apa1</i>	2 $\mu$ l	2 $\mu$ l
ddH <sub>2</sub> O	58 $\mu$ l	78 $\mu$ l

The success of the restriction digest was verified using agarose gel electrophoresis. Agarose gel electrophoresis separates DNA of different lengths (molecular weights) by applying a voltage to move a charged molecule (DNA is negatively charged due to the phosphate groups) through an agarose gel. Short linear stranded DNA molecules and plasmids travel farther than long linear stranded DNA molecules in agarose gel. The agarose gel electrophoresis was performed on the following samples: P027 without Apa1, P027 with Apa1, P087 without Apa1, and P087 with Apa1 and the results are shown in figure 62. The DNA samples without Apa1 traveled farther than the DNA samples with Apa1. These results confirmed the success of the Apa1 restriction digest.

Next, the DNA purity and density were measured using spectrophotometry. Spectrophotometry measures the sample purity and density by analyzing the ultraviolet light absorption pattern of the sample. DNA purity is determined by the ratio of light absorption at 260 nm to the light absorption at 280 nm. A pure DNA sample yields a 1.8 ratio. The spectrophotometer chosen was a Nanodrop, which obtains these measurements using the surface tension of a liquid between two optical pedestals. When a small amount of sample is placed between the optical pedestals, a liquid column is created via surface tension to form an optical path. The Nanodrop results are shown in table 12. Table 12 showed that the DNA purity was 1.85 and 1.86 for P027A and P027B respectively, but the density was too low to proceed with sample preparation. The sample density was increased with ethanol precipitation. The ethanol precipitation process involved the following steps:

1. Combined the elutes of P027A and P027B into one sample.
2. Add 10  $\mu$ l 5M  $\text{NH}_4$  Acetate
3. Add 275  $\mu$ l 100% EtOH.
4. Incubate for 2 h at  $-20^\circ\text{C}$ .
5. Spin the sample at top speed (15 800 g) for 15 min
6. Remove the EtOH
7. Wash the DNA in 100  $\mu$ l 70% EtOH
8. Spin the DNA for 5 min
9. Let the DNA dry before resuspending in 10  $\mu$ l ddH<sub>2</sub>O

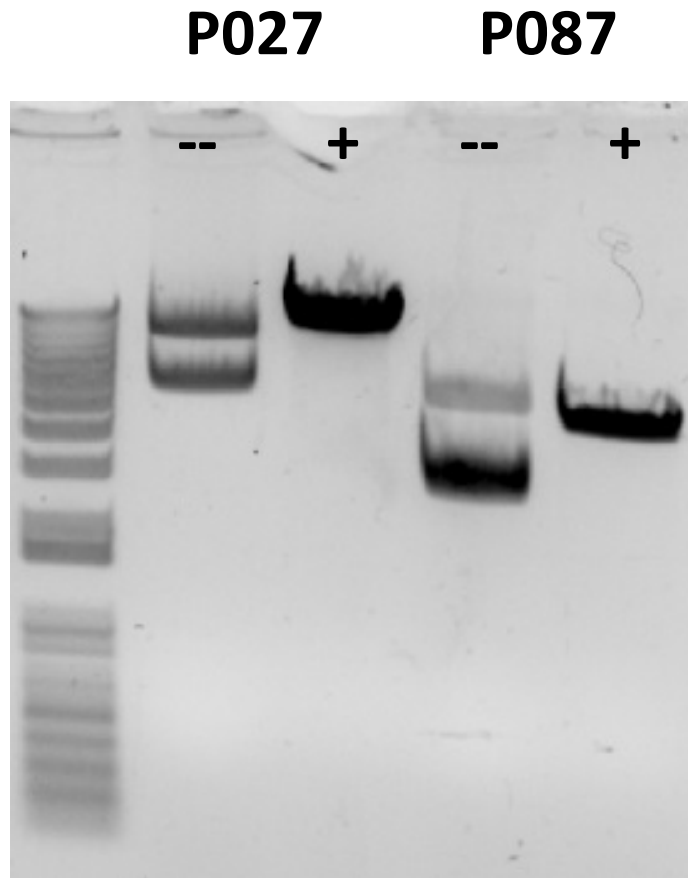


Figure 62: The agarose gel electrophoresis was used to determine the success the Apa1 digest on two different DNAs (P027 and P087). Each DNA has two columns: The negative column contains no Apa1 digest while the positive sign column contains the Apa1 digest. The Apa1 digests for both DNAs show the DNA traveled less than the no Apa1 digests. This indicates the success of the Apa1 digest.

Table 12: Nanodrop results after the APA1 digests to determine the sample density and the DNA purity.

Sample ID	ng/ $\mu$ l	A260	A280	260/280	260/230	Constant
P027 Apa1 A	229.54	4.591	2.476	1.85	2.09	50.00
P027 Apa1 B	224.01	4.480	2.411	1.86	2.27	50.00
P087 Apa1	103.35	2.067	1.127	1.83	2.2	50.00

After the ethanol precipitation, the DNA purity and density were measured again and the results are shown in table 13. The results showed that the DNA purity was 1.84 with an increased density.

The second step is the first labeling reaction. The first labeling reaction was the biotin labeling the 3' end of the DNA. The labeling reaction followed the procedure given in the Roche documentation of Biotin-16-ddUTP, which required adding the following material to the 10  $\mu$ l DNA sample:

- 4  $\mu$ l 5x TdT buffer
- 4  $\mu$ l 25 mM  $\text{CoCl}_2$
- 1  $\mu$ l 1 mM Biotin-16-ddUTP
- 1 ml TdT

Table 13: Nanodrop results after the APA1 digests with ethanol precipitation. The Nanodrop determines the sample density and the DNA purity.

Sample ID	ng/ $\mu$ l	A260	A280	260/280	260/230	Constant
P027 Apa1	1335.64	26.713	14.514	1.84	2.12	50.00
P087 Apa1	771.21	15.424	8.821	1.75	2.06	50.00

The reaction incubated at 37 °C for 15 min, then 2 µl 0.2 M EDTA with pH 9.0 was added to stop the reaction. The success of the labeling efficiency was verified using the fact that biotin reacts with streptavidin. For each DNA sample (P027 and P087), three reactions were setup: the control reaction (no streptavidin was added to the sample), streptavidin reaction (streptavidin was added to the sample), bead reaction (DNA binded to streptavidin coated microspheres). The reactions were composed of:

- Control reaction: 0.5 µl of DNA (either P027 or P087), 14.5 µl 0.1 M M PBS with pH 5.5.
- Streptavidin reaction: 0.5 µl of DNA (either P027 or P087), 5 µl Streptavidin-AF568 (1 µg ml<sup>-1</sup>)
- Beads reaction: 0.5 µl of DNA (either P027 or P087), 4 µl (Streptavidin-coated, 3 µm diameter, Spherotech), 10.5 µl 0.1 M PBS pH 5.5

Each reaction incubated for 1 h at room temperature with occasional stirring, then studied with agarose gel electrophoresis. A successful biotin labeling reaction shows that the streptavidin reaction travels a shorter distance in the agarose gel than the control reaction because the addition of streptavidin increases the molecular weight of the sample. Note, the streptavidin reaction may contain smears because of AF (Alexa-Flour). The agarose gel electrophoresis results are shown in figure 63. The streptavidin column showed significant amounts of DNA at a higher molecular weight than the DNA in the control column. The biotin labeling is successful. It is unclear why the bead columns were empty. Possible explanations include an issue with the binding reaction process, the beads were lost in the process, or the beads into load in the agarose gel.

The third step is the second restriction enzyme digest to cut the biotin-labeled DNA into two shorter strands of DNA . The restriction enzyme chosen was Sph1 (New England Biolabs), which cut the DNA at the nucleobase sequence GCATGC (5' to 3' direction) and left 3' overhangs. A successful Sph1 digest should cut the 10 kb length of DNA into a 9.5 kb length piece and a 0.5 kb length piece. The Sph1 digest occurred in a 100 µl sample that required the following material:

- 50 µl of purified biotin labeled DNA
- 10 µl 10x CutSmart buffer

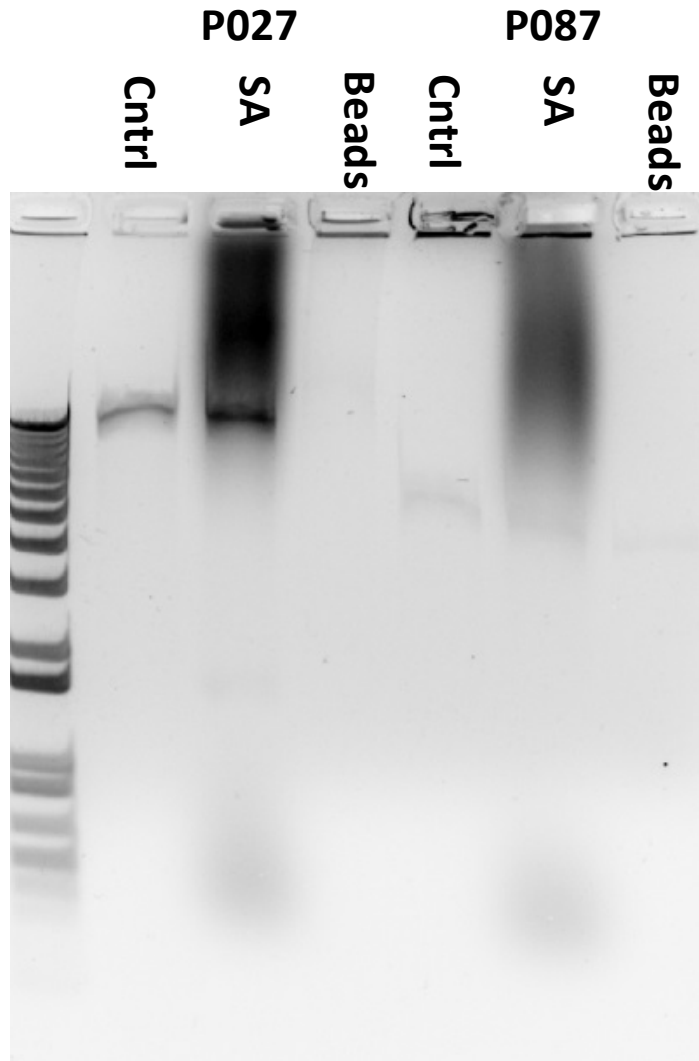


Figure 63: Agarose gel analysis to determine the success of the biotin labeling the 3' end of DNA. Each DNA (P027 and P087) had three reactions: Control (no streptavidin added to the biotin labeled DNA, Streptavidin or SA (streptavidin binded to the biotin labeled DNA), and Beads ( streptavidin coated beads binded to the biotin labeled DNA). A successful biotin labeling shows the streptavidin column moves slower in the agarose gel with the addition of streptavidin increases the molecular weight. The streptavidin column contains smears because of Alexa-Fluora. The streptavidin column contains more DNA at higher molecular weights than then control columns. This proves the biotin labeling. It is not clear why the beads column appear to be empty. Possible explanations include issues with the binding process, the beads were lost, or the beads did not travel through the agarose gel.

- 2  $\mu\text{l}$  Sph1
- 38  $\mu\text{l}$  ddH<sub>2</sub>O

The enzyme digest incubated overnight in a water bath at 37 °C. The digests were taken out of the water bath and cleaned using the PCR clean-up Gel extraction kit. The success of the Sph1 digestion was determined by comparing the sample with a second DNA sample with only Apa1 digestion using agarose gel electrophoresis. The results are shown in figure 64. The results showed the Sph1 enzyme was successful for two reasons. The first reason was the Apa1 and Sph1 column has a DNA band that traveled slighter farther than the DNA band in the Apa1 column, which was consistent with the 9.5 kb DNA piece that should be produced. The second reason was the Apa1 and Sph1 column has the additional presence of a small piece of DNA, which was consist with the 0.5 kb that should be produced.

Next, the DNA purity and concentration were measured using spectrophotometry. The results are shown in table 14. The results showed the DNA purity was 1.87, however the density is too low. The density was increased using the following procedure:

1. The sample volume was increased to 100  $\mu\text{l}$
2. Add 10  $\mu\text{l}$  3M Sodium Acetate pH 5.2
3. Add 275  $\mu\text{l}$  of 100% EtOH
4. Incubate the sample at  $-20\text{ }^{\circ}\text{C}$  for 3 h
5. Spin the sample at top speed for 15 min.
6. Remove the ethanol.
7. Wash the sample with 200  $\mu\text{l}$  70% EtOH
8. Spin the sample at top speed for 5 min
9. Air dry the sample for 5 min
10. Resuspend the sample in 10  $\mu\text{l}$  of ddH<sub>2</sub>O

The resuspended sample was analyzed using spectrophotometry and the results are shown in table 15. The results show a density increased and an purity improvement.

The final step involved a second labeling reaction. The second labeling reaction was the amino-allyl labeling the free 3' ends of the DNA. The labeling reaction followed the proce-

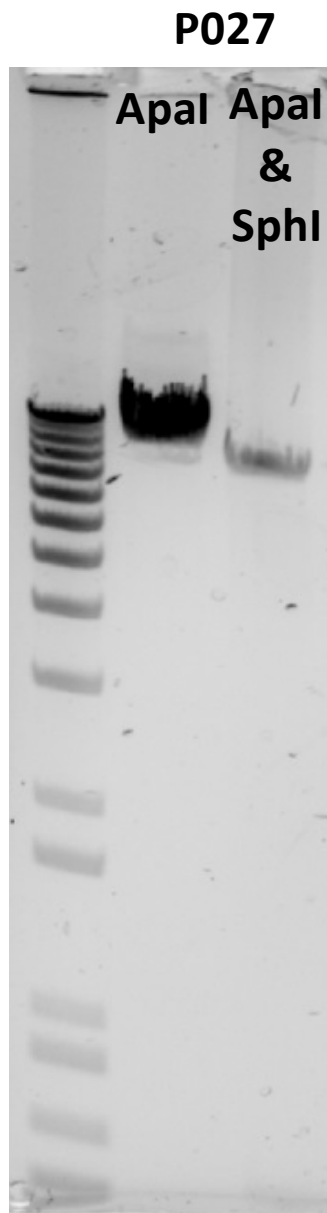


Figure 64: Agarose gel electrophoresis on the restriction digest samples: Apa1 digest, and the Apa1 and Sph1 digests. The APA1 digest has one DNA band, which is expected because the APA1 digest cuts the plasmid at one location. The Apa1 and Sph1 digests shows are two pieces of DNA. One piece traveled slightly farther than the DNA band in the Apa1 column, which indicates the 9.5 kb piece that is expected. The second piece is near the bottom edge of the gel, which indicates the presence of a smaller piece of DNA, the 0.5 kb piece that is expected.

Table 14: Nanodrop results after using the second restriction enzyme Sph1

Sample ID	ng/ $\mu$ l	A260	A280	260/280	260/230	Constant
P027 Apa1 Sph1 Biotin	110.39	2.208	1.183	1.87	2.36	50.00

Table 15: Nanodrop results after using the second restriction enzyme Sph1 and concentrating the sample.

Sample ID	ng/ $\mu$ l	A260	A280	260/280	260/230	Constant
P027 Apa1 Sph1 Biotin	724.68	14.494	7.962	1.82	1.82	50.00

cedure given in the Roche documentation for Biotin-16-ddUTP, which required the following material be added to the 10  $\mu$ l sample:

- 4  $\mu$ l 5x TdT buffer
- 4  $\mu$ l 25 mM  $\text{CoCl}_2$
- 1  $\mu$ l 2 mM Aminoallyl-dUTP
- 1 ml TdT

The reaction incubated for 1 h at 37  $^\circ\text{C}$  with mixing every 15 min. The sample concentration was analyzed with spectrophotometry and the results are shown in table 16.

**Attachment Between DNA and Flow Cell:** The attachment of the flow cell to the aminoallyl labeled end requires dissolving the 7.2  $\mu\text{g}$  of the aminoallyl-dsDNA-biotin sample

Table 16: Nanodrop results after double labeling the DNA

Sample ID	ng/ $\mu$ l	A260	A280	260/280	260/230	Constant
P027 Double Label	80.01	1.6	0.858	1.86	2.39	50.00

into PBS solution with pH7.3. The DNA and PBS solution is flowed into the flow cell and the flow cell is sealed with **tape** to prevent air from entering, The flow cell must be sealed because air can destroy the DNA. The reaction proceeded for 1 h at room temperature to allow the binding between the amino-allyl and the NHS group. Next, the flow cell was rinsed with PBS solution with pH8.3 to remove any unbounded DNA. A second rinse was performed with PBS solution with pH9.0 and the reaction proceed for 1 h at room temperature. The second rinse was needed to hydrolyze any remaining NHS groups to prevent the streptavidin coated beads from sticking to the flow chamber surface.

**Attachment Between DNA and Dielectric Bead:** The attachment of the streptavidin beads to the biotin labeled end of DNA required both the flow cell and the streptavidin beads be washed twice with PBS solution with pH7.3 and 0.1% TWEEN. After washing the beads were diluted to a concentration of 0.3% mass per volume. The beads were flowed into the flow cell and the reaction proceeded for 15 to 20 h at room temperature in the humidity chamber.

## BIBLIOGRAPHY

- [1] L. P. Ghislain, N. A. Switz, and W. W. Webb. Measurement of small forces using an optical trap. *Review of Scientific Instruments*, 65:2762–2768, 1994.
- [2] H. Felgner, O. Muller, and M. Schliwa. Calibration of light forces in optical tweezers. *Applied Optics*, 34:977–982, 1995.
- [3] J. Howard. *Mechanics of Motor Protein and the Cytoskeleton*. Sinauer Associates, Inc., 2001.
- [4] S. Ferree and H.W. Blanch. The hydrodynamics of dna electrophoretic stretch and relaxation in a polymer solution. *Biophysical Journal*, 87:468–475, 2004.
- [5] D. J. Schlingman, A. H. Mack, S. G. J. Mochrie, and L. Regan. A new method for the covalent attachment of DNA to a surface for single-molecule studies. *Collides and Surfaces B: Biointerfaces*, 83:91–95, 2011.
- [6] K. Svoboda and S. M. Block. Biological applications of optical forces. *Annual Review of Biophysics and Biomolecular Structure*, 23:247–285, 1994.
- [7] M. W. Elting and J. A. Spudich. Future challenges in single-molecule fluorescence and laser trap approaches to studies of molecular motors. *Developmental Cell*, 23:1084–1091, 2012.
- [8] E. A. Abbondanzieri, W. J. Greenleaf, J. W. Shaevitz, R. Landick, and S. M. Block. Direct observation of base-pair stepping by rna polymerase. *Nature*, 438:460–465, 2005.
- [9] H. Fu, H. Chen, J. G. Marko, and J. Yan. Two distinct overstretched dna states. *Nucleic Acids Research*, 38:5594–5600, 2010.
- [10] L. Bai, T. J. Santangelo, and M. D. Wang. Single-molecule analysis of rna polymerase transcriptional. *The Annual Review of Biophysics and Biomolecular Structure*, 25:343–360, 2006.
- [11] Y R. Chemla. Revealing the base pair stepping dynamics of nucleic acid motor protein with optical traps. *Physical Chemistry Chemical Physics*, 12:3080–3095, 2010.

- [12] F. M. Fazal and S. M. Block. Optical tweezers study life under tension. *Nature Photonics*, 5:318–321, 2011.
- [13] P. J. Elms, J. D. Chodera, C. J. Bustamante, and S. Marqusee. Limitations of constant-force-feedback experiments. *Biophysical Journal*, 103:1490–1499, 2012.
- [14] K. C. Neuman and A. Nagy. Single-molecule force spectroscopy: optical tweezers, magnetic tweezers and atomic force microscope. *Nature Methods*, 5:491–505, 2008.
- [15] K. Svoboda, C. F. Schmidt, B. J. Schnapp, and S. M. Block. Direct observation of kinesin stepping by optical trapping interferometry. *Nature*, 365:721–727, 1993.
- [16] D. E. Smith, S. J. Tans, S. B. Smith, S. Grimes, D. L. Anderson, and C. Bustamante. The bacteriophage  $\phi 29$  portal motor package DNA against a large internal force. *Nature*, 413:748–752, 2001.
- [17] M. H. Larson, J. Zhou, C. D. Kaplan, M. Palangat, R. D. Kornberg, R. Landick, and S. M. Block. Trigger loop dynamics mediate the balance between the transcription fidelity and speed of RNA polymerase II. *Proceedings of the National Academy of Sciences*, 109:6555–6560, 2012.
- [18] C. Hodges, L. Bintu, L. Lubkowska, M. Kashlev, and C. Bustamante. Nucleosomal fluctuations govern the transcriptional dynamics of RNA polymerase II. *Science*, 325:626–628, 2009.
- [19] M. D. Wang, H. Yin, R. Landick, J. Gelles, and S. M. Block. Stretching DNA with optical tweezers. *Biophysical Journal*, 72:1335–1346, 1997.
- [20] J. C. M. Gebhardt, T. Bornschlogl, and M. Rief. Full distance-resolved folding energy landscape of one single protein molecule. *PNAS*, 107:2013–2018, 2010.
- [21] I. Heller, T. P. Hoekstra, G. A. King, E. J. G. Peterman, and G. J. L. Wuite. Optical tweezers analysis of DNA-protein complexes. *Chemical Reviews*, 114:3087–3119, 2014.
- [22] Y. E. Kim, M. S. Hipp, A. Bracher, M. Hayer-Hartl, and F. U. Hartl. Molecular chaperone function in protein folding and proteostasis. *The Annual Review of Biochemistry*, 82:323–55, 2013.
- [23] M. T. Woodside and S. M. Block. Reconstructing folding energy landscapes by single-molecule force spectroscopy. *The Annual Review of Biophysics*, 43:19–39, 2014.
- [24] K. J. Freedman, S. Raza Haq, J. B. Edel, P. Jemth, and M. J. Kim. Single molecule unfolding and stretching of protein domain inside a solid state nanopore by electric field. *Scientific Reports*, 3:1638, 2013.
- [25] C. Cecconi, E. A. Shank, C. Bustamante, and S. Marqusee. Direct observation of the three-state folding of the single protein molecule. *Science*, 309:2057–2060, 2005.

- [26] E. A. Shank, C. Cecconi, J. W. Bill, S. Marqusee, and C. Bustamante. The folding cooperativity of a protein is controlled by its chain topology. *Nature*, 465:637–640, 2010.
- [27] Y. R. Chemla, K. Aathavan, J. Meiners, S. Grimes, P. J. Jardine, D. L. Anderson, and C. Bustamante. Mechanism of force generation of a viral DNA packaging motor. *Cell*, 112:683–692, 2005.
- [28] K. Visscher and S. M. Block. Versatile optical traps with feedback control. *Methods in Enzymology*, 298:460–489, 1998.
- [29] R. E. Sterba and M. P. Sheetz. Basic laser tweezers. *Methods in Cell Biology*, 55:29–41, 1998.
- [30] M. Capitanio and F. S. Pavone. Interrogating biology with force: Single molecule high-resolution measurements with optical tweezers. *Biophysical Journal*, 105:1293–1303, 2013.
- [31] T. T. Perkins. Optical traps for single molecule biophysics: a primer. *Laser & Photonics Reviews*, 3:203–220, 2009.
- [32] F. Gittes and C. F. Schmidt. Signal and noise in micromechanical measurements. *Methods in Cell Biology*, 55:129–156, 1998.
- [33] T. Aggarwal, D. Materassi, R. Davision, T. Hays, and M. Salapaka. Detection of steps in single molecule data. *Cellular and Molecular Bioengineering*, 5:14–32, 2012.
- [34] F. Gittes and C. F. Schmidt. Thermal noise limitations on micromechanical experiments. *European Biophysics Journal*, 27:75–81, 1998.
- [35] J. T. Finer, R. M. Simmons, and J. A. Spudich. Single myosin molecule mechanics: piconewton forces and nanometre steps. *Nature*, 368:113–119, 1994.
- [36] R. M. Simmons, J. T. Finer, S. Chu, and J. A. Spudich. Quantitative measurements of force and displacement using an optical trap. *Biophysical Journal*, 70:1813–1822, 1996.
- [37] D. G. Cole. Improving single-molecule experiments with feedback control of optical traps. "In publication" *Journal of Dynamic Systems, Measurement, and Control*, 2010.
- [38] J. R. Moffitt, Y. R. Chemla, D. Izhaky, and C. Bustamante. Differential detection of dual traps improves the spatial resolution of optical tweezers. *Proceedings of the National Academy of Sciences*, 103:9006–9011, 2006.
- [39] T. Aggarwal, H. Sehgal, and M. Salapaka. Robust control approach to force estimation in a constant position optical tweezers. *Review of Scientific Instruments*, 82:115108, 2011.

- [40] H. Sehgal, T. Aggarwal, and M. V. Salapaka. High bandwidth force estimation for optical tweezers. *Applied Physics Letters*, 2009:153114, 2009.
- [41] S. Roychowdhury, S. Bhaban, S. Salapaka, and M. V. Salapaka. Design of a constant force clamp and estimation of molecular motor motion using modern control approach. In *American Control Conference 2013*. American Control Conference, June 2013.
- [42] Y. Huang, P. Cheng, and C. H. Meng. Dynamic force sensing using an optically trapped probing system. *IEEE/ASME Transactions on Mechatronics*, 16:1145–1154, 2011.
- [43] A. E. Wallin, A. Salmi, and R. Tuma. Step-length measurement - theory and simulation for tethered bead constant-force single molecule assay. *Biophysical Journal*, 93:795–805, 2007.
- [44] K. C. Neuman, E. H. Chadd, G. F. Liou, K. Bergman, and S. M. Block. Characterization of photodamage to escherichia coli in optical traps. *Biophysical Journal*, 77:2856–2863, 1999.
- [45] A. Ranaweera and B. Bamieh. Modelling, identification, and control of a spherical particle trapped in an optical tweezer. *International Journal of Robust and Nonlinear Control*, 15:747–768, 2005.
- [46] D. G. Cole and J. G. Pickel. Nonlinear proportional plus integral control of optical traps for exogenous force estimation. *Journal of Dynamic Systems, Measurement, and Control*. *Accepted*, 134:011020–1 – 011020–7, 2012.
- [47] D. G. Cole. On nonlinear control of optical traps using pulling trajectory tracking for single-molecule experiments. In *Proceedings of the ASME 2011 International Design Engineering Technical Conferences & Computers and Information in Engineering Conference*, 2011.
- [48] C. Toro and D. Sharbaro. A nonlinear pi controller for optical tweezers system. In *IFAC Conference on Advances in PID Control, PID12*, March 2012.
- [49] D.G. Cole and J.G. Pickel. Nonlinear Proportional Plus Integral Control of Optical Traps for Exogenous Force Estimation. *Journal of Dynamic Systems, Measurement, and Control*. *Accepted*, 134:011020–1 – 011020–7, 2012.
- [50] S. Sastry and M. Bodson. *Adaptive Control Stability, Convergence, and Robustness*. Prentice-Hall Inc., 1989.
- [51] J. C. Doyle, B. A. Francis, and A. R. Tannenbaum. *Feedback Control Theory*. Dover Publications, INC., 2009.
- [52] R. K. Montange, M. S. Bull, E. R. Shanblatt, and T. T. Perkins. Optimizing bead size reduces error in force measurements in optical traps. *Optics Express*, 21:39–48, 2013.

- [53] E. J. G. Peterman, F. Gittes, and C. F. Schmidt. Laser-induced heating in optical traps. *Biophysical Journal*, 84:1308–1316, 2003.
- [54] A. I. Bishop, T. A. Nieminen, N. R. Heckenberg, and H. Runinsztein-Dunlop. Optical microrheology using rotating laser-trapped particles. *Physical Review Letters*, 92:198104–1 – 198104–4, 2004.
- [55] J. Wan, Y. Huang, S. Jhiang, and C. H. Menq. Real-time in situ calibration of an optically trapped probing system. *Applied Optics*, 48:4832–4841, 2009.
- [56] K. D. Wulff, D. G. Cole, and R. L. Clark. An adaptive system identification approach to optical trap calibration. *Optical Express*, 16:4420–4425, 2008.
- [57] K. D. Wulff. *Adaptive Control of an Optical Trap for Single Molecule and Motor Protein Research*. PhD thesis, Duke University, 2007.
- [58] C. C. Cheah, X. Li, X. Yan, and D. Sun. Observer-based optical manipulation of biological cells with robotic tweezers. *IEEE Transactions on Robotics*, 30:68–80, 2014.
- [59] H. Chen, C. Wang, and D. Sun. Dynamics calibration of optically trapped cells with adaptive control technology. In *2013 IEEE International Conference on Robotics and Automation*, 2013.
- [60] A. Rich. The rise of single-molecule DNA biochemistry. *Proc. Natl. Acad. Sci.*, 95:13999–14000, 1998.
- [61] T. P. J. Knowles, M. Vendruscolo, and C. M. Dobson. The amyloid state and its association with protein misfolding diseases. *Nature Reviews Molecular Cell Biology*, 15:384–396, 2014.
- [62] N. Hirokawa, S. Niwa, and Y. Tanaka. Molecular motors in neurons: Transport mechanisms and roles in brain function, development, and disease. *Neuron Review*, 68:610–638, 2010.
- [63] S. P. Jackson and J. Bartek. The DNA-damage response in human biology and disease. *Nature*, 461:1071–1078, 2009.
- [64] M. D. Khokhlova, E. V. Lyubin, A. G. Zhdanov, S. Y. Rykova, I. A. Sokolova, and A. A. Fedyanin. Normal and system lupus erythematosus red blood cell interactions studied by double trap optical tweezers: direct measurements of aggregation forces. *Journal of Biomedical Optics*, 17:025001, 2012.
- [65] Z. Yan, M. Pelton, L. Vigderman, E. R. Zubarev, and N. F. Scherer. Why single-beam optical tweezers trap gold nanowire in three dimensions. *ACS Nano*, 7:8794–8800, 2013.
- [66] O. M. Marago, P. H. Jones, P. G. Gucciardi, G. Volpe, and A. C. Ferrari. Optical trapping and manipulation of nanostructures. *Nature Nanotechnology*, 8:807–819, 2013.

- [67] A. G. Banerjee, S. Chowdhury, W. Losert, and S. K. Gupta. Real-time path planning for coordinated transport of multiple particles using optical tweezers. *IEEE Transactions on Automation Science and Engineering*, 9:669–678, 2012.
- [68] A. Ashkin. History of optical trapping and manipulation of small-neutral particle, atoms, and molecules. *IEEE Journal on Selected Topics in Quantum Electronics*, 6:841–855, 2000.
- [69] A. Ashkin. Acceleration and trapping of particles by radiation pressure. *Physical Review Letters*, 24:156–159, 1970.
- [70] A. Ashkin, J. M. Dziedzic, J. E. Bjorkholm, and S. Chu. Observation of single-beam gradient force optical trap for dielectric particles. *Optics Letters*, 11:288–290, 1986.
- [71] A. Ashkin. Forces of a single-beam gradient laser trap on a dielectric particle sphere in a ray optics regime. *Biophysical Journal*, 61:569–582, 1992.
- [72] A. Robrbach and E. H.K. Stelzer. Optical trapping of dielectric particles in arbitrary fields. *Journal of the Optical Society of America*, 18:839–853, 2001.
- [73] A. Robrbach and E. H.K. Stelzer. Trapping forces, force constant, and potential depths for dielectric sphere in the presence of spherical aberrations. *Applied Optics*, 41:2494–2506, 2002.
- [74] S. M. Block. Construction of optical tweezers. *Cells: a Laboratory Manual*, 2:81.1–81.14, 1998.
- [75] A. Ashkin, J. M. Dziedzic, and T. Yamane. Optical trapping and manipulation of single cells using infrared laser beams. *Nature*, 330:769–771, 1987.
- [76] K. C. Neuman and S. M. Block. Optical trapping. *Review of Scientific Instruments*, 75:2787–2809, 2004.
- [77] M. Born and E. Wolf. *Principles of Optics: electromagnetic theory of propagation interference and diffraction of light*. Pergamon Press, INC., sixth edition, 1980.
- [78] J. W. Goodman. *Introduction to Fourier Optics*. Roberts & Company Publishers, 2005.
- [79] K. D. Wulff, D. G. Cole, and R. L. Clark. Mathematical model of a DIC position sensing system within an optical trap. In *Proc. SPIE, Optics & Photonics*, 2005.
- [80] D. G. Cole, K. D. Wulff, and R. L. Clark. Controlling optical traps: performance and analytical limits. In *Proceeding of SPIE- The International Society for Optical Engineering*, volume 5877, pages 1–11, August 2005.
- [81] W. Denk and W. W. Webb. Optical measurements of piconewton displacements of transparent microscopic objects. *Applied Optics*, 29:2382–2391, 1990.

- [82] K. Visscher, S. P. Gross, and S. M. Block. Construction of multiple-beam optical traps with nanometer-resolution position sensing. *IEEE Journal of Selected Topics in Quantum Electronics*, 2:1066–1076, 1996.
- [83] F. Gittes and C. F. Schmidt. Interference model for back-focal-plane displacement detection in optical tweezers. *Optics Letters*, 23:7–9, 1998.
- [84] M. Born and E. Wolf. *Principles of Optics*. Pergamon Press, 1965.
- [85] A. Pralle, M. Prummer, E.L. Florin, E.H.K. Stelzer, and J.K.H. Horber. Three-dimensional high-resolution particle tracking for optical tweezers by forward scattered light. *Microscopy Research and Technique*, 44:378–386, 1999.
- [86] K. Berg-Sorensen and H. Flyvbjerg. Power spectrum analysis for optical tweezers. *Review of Scientific Instruments*, 75:594–612, 2004.
- [87] I. M. Tolic-Norrelykke, K. Berg-Sorensen, and H. Flyvbjerg. Matlab program for precision calibration of optical tweezers. *Computer Physics*, 159:225–240, 2004.
- [88] P. M. Hansen, I. M. Tolic-Norrelykke, H. Flyvbjerg, and K. Berg-Sorensen. tweezer-calib 2.0: Faster version of matlab package for precise calibration of optical tweezers. *Computer Physics Communications*, 174:518–520, 2006.
- [89] H. D. Ou-Yang. *Colloidal-Polymer Interactions: From Fundamentals to Practice*, chapter 15, pages 385–405. John Wiley & Sons, INC., 1999.
- [90] Y. G. Lee, K. W. Lyons, and T. W. Lebrun. Virtual environment for manipulating microscopic particules with optical tweezers. *Journal of Research of the National Institute of Standards and Technology*, 108:275–287, 2003.
- [91] C. A. Ibanez, H. S. Medina Cinvestav, and A. Barranon. Energy approach for microscopic particles manipulation using optical tweezers. In *Selected Papers from the WSEAS Conferences in Spain*, pages 44–50, September 2008.
- [92] C. A. Ibanez and M. S. Suarez-Castanon and L. I. Rosas-Soriano. A simple control scheme for the manipulation of a particle by means of optical tweezers. *Inter*, 21:328–337, 2011.
- [93] A. Papoulis and S. U. Pillai. *Probability, Random Variables and Stochastic Process*. McGraw Hill, fourth, international edition, 2002.
- [94] G. F. Franklin, J. D. Powell, and A. Emami-Naeini. *Feedback Control of Dynamic Systems*. Pearson, sixth edition, 2010.
- [95] J. F. Marko and E. D. Siggia. Stretching DNA. *Macromolecules*, 28:8759–8770, 1995.

- [96] C. Bouchiat, M. D. Wang, J. F. Allemand, T. Strick, S. M. Block, and V. Croquette. Estimating the persistence length of a worm-like chain molecule from force-extension measurements. *Biophysical Journal*, 76:409/413, 1999.
- [97] C. Bustamante, S. B. Smith, J. Liphardt, and D. Smith. Single-molecule studies of DNA mechanics. *Current Opinion in Structural Biology*, 10:279–285, 2000.
- [98] E. Goshen, W. Z. Zhao, G. Carmon, S. Rosen, R. Granek, and M. Feingold. Relaxation dynamics of a single dna molecule. *Physical Review E*, 71:061920, 2005.
- [99] T. T. Perkins and S. R. Quake and D. E. Smith and S. Chu. Relaxation of a signal dna molecule observed by optical microscopy. *Science*, 264:822–826, 1994.
- [100] R. F. Stengel. *Optical Control and Estimation*. Dover Publications, INC., 1994.
- [101] Chi-Tsong Chen. *Linear System Theory and Design*. CBS College Publishing, 1984.
- [102] H. K. Khalil. *Nonlinear Systems*. Prentice-Hall Inc., second edition, 1996.
- [103] S. Sastry. *Nonlinear Systems Analysis, Stability and Control*. Springer-Verlag, 1999.
- [104] W. L. Brogan. *Modern Control Theory*. Prentice Hall, third edition, 1991.
- [105] R. Hermann and A. J. Krener. Nonlinear controllability and observability. *IEEE Transactions on Automatic Control*, 22(5):728–740, 1977.
- [106] H. Hammouri and M. Farza. Nonlinear observers for locally uniformly observable systems. *ESAIM: Control, Optimisation and Calculus of Variations*, 9:353–370, 2003.
- [107] B. D. O. Anderson and J. B. Moore. *Optimal Filtering*. Dover Publications, INC., 2005.
- [108] Jeffrey B. Burl. *Linear Optimal Control  $H_2$  and  $H_\infty$  Methods*. Addison Wesley Longman, INC, 1999.
- [109] D. Kirk. *Optimal Control Theory An Introduction*. Dover Publications, INC., 2004.
- [110] A. J. Krener and M. Xiao. Nonlinear observer design in the siegel domain. *Siam Journal on Control and Optimization*, 41:932–953, 2002.
- [111] N. Kazantzis and C. Kravis. Nonlinear observer design using lyapunov’s auxiliary theorem. In *Proceedings of the 36th Conference on Decision & Control*, December 1997.
- [112] R. A. Wright, C. Kravaris, and N. Kazantzis. Model-based synthesis of nonlinear *PI* and *PID* controllers. *AIChE Journal*, 47:1805–1818, 2001.
- [113] R. Marino and P. Tomei. Global adaptive observers for nonlinear systems via filtered transformations. *IEEE Transactions on Automatic Control*, 37:1239–1245, 1992.

- [114] R. Marino and P. Tomei. Adaptive observers with arbitrary exponential rate of convergence for nonlinear systems. *IEEE Transactions on Automatic Control*, 40:1300–1304, 1995.
- [115] Q. Zhang. Adaptive observer for multiple-input-multiple-output (mimo) linear time-varying systems. *IEEE Transactions on Automatic Control*, 47:525–529, 2002.
- [116] Veronica Adetola, Martin Guay, and Devon Lehrer. Adaptive Estimation for a Class of Nonlinear Parameter Dynamical Systems. *IEEE Transactions on Automatic Control*, 59:2818–2824, 2014.
- [117] M. Farza, M. M’Saad, T. Maatoug, and M. Kamoun. Adaptive observers for nonlinear paraproblem class of nonlinear systems. *Automatica*, 45:2292–2299, 2009.
- [118] Y. Zhu and P. R. Pagilla. Adaptive controller and observer design for a class of nonlinear systems. In *Proceedings of the 42th IEEE Conference on Decision and Control*, 2003.
- [119] Y. Zhu and P. R. Pagilla. Adaptive controller and observer for a class of nonlinear systems. *Journal of Dynamic Systems, Measurement, and Control*, 128:712–717, 2006.
- [120] O. N. Starnes, J. Zhou, O. M. Aamo, and G. O. Kaasa. Adaptive observer design for nonlinear systems with parametric uncertainty in unmeasured state dynamics. In *Joint 48th IEEE Conference on Decision and Control and 28th Chinese Control Conference*, 2009.
- [121] M. Farza and I. Bouraoui and T. Menard and R. B. Abdenour. Adaptive observers for a class of uniformly observable systems with nonlinear parametrization and sampled outputs. *Automatica*, 50:2951–2960, 2014.
- [122] V. Adetola and M. Guay. Performance improvement in adaptive control of nonlinear systems. In *2009 American Control Conference*, 2009.
- [123] M. Farza, M.M’Saad, and L. Rossignol. Observer design for a class of mimo nonlinear systems. *Automatica*, 40:135–143, 2004.
- [124] K. J. Astrom and B. Wittenmark. *Adaptive Control*. Dover, second edition, 2008.
- [125] Petros A. Ioannou and Jing Sun. *Robust Adaptive Control*. Prentice Hall, 1995.
- [126] S. B. Smith, Y. Cui, and C. Bustamante. Overstretching B-DNA: The elastic response of individual double-stranded and single-stranded DNA molecules. *Science*, 271:795–799, 1996.
- [127] H. Yin, R. Landick, and J. Gelles. Tethered particle motion method for studying transcript elongation by a single RNA polymerase molecule. *Biophysical Journal*, 67:2466–2478, 1994.

- [128] A. A. Al Balushi, A. Zehtabi-Oskuie, and R. Gordon. Observing single protein binding by optical transmission through a double nanohole aperture in a metal film. *Biomedical Optics Express*, 4:1504–1511, 2013.
- [129] M. D. Wang, M. J. Schnitzer, H. Yin, R. Landick, J. Gelles, and S. M. Block. Force and velocity measured for single molecules of rna polymerase. *Science*, 282:902–907, 1998.
- [130] N. Forns, S. de Lorenzo, M. Manosas, K. Hayashi, J. M. Huguet, and F. Ritort. Improving signal/noise resolution in single-molecule experiments using molecular constructs with short handles. *Biophysical Journal*, 100:1765–1774, 2011.
- [131] R. Michel, S. Pasche, M. Textor, and D. G. Castner. Influence of peg architecture on protein adsorption and conformation. *Langmuir*, 21:12327–12332, 2005.